AI-Assisted Ultrasound-Guided High-Intensity Focused Ultrasound (USgHIFU) in Non-Invasive Surgery

by

Salman Lari

A thesis
presented to the University of Waterloo
in fulfillment of the
thesis requirement for the degree of
Doctor of Philosophy
in
Mechanical and Mechatronics Engineering

Waterloo, Ontario, Canada, 2024

© Salman Lari 2024

Examining Committee Membership

The following served on the Examining Committee for this thesis. The decision of the Examining Committee is by majority vote.

Supervisors:

Hyock Ju Kwon
Associate Professor, Dept. of Mechanical and Mechatronics Engineering,
University of Waterloo

Jong Uk Kim
Adjunct Professor, Dept. of Mechanical and Mechatronics Engineering,
University of Waterloo

Internal Members:

Arash Arami
Associate Professor, Dept. of Mechanical and Mechatronics Engineering,
University of Waterloo

Kamyar Ghavam
Associate Professor, Dept. of Mechanical and Mechatronics Engineering,
University of Waterloo

Internal-External Member:

Mohammad Kohandel
Professor, Dept. of Applied Mathematics,
University of Waterloo

External-External Member:

Gibin Powathil
Professor, Dept. of Mathematics,
Swansea University

Author's Declaration

I hereby declare that I am the sole author of this thesis. This is a true copy of the thesis, including any required final revisions, as accepted by my examiners.

I understand that my thesis may be made electronically available to the public.

Abstract

This comprehensive study combines several innovative approaches to enhance the precision and efficacy of high-intensity focused ultrasound (HIFU) for cancer treatment. HIFU, a non-invasive therapeutic technique, uses high-frequency ultrasound to ablate tumors, but requires careful planning due to its potential for collateral damage to healthy tissues. To overcome these challenges, multiple methodologies are introduced.

By employing a Physics-Informed Neural Network (PINN) integrated with a realistic breast model, breast tumors are targeted with high precision. The model utilizes a bowl-shaped acoustic transducer to focus ultrasound waves directly on the tumor, achieving intense localized heating. The PINN method efficiently solves partial differential equations in a mesh-free domain, providing high accuracy with significantly lower computational demands than traditional finite element methods (FEM).

This model is employed to understand the governing dynamics of the HIFU process, particularly the heat transfer mechanisms during sonication. Using machine learning techniques, the model simulates the absorption mechanism and temperature rise, validated through *ex vivo* experiments with bovine liver. This helps in accurately predicting and visualizing the effects of treatment, facilitating the development of personalized treatment strategies.

A novel deep learning-based optimization procedure is used for preoperative treatment planning. It determines optimal focal locations and sonication times for each ablation session, ensuring minimal tissue over- or under-treatment. This algorithm has shown high potential in handling various HIFU presurgical plans and is especially effective in creating precise treatment plans based on patient-specific material properties.

Addressing the limitations of manual HIFU operations, a real-time, low-cost image segmentation framework based on the Swin-Unet architecture is proposed. This system is trained and tested on B-mode imaging simulations and real images from HIFU-treated chicken breast, demonstrating high efficiency in lesion segmentation and offering potential for monitored, automated HIFU therapy.

By integrating these diverse approaches, the study not only enhances the thermal effects of HIFU but also offers a framework for safer, more precise, and individually tailored cancer treatments. The combined use of advanced simulation models, deep learning approaches, and innovative technologies aims to significantly improve the therapeutic outcomes of HIFU, making it a more viable option for cancer treatment with reduced risks and enhanced efficacy.

Acknowledgements

Completing this PhD journey has been one of the most challenging and rewarding experiences of my life, and it would not have been possible without the support and guidance of many individuals.

First and foremost, I would like to express my deepest gratitude to my supervisors, Prof. Hyock Ju Kwon and Prof. Jong Uk Kim, for their invaluable guidance, encouragement, and insightful feedback throughout my research. Their unwavering support and expertise have been instrumental in shaping the direction and success of this work.

I am deeply thankful to my advisory committee, Prof. Arash Arami, Prof. Kamyar Ghavam, Prof. Mohammad Kohandel, and Prof. Gibin Powathil, for their constructive critiques and thoughtful suggestions, which have helped refine this thesis. I would also like to extend my appreciation to my collaborators and colleagues, particularly Dr. Jeongwoo Han and Hossein Rajabzadeh, whose discussions and shared ideas have greatly enriched this research.

A heartfelt thanks to my family for their endless love, patience, and encouragement. To my wife, Dorsa Sadat Hosseini, for her unwavering belief in my abilities and for being my constant source of inspiration, and to my parents, Saeed and Leila, who have been my pillars of strength and motivation.

I would also like to acknowledge my friends and peers for their camaraderie and for making this journey less daunting through their companionship and moral support.

Last but not least, I am grateful to the University of Waterloo and the Department of Mechanical and Mechatronics Engineering for providing me with the resources and opportunities to conduct this research. Additionally, I extend my thanks to Waterloo Institute for Nanotechnology (WIN) for their financial support, which has made this work possible.

This thesis is a culmination of the efforts, sacrifices, and contributions of all those mentioned above, and I dedicate this work to them with immense gratitude.

Dedication

This is dedicated to the one I love.

Table of Contents

List of Figures x

List of Tables xiv

1 Introduction 1

1.1 Motivation . . . 2

1.2 Thesis Objectives . . . 2

1.3 Contributions of the Field . . . 3

1.4 Thesis Structure . . . 5

2 Literature Review 6

2.1 Simulation . . . 7

2.2 Presurgical Plan . . . 11

2.3 Segmentation . . . 20

3 Physics-Informed Neural Network (PINN) Solution for HIFU 26

3.1 HIFU Ablation Mechanism . . . 27

3.2 Governing Equations . . . 32

3.2.1 Acoustic Wave Generation and Propagation . . . 32

3.2.2 Bioheat Transfer in Breast Tissues . . . 34

3.2.3 Prediction of the Fraction of Necrotic Tissue . . . 37

3.3 Geometry of the Model . . . 38
3.4 Simulation Procedure . . . 45
3.5 Physics-Informed Neural Network (PINN) . . . 57
3.6 Finite Element Modeling . . . 65
3.6.1 Mesh Study . . . 67
3.7 Validation and Experiment . . . 76
3.7.1 Experimental Procedure . . . 76
3.7.2 Pressure Acoustics Phenomenon (Montienthong & Rattanadecho Study [114]) . . . 77
3.7.3 Heat Transfer Phenomenon (Montienthong & Rattanadecho Study [114]) . . . 79

4 Deep Learning Method for HIFU Pathway Scanning 82
4.1 Problem Description . . . 82
4.2 Image Processing Procedure . . . 84
4.3 Deep Learning Computation . . . 87
4.3.1 Model-Based Neural Network . . . 87
4.3.2 Deep Learning-Based Presurgical Plan . . . 89

5 HIFU Induced Lesion Segmentation 94
5.1 Problem Definition . . . 94
5.2 B-Mode Imaging Simulation . . . 97
5.2.1 Governing Equations . . . 97
5.2.2 k-space Method . . . 99
5.2.3 Numerical Simulation . . . 101
5.3 AI-Assisted Lesion Segmentation . . . 104
5.3.1 Swin-Unet . . . 104
5.3.2 Training Procedure . . . 108

6 Results and Discussions **111**
6.1 PINN Simulation . . . 111
6.1.1 Acoustic Field Generation . . . 112
6.1.2 Temperature Distribution . . . 112
6.1.3 Distribution of Necrotized Tissue Fraction . . . 116
6.1.4 Realistic Clinical Approach . . . 122
6.1.5 Validation and Computational Efficiency . . . 128
6.1.6 Uncertainty Quantification . . . 130
6.2 Pathway Scanning . . . 132
6.2.1 Computational Results . . . 133
6.2.2 Experimental Validation . . . 141
6.3 HIFU-Induced Lesion Segmentation . . . 146
6.3.1 B-Mode Imaging Simulation . . . 146
6.3.2 Image Segmentation . . . 149

7 Conclusion and Future Work **152**
7.1 PINN-Based HIFU . . . 152
7.2 Presurgical Planning . . . 153
7.3 Lesion Segmentation . . . 155
7.4 Limitations and Future Work . . . 155

References **159**

List of Figures

3.1 A schematic of the HIFU ablation process for the treatment of a breast tumor. 31

3.2 3D visualization of the entire geometry considered. 39

3.3 Middle cross-section view of the geometry. 41

3.4 Three distinct processes were used to build a 3D breast phantom: (a) obtaining a point cloud from the database; (b) constructing surfaces from the point cloud; and (c) producing the volume from knitted surfaces. 44

3.5 Considered 3D geometry of tissue types separately and collectively: (a) FCG tissue; (b) transitional tissue; (c) fatty tissue, muscle, and tumor; and (d) all tissues within each other as the ARBP. 46

3.6 Boundary conditions considered in different physics, (a) pressure acoustics and (b) bioheat transfer. 50

3.7 Considered cut planes that pass through the center of the tumor. 56

3.8 Diagram of PINN architecture for solving PDE. The input layer of the neural network with spatial inputs and temporal. The output layer computes the solution of the given PDE and embeds it into the loss function. PDE can have constraints such as initial conditions and boundary conditions. By minimizing the loss function, PINN can generate the solution with respect to the previous conditions. 58

3.9 Diagram of PINN architecture for solving the 3D Helmholtz equation and tBHTE to predict the temperature rise. The upper neural network with three spatial inputs x, y, and z, and the pressure result p as the output value. The lower neural network takes three previous spatial inputs as well as a temporal input, t, and produces the temperature result, T, as the output value. Other sections are PDE, initial conditions(IC) and boundary conditions (BC). The last section represents the loss functions embedded with PDE, BC and IC along with the training output T. By minimizing the loss function, PINN can generate the heat mao with respect to the previous conditions. 66

3.10 Grid independency test for each physics. 71

3.11 Optimum grid generation considered for each physics. "Pressure acoustics" physics: (a) whole geometry, (b) sliced magnified model. "Bioheat transfer" physics: (c) whole geometry, (d) sliced magnified model. 75

3.12 Comparison of the maximum total acoustic pressure and the maximum sound intensity magnitude obtained from our simulations (FEM and PINN) and the Montienthong & Rattanadecho's simulation. 78

3.13 Comparison of FEM and deep learning simulations, experimental results, and Montienthong & Rattanadecho simulation plots of the temperature distribution in the focal point during the time. 80

4.1 Schematics of the problem description. 83

4.2 Segmented breast MRI of four patients. 85

4.3 Diagram of NN architecture for finding optimal HIFU pathway. The input layer of the NN includes tumor's spatial inputs. The output layer computes the solution of the given model and embeds it into the loss function. By minimizing the loss function, NN can generate the surgical plan with respect to the previous conditions. 88

4.4 Diagram of NN architecture for solving the 2D optimal pathway scanning to predict the HIFU surgical plan. The first section is the NN with two spatial inputs z,r and the total number of sonication N, and the HIFU pathway parameters as the output value. The next two sections are acoustic and thermal analyses. The last section represents the HIFU loss function embedded with the deep learning algorithm, with the training sonication output. By minimizing the loss function, NN can generate the optimal HIFU pathway with respect to the predefined constraints. 92

5.1 The proposed intelligent HIFU therapeutical framework is applied in the image-based HIFU diagnostic and treatment processing. The framework includes diagnosis and treatment parts. In the diagnosis part, morphology and spatial information in preoperative and intra-operative medical images can be accurately obtained and provided to the treatment strategy. 96

5.2 The integration of machine learning with ultrasound imaging involves preprocessing of B-mode images taken before and after HIFU treatment by clipping them to a predetermined surgical region. The images are then resized to 224×224 gray-scale resolutions and concatenated with their pixel-wise difference to form a three-channel image that is fed to the Swin-Unet model, which outputs the segmented region of the HIFU ablation. 105

6.1 Total acoustic pressure field, (a) FEM cut plane 1, (b) FEM cut plane 2, (c) FEM cut plane 3, (d) PINN cut plane 1, (e) PINN cut plane 2, (f) PINN cut plane 3. Sound intensity magnitude (Wm^{-2}), (g) FEM cut plane 1, (h) FEM cut plane 2, (i) FEM cut plane 3, (j) PINN cut plane 1, (k) PINN cut plane 2, (l) PINN cut plane 3. 113

6.2 Absolute pressure distribution along lines passing through the tumor's center in different directions, (a) x-direction, (b) y-direction, (c) z-direction. . . . 114

6.3 Sound intensity magnitude distribution along lines passing through the tumor's center in different directions, (a) x-direction, (b) y-direction, (c) z-direction. 115

6.4 Distribution of temperature after 1 second, (a) FEM cut plane 1, (b) FEM cut plane 2, (c) FEM cut plane 3, (d) PINN cut plane 1, (e) PINN cut plane 2, (f) PINN cut plane 3. Distribution of necrotic tissue fraction after 10 s of the ablation process, (g) FEM cut plane 1, (h) FEM cut plane 2, (i) FEM cut plane 3, (j) PINN cut plane 1, (k) PINN cut plane 2, (l) PINN cut plane 3.117

6.5 Temperature distribution after 1 s along lines passing through the tumpr's center in different directions, (a) x-direction, (b) y-direction, (c) z-direction. 118

6.6 Fraction of necrotic tissue after 10 s ablation process along lines passing through tumor's center in different directions, (a) x-direction, (b) y-direction, (c) z-direction. 120

6.7 Temperature and fraction of necrotic tissue at the tumor's center during ablation time: (a) Temperature change, (b) fraction of necrotic tissue. . . . 121

6.8 (a-f) sound intensity magnitude in the cut plane 1 during each of the three lesion processes for FEM and PINN, (g-l) temperature distribution in the cut plane at the end of each lesson process for FEM and PINN, (m-r) fraction of necrotic tissue distribution in the cut plane 1 at the end of each lesion process for FEM and PINN. 123

6.9 Temperature and the fraction of necrotic tissue after 6 s, 17 s, 28 s, and 100 s along the line passing through the tumor's center in the x direction. . . . 125

6.10 The process that AI finds the best presurgical plan for a desired tumor. . . 134

6.11 Presurgical plan for patient 1. 137

6.12 Presurgical plan for patient 2. 137

6.13 Presurgical plan for patient 3. 137

6.14 Presurgical plan for patient 4. 137

6.15 Comparison of the numerical simulation with experimental treatment plan composed of 3 sonications. 142

6.16 Comparison of simulation and experimental results for the temperature distribution in the focal point during HIFU sonications including 10 s heating and 90 s cooling. 144

6.17 Comparison of the AI proposed method with conventional treatment plan. 145

6.18 A series of frames from a simulation study, showcasing the progression and visualization of thermal dose accumulation induced by HIFU and the corresponding B-mode ultrasound images. Each frame sequentially reveals the development of the thermal region and its detection via B-mode imaging, demonstrating the dynamic response of tissue to HIFU therapy over time. . 147

6.19 A detailed evaluation of the proposed framework's performance shows that the red areas represent the actual lesion, while the green regions indicate the segmented areas. Any discrepancies between the red and green regions in each sub-image are considered errors in HIFU segmentation. 149

6.20 A detailed evaluation of the proposed framework's performance for *ex vivo* experiment shows that the blue areas represent the actual lesion, while the yellow regions indicate the segmented areas. Any discrepancies between the blue and yellow regions in each sub-image are considered errors in HIFU segmentation. 151

List of Tables

3.1 Thermophysical and acoustic properties of different materials [14, 166, 135, 151, 110, 28, 65, 59, 134]. . . . 49

3.2 Quantitative amounts and relative errors of different considered mesh cases for each of the physics. . . . 73

3.3 Comparison between our simulations results, experiment, and Montienthong & Rattanadecho's simulation results [114]. . . . 81

6.1 Validation Metrics for Comparison with FEM Results. . . . 129

6.2 Computational Time and Resource Usage Comparison. . . . 129

6.3 Sensitivity Analysis Results. . . . 131

6.4 Uncertainty Quantification Results. . . . 131

6.5 Treatment parameters calculated by the proposed algorithm for each patient. 139

6.6 Quantitative comparison between our previous work [87] and the current AI approach. . . . 140

6.7 Quantitative comparison between experiments and simulations. . . . 140

6.8 Quantitative comparison between the proposed AI method and the conventional approach. . . . 146

6.9 The results present the performance evaluation of the proposed segmentation framework. Each row summarizes an experiment, detailing the mean absolute errors and dice scores to assess the framework's performance. . . . 150

Chapter 1

Introduction

The need for advanced, non-invasive cancer treatments has grown in urgency with the increasing global incidence of breast cancer. Traditional treatments, though effective, often involve invasive procedures, leading to significant physical and emotional impacts on patients. This context has paved the way for High-Intensity Focused Ultrasound (HIFU) as a promising alternative. HIFU, which uses high-frequency ultrasound waves to target and ablate tumors without requiring surgical incisions, offers distinct advantages, such as reduced recovery times, minimal trauma, and cost-effectiveness, positioning it as an innovative approach in oncology.

This thesis explores the potential of HIFU when enhanced through artificial intelligence (AI), focusing on a unique AI-assisted, ultrasound-guided HIFU (USgHIFU) system aimed at improving precision, safety, and efficacy in treating breast tumors. Central to this approach is the application of a Physics-Informed Neural Network (PINN) that simulates the complex dynamics of ultrasound energy propagation within biological tissues. This neural network provides a solution that not only addresses the thermal and acoustic challenges associated with HIFU but also adapts to individual anatomical variances, thus paving the way for highly personalized treatment strategies.

The study proposes a comprehensive framework that integrates deep learning for optimized preoperative planning and real-time treatment monitoring. Additionally, a novel segmentation technique based on the Swin-Unet architecture has been developed to enable precise lesion detection, reducing risks associated with incomplete ablation. By integrating these elements, this research aspires to advance HIFU's clinical applications and establish a robust foundation for future non-invasive cancer therapies.

1.1 Motivation

This thesis investigates a revolutionary approach to non-invasive cancer treatment through HIFU guided by ultrasound imaging and augmented by AI. With the increasing prevalence of cancer globally, there is an urgent need for safer, effective, and patient-friendly alternatives to traditional surgery. Conventional cancer treatments, while effective, often bring about adverse physical and emotional impacts, emphasizing the importance of non-invasive techniques. HIFU presents an attractive solution by focusing ultrasound energy directly on the tumor, raising the temperature to therapeutic levels, and ablating the cancerous tissue without the need for incisions. Yet, HIFU's practical application faces challenges, such as ensuring precision targeting, avoiding damage to surrounding healthy tissue, and maintaining effectiveness across varying anatomical complexities.

The development of AI technologies has provided an unprecedented opportunity to address these challenges. This research leverages a PINN model, allowing for the accurate simulation of ultrasound interactions within biological tissues, which is instrumental in optimizing HIFU treatments. Additionally, advanced machine learning techniques enable the study to optimize preoperative treatment planning, automate lesion segmentation, and improve real-time monitoring—core aspects that traditional methods struggle to handle efficiently. The integration of Swin-Unet architecture for real-time segmentation further refines the precision of HIFU therapy, thus reducing treatment risks and ensuring comprehensive tumor coverage. This framework's potential extends to enhancing the safety, efficacy, and personalization of cancer treatments, presenting HIFU as a viable, patient-centered alternative in oncology.

By bridging machine learning with HIFU, this thesis lays the groundwork for advanced, precise, and safer cancer treatments, envisioning a future where non-invasive therapies offer effective alternatives to conventional procedures. The insights from this work contribute to a broader vision of AI-driven healthcare, where precision, personalized care, and minimal patient trauma are achievable goals in treating complex medical conditions like cancer.

1.2 Thesis Objectives

The primary objective of this thesis is to enhance the precision, safety, and efficacy of HIFU therapy for non-invasive cancer treatment, specifically targeting breast tumors. This objective is pursued through the integration of AI with USgHIFU systems. To achieve this overarching goal, the following specific objectives are set:

1. **Develop a PINN Model:** Construct a deep-learning-based PINN model to simulate the propagation of ultrasound waves in biologically realistic breast tissue. This model aims to solve complex partial differential equations governing heat and acoustic wave interactions, with high computational efficiency compared to traditional finite element methods.

2. **Optimize HIFU Treatment Pathways:** Establish a deep learning-based optimization procedure to improve preoperative treatment planning. The goal is to determine optimal focal locations, sonication times, and scanning pathways that minimize both treatment duration and collateral damage to healthy tissues. This personalized planning will ensure the comprehensive ablation of tumor tissues with minimal exposure to surrounding areas.

3. **Enhance Real-Time Monitoring through Image Segmentation:** Design and implement an advanced image segmentation framework based on the Swin-Unet architecture to accurately detect and delineate HIFU-induced lesions in real-time. This system will assist in reducing manual intervention, increase lesion segmentation accuracy, and facilitate automated feedback for adaptive treatment monitoring.

4. **Experimental Validation and Personalized Treatment Strategy:** Validate the proposed models through *ex vivo* experiments using biological tissues to confirm their accuracy in predicting thermal and acoustic effects. The experimental phase aims to develop a personalized treatment strategy that integrates AI, computational modeling, and empirical data to offer safer and more precise HIFU therapies.

By achieving these objectives, this thesis aims to establish a holistic, AI-enhanced HIFU system that not only targets tumor tissues with high precision but also facilitates real-time monitoring and individualized treatment planning, contributing to the broader adoption of non-invasive cancer therapies in clinical practice.

1.3 Contributions of the Field

This thesis makes several key contributions to the field of HIFU therapy, especially in the context of breast cancer treatment using AI-assisted USgHIFU systems. The major contributions are as follows:

1. **Development of a PINN Model for HIFU Simulation:** This work introduces a novel PINN model to simulate the complex physical interactions of ultrasound

waves with biological tissues in a three-dimensional, anatomically realistic breast phantom. By leveraging the PINN approach, the computational challenges associated with traditional methods such as finite element modeling are mitigated, leading to improved simulation accuracy and efficiency for HIFU therapy applications.

2. **Personalized Preoperative Treatment Planning Using Deep Learning:** A significant contribution of this thesis is the development of a deep learning-based optimization framework for personalized preoperative planning. By employing machine learning techniques, the optimal focal locations, scanning pathways, and sonication times for HIFU treatment are identified, reducing both treatment time and risks associated with overtreatment or undertreatment of tissues. This approach provides a new way to achieve precise, patient-specific therapeutic outcomes.

3. **Real-Time Image Segmentation for Automated HIFU Therapy Monitoring:** The thesis also presents an innovative real-time image segmentation framework utilizing the Swin-Unet architecture, which is used for monitoring HIFU therapy. This segmentation approach is validated using both simulated and real imaging data, demonstrating its effectiveness in accurately identifying ablated regions. The framework enhances the precision of treatment and reduces the dependence on manual interventions, thereby contributing to automated, efficient HIFU treatment systems.

4. **Experimental Validation and Translation to Clinical Applications:** Experimental validation through *ex vivo* studies involving bovine liver is conducted to assess the accuracy of the proposed methods in predicting temperature distribution and necrotic tissue fraction. These experiments confirm the ability of the proposed models to predict outcomes reliably, thus providing strong evidence for the potential clinical application of AI-enhanced HIFU therapy in cancer treatment.

5. **Holistic Framework for Safer, Non-Invasive Cancer Treatment:** By integrating advanced simulation models, optimization algorithms, and real-time monitoring solutions, this work provides a holistic framework for safer, non-invasive cancer treatment using HIFU. The proposed framework aims to make HIFU a more viable, accessible option in clinical oncology by improving both precision and safety, ultimately advancing the capabilities of non-invasive therapeutic technologies.

Overall, this thesis contributes novel methodologies that combine AI, deep learning, and medical physics to overcome current limitations in HIFU treatment. These advancements have the potential to significantly impact both the research community and clinical practice, offering a pathway toward more precise and personalized cancer treatments.

1.4 Thesis Structure

The thesis is organized into seven chapters, each of which addresses a specific aspect of the research:

1. **Introduction:** This chapter provides an overview of the motivation for the research, the significance of HIFU in non-invasive cancer treatment, and the role of artificial intelligence in enhancing HIFU therapy. It outlines the main objectives and contributions of the thesis.

2. **Literature Review:** This chapter presents a comprehensive review of the existing literature related to HIFU, AI-assisted treatment techniques, and relevant computational models. It highlights the current challenges and knowledge gaps that this research aims to address.

3. **PINN Model for HIFU:** This chapter details the development of the PINN model for simulating ultrasound wave propagation and heat transfer in biological tissues. The methodology, underlying mathematical models, and advantages of using PINNs are discussed in depth.

4. **Deep Learning for Personalized Preoperative Planning:** This chapter describes the design and implementation of the deep learning-based optimization framework for preoperative planning. It covers the methods used to identify optimal sonication parameters and scanning pathways for personalized HIFU treatment.

5. **Real-Time Image Segmentation Framework:** This chapter focuses on the development of the Swin-Unet-based image segmentation framework for real-time monitoring of HIFU therapy. The approach, training process, and experimental validation are discussed.

6. **Experimental Validation and Results:** This chapter presents the experimental setup, validation studies, and results obtained from ex vivo experiments. It demonstrates the accuracy and reliability of the proposed models in predicting temperature distribution and tissue necrosis.

7. **Conclusion and Future Work:** The final chapter summarizes the key findings and contributions of the research. It also discusses the limitations of the current work and provides suggestions for future research directions to further enhance the efficacy of AI-assisted HIFU therapy.

Chapter 2

Literature Review

With cancer incidence on the rise, as noted by the World Health Organization (WHO) with expectations to triple by 2030 [14], the need for innovative and effective treatment methods has never been more pressing. Breast cancer specifically continues to pose a significant risk, leading to 284,200 new cases and 44,130 deaths in 2021 in the United States alone [140]. Traditional surgical interventions, while effective, come with significant limitations and risks, particularly for patients with early-stage tumors who might benefit from less invasive treatments [114]. These limitations have driven a growing demand for alternative treatments that can offer similar or better efficacy with reduced invasiveness and fewer side effects.

High-Intensity Focused Ultrasound (HIFU) emerges as a promising solution to these challenges. This innovative technology uses high-frequency sound waves to precisely target and destroy cancer cells without the need for surgical incisions, thereby minimizing physical trauma and recovery time for patients [114, 78]. HIFU has demonstrated significant efficacy in treating both benign and malignant tumors, showcasing its versatility and potential as a mainstream cancer treatment.

One of the key advantages of HIFU over traditional surgical methods is its non-invasive nature, which not only reduces the risk of infection and other complications associated with surgery but also improves the overall patient experience and comfort. Additionally, HIFU is cost-effective, potentially reducing the financial burden on healthcare systems and patients [158].

Another noteworthy benefit of HIFU is its ability to enhance drug delivery. By disrupting cell membranes, HIFU can facilitate the more effective penetration of chemotherapeutic

agents, thereby improving their efficacy and potentially reducing the required dosage and associated side effects [158].

Overall, the integration of HIFU into cancer treatment protocols represents a groundbreaking advancement in oncology, offering a safer, more effective, and less invasive alternative to traditional surgical interventions. As research and clinical applications continue to evolve, HIFU has the potential to significantly impact the management of various types of cancer, improving patient outcomes and quality of life.

Recent studies highlight HIFU's potential as a non-invasive method for breast tumor removal, offering significant advancements in cancer treatment with minimal physical trauma to patients. Deckers et al. [32] evaluated a specialized breast MRHIFU system, demonstrating its capability to precisely target and ablate tumor tissues while preserving surrounding healthy tissues. Similarly, Peek et al. [128] reviewed various applications of HIFU in breast cancer treatment, emphasizing its versatility and efficacy in clinical settings. Feril et al. [45] focused on the clinical use of HIFU specifically for breast cancer, showcasing promising results in terms of tumor reduction and patient outcomes.

2.1 Simulation

Despite these numerous experimental inquiries into HIFU, a notable gap remains in comprehensive studies simulating its complex multiphysics phenomena on realistic models. This gap hinders a deeper understanding of the intricate interactions between ultrasound waves and biological tissues, which is crucial for optimizing treatment protocols and improving patient outcomes. Addressing this gap is essential for advancing the clinical application of HIFU and ensuring its safety and effectiveness across diverse patient populations.

In response to this need, our current research develops a deep-learning model to explore HIFU's effectiveness, building on insights from recent, significant analytical and numerical studies in this area. By leveraging the power of deep learning, we aim to simulate the complex interactions within the human body more accurately, providing a robust framework for predicting treatment outcomes and tailoring HIFU protocols to individual patient needs. This approach not only enhances our understanding of HIFU's therapeutic mechanisms but also paves the way for personalized cancer treatment strategies, potentially revolutionizing the landscape of non-invasive oncology treatments.

In recent years, significant advancements have been made in simulating the effects of HIFU on various tissues, contributing to a deeper understanding of its therapeutic potential and optimization. Yoon and colleagues [177] developed a multi-resolution simulation using

the finite-difference time-domain formulation for acoustic wave transmission, providing a detailed analysis of how acoustic waves propagate through different tissue types. This foundational work paved the way for more precise modeling of HIFU applications.

Building on this, Gupta et al. [52] and Rezaeian et al. [139] focused on the thermal behavior of tissues under HIFU treatment. Gupta's team explored the delivery of thermosensitive liposomal doxorubicin using HIFU, showcasing how targeted heat can enhance drug delivery and efficacy in cancer treatment. Rezaeian et al.'s study further elucidated the complex thermal dynamics involved, highlighting critical factors that influence the treatment's effectiveness and safety.

Montienthong et al. [114] specifically addressed HIFU ablation in breast cancer treatment using a two-dimensional model. Their research demonstrated the potential of HIFU to precisely target and ablate tumor tissues while minimizing damage to surrounding healthy tissues. This study reinforced the importance of accurate modeling in developing effective HIFU treatment protocols.

Further expanding the understanding of thermal effects, Gupta et al. [53] investigated the thermal wave model for bioheat transfer, providing a nuanced perspective on heat distribution during HIFU treatment. This work contrasted with Kaczmarek et al.'s [77] use of Pennes' bio-heat equation to examine the impact of magnetic nanoparticles on heat transfer during ultrasound hyperthermia. These studies collectively highlighted the diverse methodologies and models used to simulate heat transfer, each contributing unique insights into optimizing HIFU therapy.

Additionally, Mohammadpour et al. [113] studied heat transfer and hemodynamics in HIFU ablation of the porous liver. Their comprehensive approach integrated the complexities of liver tissue structure and blood flow, providing a holistic view of HIFU's multifaceted effects on biological tissues. This research emphasized the importance of considering hemodynamic factors in developing accurate and effective HIFU treatment plans.

Overall, these studies illustrate the rapid advancements in simulating HIFU's effects, underscoring the importance of detailed and accurate models in enhancing the efficacy and safety of HIFU treatments. By continuing to refine these models and integrating new insights, researchers can further optimize HIFU protocols, ultimately improving patient outcomes and expanding the clinical applications of this promising technology.

The literature on HIFU has been constrained by a lack of comprehensive 3D modeling and the absence of studies using anatomically accurate breast phantoms due to their inherent complexity. Traditional numerical methods often fall short in capturing the intricate details required for precise simulations of HIFU treatment, particularly in

the context of complex biological structures like the breast. To bridge this gap, leveraging machine learning and deep neural networks has become increasingly effective. These advanced computational techniques extend to scientific computing, where they facilitate differential and integral calculations, offering a robust alternative to traditional numerical methods [5, 40, 124, 146, 130, 4, 108, 8, 150].

Machine learning, particularly deep learning, has revolutionized the way researchers approach the simulation and analysis of medical procedures. The use of deep neural networks allows for the processing of large datasets and the extraction of complex patterns that might be overlooked by conventional methods. This shift towards employing deep learning for obtaining numerical solutions and handling the challenges of data acquisition in the medical field has led to significant advancements in HIFU research.

One of the most promising developments in this area is the advent of physics-informed neural networks (PINNs). PINNs are designed to integrate the fundamental laws of physics directly into the training process of neural networks, ensuring that the solutions they generate adhere to the underlying physical principles governing the problems [137]. This approach not only enhances the accuracy of simulations but also provides a powerful tool for modeling realistic clinical procedures. By incorporating the physics of HIFU into neural network models, researchers can simulate detailed ablation processes with a high degree of precision.

The application of PINNs in HIFU research offers several advantages. First, it allows for the creation of highly accurate 3D models that can capture the complex interactions between ultrasound waves and biological tissues. These models can simulate the effects of HIFU on breast tissue with unprecedented detail, providing insights that are critical for optimizing treatment protocols. Second, PINNs can handle the variability and complexity of patient-specific anatomical features, leading to more personalized and effective treatment plans.

Furthermore, the integration of machine learning techniques in HIFU research addresses the limitations associated with data acquisition and computational resources. Deep learning models can process vast amounts of medical data, identifying patterns and correlations that can inform the development of more effective and targeted therapies. This capability is particularly valuable in the context of HIFU, where precise targeting and control are essential for successful treatment outcomes.

In conclusion, the use of machine learning and deep neural networks, particularly through the implementation of PINNs, represents a significant advancement in the field of HIFU research. These techniques offer a comprehensive approach to modeling and simulating the complex phenomena associated with HIFU treatment, paving the way for more

accurate, efficient, and personalized cancer therapies. As the field continues to evolve, the integration of these advanced computational methods will undoubtedly enhance our understanding and application of HIFU, ultimately improving patient outcomes and expanding the horizons of non-invasive cancer treatment.

PINNs have revolutionized the approach to solving nonlinear partial differential equations (PDEs) by leveraging deep learning to approximate solutions while adhering to physical laws, thereby significantly reducing computational demands compared to traditional methods like the finite difference method (FDM) and finite element method (FEM) [33, 13, 136, 156, 97, 102, 6, 107, 3, 7]. The innovative integration of PINNs in computational science has opened new avenues for efficiently solving complex problems that involve highly nonlinear dynamics and intricate geometries.

This study harnesses the power of PINNs to utilize a 3D model based on an anatomically realistic breast phantom (ARBP) generated from T1-weighted MRIs, ensuring that the intricate anatomical details of the breast are accurately reflected in the simulations. The use of ARBPs significantly enhances the precision and clinical relevance of HIFU simulations, allowing for more reliable predictions of treatment outcomes.

The adoption of anatomically realistic models is a critical step forward in simulating HIFU treatments. These models can capture the complex interactions between ultrasound waves and heterogeneous tissue structures, which are often oversimplified in traditional models. By accurately representing the breast's anatomy, including variations in tissue density and composition, the simulations can provide deeper insights into the thermal and mechanical effects of HIFU on cancerous tissues.

Furthermore, this research explores realistic HIFU ablation processes by simulating multiple lesion points within the breast tissue. The ability to model and assess the cumulative effects of these lesion points on necrotic tissue is crucial for understanding the comprehensive impact of HIFU treatments. This approach not only demonstrates the deep-learning platform's capability to mirror actual clinical treatments but also provides a valuable tool for optimizing HIFU protocols.

By leveraging PINNs, the study showcases how deep learning can be effectively applied to simulate the nonlinear and multiphysics phenomena inherent in HIFU therapy. This method offers a more efficient and accurate alternative to traditional numerical techniques, reducing computational time and resources while maintaining high fidelity to the physical principles governing tissue response to ultrasound waves.

The findings underscore the potential of PINNs to transform medical imaging and therapy planning by providing clinicians with advanced tools for predicting treatment outcomes with greater accuracy. The integration of machine learning with traditional

physics-based modeling represents a paradigm shift in how complex biomedical problems are approached, paving the way for more personalized and effective treatment strategies.

In conclusion, the utilization of PINNs in this study exemplifies the cutting-edge advancements in computational modeling for HIFU treatments. By combining ARBP with deep learning techniques, this research not only enhances the accuracy and efficiency of simulations but also bridges the gap between theoretical models and clinical applications. This innovative approach holds great promise for improving the efficacy and safety of HIFU therapies, ultimately leading to better patient outcomes and expanding the possibilities for non-invasive cancer treatments.

This study presents a comprehensive method for predicting the outcomes of HIFU therapy using an ARBP. Our approach involves a multi-stage simulation process meticulously designed to ensure accuracy and clinical relevance. The process begins with generating an acoustic wave, simulating the propagation of ultrasound through heterogeneous breast tissue. This step is crucial for capturing the interaction between the acoustic wave and the different tissue types present in the breast.

Following the generation of the acoustic wave, we compute the acoustic intensity distribution within the tissue. This step involves calculating how the ultrasound energy disperses throughout the breast, focusing particularly on the tumor area. Accurate computation of acoustic intensity is vital for determining how effectively the ultrasound targets the tumor.

Next, the absorbed acoustic energy is incorporated into a bioheat transfer model to estimate the generated heat and resulting temperature increase in the tumor area. This stage of the simulation uses principles of thermodynamics to predict how the absorbed energy converts into heat and raises the temperature of the targeted tissue. The bioheat transfer model is essential for understanding the thermal effects of HIFU, which are responsible for inducing necrosis in cancer cells.

The culmination of this process allows for determining the percentage of necrotic tissue within the tumor. By estimating the extent of tissue damage caused by the thermal effects, we can predict the therapeutic efficacy of the HIFU treatment. This detailed simulation provides insights into how different parameters and settings of the HIFU device can be optimized for maximum effectiveness.

2.2 Presurgical Plan

The primary therapeutic effect of HIFU treatment is tissue heating, which is achieved through the absorption of acoustic energy and its subsequent conversion to heat. This

localized heating can induce necrosis by causing almost instant protein coagulation, which irreversibly damages key cytosolic and mitochondrial enzymes critical for cell survival and function [121]. The mechanism relies on the precise focusing of the HIFU beam at a specific target within the tissue, thereby elevating the temperature to cytotoxic levels only within a confined volume. This precision ensures that thermal damage is localized, minimizing collateral damage to surrounding healthy tissues. Typically, the affected area is relatively small, with a diameter of approximately 1-2 mm and a length of about 10 mm, allowing for precise ablation of the targeted tissue [100].

Despite its precision, the small focal region of HIFU necessitates a comprehensive scanning pathway to ensure the entire tumor is treated. Without adequate coverage, there is an increased risk of incomplete ablation, which can lead to metastasis post-therapy. This challenge has been highlighted in recent studies, emphasizing the need for meticulous planning and execution of the HIFU treatment to cover the entire tumor mass effectively [172, 10, 82]. Moreover, the studies underscore the importance of monitoring and adjusting the treatment parameters in real-time to adapt to the dynamic biological environment and ensure thorough and uniform thermal exposure throughout the tumor.

Furthermore, the precision of HIFU treatment not only minimizes damage to adjacent healthy tissues but also allows for repeated treatments if necessary. This capability is particularly beneficial for managing recurrent tumors or for incremental ablation, where the entire tumor is not targeted in a single session. By carefully controlling the energy delivery and the scanning pattern, clinicians can maximize the therapeutic effects while minimizing the risk of adverse outcomes.

In summary, while HIFU offers a highly targeted approach to tumor ablation through localized heating and protein coagulation, its effectiveness is contingent upon precise targeting and comprehensive coverage of the tumor. Ongoing advancements in imaging and treatment planning are essential to overcome the challenges associated with its focal nature and to mitigate the risks of metastasis associated with incomplete treatment [172, 10, 82]. These developments are crucial for enhancing the efficacy and safety of HIFU as a minimally invasive treatment modality for various types of tumors.

HIFU remains a treatment modality in development, despite its distinctiveness and the promising initial clinical findings reported in several studies [184, 10, 138]. While HIFU's non-invasive nature and precision in targeting specific tissue areas offer significant advantages over traditional surgical methods, several technical issues currently hinder its widespread adoption among patients and clinicians.

One major challenge is the treatment of large tumors, particularly those embedded within or adjacent to critical normal tissues. The treatment of such tumors often necessi-

tates extremely long treatment times. This is because numerous heating pulses must be meticulously placed and applied to cover the entire tumor volume, ensuring that all malignant cells are subjected to cytotoxic temperatures. This meticulous process is essential to prevent the survival of residual cancer cells, which could lead to recurrence. However, the lengthy duration required for these procedures can be a significant drawback, limiting the practicality and patient throughput in clinical settings [44, 111, 17].

Furthermore, the inherent small focal region of HIFU adds another layer of complexity. The focal spot of HIFU is typically very small, often with a diameter of just a few millimeters. This necessitates precise alignment and multiple adjustments during the treatment to ensure the entire tumor is covered. The proximity of troublesome cancer cells to normal tissue, often less than 50 micrometers, increases the risk that some malignant cells may escape the treatment. This small margin for error requires highly accurate imaging and targeting systems to ensure that the HIFU energy is delivered precisely where it is needed, without affecting the surrounding healthy tissues [80].

Additionally, the heterogeneity of tumor tissue and the varying acoustic properties within a tumor can affect the distribution of HIFU energy, leading to uneven heating and potential areas of under-treatment. This variability necessitates real-time monitoring and adjustments during the procedure, further complicating the treatment process. Advanced imaging techniques, such as MRI-guided HIFU, have been developed to address these challenges, providing real-time feedback and enabling more accurate targeting. However, these technologies are expensive and require specialized equipment and expertise, which may not be readily available in all clinical settings.

Moreover, patient movement during treatment, whether due to breathing or involuntary motions, can disrupt the precise targeting required for effective HIFU therapy. Strategies to mitigate this include motion compensation algorithms and immobilization techniques, but these add to the complexity and duration of the treatment.

In summary, while HIFU presents a promising, non-invasive treatment option with distinct advantages, several technical and practical challenges must be addressed to enable its broader adoption. The need for prolonged treatment times, precise targeting of small focal regions, and the management of tumor heterogeneity and patient movement are significant hurdles. Ongoing research and technological advancements aim to overcome these challenges, paving the way for HIFU to become a more widely used therapy in the future [44, 111, 17].

Recent advances in numerical methods and information technology have significantly enhanced the capability to create detailed models that accurately describe the underlying physical behavior of focused ultrasonic waves and temperature distribution in heteroge-

neous tissue. These sophisticated models, which integrate complex algorithms and high-performance computing, provide a more precise understanding of how ultrasonic energy interacts with various tissue types, leading to improved predictability and control in HIFU treatments [153].

As a result, these advanced tools can be utilized for a wide range of clinical purposes. One crucial application is in patient selection. By accurately modeling the anatomical structures and properties of tissues, clinicians can determine whether a patient is a suitable candidate for HIFU surgery. This involves assessing the patient's anatomy to ensure that the ultrasonic waves can be effectively focused on the target tissue without causing undue harm to surrounding healthy tissues. This capability enhances the safety and efficacy of the treatment, ensuring that only those patients who are likely to benefit from the procedure are selected.

Another important application is treatment verification. Detailed numerical models can be used to analyze the cause of adverse events or treatment failures by providing insights into the exact interaction between the ultrasonic waves and the tissue. This post-treatment analysis can identify potential issues such as incomplete ablation or unexpected tissue responses, allowing for adjustments in future treatments to mitigate similar risks.

Moreover, the optimization of the scanning pathway, which involves determining the optimal transducer location and sonication parameters, is essential for delivering ultrasonic energy precisely to the intended target volume. The ability to model and simulate different scanning pathways helps in reducing treatment time significantly. By carefully planning the transducer movements and energy delivery parameters, clinicians can ensure that the entire tumor volume is covered efficiently, minimizing the risk of leaving untreated cancerous cells that could lead to metastasis.

The precision offered by these advanced models also aids in tailoring treatment plans to individual patients. Factors such as the size, shape, and location of the tumor, as well as the surrounding anatomical structures, can be accounted for in the treatment planning process. This personalized approach ensures that the ultrasonic energy is delivered in the most effective manner, enhancing treatment outcomes and reducing the likelihood of side effects.

Furthermore, the integration of real-time imaging with these numerical models allows for dynamic adjustments during the procedure. Real-time feedback ensures that the treatment remains on course, and any deviations can be corrected immediately, thus maintaining the accuracy and effectiveness of the HIFU therapy.

In summary, the advancements in numerical methods and information technology have revolutionized the application of HIFU by providing detailed, accurate models of ultrasonic

wave behavior and temperature distribution in heterogeneous tissues. These models not only facilitate better patient selection and treatment verification but also optimize the scanning pathways, thereby reducing treatment times and improving overall treatment efficacy. Such technological advancements are crucial for the ongoing development and wider adoption of HIFU as a reliable and effective treatment modality [153].

There are two primary methods to deliver energy to the target region in HIFU treatment: sequential discrete mode and continuous scanning mode [47, 173]. In the sequential discrete mode, localized treatments are administered sequentially by moving the HIFU transducer in a stepwise manner. Each discrete step targets a specific area before moving to the next, allowing for precise control over the treatment region. However, this method can lead to thermal diffusion and heat accumulation from the adjacent treated areas. As a result, the size of the lesion may gradually increase during the sequential discrete HIFU therapy, potentially causing insufficient treatment of the initial spots and overtreatment of the later ones. This can lead to uneven thermal doses and variability in treatment efficacy [29, 186, 185].

In continuous scanning mode, the HIFU transducer moves at a constant speed along a pre-designed trajectory, delivering energy continuously to the target region. This method helps maintain a more uniform temperature distribution and reduces the risk of thermal damage to surrounding tissues. However, the continuous movement requires precise planning and control to ensure that the entire tumor volume is adequately treated without gaps.

To address the challenges of heat accumulation and diffusion, researchers have investigated various navigation algorithms and heating protocols. For instance, Giannakou et al. [48] evaluated six alternative navigation algorithms to determine the amount of transducer-generated heating in the pre-focal area. Their findings highlighted the importance of optimizing the transducer's movement and heating patterns to minimize pre-focal heating and ensure consistent lesion formation. Additionally, Fennessy and Tempany [44] recommend a regimen of 20-40 seconds of heating followed by 80-90 seconds of cooling. According to their protocol, delivering the appropriate dosage with 30 seconds of heating followed by 60 seconds of cooling would take approximately 2.5 hours. This highlights the significant time investment required for thorough treatment using sequential discrete mode.

Clinical practitioners can shorten treatment times by employing phased array technology, which allows for the formation of multiple focus patterns and precise control over the treatment parameters. By adjusting the electrical power delivered to the transducer, the sequence of focal zones, the length of heating pulses, and the cooling intervals between pulses,

clinicians can optimize the treatment process [142]. Historically, researchers have modified fixed treatment paths by altering one of these variables due to the computational complexity involved in simultaneously optimizing multiple parameters [44, 64, 170, 105, 104, 12]. For example, variations in applied power magnitude [170], ultrasound frequency [170], or inter-sonication delay periods [105] have been explored to enhance treatment efficacy.

Most researchers utilize defined heating pulses and inter-pulse cooling times to prevent scorching of normal tissue and ensure safety. These regimens often involve cautious heating and cooling intervals, which, while effective and safe, result in prolonged treatment times [44, 64, 105, 104]. The challenge lies in balancing the need for thorough tumor ablation with the practical constraints of treatment duration. Continuous efforts are being made to refine these protocols and develop more efficient treatment strategies that maintain the delicate balance between efficacy and safety.

In summary, both sequential discrete mode and continuous scanning mode have their respective advantages and challenges. Optimizing these energy delivery methods through advanced algorithms, phased array technology, and precise control of treatment parameters is essential for improving the effectiveness and efficiency of HIFU treatments. Ongoing research and technological advancements continue to enhance our understanding and capability in this field, paving the way for more effective and time-efficient HIFU therapies [47, 173, 29, 186, 185, 48, 44, 142, 64, 170, 105, 104, 12].

Payne et al. [127] presented the findings of a novel optimization approach that aims to reduce HIFU treatment periods by minimizing individual heating and interpulse cooling times while adhering to normal tissue constraint limits at each sonication site. Their method involves a meticulous balance between delivering sufficient energy to ablate the tumor tissue and allowing adequate cooling to prevent thermal damage to surrounding healthy tissues. By optimizing these parameters, they demonstrated a significant reduction in overall treatment time, making the procedure more efficient and potentially more comfortable for patients.

Building on these principles, Fan and Hynynen [43] explored the feasibility of noninvasive tumor surgery using focused transducers or phased arrays to deliver several sonications. Their work illustrated the potential of these advanced technologies to concentrate ultrasonic energy precisely on the tumor, reducing the need for invasive procedures. This approach leverages the precision of phased arrays to control the focus and intensity of the ultrasound waves, allowing for targeted ablation of tumor tissues while sparing surrounding healthy structures.

Liu et al. [93] conducted a numerical investigation into two heuristic scanning routes: the shortest distance and the greatest distance between sequential small rapid scanning

volumes. Their study aimed to determine the most efficient scanning pathway to achieve comprehensive tumor ablation within the shortest possible time. They found that the choice of scanning route could result in cumulative heating time differences of several minutes, even when cooling times were fixed at one minute between sonications. This highlights the importance of optimizing the scanning pathway to enhance the efficiency of HIFU treatments.

A volumetric sonication approach, as suggested by Kohler et al. [84], involves guiding the focus point along a preset trajectory consisting of numerous concentric outward-moving circles. This method aims to create uniform volume ablations, ensuring that the entire tumor mass is effectively treated. The volumetric approach was further extended by Enholm et al. [41], who built upon the group's previous work with nested spirals [118, 117]. This innovative technique involves systematically moving the focal point in a spiral pattern to achieve comprehensive ablation of the tumor volume. The use of concentric circles and nested spirals helps in distributing the energy evenly across the target area, minimizing the risk of residual cancer cells and improving treatment outcomes.

These advancements in optimization techniques for HIFU treatments underscore the importance of precise control over sonication parameters and scanning pathways. By minimizing treatment times and ensuring thorough ablation of tumor tissues, these methods contribute to the development of more effective and efficient HIFU therapies. The integration of numerical modeling, heuristic algorithms, and advanced sonication techniques represents a significant step forward in the field, paving the way for improved patient outcomes and broader clinical adoption of HIFU technology.

In conclusion, the continuous evolution of optimization approaches in HIFU treatment, from minimizing individual heating and cooling times to optimizing scanning pathways and developing volumetric sonication techniques, reflects the dynamic nature of this field. Researchers are increasingly able to achieve precise and efficient tumor ablation, reducing treatment times and enhancing the safety and efficacy of HIFU therapy. The collective efforts of Payne et al., Fan and Hynynen, Liu et al., Kohler et al., and Enholm et al. demonstrate the potential of these innovative methods to transform HIFU into a widely accepted and effective treatment modality for various types of tumors [127, 43, 93, 84, 41, 118, 117].

Based on the minimal time formulation from optimal control theory [99], a scanning path optimization algorithm was designed to treat the tumor volume as quickly as possible while maintaining the temperature in the healthy tissue below the safe threshold of 42°C. This approach leverages advanced mathematical techniques to identify the most efficient scanning path, reducing overall treatment time and minimizing the risk of thermal damage

to adjacent healthy tissues. In theoretical simulations, this method requires a significant number of phased array elements (530) and focal points within the target area (300 for a sphere with a radius of 1.9 cm). However, such high requirements are currently beyond the capabilities of most commercially available HIFU systems, indicating a need for further technological advancements to make this approach more widely accessible.

Luo et al. [98] proposed an optimal sequential discrete mode that alternates between long and short exposure durations at treatment locations. This method aims to reduce the cumulative thermal impact on nearby treated spots, thereby generating uniformly sized lesions and improving overall treatment efficiency. By carefully managing the exposure durations, this approach mitigates the risk of overtreatment and enhances the precision of tumor ablation.

In experiments with gel phantoms and *ex vivo* bovine liver samples, Zhou et al. [187] compared two innovative scanning pathways—spiral scanning from the center to the outside and spiral scanning from the outside to the center—with traditional raster scanning. Their findings indicated that spiral scanning methods could provide more uniform heating and better lesion formation compared to raster scanning, potentially leading to more effective and efficient HIFU treatments.

Coon et al. [26] explored the concept that adjusting the course of a HIFU therapy's N focus zone heating pulse can significantly shorten treatment duration. Their research demonstrated that by optimizing the sequence and timing of heating pulses, it is possible to achieve faster and more uniform tumor ablation.

A comprehensive study by Qian et al. [131] investigated the lesion development generated by HIFU operating in continuous scanning mode along a spiral channel. Both theoretical and experimental analyses revealed that continuous spiral scanning could produce consistent and uniform lesions, enhancing the effectiveness of HIFU therapy.

Other optimization methods have been explored to enhance the impact of sequential discrete mode treatments. For instance, combining HIFU with induced biological effects in tissue has shown promise in boosting treatment efficacy. Studies by Čudová et al. [27] and Liu et al. [92] highlight the potential benefits of integrating biological response modulation with precise ultrasound delivery to improve treatment outcomes.

Despite these advancements, more investigation is required to concurrently optimize the scan path, treatment time, and minimize invasion into normal tissue. The integration of these factors remains a critical challenge in the field of HIFU therapy. Future research should focus on developing comprehensive optimization frameworks that address these multiple objectives, ensuring that HIFU treatments are not only effective and efficient but also safe for patients.

In conclusion, the ongoing development of optimization algorithms for HIFU treatment is crucial for enhancing its clinical application. By refining scanning paths, adjusting exposure durations, and integrating biological effects, researchers are making significant strides towards more effective and patient-friendly HIFU therapies. However, achieving the ideal balance between treatment efficacy, efficiency, and safety requires continued innovation and rigorous investigation [99, 98, 187, 26, 131, 87, 27, 92].

An ML-based approach to solving the treatment planning problem is presented in this study. The aim is to propose a novel scanning path method to compute the best presurgical plan based on the target volume. This innovative method leverages machine learning to enhance the precision and efficiency of HIFU treatment planning. Specifically, the planned goal volume and organs at risk are used as inputs for the machine learning model. Using these inputs, the ML approach generates a viable treatment plan that optimizes the scanning path and treatment parameters.

Central to this approach is the implementation of an iterative artificial neural network (ANN), which considers multiple potential solutions and selects the optimal plan based on predefined constraints such as the safe temperature threshold for surrounding healthy tissues and the required ablation depth for the tumor. The ANN's iterative nature allows it to refine its predictions and improve the treatment plan's accuracy over successive iterations. This capability is crucial for adapting to the complex and variable nature of biological tissues, ensuring that the treatment is both effective and safe.

The methodology is validated through both numerical simulations and experimental studies. Numerically, the ANN is trained on a comprehensive dataset that includes various tumor geometries, tissue properties, and clinical constraints. These simulations help in understanding how the ML model performs under different conditions and allow for fine-tuning of the ANN's parameters. Experimentally, the proposed method is tested using phantom models and *ex vivo* tissue samples to evaluate its practical applicability. These experiments provide critical insights into the real-world performance of the ML-based approach, highlighting its strengths and potential areas for improvement.

As a result of this comprehensive approach, HIFU treatment time can be significantly reduced. The optimized scanning path minimizes the time required to cover the entire tumor volume, thereby enhancing the efficiency of the procedure. Additionally, the precise targeting capabilities of the ML model help in minimizing the risk of metastasis by ensuring that no cancerous cells are left untreated. This is particularly important in preventing the spread of cancer and improving patient outcomes.

Moreover, the proposed study can avoid possible overheating and necrosis of normal tissue. By adhering to the predefined constraints on temperature and exposure duration,

the ANN ensures that the delivered energy remains within safe limits, protecting healthy tissues from thermal damage. This aspect of the approach is crucial for maintaining the safety and comfort of the patient during and after the procedure.

Despite its ease of use, the ML-based approach offers substantial improvements in HIFU patient targeting and treatment times. The automated nature of the treatment planning process reduces the need for manual intervention, allowing clinicians to focus on other critical aspects of patient care. Furthermore, the reduction in treatment times translates to increased throughput in clinical settings, enabling more patients to benefit from HIFU therapy.

In conclusion, the integration of machine learning into HIFU treatment planning represents a significant advancement in the field. By combining the predictive power of ANNs with rigorous numerical and experimental validation, this approach enhances the precision, efficiency, and safety of HIFU treatments. The resulting improvements in clinical outcomes underscore the potential of ML-based methods to revolutionize cancer treatment, offering new hope to patients and healthcare providers alike.

2.3 Segmentation

Breast ultrasound (BUS) imaging provides a safe, affordable, and high frame rate alternative to traditional MRI imaging [24, 123]. The non-ionizing nature of ultrasound makes it a safe option, especially for repeated use, while its affordability and high frame rates enhance its practicality for widespread screening and real-time imaging. However, the effectiveness of BUS imaging is highly dependent on the expertise of experienced radiologists who are necessary to analyze the images and make accurate diagnoses. This reliance on human expertise highlights the need for computer-aided diagnosis (CADx) devices that can aid in the detection and analysis of breast abnormalities, thereby standardizing and potentially improving diagnostic accuracy.

CADx devices are not only beneficial for diagnostic purposes but also play a crucial role in assisting HIFU surgical operations. These devices can analyze ultrasound images and provide real-time feedback to physicians, which is essential during minimally invasive procedures like HIFU. One of the most important features of CADx devices is the capability for online monitoring of surgery. This feature allows for continuous observation and assessment of the treatment area, enabling physicians to make informed decisions during surgery.

Online monitoring is particularly valuable because it helps physicians to adapt and

update treatment plans dynamically based on the real-time conditions observed during the procedure. This adaptability can lead to more precise targeting of the treatment area, minimizing damage to surrounding healthy tissues and improving overall surgical outcomes. By providing real-time data and analysis, CADx devices enhance the physician's understanding of the surgical process, leading to better decision-making and potentially higher success rates for HIFU treatments. This integration of advanced imaging technology with surgical practice represents a significant step forward in the field of medical imaging and interventional procedures.

Having a low-cost, real-time, and accurate ablation segmentation procedure is a crucial aspect of online monitoring during HIFU surgeries. Effective segmentation is essential for ensuring precise targeting and treatment of the affected tissue, thereby enhancing the overall efficacy and safety of the procedure. While B-mode imaging is considered a low-cost and real-time imaging system, it suffers from limitations in resolution and image quality compared to MRI systems. These limitations can hinder its accuracy and reliability for use in CADx systems, which demand high precision for effective monitoring and intervention.

To address these challenges, this project proposes a novel B-mode image segmentation framework specifically designed for HIFU ablation monitoring. The framework leverages advanced image processing techniques to enhance the segmentation accuracy of HIFU ablated lesions. By refining the segmentation process, the framework ensures that the low-cost and real-time advantages of B-mode imaging are retained while significantly improving the accuracy of lesion detection and delineation. This improvement is critical for real-time surgical guidance, enabling physicians to adjust treatment plans dynamically based on precise, up-to-date imaging data.

The proposed framework employs sophisticated algorithms to process B-mode images, extracting relevant features and accurately identifying the boundaries of ablated tissue. This capability allows for more effective and precise control over the HIFU treatment, reducing the risk of damage to surrounding healthy tissues and increasing the likelihood of successful outcomes. Additionally, by maintaining the cost-effectiveness and real-time benefits of B-mode imaging, the framework offers a practical solution that can be widely implemented in clinical settings.

In summary, this project successfully bridges the gap between the low-cost, real-time advantages of B-mode imaging and the high accuracy required for effective CADx systems in HIFU therapy. The innovative segmentation framework enhances the utility of B-mode imaging, making it a viable option for real-time monitoring and guidance during HIFU surgeries, thus contributing to improved patient outcomes and broader accessibility to advanced therapeutic techniques.

One of the critical stages in HIFU therapy is detecting and separating the thermal ablated region, i.e., thermal ablated segmentation, from the non-ablated regions. This step is essential for making the treatment planning more efficient in terms of the number of sonications and overall efficacy. By accurately identifying the ablated areas, HIFU surgery becomes less harmful to non-cancerous adjacent cells, thereby reducing potential collateral damage and increasing the likelihood of successful treatment outcomes. Furthermore, effective ablation segmentation can be integrated into HIFU path planning systems, where the therapy operates based on feedback from a pre-defined plan, enhancing precision and control during the procedure.

Deep learning models have emerged as a powerful tool in medical image segmentation tasks, providing an end-to-end pipeline that covers both feature extraction and classification simultaneously. These models have garnered significant attention due to their effectiveness in various segmentation applications [2, 183]. Despite recent advancements in ultrasound imaging segmentation [182, 144, 74, 112], thermal ablation segmentation from ultrasound imaging, such as B-Mode imaging, remains challenging. The current models often lack the pixel-level sensitivity required to accurately distinguish all ablated pixels, frequently misclassifying non-ablated adjacent pixels as ablated. This inaccuracy can lead to incomplete or ineffective therapy.

To address this limitation, this study proposes a novel deep pixel-wise segmentation model specifically designed for ultrasound thermal ablation segmentation. This model is more sensitive to the subtle differences between ablated and non-ablated pixels, improving the accuracy of segmentation. Our approach ensures that the deep learning model can correctly identify the ablated regions, enhancing the precision of HIFU therapy and reducing the risk of damaging healthy tissues.

The main contributions of this paper are twofold. First, to the best of our knowledge, this study is the first to address the problem of breast tumor ablation segmentation using B-Mode imaging during HIFU therapy. This represents a significant advancement in the application of ultrasound imaging for HIFU treatments. Second, we introduce a novel pixel-wise segmentation deep neural model that accurately identifies the boundaries between ablated and non-ablated regions. This model enhances the precision of thermal ablation segmentation, providing a more reliable tool for real-time monitoring and feedback during HIFU procedures, ultimately improving patient outcomes and advancing the field of therapeutic ultrasound.

Ultrasound image segmentation has received increasing attention, and a diverse range of non-deep-learning models has been proposed to address this problem. These models include deformable models [179], threshold-based techniques [141, 51, 9], clustering-based

techniques [115], and several other families of techniques [67, 174]. For instance, Liu et al. [94] employed anisotropic diffusion filtering to reduce speckle noise in ultrasound images. The filtered and enhanced image is then processed using a Normalized Cut (NC) algorithm to divide it into several small sections. These sections are subsequently merged into larger regions using region merging techniques. Finally, potential lesions are extracted through morphological operations.

Quan et al. [132] suggested an alternative approach by using region-based NC instead of pixel-based NC. Their method involves iterative clustering to break the filtered image into a series of over-segmented regions, which are treated as nodes rather than individual pixels. This enhances the contrast between the region of interest (ROI) and the background. In the final stage, NC is applied to merge the over-segmented regions and accurately segment the ROI.

Zhou et al. [188] demonstrated the use of Gaussian filtering and histogram equalization to smooth and enhance the contrast of breast ultrasound (BUS) images. They then applied a pyramid mean shift filter to increase image homogeneity. The final segmentation stage involves the use of NC and morphological techniques to achieve precise segmentation.

Zhang et al. [180] conducted a comparative study on various preprocessing nonlinear techniques, highlighting their effectiveness in improving segmentation outcomes. These methods have shown promise for high-precision, autonomous breast lesion identification and for optimizing HIFU focus distribution strategies, thereby enhancing the overall effectiveness of ultrasound imaging in medical diagnostics and treatment planning.

Intra-operative image-guided treatment has been the focus of numerous image-assisted surgical investigations, demonstrating its potential to enhance the precision and efficacy of surgical procedures [116, 42]. Liao et al. proposed an innovative integrated diagnostic and therapy system designed for precision neurosurgery. This system utilizes intra-operative 5-aminolevulinic acid-induced fluorescence to guide robotic laser ablation, providing real-time feedback and improving surgical accuracy [91].

Several studies have explored the integration of various preoperative and intra-operative medical imaging techniques, including MRI, computed tomography (CT), and X-ray imaging, to support and enhance image-assisted surgical procedures [37, 68]. These integrated approaches aim to leverage the strengths of each imaging modality to provide comprehensive and accurate visual information during surgery.

While these studies discuss the utilization of different imaging modalities and the integration of images, they often maintain a clear distinction between diagnostic and treatment processes. This separation highlights the need for further research and development

to create seamless systems that combine diagnostic imaging with real-time therapeutic interventions, ultimately improving patient outcomes and surgical precision.

The family of deep neural networks has recently achieved significant progress in medical imaging tasks. When sufficient training data is available, these models often deliver results that are markedly superior to those produced by non-deep learning models. For instance, RDAU-NET [189] introduces a Unet-based architecture specifically designed for breast tumor segmentation. This model incorporates residual connections to facilitate the learning process and attention gate modules to produce sharp edges and increase the receptive field, enhancing the accuracy of segmentation.

Similarly, Xu et al. proposed an improved Unet model augmented with residual connections [161]. Their approach also integrates four popular loss functions, resulting in a more effective learning procedure. This combination of residual connections and multiple loss functions helps the model to converge more efficiently and improves segmentation performance.

In addition to these models, several other recent advancements in breast lesion segmentation have been made. SMU-Net [122], GC-Net [175], and the work described in [120] represent state-of-the-art approaches in this domain. These models impose various priors, such as edge, position, and shape information, on the extracted high-level features from the convolutional layers. By integrating these priors, the models enhance the accuracy and reliability of the segmentation results.

These advancements demonstrate the potential of deep neural networks in medical imaging, particularly in tasks requiring precise and accurate segmentation, such as breast tumor detection. The use of advanced architectures and the integration of multiple loss functions and priors are key factors contributing to the superior performance of these models.

When comparing the reported results of non-deep learning models with those of deep learning models, it becomes clear that deep learning models offer superior performance in terms of both accuracy and generalization. Deep learning models, due to their complex architectures and large-scale data processing capabilities, consistently achieve higher levels of accuracy in various medical imaging tasks compared to traditional non-deep learning approaches. They excel in feature extraction and pattern recognition, leading to more precise and reliable outcomes across a range of imaging applications [60, 90].

Despite these advancements, current deep neural network models still face significant challenges, particularly in the context of HIFU therapy. Specifically, these models struggle with accurately distinguishing between coagulated tumor tissue and normal tissue in ultrasound B-Mode images. This limitation presents a serious obstacle in pre-surgical planning

and reduces the effectiveness of online monitoring during HIFU therapeutic procedures. Accurate differentiation between coagulated and normal tissue is crucial for assessing treatment progress and making real-time adjustments to the therapy [56, 85].

The following section of this thesis addresses this critical limitation by proposing a novel method designed to improve the sensitivity of deep learning models in distinguishing between coagulated tumor parts and healthy tissue. This method involves a detailed, step-by-step procedure for tracking HIFU lesions, aimed at enhancing the precision of tumor monitoring and optimizing therapeutic outcomes. The proposed approach integrates advanced techniques to refine image analysis processes, thereby overcoming current shortcomings and advancing the capabilities of HIFU therapeutic systems [165, **?**].

By tackling these challenges, the proposed method seeks to bridge the gap between existing deep learning models and the specific demands of HIFU therapy, offering potential solutions for more effective pre-surgical planning and real-time therapeutic adjustments.

Chapter 3

Physics-Informed Neural Network (PINN) Solution for HIFU

This chapter provides a concise overview of the HIFU ablation process, which is a minimally invasive therapeutic technique used to precisely target and destroy pathological tissue through focused ultrasound energy. It begins by outlining the basic principles of HIFU ablation, including the generation and focusing of high-frequency sound waves, the mechanism of thermal and mechanical effects on tissues, and the criteria for effective ablation [89].

Following this introduction, the chapter proceeds to elaborate on the governing equations and mathematical models involved in the HIFU ablation process. This includes the bioheat transfer equation, which describes the distribution of heat within the tissue, and the acoustic wave equation, which models the propagation of ultrasound waves through different tissue types. These equations are critical for predicting the temperature rise and thermal dose delivered to the target area, ensuring precise control over the ablation process.

The following sections offer vital details concerning the deep-learning modeling procedure at various stages. Initially, data preprocessing techniques are discussed, including the acquisition and augmentation of medical imaging data to train the deep-learning models. Subsequently, the architecture of the deep neural networks used for HIFU ablation modeling is described, highlighting the use of convolutional layers for feature extraction, recurrent layers for temporal data analysis, and attention mechanisms for enhancing model accuracy.

Additionally, the sections cover the training and validation process, explaining the selection of loss functions, optimization algorithms, and evaluation metrics to ensure robust

model performance. Techniques for model interpretability and explainability are also addressed, providing insights into how the deep-learning models make predictions and identify critical features in the medical images.

Finally, the section discusses the integration of the deep-learning models with real-time HIFU ablation systems, including the challenges of real-time data processing, system latency, and ensuring safety and efficacy during clinical procedures. The potential for future advancements and applications of deep-learning models in HIFU ablation and other therapeutic modalities is also explored, highlighting ongoing research and development efforts in this innovative field.

3.1 HIFU Ablation Mechanism

HIFU ablation refers to a non-invasive medical procedure in which an ultrasound transducer generates focused ultrasonic beams that penetrate soft tissue to specifically target and destroy tumors [160]. This advanced technique involves the precise focusing of ultrasound beams, which allows for high intensities to be concentrated within a small and compact volume, typically around 1 mm in diameter and 10 mm in length. The focused energy results in sound intensities in the focal region that range from approximately 100 to 10,000 W/cm^2, with peak compression pressures reaching up to 70 MPa and peak rarefaction pressures reaching up to 20 MPa.

The HIFU ablation technique leverages two primary mechanisms to achieve its therapeutic effects: thermal and mechanical. The thermal effect occurs as the focused ultrasound waves cause rapid heating in the target tissue, raising the temperature to levels that induce coagulative necrosis, effectively destroying the tumor cells. This localized heating ensures that the surrounding healthy tissues remain largely unaffected, thereby minimizing collateral damage and preserving normal tissue function.

In addition to thermal effects, mechanical effects also play a crucial role in HIFU ablation. These include acoustic cavitation and radiation force, which contribute to the mechanical disruption of tumor cells. Acoustic cavitation involves the formation, growth, and collapse of microbubbles within the tissue, generating high shear forces that can mechanically damage cellular structures. The radiation force, on the other hand, exerts pressure on the tissue, further aiding in the mechanical disintegration of the tumor [184].

The combination of these thermal and mechanical effects makes HIFU ablation a powerful and precise method for non-invasive tumor treatment. The ability to focus ultrasound beams with such high intensity and precision allows for targeted tumor destruction while

sparing adjacent healthy tissues, offering a promising alternative to conventional surgical procedures. Ongoing research and technological advancements continue to enhance the efficacy and safety of HIFU ablation, expanding its applications in clinical oncology and other medical fields.

The thermal effect of HIFU involves the generation of heat due to the absorption of acoustic energy by the targeted tissue. As the focused ultrasound beams converge on a specific area, the energy is transformed into heat, leading to a rapid increase in the local tissue temperature. This localized heating is highly controlled, allowing for precise targeting of tumor cells while sparing surrounding healthy tissues.

When the temperature in the focal region is raised above 60 °C for a duration of at least 1 second, it typically results in the rapid and irreversible death of cells through a process known as coagulation necrosis. This elevated temperature denatures cellular proteins and causes the disruption of cell membranes, leading to cell death. The affected tissue subsequently undergoes a series of biological responses, including inflammation and fibrosis, ultimately resulting in the resorption or stabilization of the treated area.

The efficiency and effectiveness of the thermal ablation process depend on several factors, including the intensity of the ultrasound beam, the duration of exposure, and the acoustic properties of the tissue. The focused nature of HIFU ensures that the high temperatures are confined to the target area, minimizing damage to adjacent tissues and reducing the risk of complications.

In clinical practice, HIFU treatment is typically monitored in real-time using imaging modalities such as ultrasound or MRI. These imaging techniques allow clinicians to visualize the target tissue and adjust the treatment parameters as needed to ensure optimal heating and ablation of the tumor cells. The ability to precisely control the thermal dose delivered to the tissue is a significant advantage of HIFU over other thermal ablation techniques, such as radiofrequency or microwave ablation.

The application of HIFU in oncology has shown promising results for the treatment of various types of tumors, including those in the liver, prostate, kidney, and pancreas. The non-invasive nature of HIFU, combined with its ability to selectively destroy tumor cells, makes it an attractive option for patients who may not be candidates for traditional surgical interventions. Moreover, ongoing advancements in HIFU technology and treatment protocols continue to enhance its efficacy and expand its clinical applications [184].

In summary, the thermal effect of HIFU plays a crucial role in the ablation of tumor cells through the controlled generation of heat, leading to coagulation necrosis. This precise and targeted approach offers a powerful tool for the non-invasive treatment of various cancers, providing an effective alternative to conventional surgical methods.

The mechanical effects induced by HIFU, including cavitation, micro-streaming, and radiation force, play a significant role in the therapeutic application of this technology. These effects occur when high-intensity acoustic pulses interact with the targeted tissue, leading to various mechanical disruptions that can contribute to the ablation process.

Cavitation involves the formation, growth, and collapse of microbubbles within the tissue. When these bubbles collapse, they generate intense local shear forces and shock waves that can mechanically disrupt cell membranes and other cellular structures, leading to cell death. Cavitation can enhance the overall effectiveness of HIFU by creating additional pathways for tissue damage beyond thermal effects.

Micro-streaming refers to the rapid, small-scale fluid movements induced by the oscillation of microbubbles in an acoustic field. These micro-streaming currents can exert mechanical stress on cellular components, contributing to the breakdown of tumor cells. This phenomenon can increase the permeability of cell membranes, making cells more susceptible to damage from other mechanisms.

Radiation force is the unidirectional force exerted by the ultrasound wave as it propagates through the tissue. This force can induce mechanical stress and deformation in the targeted area, leading to further disruption of cellular structures. Radiation force can also enhance the penetration of therapeutic agents into the tumor tissue when used in combination with other treatments.

Despite the potential benefits of these mechanical effects, the thermal process remains the preferred method for tissue ablation in HIFU treatments due to its better understanding and controllability. The thermal effect, which involves the absorption of acoustic energy and subsequent heating of the tissue, allows for precise targeting and destruction of tumor cells through coagulation necrosis. This controlled heating can be accurately monitored and adjusted in real-time, providing a reliable and predictable outcome.

The mechanical effects, while powerful, can be more difficult to control and predict compared to thermal effects. Cavitation, for example, can be highly variable and dependent on the specific acoustic environment and tissue properties. Uncontrolled cavitation can potentially lead to unintended damage to surrounding healthy tissues, posing a risk to patient safety.

Therefore, in clinical practice, the thermal ablation approach is generally favored for its precision and predictability. However, researchers continue to explore ways to harness and control the mechanical effects of HIFU to enhance its therapeutic efficacy. Advances in imaging and monitoring technologies, as well as a deeper understanding of the underlying mechanisms, may lead to more effective and safe use of mechanical effects in the future [184].

In summary, while the mechanical effects of HIFU, such as cavitation, micro-streaming, and radiation force, contribute to the ablation process, the thermal method remains the preferred approach due to its greater control and predictability. Future advancements in HIFU technology may enable better utilization of mechanical effects to improve therapeutic outcomes.

HIFU is rapidly gaining recognition in the medical field as a highly effective non-invasive ablation technique across a variety of clinical applications. This method utilizes focused ultrasound waves to precisely target and destroy pathological tissues, making it a valuable tool in the treatment of tumors and other medical conditions without the need for incisions or invasive procedures.

One of the major advantages of HIFU is its ability to complete treatments in a single session. During a typical HIFU procedure, the patient can be fully conscious, lightly sedated, or under mild general anesthesia, depending on the specific clinical requirements and the location of the treatment area. This flexibility in anesthesia options contributes to the overall patient comfort and minimizes the risks associated with more extensive surgical procedures [159].

HIFU has been successfully applied in the treatment of various types of tumors, including those in the liver, prostate, kidney, and pancreas. Its precision and non-invasive nature make it particularly suitable for patients who may not be ideal candidates for traditional surgery due to age, comorbidities, or other risk factors. Additionally, HIFU is being explored for its potential in treating non-tumorous conditions such as uterine fibroids, essential tremors, and even certain neurological disorders.

The schematic depiction of the HIFU ablation process for a breast tumor, as illustrated in Fig. 3.1, provides a clear understanding of how the technology works. In this schematic, the focused ultrasound waves are directed towards the tumor through the patient's skin, converging at the targeted tissue to induce localized heating and mechanical disruption. The surrounding healthy tissues remain largely unaffected due to the precision of the focused energy, which minimizes collateral damage and enhances the safety profile of the treatment.

Moreover, the real-time imaging capabilities integrated with HIFU systems, such as MRI or ultrasound guidance, play a crucial role in the success of the procedure. These imaging modalities allow clinicians to accurately visualize the target area, monitor the ablation process, and make necessary adjustments to ensure complete and effective treatment. This real-time feedback is essential for optimizing treatment outcomes and reducing the likelihood of incomplete ablation or damage to adjacent structures.

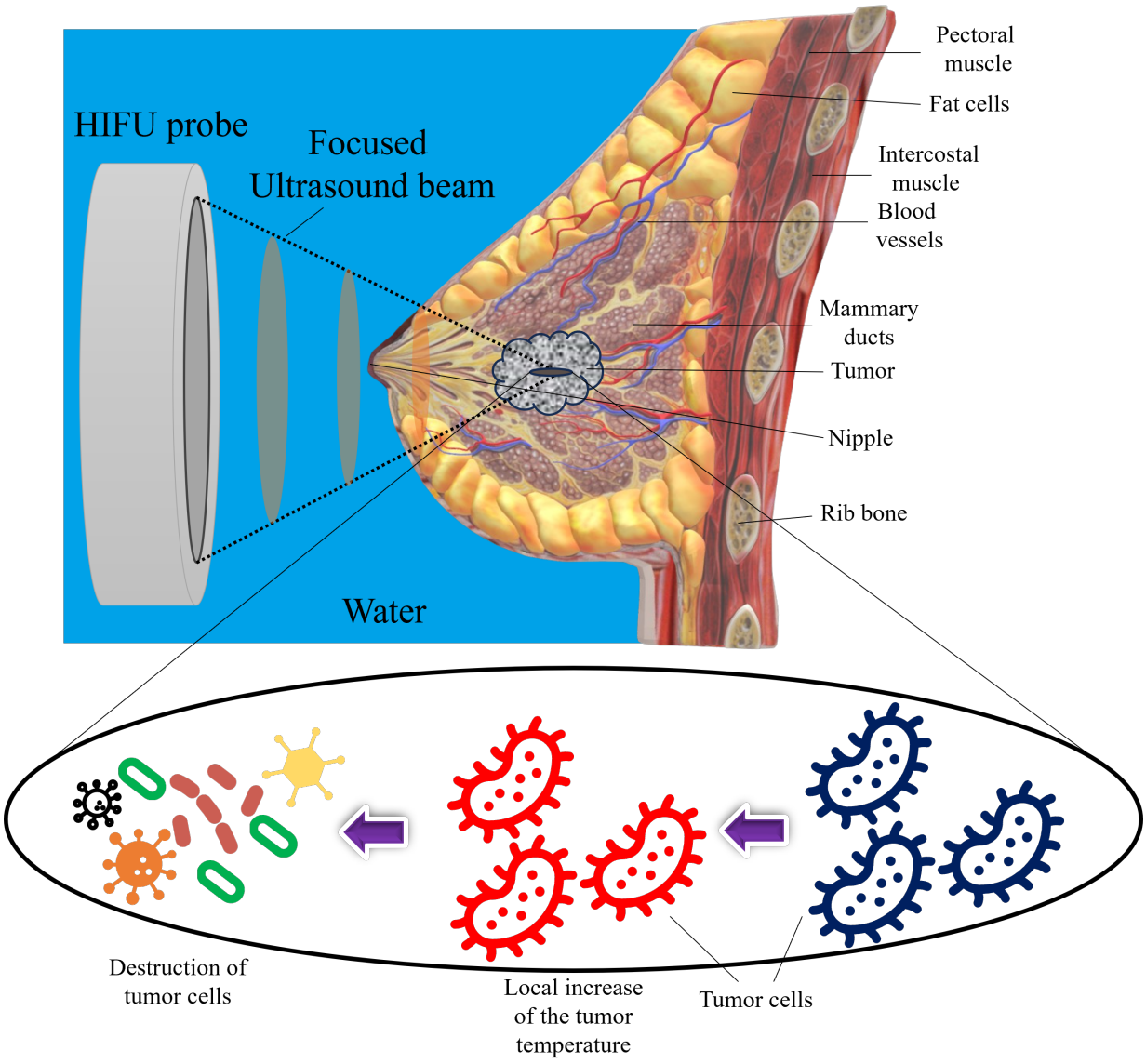


Figure 3.1: A schematic of the HIFU ablation process for the treatment of a breast tumor.

As the technology continues to advance, ongoing research and clinical trials are expanding the applications of HIFU and improving its efficacy. New developments in transducer design, imaging techniques, and treatment protocols are enhancing the precision and versatility of HIFU, making it an increasingly attractive option for both patients and healthcare providers.

In conclusion, HIFU represents a significant advancement in non-invasive medical treatments, offering a safe, effective, and patient-friendly alternative to traditional surgical methods. Its ability to deliver precise, targeted therapy with minimal recovery time is driving its adoption across a wide range of clinical applications, solidifying its role as a cutting-edge tool in modern medicine [159].

3.2 Governing Equations

In this section, we delve into the essential equations and procedural steps necessary to comprehensively simulate the process of HIFU ablation. This simulation involves a multiphysics approach that integrates acoustic wave propagation, heat generation and transfer, and biological tissue response to provide a detailed understanding of the ablation process.

3.2.1 Acoustic Wave Generation and Propagation

To accurately represent the fixed acoustic field within our HIFU modeling approach, we address the inhomogeneous Helmholtz equation. This equation is pivotal for describing the propagation of acoustic waves in a medium with varying properties, which is essential for understanding how ultrasound waves behave in biological tissues. The specific form of this equation can be found in reference [66]:

$$\nabla \cdot \left(-\frac{1}{\rho}(\nabla p - \overrightarrow{q_d}) \right) - \frac{k^2 p}{\rho} = Q_m \tag{3.1}$$

In this equation, several critical parameters are defined, ρ represents the density of the tissue, which varies depending on the type of tissue and its composition. p represents the total pressure field generated by the acoustic waves. k is the wave number, which is related to the frequency of the ultrasound and the speed of sound in the tissue. q_d denotes the source of the dipole domain, accounting for the directional nature of the acoustic sources. Q_m represents the source of the monopole domain, corresponding to the omnidirectional sources within the medium.

Solving the inhomogeneous Helmholtz equation allows us to model how the acoustic waves propagate through the heterogeneous medium of breast tissue. This includes the interaction of waves with various tissue interfaces, the reflection and refraction phenomena, and the focusing of energy at the target site. The equation encapsulates both the wave-like nature of ultrasound propagation and the complexities introduced by the tissue's inhomogeneities.

To solve this equation, we employ numerical methods such as the FEM or the boundary element method (BEM). These methods discretize the tissue volume and apply the Helmholtz equation to each discrete element, enabling the calculation of the pressure field throughout the tissue. This computational approach ensures that the detailed structure and properties of the tissue are accurately represented.

The solutions to the Helmholtz equation provide the spatial distribution of the acoustic pressure, which is crucial for the subsequent steps in the HIFU simulation process. Specifically, the pressure field is used to calculate the intensity and absorption of ultrasound energy within the tissue, leading to localized heating and therapeutic effects.

In summary, the inhomogeneous Helmholtz equation (3.1) serves as a fundamental component in modeling the fixed acoustic field in HIFU treatments. By accurately solving this equation, we can predict how ultrasound waves interact with biological tissues, enabling precise targeting and effective tumor ablation. This modeling approach forms the foundation for understanding and optimizing HIFU therapy, ensuring its efficacy and safety in clinical applications.

As acoustic waves travel through breast tissues during HIFU treatment, they undergo a reduction in intensity, a phenomenon known as attenuation. Attenuation is caused by the absorption and scattering of the ultrasound energy within the tissue, leading to a decrease in wave amplitude as the distance from the source increases. This effect is crucial to account for, as it directly influences the distribution of energy and the efficacy of the treatment.

Different types of tissues, such as fat, glandular tissue, and tumors, exhibit varying levels of attenuation due to their unique acoustic properties. To accurately model the HIFU process, it is essential to employ a customized attenuation model for each tissue type, utilizing specific attenuation coefficients (α_a). These coefficients represent the rate at which the ultrasound intensity diminishes per unit distance traveled within the tissue.

The inclusion of attenuation in the modeling process results in the wave number (k) becoming a complex value, as described by the following equation [66]:

$$k = \frac{\omega}{c} - i\alpha_a \tag{3.2}$$

In this equation, ω represents the angular frequency of the ultrasound waves. c represents the speed of sound in the tissue. α_a is the attenuation coefficient, which varies depending on the tissue type.

The complex wave number k incorporates both the real part, $\frac{\omega}{c}$, which accounts for the phase velocity of the wave, and the imaginary part, α_a, which represents the attenuation. The imaginary component introduces an exponential decay term in the wave equation, effectively modeling the energy loss as the waves propagate through the tissue.

To implement this attenuation model in the HIFU simulation, we first identify the specific tissues involved and assign appropriate attenuation coefficients. For example, adipose (fat) tissue typically has a lower attenuation coefficient compared to glandular or tumor tissues, reflecting its different acoustic absorption properties. By accurately assigning these coefficients, we ensure that the simulation reflects the true behavior of ultrasound waves in a heterogeneous tissue environment.

The next step involves solving the modified Helmholtz equation with the complex wave number, which allows us to compute the attenuated pressure field within the breast tissue. This pressure field is essential for determining the spatial distribution of absorbed acoustic energy, which in turn dictates the thermal and mechanical effects on the tissue.

By incorporating tissue-specific attenuation coefficients, the model can predict more accurately the intensity and distribution of the ultrasound waves, leading to better treatment planning and optimization. The ability to simulate how attenuation affects wave propagation helps in designing HIFU protocols that maximize tumor ablation while minimizing damage to surrounding healthy tissues.

In summary, the customized attenuation model, represented by the complex wave number equation (3.2), plays a critical role in accurately simulating HIFU treatments. By accounting for the unique attenuation properties of different tissue types, we can enhance the precision and effectiveness of the therapy, ultimately improving patient outcomes and advancing the application of HIFU in clinical practice.

3.2.2 Bioheat Transfer in Breast Tissues

In the context of simulating temperature distribution in biological tissues during HIFU treatments, Penne's bio-heat transfer equation is employed to model the complex interactions between heat generation, transfer, and dissipation. This equation is crucial for

predicting the thermal effects of focused ultrasound energy on tissues, ensuring precise control and effective treatment outcomes. The bio-heat transfer equation, as presented in reference [129], is given by:

$$\rho c_p \frac{\partial T}{\partial t} = k_h \nabla^2 T + \omega_b \rho_b c_{p,b} (T_b - T) + Q_{met} + Q_S \tag{3.3}$$

This mathematical equation incorporates multiple variables that correspond to the physical properties of both tissue and blood, capturing the key factors influencing thermal dynamics in biological systems. Here's a detailed breakdown of the terms and their significance: ρ represents the density of the tissue, indicating how much mass per unit volume is present, which affects how the tissue stores and transfers heat. c_p denotes the specific heat capacity at constant pressure of the tissue, reflecting the amount of heat required to raise the temperature of the tissue by one degree Celsius. k_h is the heat conduction coefficient of the tissue, describing how efficiently heat is conducted through the tissue material. ω_b indicates the local blood perfusion rate, which is crucial for modeling the convective heat transfer due to blood flow. ρ_b represents the density of the blood, affecting how much heat the blood can carry away from the heated tissue. $c_{p,b}$ is the specific heat capacity of the blood, signifying the amount of heat required to raise the temperature of blood by one degree Celsius. T_b refers to the local temperature of the arterial blood, providing a baseline for the temperature differential driving heat transfer between blood and tissue. Q_{met} signifies the rate at which metabolic heat is generated in the region, accounting for the endogenous heat produced by cellular processes. Q_S denotes the heat source rate, which corresponds to the power absorbed by the acoustic waves (the dissipated acoustic power), representing the external energy input from the HIFU treatment.

The left side of the equation, $\rho c_p \frac{\partial T}{\partial t}$, represents the rate of change of thermal energy in the tissue. It balances the various sources and sinks of heat on the right side, ensuring a comprehensive description of thermal dynamics.

The term $k_h \nabla^2 T$ captures the diffusion of heat within the tissue, driven by temperature gradients. The term $\omega_b \rho_b c_{p,b} (T_b - T)$ models the convective heat transfer due to blood perfusion, which can significantly affect temperature distribution, especially in highly vascularized tissues. The metabolic heat generation, Q_{met}, adds an endogenous heat source, while the acoustic power, Q_S, represents the exogenous heat source from the HIFU procedure.

By solving Penne's bio-heat transfer equation, we can predict the spatial and temporal temperature distribution within the targeted tissue. This enables the assessment of thermal

damage and the optimization of HIFU parameters to maximize treatment efficacy while minimizing collateral damage to surrounding healthy tissues.

In practical applications, numerical methods such as finite element analysis (FEA) are often used to solve this equation, taking into account the heterogeneous nature of biological tissues and the complex boundary conditions present in the human body. These simulations provide valuable insights into the thermal behavior of tissues under HIFU treatment, guiding the development of safe and effective clinical protocols.

In summary, Penne's bio-heat transfer equation is a fundamental tool in the simulation of HIFU-induced thermal effects. By accurately modeling the heat generation, transfer, and dissipation within biological tissues, it allows for precise control over the ablation process, ensuring the successful destruction of pathological tissues while preserving healthy ones [129].

Once the acoustic field is resolved, the next step is to determine the acoustic pressure field, which is crucial for understanding how the ultrasound waves propagate through the tissue. The acoustic pressure field provides detailed information about the distribution of pressure amplitudes within the tissue, which is necessary for subsequent calculations of acoustic intensity and heat generation.

Following the determination of the acoustic pressure field, the computation of the acoustic intensity field is performed. The acoustic intensity field represents the power transmitted by the acoustic waves per unit area and is essential for quantifying the energy available for tissue heating. According to references [66, 57], the value of Q_S, required for the thermal simulation, is calculated using the following equation:

$$Q_S = 2\alpha_a I = \left| \mathrm{Re}\left(\frac{1}{2} p v\right) \right| \tag{3.4}$$

In this equation, α_a represents the attenuation coefficient, I represents the magnitude of acoustic intensity, p represents the acoustic pressure, and v represents the vector of acoustic particle velocity. The term Q_S signifies the rate of heat source, which corresponds to the power absorbed by the acoustic waves, effectively translating the acoustic energy into thermal energy within the tissue.

Additionally, the magnitude of sound intensity refers to the power conveyed by the acoustic waves per unit area in a direction perpendicular to that area. This is defined as follows, according to reference [81]:

$$I = \frac{p_A^2}{2\rho c} \tag{3.5}$$

In this equation, p_A represents the amplitude of pressure oscillation at the pressure anti-node, while ρ and c represent the density and speed of sound, respectively. The sound intensity, I, is a critical parameter as it quantifies the energy flux through the tissue, directly influencing the heating effect.

By incorporating the acoustic intensity and pressure values, the heat source term Q_S can be accurately computed, which is then used in the bio-heat transfer equation to simulate the thermal distribution within the tissue. This process involves solving the bio-heat transfer equation to predict the temperature rise and distribution resulting from the absorbed acoustic energy.

3.2.3 Prediction of the Fraction of Necrotic Tissue

The evaluation of tissue injury resulting from the hyperthermia process in HIFU treatments can be effectively conducted using the Arrhenius kinetic model. This model describes the thermal damage to biological tissues as a result of elevated temperatures, providing a quantitative framework for predicting the extent of tissue injury. The Arrhenius model, as described in references [86, 168], is given by:

$$\frac{\partial \alpha}{\partial t} = (1-\alpha)^n A e^{-\frac{\Delta E}{RT}} \tag{3.6}$$

In this equation, α represents the degree of tissue injury, which varies from 0 (no injury) to 1 (complete necrosis). n denotes the polynomial order within the equation, capturing the complexity of the reaction kinetics. R is the universal gas constant, a fundamental constant in thermodynamics. T corresponds to the tissue temperature at any given time. A is the frequency factor, which indicates how often the reactants approach the activation barrier per unit time. ΔE is the activation energy, representing the energy barrier that must be overcome for the tissue damage reaction to occur.

These parameters, A and ΔE, are specific to the particular tissue type and have been empirically determined for various tissues. For breast tissue, these parameters have been calculated as $A = 1.18 \times 10^{44}$ s^{-1} and $\Delta E = 3.02 \times 10^5$ J mol^{-1}. These values are critical for accurately modeling the thermal response of breast tissue during HIFU treatment.

Once the degree of tissue injury (α) is determined using the Arrhenius equation, it is necessary to translate this injury level into a more clinically relevant measure: the fraction of necrotic tissue. The fraction of necrotic tissue (θ_d) indicates the proportion of tissue that has undergone irreversible damage and necrosis. This can be expressed accordingly, as detailed in reference [168]:

$$\theta_d = \min(\max(\alpha, 0), 1) \tag{3.7}$$

This equation ensures that θ_d is bounded between 0 and 1, where 0 indicates no necrosis and 1 indicates complete necrosis. The use of the min and max functions ensures that the fraction of necrotic tissue is constrained within this biologically meaningful range.

The integration of these equations into the HIFU simulation framework allows for a comprehensive assessment of tissue injury. Using the bio-heat transfer equation, the spatial and temporal distribution of temperature within the tissue is simulated based on the absorbed acoustic energy. The Arrhenius equation is applied to the simulated temperature data to calculate the degree of tissue injury (α) over time. This step involves solving the differential equation for α at each point in the tissue. The degree of injury is then converted into the fraction of necrotic tissue (θ_d) using equation (4.3). This provides a clear measure of the extent of irreversible damage. The results are visualized to provide a detailed map of tissue necrosis, allowing for the evaluation of treatment efficacy and the optimization of HIFU parameters to maximize tumor ablation while minimizing damage to surrounding healthy tissue.

By employing the Arrhenius kinetic model and these associated equations, clinicians and researchers can gain a deeper understanding of the thermal effects of HIFU on biological tissues. This approach provides a robust framework for predicting tissue response, guiding treatment planning, and ensuring the safe and effective application of HIFU in clinical practice [86, 168].

3.3 Geometry of the Model

All geometry processing presented in this study utilizes the commercial software "MATLAB" [103]. MATLAB is a powerful tool for numerical computing and visualization, making it ideal for handling the complex simulations required for HIFU treatments. The software is used to develop and implement the algorithms necessary for modeling the acoustic and thermal interactions within the breast tissue.

A technique called ARBP, previously described, is employed in the simulations. The ARBP method is particularly useful for accurately modeling the boundaries and interactions of acoustic waves within the tissue environment. In the experimental setup, the geometry includes a water tank where the breast tissue model is placed.

Within the tank, an acoustic transducer is submerged at the bottom. This transducer generates an ultrasound wave that propagates through the water and into the breast tissues.

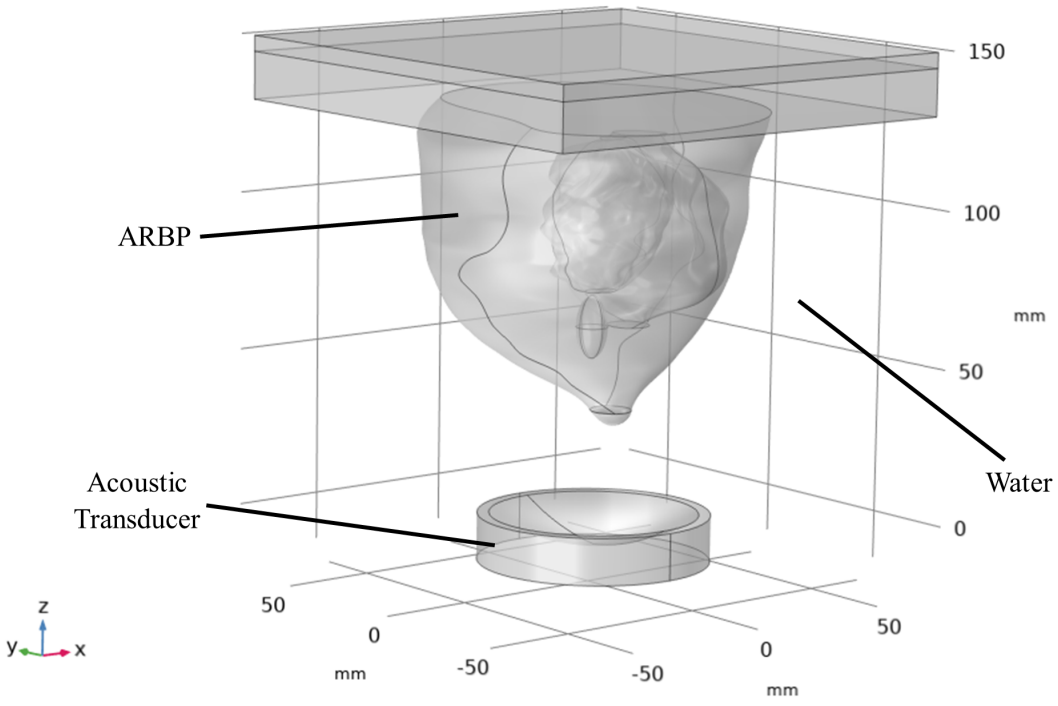


Figure 3.2: 3D visualization of the entire geometry considered.

The transducer is designed in the form of a bowl with a focal length of 51.74 mm, which is selected based on the position of the tumor's center. The bowl-shaped design ensures that the ultrasound waves converge at a specific focal point, which is aligned with the center of the tumor. This alignment is crucial for concentrating the acoustic pressure precisely on the tumor, leading to a rapid temperature increase and effective tissue ablation.

The entire geometry of the experimental setup is depicted in Fig. 3.2. This figure provides a comprehensive view of the water tank, the submerged transducer, and the breast tissue model. It illustrates how the ultrasound waves are focused on the tumor, highlighting the spatial arrangement of the components.

For a clearer representation of the acoustic transducer, a cross-section view of the model passing through the middle of the geometry is shown in Fig. 3.3. In this illustration, the key dimensions of the transducer are detailed, including its focal length (radius of curvature) of 51.74 mm and its aperture of 64 mm. The cross-sectional view helps to visualize the

curvature of the transducer and its focusing capabilities.

Using MATLAB, the geometry of the water tank, breast tissue, and transducer is modeled accurately. This includes defining the dimensions and spatial relationships of all components. The bowl-shaped transducer is designed to focus ultrasound waves precisely at the tumor center. The dimensions, such as the focal length and aperture, are chosen to ensure optimal focusing. The ARBP technique is used to simulate the boundary conditions and interactions of the acoustic waves within the water and tissue environment. This includes modeling the propagation, reflection, and absorption of the waves. The results of the simulations, including the pressure and temperature fields, are visualized using MATLAB's powerful graphical capabilities. Figs. 3.2 and 3.3 provide detailed visualizations that help to understand the focusing and heating effects of the transducer.

By employing MATLAB and the ARBP technique, the simulations can accurately predict the behavior of ultrasound waves and their interactions with the tissue. This approach allows for precise control over the treatment parameters, ensuring that the acoustic pressure is focused on the tumor to achieve effective ablation while minimizing damage to surrounding healthy tissues.

In summary, the use of MATLAB for geometry processing and the implementation of the ARBP technique within a water tank setup provide a robust framework for simulating and visualizing HIFU treatments. The detailed geometry and careful design of the transducer ensure that the acoustic waves are accurately focused on the tumor, leading to successful tissue ablation and improved treatment outcomes [103].

This section outlines the procedure for incorporating and utilizing 3D grid-based numerical breast models with accurate anatomical details in deep learning and FEM simulations. The numerical breast model used in the simulations was obtained from the UWCEM repository [1], which houses a comprehensive collection of numerical breast models derived from MRI scans. These models are meticulously designed to accurately represent the anatomy of breasts and are instrumental in the detection and treatment planning for breast cancer.

The UWCEM repository's models are based on a series of T1-weighted MRI scans taken from patients positioned face-down. T1-weighted images are generated using specific time intervals for pulse sequences, known as TE (time to echo) and TR (time of repetition). These sequences highlight the anatomical structures of the breast tissues, providing detailed images that can be used to create accurate 3D models.

For the simulations described in this section, a numerical breast model identified as Breast ID 070604PA1 and classified as Class 2 was selected from the repository. The classification of the breast models is based on the American College of Radiology's density categories [133]. These categories are Class 1, mostly fat, with less than 25% glandular

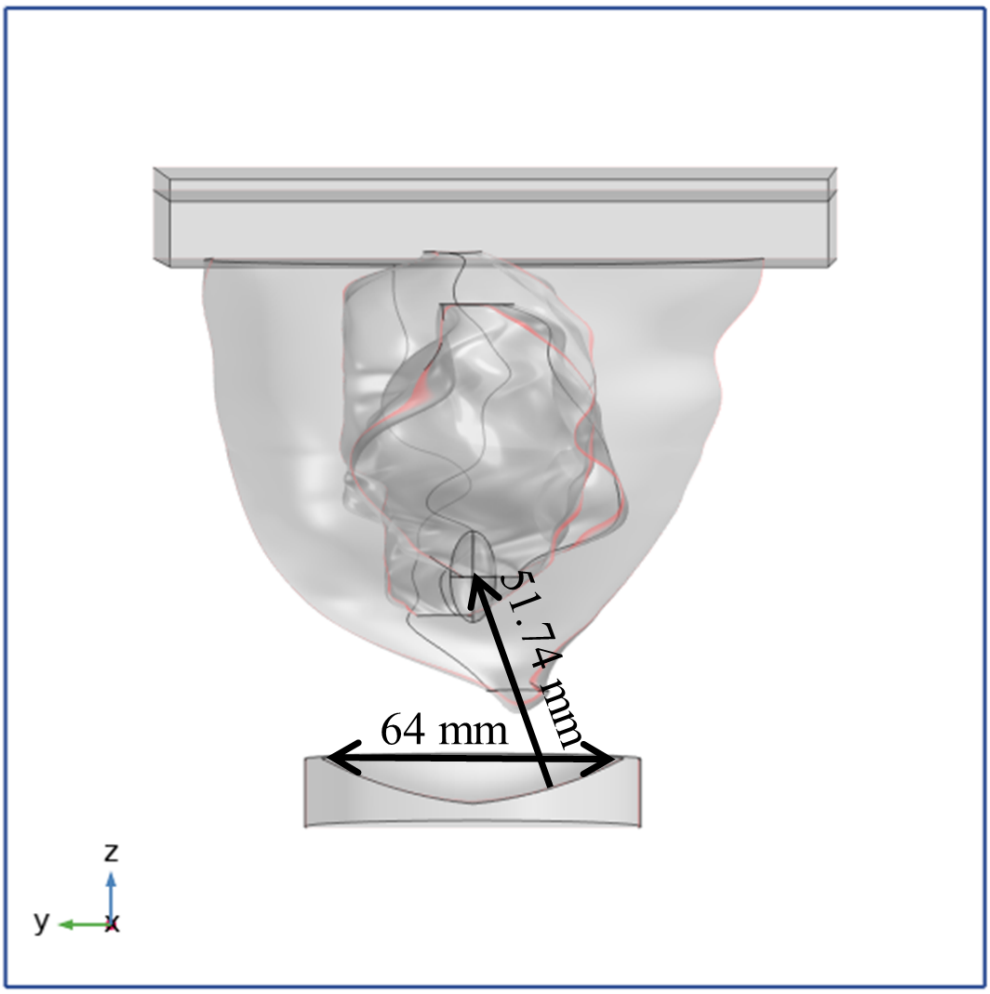


Figure 3.3: Middle cross-section view of the geometry.

tissue. Class 2, some fibro-connective and glandular tissue. Class 3, heterogeneously dense breasts, containing 51% to 75% glandular tissue. And Class 4, extremely dense breasts, with over 75% glandular tissue.

The chosen model, classified as Class 2, represents a breast with a moderate amount of fibro-connective and glandular tissue. This classification is crucial as it impacts the acoustic properties and the effectiveness of HIFU treatments. The model provides a realistic representation of breast anatomy, incorporating various tissue types, including fat, glandular tissue, and fibro-connective structures.

The numerical breast model is downloaded from the UWCEM repository. The model includes detailed anatomical features based on the MRI scans, ensuring accurate representation. The acquired model is preprocessed to fit the simulation requirements. This includes segmenting different tissue types, assigning appropriate acoustic and thermal properties, and creating a 3D grid that represents the tissue structure. The preprocessed model is integrated into the deep learning framework and FEM simulations. In the deep learning context, the model is used to train algorithms to detect and analyze breast cancer. In FEM simulations, the model aids in studying the interaction of ultrasound waves with the breast tissues, helping to optimize HIFU treatment parameters. The simulations are executed, utilizing the detailed breast model to provide realistic and accurate results. The FEM simulations, in particular, benefit from the anatomical details, enabling precise modeling of acoustic wave propagation, heat generation, and tissue response. The simulation results are validated against clinical data to ensure accuracy. Detailed analysis is conducted to understand the impact of various parameters on the treatment outcomes and to refine the simulation models further.

The use of accurately classified numerical breast models, such as Breast ID 070604PA1, allows for more precise and effective simulations, enhancing the predictive power of deep learning models and the reliability of FEM analyses. This approach ultimately contributes to improved diagnosis, treatment planning, and therapy outcomes for breast cancer patients [1, 133].

By utilizing the data mentioned earlier and employing a MATLAB [103] function connected to the breast phantom's tissue types, a 3D point cloud is generated within the spatial coordinates. These point clouds, which accurately represent different tissue types, serve as the foundational data for constructing a detailed 3D model of the breast phantom. The point clouds are then processed using SOLIDWORKS software to convert them into surfaces and volumes, resulting in the creation of a comprehensive and anatomically accurate 3D model of the breast phantom [155].

The process begins with the generation of the point clouds in MATLAB, where each

point is mapped to specific spatial coordinates based on the tissue type it represents. The point clouds for different tissue types such as fibro-connective and glandular tissue (FCG), transitional tissue, fatty tissue, and muscle are extracted and visualized. These point clouds are then imported into SOLIDWORKS, a CAD software known for its robust capabilities in handling complex geometries and creating detailed 3D models.

In SOLIDWORKS, the surfaces are formed by connecting relevant points from each tissue type. This step involves using the software's surface modeling tools to create continuous surfaces that accurately represent the boundaries of each tissue type. The software's algorithms ensure that the surfaces are smooth and free of gaps, providing a realistic depiction of the anatomical structures. These surfaces are subsequently interconnected to form a closed volume, which accurately replicates the various tissue types present in the breast phantom.

To simplify the process and create an ARBP, four specific tissue types are isolated: FCG, transitional tissue, fatty tissue, and muscle. Each tissue type is modeled separately to ensure that the unique properties and spatial distribution are accurately captured. Relevant information regarding these tissue types is extracted from the provided database and used to guide the modeling process.

Once the surfaces are created, they are stitched together to form a closed volume. This volume is then refined to ensure that it accurately reflects the anatomical features and spatial relationships of the different tissue types. The final 3D model is a detailed and realistic representation of the breast phantom, suitable for use in simulations and other applications.

Fig. 3.4 provides a visual representation of the multiple steps involved in generating a 3D breast phantom. The figure showcases the point cloud obtained from the database, the surfaces derived from this point cloud, and the resulting volume corresponding to fatty tissue. The visualization in Fig. 3.4 helps to illustrate the transformation process from raw point cloud data to a finished 3D model.

Each tissue type is transformed into a 3D object following the detailed steps depicted in Fig. 3.4, enabling a better understanding of the entire process. This comprehensive approach ensures that the final model is not only anatomically accurate but also functional for various applications, including medical simulations, treatment planning, and educational purposes. By following these steps, the resulting 3D breast phantom provides a valuable tool for advancing research and improving clinical outcomes in breast cancer diagnosis and treatment [103, 155].

Our simulations involve representing the tumor as an ellipsoid object with specific dimensions: 10 mm in the z-axis diameter, and 5 mm in the x-axis and y-axis diameters.

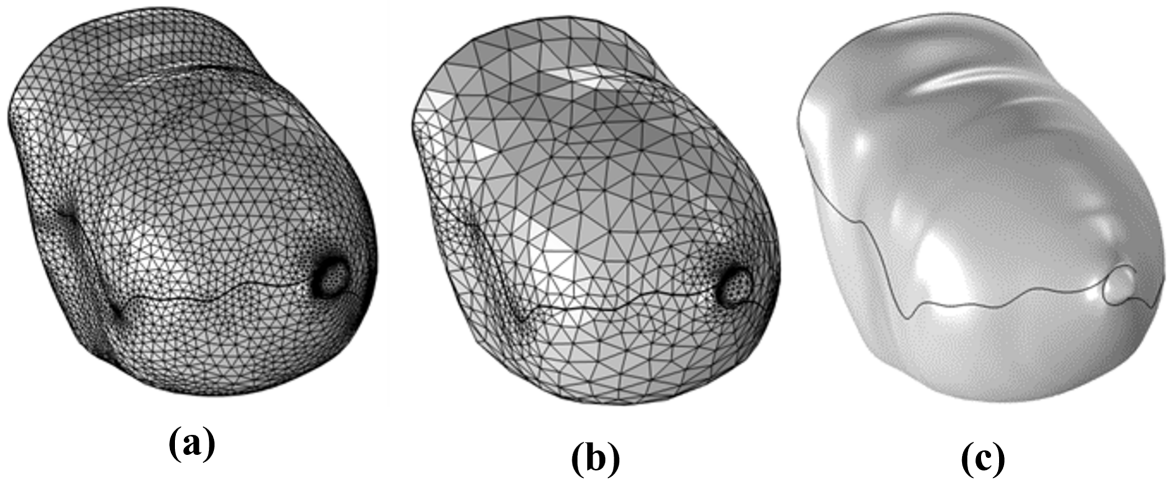


Figure 3.4: Three distinct processes were used to build a 3D breast phantom: (a) obtaining a point cloud from the database; (b) constructing surfaces from the point cloud; and (c) producing the volume from knitted surfaces.

This particular configuration accurately models a small, early-stage tumor. Such tumors are classified as T1c, which signifies that the tumor is greater than 1 cm but not more than 2 cm in its greatest dimension and has not spread to lymph nodes or other parts of the body [83]. This classification indicates a relatively early stage of cancer development, where treatment and management options are most effective.

In our model, the tumor is strategically positioned within the fatty tissue of the breast phantom. This placement is crucial for simulating a realistic scenario, as fatty tissue is a common site for the development of breast tumors. The accurate representation of the tumor's location within the breast's anatomical structure allows for more precise simulation results, particularly in the context of HIFU treatment planning and execution.

The various tissue types mentioned earlier—FCG, transitional tissue, fatty tissue, and muscle—are integrated into the simulation model to create an ARBP. Each tissue type is assigned its respective acoustic and thermal properties, which are essential for accurately modeling the propagation of ultrasound waves and the resulting thermal effects.

In our simulations, the ARBP model includes the tumor and its surrounding tissues, providing a comprehensive framework for studying the interactions between the ultrasound waves and the different tissue types. The realistic geometry and material properties ensure

that the simulations can predict the behavior of the ultrasound waves and their impact on the tumor and surrounding tissues with high fidelity.

Fig. 3.5 illustrates the detailed configuration of the ARBP model, highlighting the tumor's location within the fatty tissue. This figure is essential for visualizing the spatial relationships between the different tissue types and understanding the setup of the simulation environment. The figure shows how the ellipsoid tumor is embedded within the fatty tissue, surrounded by other breast tissues, thus providing a clear context for the simulation results.

The use of an ellipsoid shape for the tumor allows for a more realistic representation of tumor geometry, as real tumors are often irregular and not perfectly spherical. This choice enhances the accuracy of the simulation by better mimicking the actual conditions found in clinical scenarios. Moreover, the small size and early-stage classification of the tumor align with the clinical focus on early detection and treatment, making the simulation relevant for real-world applications.

By incorporating these detailed anatomical and physiological characteristics into our simulations, we can more effectively study the efficacy of HIFU treatments. The ability to accurately simulate the acoustic and thermal interactions within the breast tissues helps in optimizing treatment parameters, improving targeting precision, and minimizing collateral damage to healthy tissues. This approach ultimately aims to enhance the effectiveness of HIFU as a non-invasive treatment option for breast cancer.

In conclusion, the detailed representation of the tumor and surrounding tissues in our ARBP model, as depicted in Fig. 3.5, plays a crucial role in the accuracy and relevance of our simulations. This comprehensive modeling approach ensures that our findings can be effectively translated into clinical practice, contributing to better treatment outcomes for patients with early-stage breast cancer [83].

3.4 Simulation Procedure

This section provides a comprehensive demonstration and explanation of the numerical modeling process for HIFU. Each step is meticulously outlined, detailing the necessary data, material properties, and the initial and boundary conditions required for each physical phenomenon involved in the process.

The first step focuses on simulating the generation of ultrasonic waves within the specified domain. This involves understanding the propagation of these waves through various tissues and materials, considering factors such as wave frequency, amplitude, and the

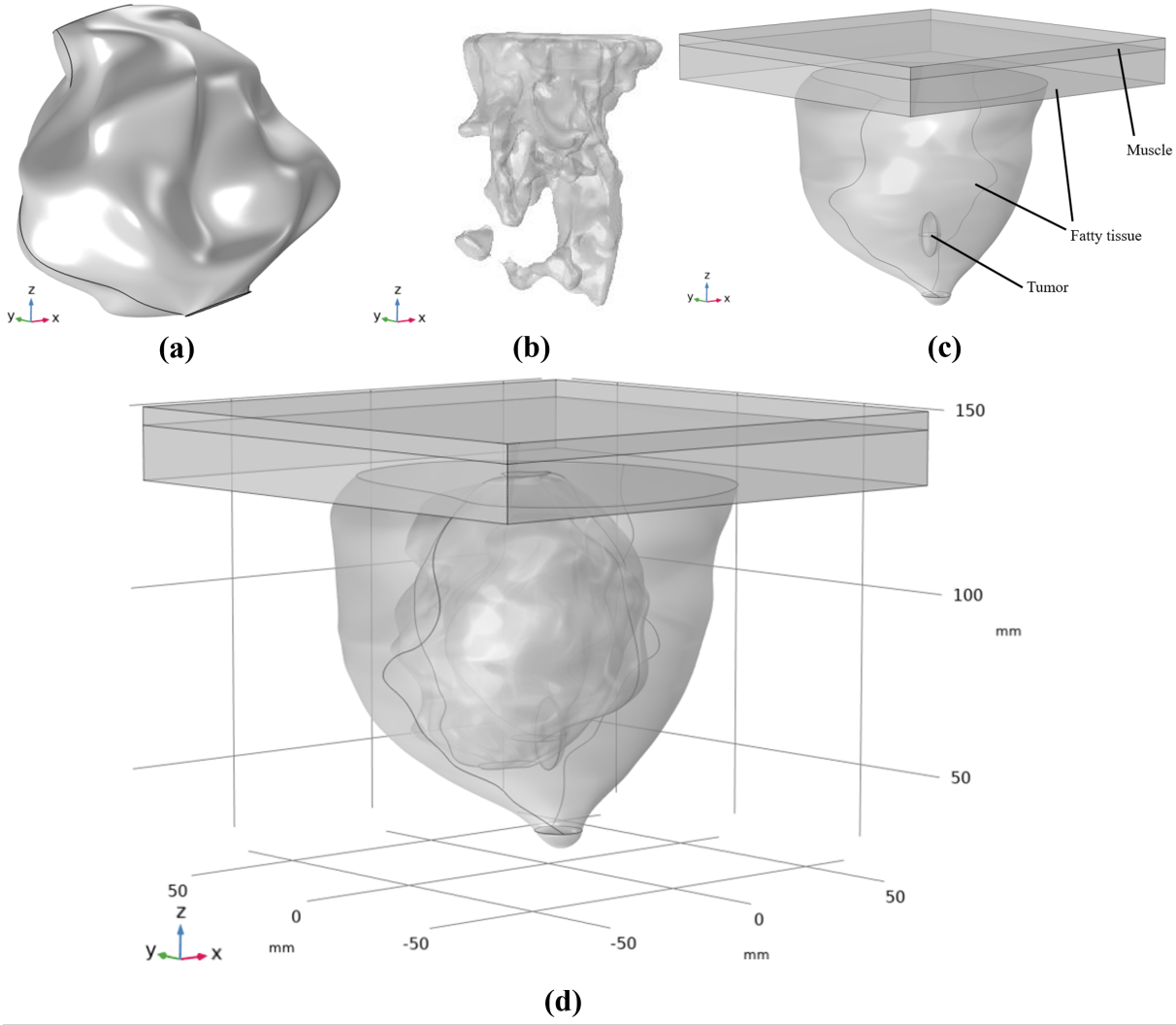


Figure 3.5: Considered 3D geometry of tissue types separately and collectively: (a) FCG tissue; (b) transitional tissue; (c) fatty tissue, muscle, and tumor; and (d) all tissues within each other as the ARBP.

acoustic properties of the medium. Accurate representation of these properties is crucial to ensure the simulation mimics real-world conditions as closely as possible.

In the second step, the simulations involve the generation of heat and the subsequent transfer of this heat within the breast phantom. This step requires a detailed thermal analysis, accounting for the thermal conductivity, specific heat capacity, and density of the breast tissue. The heat generated by the ultrasonic waves causes localized temperature increases, which must be accurately modeled to predict the thermal effects on the tissue. The transfer of heat through conduction and, potentially, perfusion within the tissue is also considered, as these factors influence the overall thermal response of the tissue.

Overall, the numerical modeling process for HIFU presented in this section provides a detailed roadmap, guiding through each phase with a clear explanation of the physics involved and the necessary parameters. This ensures that the simulation is robust and reliable, providing valuable insights into the behavior of ultrasonic waves and heat transfer in biological tissues.

The initial step in the numerical modeling process concentrates on the consideration of pressure acoustics in frequency-domain physics. At the boundary of the transducer aperture, an input displacement amplitude (d_0) is introduced to initiate the simulation. This displacement amplitude is set at 3.8 nm, ensuring precise control over the initial conditions of the simulation.

According to Diaz et al. [34], when the input pressure remains below $p_0 = 0.35$ MPa, the solutions obtained for a similar HIFU setup are within the linear regime. This implies that the behavior of the acoustic waves can be accurately predicted using linear equations, which simplifies the computational model and enhances its efficiency. However, as the input pressure increases beyond this threshold, the results enter a nonlinear regime. In this regime, the relationship between pressure and displacement becomes more complex, leading to deviations from the linear solution, particularly in the focal region where the acoustic energy is concentrated.

The solution of the acoustic pressure equation (Eq. 3.1) assumes linearity in the propagation of acoustic waves. This means that the model does not consider the nonlinear effects that can occur at higher pressures, where the acoustic waves may interact in more complex ways. Additionally, the magnitude of shear waves in the tissue is significantly smaller than that of pressure waves, which allows for the simplification of the model by neglecting shear waves and their associated nonlinear effects.

Based on these assumptions, the input pressure for the simulation is set at approximately 0.1 MPa. This value ensures that the simulation remains within the linear regime, providing accurate and reliable results. The acoustic frequency is considered to be 1.1 MHz,

which is a typical frequency for HIFU applications. This frequency is chosen to balance the penetration depth and the resolution of the ultrasonic waves, ensuring effective targeting of the tissue while maintaining a high level of precision.

Overall, this step lays a solid foundation for the numerical modeling process, establishing the initial conditions and parameters necessary for accurate simulation of pressure acoustics in HIFU applications. By carefully selecting the input pressure and frequency, and by focusing on the linear regime, the model provides a robust framework for subsequent steps in the simulation process.

Following the simulation of acoustic wave propagation within the breast phantom, the next step involves incorporating time-dependent bioheat transfer physics to model the thermal effects induced by the ultrasonic waves. This step is crucial for understanding the thermal dynamics within the tissue and predicting the extent of tissue ablation.

To begin, the acoustic intensity field is determined based on the previously calculated acoustic pressure field. This intensity field provides the necessary data to compute the thermal energy imparted to the tissue. The heat source (Q_S) responsible for this thermal energy is calculated using Eq. 3.4, which accounts for the conversion of acoustic energy into heat within the tissue. This equation considers factors such as the absorption coefficient of the tissue and the intensity of the acoustic waves.

In our simulations, the duration of the acoustic wave presence is set to 1 second. This short duration is chosen to represent the initial phase of the HIFU treatment, where the ultrasonic waves are actively delivering energy to the targeted tissue. During this 1-second period, the heat source generated by the ultrasonic waves is active, leading to a rapid increase in temperature within the focal region.

Following this initial 1-second period, the simulation continues for an additional 4 seconds without the presence of the heat source. This phase simulates the cooling down process of the tissue, allowing for the analysis of the thermal relaxation and heat dissipation that occur after the cessation of the ultrasonic waves. The total simulation time of 5 seconds provides a comprehensive view of the thermal response of the tissue, encompassing both the heating and cooling phases.

The primary objective of this thermal simulation is to determine the extent of necrotic tissue resulting from the 5-second exposure to elevated temperatures. By analyzing the temperature distribution and the thermal dose delivered to the tissue, it is possible to predict the regions where irreversible thermal damage occurs. This information is critical for assessing the efficacy of the HIFU treatment and ensuring that the targeted tissue is effectively ablated while minimizing damage to surrounding healthy tissue.

Overall, this step integrates the acoustic and thermal aspects of the HIFU process, providing a detailed understanding of the thermal dynamics and their impact on tissue ablation. By incorporating time-dependent bioheat transfer physics, the simulation offers valuable insights into the thermal behavior of the tissue and the effectiveness of the HIFU treatment.

To calculate the fraction of necrotic tissue, thermal damage is quantified in the simulation using the Arrhenius kinetics formula (Eq. 3.5). This formula allows for the prediction of tissue damage based on the time-temperature history of the tissue, providing a means to estimate the extent of necrosis resulting from the HIFU treatment.

The simulation also includes considerations for heat transfer through free convection and radiation to accurately capture the thermal effects within the tissue environment. Free convection refers to the heat transfer that occurs due to the movement of fluid, in this case, the interstitial fluid within the tissue, which can affect the overall temperature distribution. Radiation, although typically less significant in biological tissues, is also accounted for to ensure a comprehensive thermal model.

Moreover, the impact of blood perfusion on cooling the breast and tumor area is integrated into the simulation, as outlined in Eq. 3.3. Blood perfusion is a critical factor in thermal simulations as it represents the cooling effect provided by the circulation of blood, which can significantly influence the temperature dynamics within the tissue. The properties of blood, such as its thermal conductivity and specific heat, along with the blood perfusion rate and metabolic heat generation for each tissue type, are provided in Table 3.1. These parameters are essential for accurately modeling the heat transfer and ensuring that the simulation reflects the physiological conditions.

Table 3.1: Thermophysical and acoustic properties of different materials [14, 166, 135, 151, 110, 28, 65, 59, 134].

Materials	ρ (kgm^{-3})	c_p ($Jkg^{-1}K^{-1}$)	k_h ($Wm^{-1}K^{-1}$)	c (ms^{-1})	α_a ($dBm^{-1}MHz^{-1}$)	Q_{met} (Wm^{-3})	ω_b (s^{-1})
FCG tissue	1050	3770	0.48	1470	87	700	0.0067
Transitional tissue	990	3270	0.345	1463.5	75	700	0.0067
Fatty tissue	930	2770	0.21	1457	48	700	0.0067
Tumor	1050	3852	0.54	1509	57	5790	0.005
Muscle	1100	3800	0.48	1588.4	109	5790	0.005
Water	997	4184	0.598	1480	0.22	-	-
Blood	1050	3617	0.52	1540	20	-	-

Fig. 3.6 illustrates the diverse boundary conditions considered for each of the mentioned

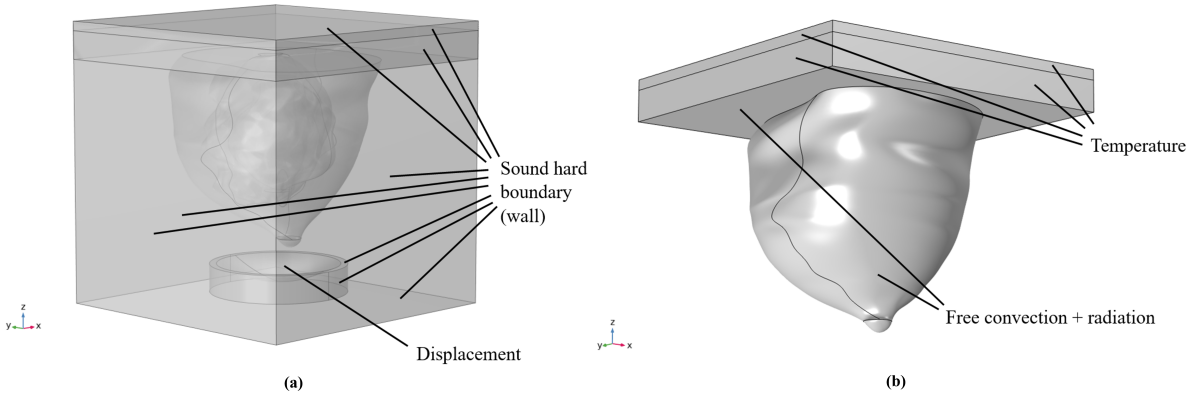


Figure 3.6: Boundary conditions considered in different physics, (a) pressure acoustics and (b) bioheat transfer.

physics. These boundary conditions include the interfaces between different tissue types, the external surfaces of the breast phantom exposed to the environment, and any interfaces where convection and radiation are significant. By carefully defining these boundary conditions, the simulation can more accurately represent the real-world scenario, providing reliable predictions of thermal behavior and tissue damage.

In summary, the calculation of necrotic tissue fraction involves a detailed thermal analysis using the Arrhenius kinetics formula, consideration of heat transfer through convection and radiation, and the impact of blood perfusion. By incorporating these factors and accurately modeling the boundary conditions, the simulation provides a robust framework for predicting the extent of thermal damage and the effectiveness of the HIFU treatment in inducing necrosis within the targeted tissue.

As depicted in Fig. 3.6, the boundary conditions for the frequency domain pressure acoustics physics involve considering a sound hard boundary for the water tank and transducer walls. This means that these boundaries are assumed to perfectly reflect sound waves, without any penetration or transmission of acoustic energy. Such a condition is appropriate for materials and surfaces that are much denser and more rigid compared to the medium in which the sound is propagating, like the walls of a water tank or the solid structure of a transducer.

Since the chest wall and other boundaries within the breast tissue are situated far from the acoustic source (the transducer's membrane), it is reasonable to assume them

as sound hard boundaries as well. This assumption simplifies the modeling process by treating these distant boundaries as reflective surfaces, ensuring that the acoustic energy is contained within the primary region of interest where the tissue interaction occurs.

A sound-hard boundary refers to a boundary where the normal components of acceleration and velocity are both zero. In practical terms, this means that when an acoustic wave encounters such a boundary, it is reflected back into the medium without any loss of energy. This reflection is characterized by a phase reversal of the wave upon hitting the boundary, which is crucial for accurately simulating the behavior of acoustic waves in a confined space.

By applying these sound hard boundary conditions, the simulation ensures that the acoustic waves are effectively confined and reflected within the intended domain. This confinement is essential for accurately modeling the propagation and focusing of the ultrasonic waves, particularly in scenarios where precise control over wave behavior is necessary, such as in HIFU treatments.

Furthermore, these boundary conditions help in maintaining the integrity of the acoustic field within the simulation, preventing unrealistic dispersion of energy that could occur if more complex or less defined boundary conditions were used. The sound hard boundary assumption thus provides a reliable and straightforward approach to simulate the interaction of ultrasonic waves with various boundaries in the system, ensuring that the primary focus remains on the targeted tissue region.

In summary, the boundary conditions for the frequency domain pressure acoustics physics, as depicted in Fig. 3.6, involve the use of sound hard boundaries for the water tank, transducer walls, chest wall, and other distant boundaries within the breast tissue. This approach simplifies the modeling process while ensuring accurate reflection and confinement of acoustic energy, which is critical for the precise simulation of ultrasonic wave propagation in HIFU applications.

To apply the input pressure signal, the transducer's membrane is assigned a normal displacement boundary condition, with the previously mentioned input displacement amplitude set at 3.8 nm. This specific displacement amplitude ensures precise control over the initial conditions of the acoustic wave propagation, allowing for accurate simulation of the ultrasonic waves generated by the transducer.

For modeling heat transfer within the body, bioheat transfer physics plays a crucial role. This modeling incorporates both heat flux and radiation from the skin to the surrounding air as boundary conditions. Heat flux refers to the rate of heat transfer per unit area across the skin surface, influenced by factors such as skin conductivity and the temperature gradient between the skin and the environment. Radiation, on the other hand, accounts for

the thermal energy emitted by the skin as infrared radiation, which can affect the overall heat dissipation from the body.

To ensure realistic simulation conditions, the temperature across internal boundaries within the body is assumed to be the normal human body temperature of 37°C. This temperature is set as the temperature boundary condition, providing a stable reference point for the thermal calculations. By maintaining this constant temperature at internal boundaries, the model accurately reflects the thermal environment of the human body under normal physiological conditions.

The equations corresponding to these boundary conditions are essential for defining the heat transfer processes and are detailed in the reference provided by Wang et al. [168]. These equations form the mathematical foundation for the bioheat transfer model, incorporating factors such as thermal conductivity, specific heat capacity, and perfusion rates of different tissues. By applying these equations, the simulation can accurately predict the temperature distribution and thermal effects within the body during the HIFU treatment.

In summary, the application of the input pressure signal involves assigning a normal displacement boundary condition to the transducer's membrane with an amplitude of 3.8 nm. For heat transfer modeling within the body, bioheat transfer physics incorporates heat flux and radiation from the skin to the surrounding air as boundary conditions. The internal body temperature is assumed to be a constant 37°C, set as the temperature boundary condition to ensure accuracy. The relevant equations for these boundary conditions are provided by Wang et al. [168], forming the basis for the thermal simulations in this study.

$$\text{Sound hard boundary (wall):} \quad -\overrightarrow{n}.(-\frac{1}{\rho}(\nabla p - q_d)) = 0 \tag{3.8}$$

$$\text{Normal displacement:} \quad -\overrightarrow{n}.(-\frac{1}{\rho}(\nabla p - q_d)) = (i\omega)^2 d_0 \tag{3.9}$$

$$\text{Convective heat flux:} \quad -\overrightarrow{n}.\overrightarrow{q} = h(T_\infty - T) \tag{3.10}$$

$$\text{Surface to ambient radiation:} \quad -\overrightarrow{n}.\overrightarrow{q} = \epsilon\sigma_{SB}(T_\infty^4 - T^4) \tag{3.11}$$

$$\text{Temperature:} \quad T = 310.15K \tag{3.12}$$

The mentioned equations involve various critical variables that play distinct roles in accurately modeling the physical phenomena under study. $\overrightarrow{n}$ represents the surface normal vector. It is a vector that is perpendicular to a surface at a given point. In the context of boundary conditions, $\overrightarrow{n}$ is used to define the direction of various physical quantities, such as heat flux or acoustic waves, relative to the surface. ρ stands for density, a fundamental property of materials that describes the mass per unit volume. In thermal and acoustic simulations, ρ is crucial for calculating the propagation of waves and heat within different media, as it influences inertia and energy storage. p represents total pressure. In acoustics, p is essential for describing the pressure variations caused by sound waves. Accurate modeling of p allows for the simulation of acoustic wave propagation and interactions within the medium. q_d denotes the dipole domain source, which refers to a type of acoustic source that generates sound by oscillating dipoles. It is used in simulations to model sources of sound within the domain. d_0 is the displacement amplitude of the input pressure signal. It defines the initial amplitude of the transducer's membrane displacement, which in turn affects the intensity and characteristics of the generated acoustic waves. q represents the heat transfer vector. It describes the rate and direction of heat flow within the material. The vector q is essential for determining how thermal energy is distributed and transferred throughout the simulated domain. h stands for the heat convection coefficient. It quantifies the rate of heat transfer between a solid surface and a fluid (such as air) in contact with it. The coefficient h is critical for modeling convective heat transfer at the boundaries of the domain. T_∞ represents the ambient temperature, which is the temperature of the surrounding environment. T_∞ serves as a reference temperature for calculating heat exchange between the body and its surroundings. T is the temperature within the domain. T is a central variable in thermal simulations, as it describes the thermal state of the material at any given point in space and time. ϵ denotes the surface emissivity, a measure of how effectively a surface emits thermal radiation compared to a perfect black body. ϵ is crucial for calculating radiative heat transfer from surfaces. σ_{SB} stands for the Stefan-Boltzmann constant, a physical constant that describes the power radiated from a black body in terms of its temperature. It is used in the equation for radiative heat transfer to quantify the energy emitted by surfaces due to thermal radiation.

These variables collectively form the foundation of the equations used in the simulation, enabling the accurate modeling of both acoustic and thermal phenomena. By understanding and appropriately applying these variables, the simulation can provide precise predictions of wave propagation, heat distribution, and the overall behavior of the system under study.

In this study, the heat convection coefficient between the breast skin and the surrounding air is assigned a value of 5 $\mathrm{W/m^2K}$. This value is chosen based on previous research

findings [166, 38], ensuring accurate representation of the convective heat transfer occurring at the skin-air interface. Convective heat transfer plays a significant role in cooling the skin surface, influencing the overall temperature distribution within the breast tissue during and after the HIFU treatment.

The ambient air temperature is assumed to be 293.15 K (20°C), a standard room temperature often used in thermal simulations to provide a consistent reference point. This assumption allows for a realistic modeling environment that reflects typical conditions under which HIFU treatments might be performed.

The surface emissivity of the skin is considered to be 0.98, as supported by research [22]. Emissivity is a critical parameter in radiative heat transfer, determining how efficiently the skin surface emits thermal radiation. A high emissivity value of 0.98 indicates that the skin surface is nearly a perfect emitter of thermal radiation, which is essential for accurately modeling the radiative cooling effects.

Detailed information about the properties of all the materials utilized in the study can be found in Table 3.1. This table includes crucial thermal and physical properties such as thermal conductivity, specific heat capacity, and density for each material involved in the simulation. These properties are fundamental to the accurate modeling of heat transfer processes within the breast tissue and surrounding environment.

By integrating these well-established parameters and properties into the simulation, the study ensures a high level of accuracy and reliability in predicting the thermal behavior of the breast tissue during HIFU treatment. This comprehensive approach allows for a detailed analysis of the convective and radiative cooling mechanisms, providing valuable insights into the effectiveness and safety of the HIFU procedure.

The provided table contains various critical properties that are essential for accurately modeling the thermal and acoustic behavior of tissues and materials involved in the simulation. These properties include:

1. Density (ρ): This is the mass per unit volume of the material, measured in kilograms per cubic meter (kg/m^3). Density affects both the thermal and acoustic properties of the tissue, influencing heat capacity, thermal conductivity, and the propagation of sound waves.

2. Specific Heat under Constant Pressure (C_p): This represents the amount of heat required to raise the temperature of one kilogram of the material by one degree Celsius (J/kg·K). It is crucial for determining the thermal response of the tissue to the absorbed acoustic energy.

3. Thermal Conductivity (k): Measured in watts per meter-kelvin (W/m·K), thermal conductivity describes the ability of a material to conduct heat. Higher values indicate

better heat conduction, which impacts the distribution of thermal energy within the tissue.

4. Speed of Sound (c): This is the speed at which sound waves propagate through the material, measured in meters per second (m/s). The speed of sound is essential for accurately simulating the propagation of acoustic waves in HIFU treatments.

5. Acoustic Attenuation Coefficient (α_a): Measured in decibels per meter (dB/m), this coefficient describes the loss of acoustic energy as sound waves travel through the material. It is a crucial factor in determining the effective range and intensity of the acoustic waves.

6. Metabolic Heat Generation Rate (Q_{met}): This represents the rate at which metabolic processes generate heat within the tissue, measured in watts per cubic meter (W/m^3). It is an important consideration for accurately modeling the baseline thermal state of the tissue.

7. Blood Perfusion Rate (ω_b): Measured in cubic meters per second per cubic meter of tissue ($m^3/s{\cdot}m^3$), this rate describes the volumetric flow of blood through the tissue. Blood perfusion significantly influences the cooling of the tissue and the overall thermal response during HIFU treatment.

To assess the simulation outcomes, three cross-sectional planes were taken into account, intersecting at the center of the tumor. These planes are depicted in Fig. 3.7 and consist of the x-y, x-z, and y-z surfaces. Each plane provides a different perspective on the spatial distribution of thermal and acoustic effects within the tissue.

1. X-Y Plane: This horizontal cross-section allows for the examination of the distribution of thermal and acoustic energy across the width and length of the tissue, providing insights into how the energy propagates laterally.

2. X-Z Plane: This vertical cross-section enables the analysis of the energy distribution along the depth and height of the tissue. It is particularly useful for understanding the penetration depth of the acoustic waves and the resulting thermal effects.

3. Y-Z Plane: This vertical cross-section, perpendicular to the x-z plane, provides additional information on the distribution of energy along the other vertical axis, complementing the insights gained from the x-z plane.

By examining these three cross-sectional planes, the simulation provides a comprehensive view of the thermal and acoustic interactions within the tissue, allowing for a detailed assessment of the HIFU treatment's effectiveness and safety.

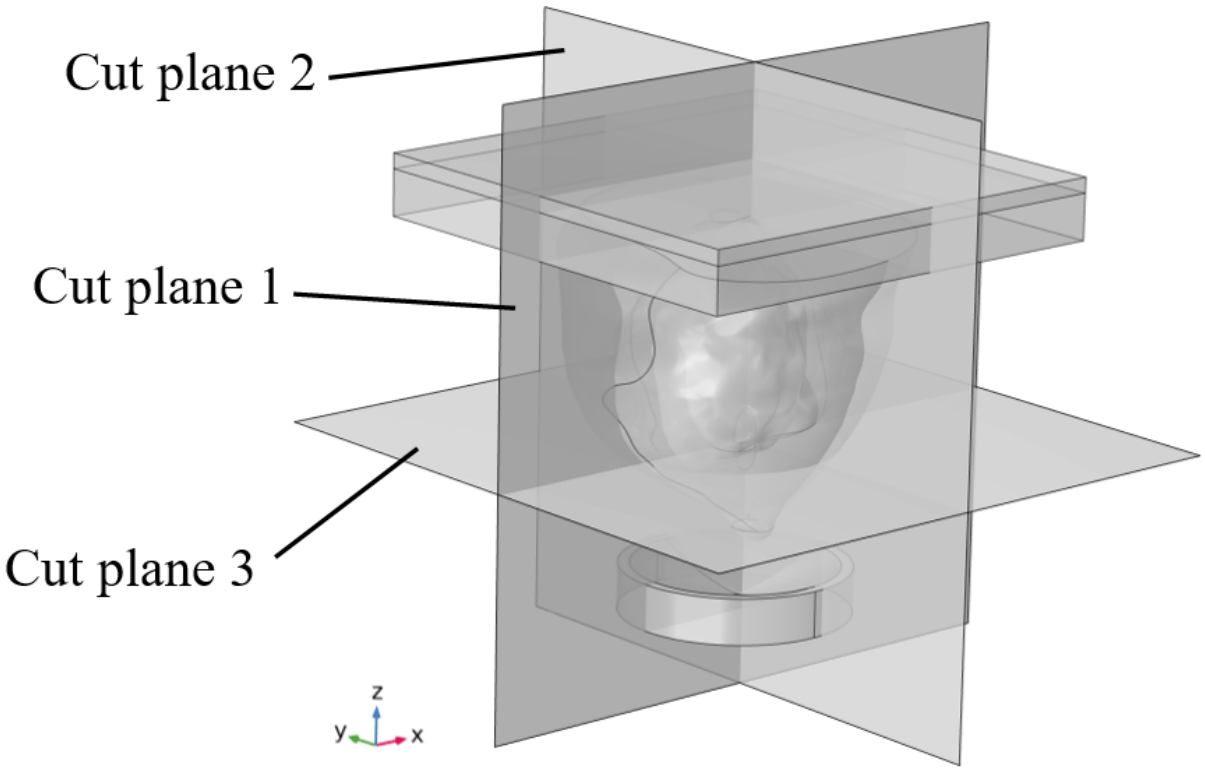


Figure 3.7: Considered cut planes that pass through the center of the tumor.

3.5 Physics-Informed Neural Network (PINN)

Training a deep learning algorithm to accurately identify a nonlinear mapping between high-dimensional input and output data pairs is a challenging task due to the complexity and variability of the data. Researchers have discovered that certain empirically validated rules can guide the time-dependent dynamics within a predefined system, providing a structured approach to learning complex patterns [156, 97, 58]. These rules, often derived from the physical or theoretical properties of the system, serve as a form of prior knowledge that can be integrated into the learning process.

By incorporating this underlying information as a regularization factor, we can constrain the solution space to a permissible domain during computations. This approach helps to prevent overfitting, ensuring that the model remains robust and capable of generalizing well to unseen data. The regularization process effectively reduces the complexity of the model, making it more efficient and stable during training.

Integrating this structured information into a learning algorithm enhances the informative value of the data. This means that the algorithm can make better use of the available data, extracting meaningful patterns and relationships that might be missed by a purely data-driven approach. As a result, the algorithm can achieve optimized solutions that are not only accurate but also aligned with the underlying principles of the system being studied.

Moreover, incorporating such prior knowledge allows the algorithm to generalize well even with limited training samples. This is particularly important in scenarios where collecting large datasets is impractical or expensive. By leveraging the known dynamics and constraints of the system, the algorithm can learn effectively from smaller datasets, maintaining high performance and reliability [102, 6].

In summary, the integration of empirically validated rules and structured information as regularization factors in deep learning algorithms provides significant advantages. It constrains the solution space, enhances the informative value of the data, and enables the algorithm to achieve optimized and generalizable solutions, even with limited training samples. This approach represents a powerful strategy for tackling the complexities of high-dimensional, nonlinear mapping tasks.

Given the recent progress in physics-based deep learning techniques, a neural network can be illustrated as depicted in Fig. 3.8. This neural network comprises several essential components: an input layer, output layer, multiple hidden layers, and associated weights and biases. Each layer is composed of neurons, which are the fundamental units that process information by applying a series of mathematical operations.

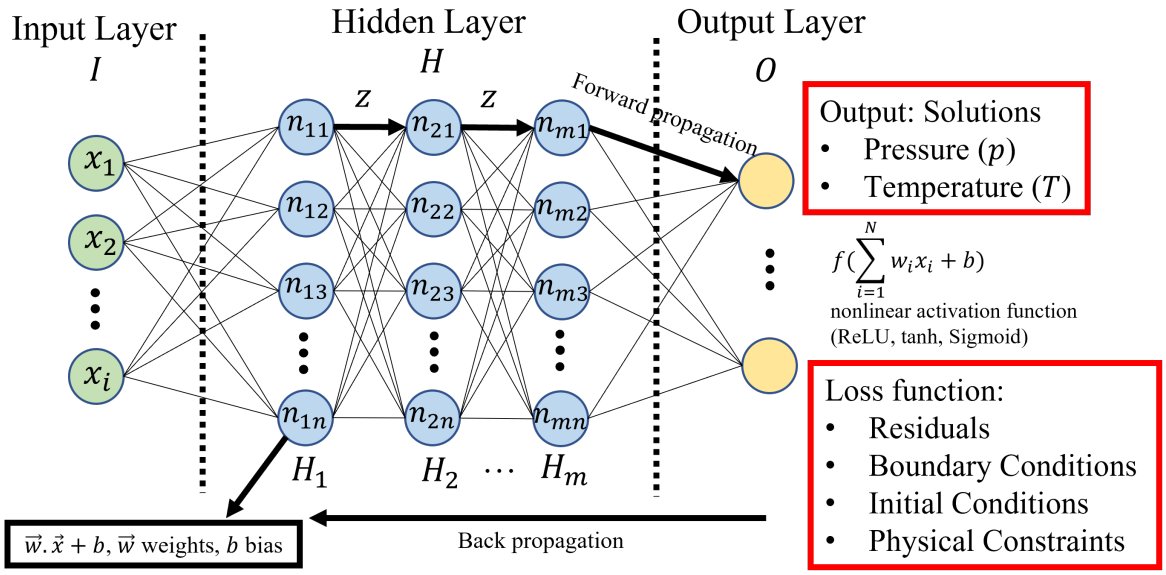


Figure 3.8: Diagram of PINN architecture for solving PDE. The input layer of the neural network with spatial inputs and temporal. The output layer computes the solution of the given PDE and embeds it into the loss function. PDE can have constraints such as initial conditions and boundary conditions. By minimizing the loss function, PINN can generate the solution with respect to the previous conditions.

The input layer receives the high-dimensional data, representing the initial conditions and parameters of the problem. The information then flows through the hidden layers, where each neuron applies a weighted sum of its inputs, adds a bias, and passes the result through an activation function. This process allows the network to learn complex, nonlinear mappings from the input to the output. The output layer produces the final predictions, which in this context, are the solutions to the partial differential equations (PDEs) being studied.

This architecture has proven effective in handling PDEs and predicting their solutions. By incorporating the given linear or nonlinear PDEs into the loss function, the neural network can be trained to minimize the error between the predicted and true solutions. The loss function is designed to account for initial conditions, boundary conditions, and other constraints relevant to the problem. This integration ensures that the network's predictions adhere to the underlying physics governing the system.

Training this neural network to anticipate the behavior of a predetermined computational domain becomes feasible through the utilization of equations governed by specific physics laws. For instance, the neural network can be trained using data generated from the Navier-Stokes equations for fluid dynamics, Maxwell's equations for electromagnetics, or the Schrödinger equation for quantum mechanics. By embedding these equations into the network's framework, the model can learn to predict the system's behavior accurately under various conditions.

The ability to solve PDEs using neural networks offers several advantages. Traditional numerical methods, such as finite element or finite difference methods, often require significant computational resources and can be challenging to apply to complex, high-dimensional problems. In contrast, physics-based neural networks can provide approximate solutions more efficiently, especially once trained. Additionally, these models can generalize to new, unseen scenarios, making them valuable for simulations and predictive modeling in various scientific and engineering applications.

In summary, the neural network illustrated in Fig. 3.8 is designed to handle PDEs by incorporating the equations into the loss function and considering relevant constraints. This approach leverages recent advancements in physics-based deep learning to train the network to predict the behavior of systems governed by specific physics laws. The architecture's ability to process complex, high-dimensional data and provide accurate, generalizable solutions highlights its potential in solving challenging problems in science and engineering.

The deep learning configuration involves a sophisticated approach to modeling and simulating the interactions of ultrasonic waves and heat transfer within a biological tissue domain. The process begins with the transmission of waves from concave ultrasound trans-

ducers. This transmission is modeled by solving the Helmholtz equation, which describes the behavior of acoustic waves in a medium. The Helmholtz equation is particularly well-suited for this purpose because it accounts for the wave-like properties of sound, including reflection, refraction, and diffraction.

Once the Helmholtz equation is solved, the resulting wave field is used as the input for the next stage in the simulation, which involves a PINN simulator. The PINN framework leverages deep learning techniques while incorporating the governing physical laws directly into the neural network's structure. This approach ensures that the predictions made by the neural network adhere to the underlying physics, leading to more accurate and reliable results.

Subsequently, the predicted output from the first PINN simulator, which represents the acoustic wave field, is utilized as an external heat source feature in the time-dependent bio-heat transfer equation (tBHTE). The tBHTE describes how heat is generated, distributed, and dissipated within biological tissues over time. By incorporating the acoustic wave field as a heat source, the model can accurately simulate the thermal effects induced by the ultrasonic waves.

This value, representing the heat generated by the ultrasonic waves, is then passed to a second PINN structure that incorporates a 3D time-dependent bio-heat transfer equation (3D tBHTE). This second PINN structure is designed to predict heat conduction within the tissue, taking into account the three-dimensional nature of the problem. The inclusion of 3D tBHTE allows for a more detailed and accurate representation of the heat distribution and transfer processes within the tissue.

As the second PINN structure processes the input data, it generates a comprehensive temperature map within the tissue domain. This temperature map is crucial for understanding the thermal dynamics and effects of the ultrasonic waves on the tissue. By predicting the temperature distribution, the model can identify regions of the tissue that experience significant heating, which is essential for applications such as HIFU treatments.

In summary, the deep learning configuration involves a multi-stage process where acoustic waves transmitted from concave ultrasound transducers are modeled using the Helmholtz equation and passed through a series of PINN simulators. The first PINN simulator predicts the wave field, which is used as a heat source in the tBHTE. The second PINN simulator then uses this information to predict heat conduction and generate a detailed temperature map within the tissue. This integrated approach leverages the strengths of both deep learning and physics-based modeling to provide accurate simulations of the thermal effects of ultrasonic waves in biological tissues.

To create the plot illustrating wave propagation and the resulting heat map, the solution of PDEs using a PINN requires the careful setup of several key components. These components ensure that the simulation accurately captures the physical phenomena and produces reliable results. The temporal domain defines the time frame over which the simulation runs. It includes the start and end times and the time step size, which determines the resolution of the temporal data. The spatial domain specifies the physical space in which the simulation occurs. It includes the dimensions of the tissue or medium being studied and the spatial resolution, which determines the granularity of the spatial data. The Helmholtz equation is used to model the propagation of acoustic waves in the medium. In the frequency domain, it accounts for the steady-state behavior of the waves. Setting up this equation involves defining the wave frequency, the speed of sound in the medium, and any sources or sinks of acoustic energy.

The tBHTE models the heat transfer within the tissue over time. It includes terms for heat conduction, metabolic heat generation, and heat loss due to blood perfusion. Setting up the tBHTE requires defining the thermal properties of the tissue, such as thermal conductivity, specific heat capacity, and perfusion rates. Boundary conditions are essential for solving PDEs as they define how the system interacts with its surroundings. For the Helmholtz equation, boundary conditions might include sound-hard (reflective) or sound-soft (absorptive) surfaces. For the tBHTE, boundary conditions could involve specifying temperatures or heat fluxes at the tissue boundaries.

Initial conditions provide the starting values for the simulation. For the Helmholtz equation, this could be the initial displacement or pressure field. For the tBHTE, it might be the initial temperature distribution within the tissue. Hyperparameters are critical settings that influence the performance and accuracy of the PINN. These include the learning rate, the number of hidden layers and neurons in the neural network, the activation functions, and the number of training iterations. Selecting appropriate hyperparameters is crucial for ensuring that the PINN converges to an accurate solution.

Before the simulation can begin, it is necessary to collect and preprocess any empirical data required to train the PINN. This might include experimental measurements of acoustic wave propagation or temperature distributions within the tissue. The PINN is trained by minimizing a loss function that incorporates the PDEs, initial conditions, boundary conditions, and any available data. The loss function quantifies the difference between the predicted and true solutions, guiding the network to learn the correct mappings.

Once the PINN has been trained and the simulation is complete, the results are post-processed to generate the final plots. This involves extracting the predicted wave propagation and temperature data, and visualizing them using appropriate plotting tools. The

wave propagation plot shows how the acoustic waves move through the medium, while the heat map illustrates the resulting temperature distribution within the tissue.

By meticulously setting up and integrating these components, the PINN can accurately solve the Helmholtz and bio-heat transfer equations, providing a detailed and reliable simulation of wave propagation and heat transfer in biological tissues. This approach combines the power of deep learning with the rigor of physics-based modeling, enabling the creation of insightful visualizations that enhance our understanding of these complex processes.

Table 3.1 presents the necessary attributes for accurately simulating the temperature increase caused by a concave ultrasound transducer. These attributes are critical for defining the behavior of the system and ensuring that the simulation reflects the real-world physical phenomena. The table includes parameters associated with the tBHTE and the external heat source Q_S, which collectively influence the thermal response of the tissue.

1. Thermal Properties of Tissues:
- Density (ρ): The mass per unit volume of the tissue, which affects how heat is stored and transferred within the tissue.
- Specific Heat Capacity (C_p): The amount of heat required to raise the temperature of a unit mass of the tissue by one degree Celsius. This parameter influences the rate of temperature change in response to the absorbed heat.
- Thermal Conductivity (k): The ability of the tissue to conduct heat. Higher thermal conductivity means heat can spread more quickly through the tissue.

2. Blood Perfusion and Metabolic Heat Generation:
- Blood Perfusion Rate (ω_b): The rate at which blood flows through the tissue, which contributes to the cooling effect as blood carries heat away from the heated region.
- Metabolic Heat Generation Rate (Q_{met}): The rate at which the tissue generates heat through metabolic processes, providing a baseline level of heat that must be accounted for in the simulation.

3. Acoustic and Thermal Source Parameters:
- External Heat Source (Q_S): The heat generated by the ultrasonic waves as they interact with the tissue. This parameter is crucial for determining the initial heat input from the ultrasound transducer.
- Acoustic Attenuation Coefficient (α_a): The rate at which the intensity of the ultrasound waves decreases as they propagate through the tissue. This attenuation affects how much acoustic energy is converted into heat.

4. Boundary and Initial Conditions:
- Boundary Conditions: Conditions that define the interaction of the tissue with its sur-

roundings, such as convective heat loss at the skin surface or reflective acoustic boundaries. - Initial Conditions: The starting temperature distribution and other initial state variables within the tissue before the application of the ultrasound.

By incorporating these attributes, the simulation can accurately model the temperature increase resulting from the ultrasound transducer. The thermal properties of the tissues ensure that heat transfer is correctly represented, while the blood perfusion and metabolic heat generation provide a realistic baseline for the tissue's thermal state. The acoustic and thermal source parameters determine how much heat is generated and how it spreads, and the boundary and initial conditions ensure that the simulation starts with realistic settings and interacts with its environment in a physically accurate manner.

In summary, Table 3.1 contains a comprehensive set of parameters essential for the simulation of temperature increase due to a concave ultrasound transducer. These parameters enable the accurate modeling of the thermal effects within the tissue, providing valuable insights into the efficacy and safety of ultrasound-based treatments.

Once the wave equation and constraints for creating a concave transducer are implemented in the neural network (Eq. 3.1), the resulting value is utilized as the external heat source in the subsequent thermal simulations. This initial step involves solving the Helmholtz equation or a similar wave equation that models the behavior of the acoustic waves generated by the concave ultrasound transducer. By accurately capturing the wave propagation, reflection, and absorption characteristics, the neural network can determine the precise distribution of acoustic energy within the tissue.

The value obtained from this wave equation simulation represents the acoustic energy converted into heat, which is then used as the external heat source Q_S in the bio-heat transfer simulations. This integration allows the Physics-Informed Neural Network (PINN) to simulate heat conduction within the tissue, taking into account all the relevant features such as tissue properties, blood perfusion, and metabolic heat generation. The PINN leverages this information to predict the spatial and temporal distribution of heat, ensuring that the simulation reflects the real-world thermal dynamics.

Next, the time-dependent bio-heat transfer equation (tBHTE) is incorporated into the neural network as the primary partial differential equation (PDE) to solve the problem outlined in Eq. 3.3. The tBHTE describes how heat diffuses through the tissue over time, considering conduction, perfusion, and metabolic heat generation. By embedding the tBHTE into the neural network framework, the PINN can directly account for the complex interactions between these factors.

Incorporating the tBHTE into the neural network involves defining the appropriate boundary and initial conditions. Boundary conditions specify how the tissue exchanges

heat with its surroundings, such as through convective and radiative heat losses at the skin surface. Initial conditions provide the starting temperature distribution within the tissue, setting the baseline for the thermal simulation.

The neural network then iteratively solves the tBHTE, adjusting its parameters to minimize the loss function, which quantifies the difference between the predicted and actual temperature distributions. This process ensures that the neural network accurately captures the thermal behavior of the tissue in response to the applied ultrasound energy.

By combining the wave equation and the tBHTE within the PINN framework, the neural network can simulate the entire process from acoustic wave generation to heat conduction and temperature rise within the tissue. This comprehensive approach allows for a detailed analysis of the thermal effects induced by the concave ultrasound transducer, providing valuable insights into the efficacy and safety of ultrasound-based treatments.

In summary, the integration of the wave equation and constraints for the concave transducer into the neural network provides the necessary external heat source for the thermal simulations. The subsequent incorporation of the tBHTE as the primary PDE enables the PINN to accurately model heat conduction within the tissue, considering all relevant physiological and physical factors. This holistic simulation approach enhances our understanding of the thermal dynamics involved in ultrasound treatments, paving the way for optimized and effective therapeutic applications.

Subsequently, our model incorporates the embedded equation within the neural network, which consists of 9 hidden layers with 20 neurons in each layer, to forecast the output of the associated tBHTE using spatial and temporal inputs. This deep architecture is designed to capture the complex relationships and interactions between the input variables and the resulting thermal distribution within the tissue.

The neural network receives spatial and temporal inputs, which include coordinates within the tissue domain and the corresponding time points. These inputs allow the network to learn how the temperature evolves over time and space in response to the heat generated by the ultrasound transducer. The depth and width of the network, with 9 hidden layers and 20 neurons per layer, provide sufficient capacity to model the intricate patterns of heat conduction and diffusion.

The training output of the neural network is responsible for simulating thermal conduction within a real-life bio-tissue domain. During training, the network adjusts its internal parameters, such as weights and biases, to minimize the residuals of the PDEs. The residual is the difference between the left-hand side and right-hand side of the tBHTE, evaluated at various points within the domain. By minimizing these residuals, the network ensures that its predictions satisfy the governing equations as closely as possible.

To approximate the solution of the PDE, the neural network employs a deep learning algorithm that iteratively refines its parameters. This optimization process involves backpropagation and gradient descent, where the network calculates gradients of the loss function (which measures the residuals) with respect to its parameters and updates them to reduce the loss. Over many iterations, the network learns to accurately approximate the temperature distribution resulting from the heat source.

The depicted neural network in Fig. 3.9 represents the architecture of the PINN utilized in the proposed methodology. This figure illustrates the flow of data through the network, from the input layer through the hidden layers to the output layer. Each neuron in the hidden layers applies a nonlinear activation function to its inputs, enabling the network to model nonlinear relationships inherent in the thermal conduction process.

By incorporating the embedded equation and leveraging the deep architecture of the neural network, the model can effectively simulate the thermal behavior of bio-tissue under ultrasound heating. This approach combines the strengths of traditional PDE-based modeling with the flexibility and scalability of deep learning, resulting in a powerful tool for predicting temperature distributions in complex biological systems.

In summary, the neural network with 9 hidden layers and 20 neurons per layer is designed to forecast the output of the tBHTE using spatial and temporal inputs. The training process minimizes the residuals of the PDE, ensuring accurate simulations of thermal conduction within bio-tissue. The architecture of the PINN, as shown in Fig. 3.9, exemplifies the advanced methodology employed in this study to model the intricate thermal dynamics induced by ultrasound treatment.

3.6 Finite Element Modeling

The FEM simulation utilizes quadratic Lagrange discretization for both the pressure acoustics and bioheat transfer phenomena. This discretization approach is chosen for its accuracy and ability to capture the complex behavior of acoustic waves and thermal conduction within the simulated tissue. Quadratic Lagrange elements provide a higher-order approximation compared to linear elements, which is crucial for modeling the intricate variations in pressure and temperature fields.

The simulations were performed on a high-performance computing system equipped with an Intel Core i7-1065G7 Processor running at 1.5 GHz and 16 GB DDR4 RAM. Despite the advanced hardware, each simulation took approximately 115 hours to complete. The substantial computation time is primarily attributed to the pressure acoustics

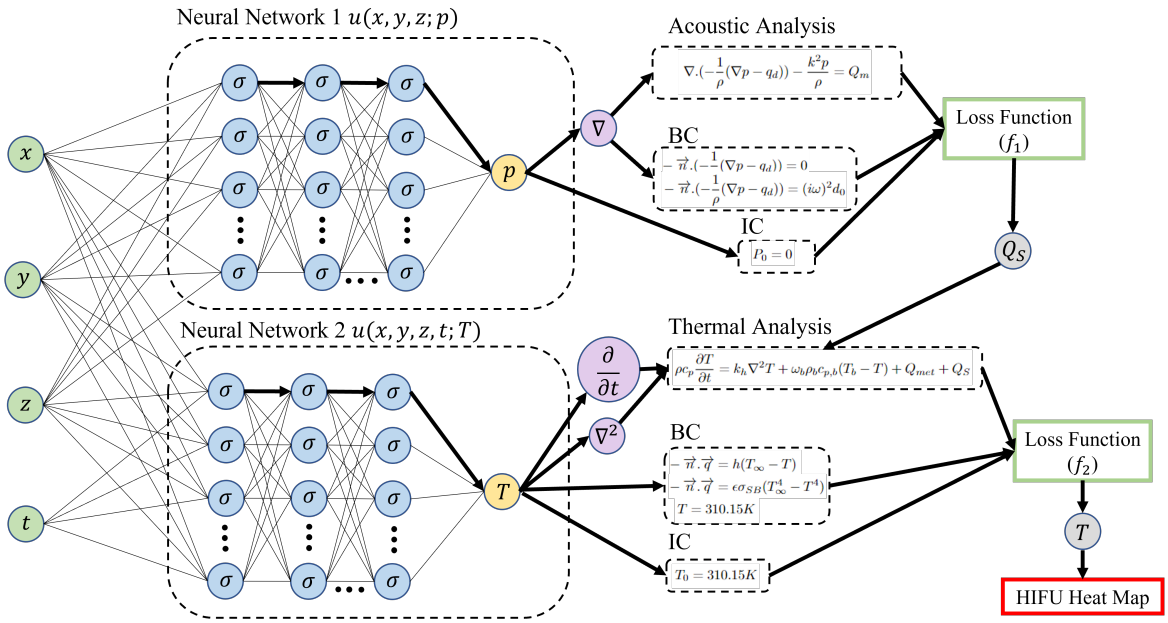


Figure 3.9: Diagram of PINN architecture for solving the 3D Helmholtz equation and tBHTE to predict the temperature rise. The upper neural network with three spatial inputs x, y, and z, and the pressure result p as the output value. The lower neural network takes three previous spatial inputs as well as a temporal input, t, and produces the temperature result, T, as the output value. Other sections are PDE, initial conditions(IC) and boundary conditions (BC). The last section represents the loss functions embedded with PDE, BC and IC along with the training output T. By minimizing the loss function, PINN can generate the heat mao with respect to the previous conditions.

simulation, which requires very fine meshes to accurately resolve the acoustic wave phenomena. Fine meshes are necessary to capture the detailed wave interactions, reflections, and absorptions that occur within the tissue and at its boundaries.

The computational demand is further intensified by the need to maintain stability and accuracy over the entire simulation domain. The fine mesh density results in a large number of elements and nodes, increasing the computational load and memory requirements. This level of detail is essential for ensuring that the acoustic waves are accurately represented, which directly impacts the subsequent bioheat transfer simulation.

The subsequent subsection will provide a detailed explanation of the required mesh grids for each step mentioned. This includes the specific mesh densities and element types used for both the pressure acoustics and bioheat transfer simulations. Proper meshing is critical for achieving convergence and obtaining reliable results. The mesh grids must be carefully designed to balance accuracy with computational efficiency, considering factors such as element size, aspect ratio, and distribution.

The various boundary conditions considered for each of the mentioned physics can be observed in Fig. 3.6. These boundary conditions play a vital role in defining how the acoustic and thermal fields interact with the environment and with different tissue interfaces. For instance, sound-hard and sound-soft boundaries are used in the pressure acoustics simulation to model reflective and absorptive surfaces, respectively. In the bioheat transfer simulation, boundary conditions such as convective heat transfer and radiation are applied to simulate heat exchange with the surrounding air.

In summary, the FEM simulation employs quadratic Lagrange discretization for both pressure acoustics and bioheat transfer, with simulations performed on a high-performance computing system. The fine meshes required for accurate pressure acoustics simulation significantly contribute to the computational time, which is approximately 115 hours per simulation. The following subsection will delve into the specifics of the mesh grids used, and Fig. 3.6 illustrates the various boundary conditions applied in the simulations.

3.6.1 Mesh Study

The mesh size plays a crucial role in accurately simulating the acoustic wave propagation and the subsequent thermal effects within the tissue. In particular, the FEM simulation of "pressure acoustics" requires significantly finer meshes compared to the simulation of "bioheat transfer." This is because the acoustic waves, characterized by their high frequencies and small wavelengths, necessitate a higher resolution to capture the detailed variations in pressure fields accurately.

For the "pressure acoustics" simulation, the fine meshes are essential to resolve the intricate wave phenomena such as reflections, refractions, and diffractions that occur within the tissue and at its boundaries. These phenomena are sensitive to the mesh size, and any coarseness could lead to inaccuracies in the wave propagation model, potentially distorting the simulation results. As a rule of thumb, the element size in the mesh should be a small fraction of the acoustic wavelength to ensure that the wave is well-represented. This requirement leads to a significantly higher number of elements and nodes, increasing the computational load and memory requirements.

In contrast, the "bioheat transfer" simulation can be performed with relatively coarser meshes. The thermal conduction process involves the diffusion of heat, which is a slower and less oscillatory phenomenon compared to acoustic wave propagation. Therefore, the temperature gradients within the tissue do not change as rapidly or require as high a spatial resolution to model accurately. Coarser meshes are sufficient to capture the essential features of heat diffusion and the resultant temperature distribution within the tissue.

Due to these differing requirements, two distinct sets of meshes have been utilized to solve these two physics phenomena. For the pressure acoustics simulation, a fine mesh with small element sizes is employed, ensuring that the acoustic waves are accurately captured and modeled. This mesh must be carefully constructed to balance the need for detail with computational feasibility, often necessitating advanced meshing techniques and optimization strategies.

For the bioheat transfer simulation, a coarser mesh is utilized. This mesh still needs to be sufficiently detailed to model the overall temperature distribution and thermal gradients within the tissue accurately. However, it does not require the same level of refinement as the pressure acoustics mesh, allowing for a reduction in computational complexity and processing time.

The use of two distinct mesh sets allows the simulations to be optimized for each physical phenomenon, ensuring accuracy while managing computational resources efficiently. This approach highlights the importance of tailored meshing strategies in multiphysics simulations, where different processes may have vastly different spatial resolution requirements.

In summary, the FEM simulation employs fine meshes for pressure acoustics to capture the high-frequency wave phenomena accurately, and coarser meshes for bioheat transfer to model the slower thermal conduction processes. This dual-mesh strategy ensures that both simulations are performed with the appropriate level of detail, optimizing accuracy and computational efficiency.

In order to achieve precise solutions for the acoustic equations, a highly refined mesh

set is employed for both the ARBP and the surrounding water. The maximum mesh size used in these regions is $\lambda/4$, where λ represents the wavelength of the acoustic waves. This fine mesh resolution is critical for accurately modeling the propagation and interaction of acoustic waves, as it ensures that the waveforms are properly captured and any potential distortions are minimized.

To further enhance the accuracy, particularly in areas where the acoustic phenomena are most complex, such as within the tumor tissue, an even finer mesh with a maximum mesh size of $\lambda/8$ is utilized. This level of refinement is necessary to accurately capture the sharp pressure gradients that occur in the focal region, where the ultrasound waves are concentrated. The finer mesh allows for a more detailed representation of the acoustic pressure field, ensuring that the simulation can accurately predict the localized effects of the ultrasound waves.

Moreover, the mesh refinement strategy is adaptive, varying based on the proximity to the focal point of the acoustic waves. In regions close to the focal point, where the acoustic intensity and pressure gradients are highest, finer meshes are employed to ensure that the simulation accurately captures the detailed behavior of the waves. As one moves farther away from the focal point, the pressure gradients tend to decrease, and the acoustic field becomes less complex. In these regions, larger mesh sizes can be used without significantly compromising the accuracy of the results. This adaptive meshing approach optimizes computational resources by focusing the highest resolution where it is most needed, while using coarser meshes in less critical areas.

This strategy not only ensures high accuracy in the critical regions of the simulation but also improves computational efficiency. By employing finer meshes selectively, the simulation can maintain a manageable computational load while still achieving precise results. The use of larger meshes in less critical areas helps to reduce the overall number of elements and nodes, thereby decreasing the computational time and memory requirements.

In summary, to achieve precise solutions for the acoustic equations, a highly refined mesh set is used for the ARBP and surrounding water, with a maximum mesh size of $\lambda/4$. An even finer mesh with a maximum size of $\lambda/8$ is utilized for the tumor tissue to capture sharp pressure gradients accurately. The mesh size is adaptively varied based on proximity to the focal point, using finer meshes in regions with high acoustic intensity and larger meshes in less critical areas. This approach ensures high accuracy and computational efficiency in the simulation.

In this research, multiple computational meshes were generated to ensure the accuracy and reliability of the simulation results, particularly focusing on the pressure acoustics phenomena. The primary goal was to achieve grid independence, a state where further

refinement of the mesh does not significantly alter the results, indicating that the solution is sufficiently accurate.

To assess grid independence, the maximum sound intensity magnitude at the focal point was computed for each mesh configuration. This focal point is the critical region where the ultrasound waves converge and generate the highest acoustic pressure. By comparing the sound intensity magnitudes across different mesh densities, it was possible to determine whether the simulations were stable and accurate or if further refinement was necessary.

The ideal number of grids was identified by striking a balance between computational cost and simulation accuracy. Computational cost includes factors such as processing time, memory usage, and overall computational resources required to perform the simulation. Simulation accuracy is crucial for ensuring that the results are reliable and can be used to predict real-world phenomena accurately.

The process involved generating increasingly finer meshes and observing the changes in the simulation outcomes. If finer meshes did not yield any significant changes in the simulation results, it indicated that the solution had reached grid independence. In such cases, the most refined grid that achieved this state was selected. This approach ensures that the simulation is both accurate and efficient, avoiding unnecessary computational expense while maintaining high-quality results.

The outcomes of this mesh analysis for the "pressure acoustics" physics are depicted in Fig. 3.10a. This figure illustrates the relationship between mesh refinement and the resulting sound intensity magnitudes at the focal point. It shows how the results stabilize as the mesh becomes finer, indicating the point at which further refinement does not lead to significant improvements in accuracy.

This meticulous approach to mesh generation and analysis is critical for ensuring the validity of the simulation. By carefully evaluating the impact of mesh size on the simulation results, the research ensures that the conclusions drawn from the study are based on robust and reliable data. The chosen mesh configuration reflects an optimal balance, providing high accuracy without incurring excessive computational costs.

In summary, this research involved generating multiple computational meshes and computing the maximum sound intensity magnitude at the focal point to assess grid independence. The ideal number of grids was determined by balancing computational cost and simulation accuracy. When finer meshes did not result in significant changes in the results, the most refined grid was selected to achieve grid independence. The outcomes of this mesh analysis for the pressure acoustics physics are illustrated in Fig. 3.10a, demonstrating the stabilization of results with increasing mesh refinement. This approach ensures accurate and efficient simulations, providing reliable data for further analysis and application.

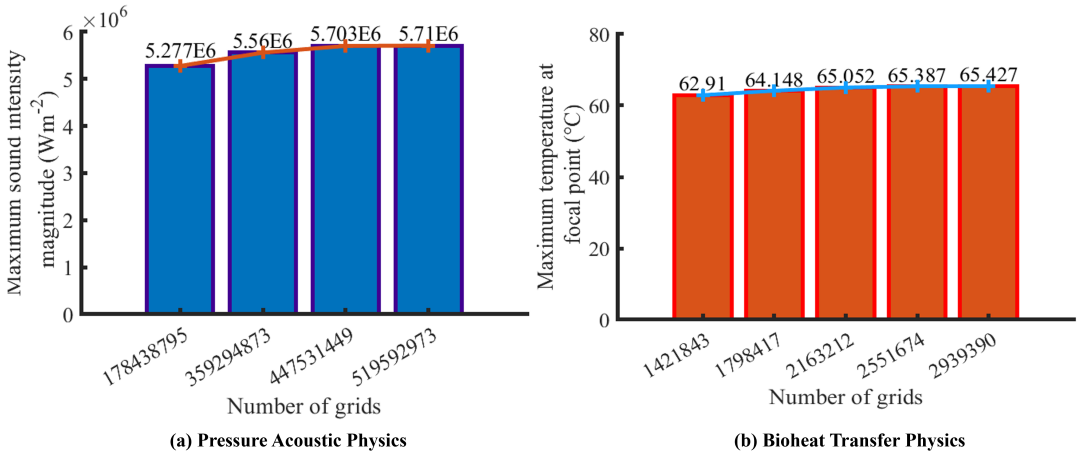


Figure 3.10: Grid independency test for each physics.

To achieve high precision in solving the bioheat transfer equations, significantly larger meshes are necessary compared to those used for the pressure acoustics simulations. The bioheat transfer equations describe the distribution and conduction of heat within the biological tissue, and the thermal gradients involved are generally smoother and less steep than the pressure gradients associated with acoustic waves. Therefore, larger mesh elements can be used without compromising the accuracy of the thermal simulation.

To minimize the overall simulation time while maintaining accuracy, a distinct set of meshes is employed specifically for the bioheat transfer physics. This approach allows for optimized resource allocation, ensuring that the computational efforts are focused appropriately for each type of physical phenomenon being simulated. Using larger meshes for the bioheat transfer simulations reduces the number of elements and nodes, thus lowering the computational load and speeding up the simulation process.

Similar to the pressure acoustics case, multiple computational mesh samples are created to address the bioheat transfer phenomenon. These samples are systematically refined to evaluate their impact on the simulation results. The primary metric for assessing the mesh quality and achieving grid independence in this context is the maximum temperature attained at the focal point during the ablation process. This focal point is the area where the ultrasonic energy is concentrated, leading to the highest temperatures and the most significant thermal effects.

By measuring the maximum temperature at the focal point across different mesh samples, researchers can determine whether the simulation results stabilize as the mesh is refined. If the results show minimal changes with further mesh refinement, it indicates that the solution has achieved grid independence, meaning that the mesh is sufficiently fine to capture the essential thermal behavior without further increasing the computational cost.

The results of this grid independence analysis for the bioheat transfer physics are presented in Fig. 3.10b. This figure illustrates the relationship between mesh size and the maximum temperature at the focal point, highlighting how the temperature readings converge as the mesh becomes finer. It demonstrates the point at which further refinement does not lead to significant improvements in accuracy, thereby confirming grid independence.

By carefully conducting this mesh analysis, the research ensures that the bioheat transfer simulations are both accurate and efficient. The selected mesh configuration strikes a balance between precision and computational feasibility, providing reliable results without unnecessary computational expense.

In summary, achieving high precision in solving bioheat transfer equations requires significantly larger meshes than those used for pressure acoustics. To minimize simulation time, a distinct set of meshes is employed for the bioheat transfer physics. Multiple computational mesh samples are created, and the maximum temperature at the focal point during ablation is measured to investigate grid independence. The results of this grid independence analysis are presented in Fig. 3.10b, showing how the maximum temperature stabilizes with mesh refinement, confirming the achievement of grid independence and ensuring accurate and efficient thermal simulations.

Fig. 3.10 demonstrates a convergence trend as the number of grids increases, showing that the maximum intensity magnitude in the "pressure acoustics" simulations and the maximum temperature in the "bioheat transfer" simulations reach a nearly constant level. This indicates that further refinement of the mesh does not significantly alter the results, confirming that grid independence has been achieved.

Table 3.2 provides a detailed comparison of numerical values and differences between multiple simulated scenarios. This comparison is aimed at identifying the optimal mesh configuration for both the "pressure acoustics" and "bioheat transfer" physics, balancing accuracy with computational efficiency. By examining these scenarios, we can determine the point at which additional computational resources do not yield significant improvements in accuracy.

For the "pressure acoustics" simulations, it is observed that the maximum intensity magnitude for scenarios 1.3 and 1.4 is significantly similar, as depicted in Fig. 3.10a and

Table 3.2: Quantitative amounts and relative errors of different considered mesh cases for each of the physics.

Pressure acoustic physic			
Case	Grid Numbers	Maximum sound intensity magnitude (Wm^{-2})	% Relative error in comparison with the optimum case
1.1	178438795	5276891	-7.471 %
1.2	359274873	5560187	-2.504 %
1.3	**447531449**	**5702988**	**-**
1.4	519592973	5702988	0.116 %
Bioheat transfer physic			
Case	Grid Numbers	Maximum temperature generated at focal point (°C)	% Relative error in comparison with the optimum case
2.1	1421843	62.90969	-3.788 %
2.2	1798417	64.14794	-1.895 %
2.3	2163212	65.05169	-0.512 %
2.4	**2551674**	**65.38679**	**-**
2.5	2939390	65.4274	0.062 %

detailed in Table 3.2. The negligible difference between these two scenarios indicates that further mesh refinement beyond scenario 1.3 does not provide substantial benefits in terms of accuracy. Therefore, to reduce computational costs without compromising the precision of the simulation, scenario 1.3 is selected as the optimal mesh configuration for "pressure acoustics".

Similarly, for the "bioheat transfer" simulations, the maximum temperature generated at the focal point for scenarios 2.4 and 2.5 is approximately equal, as shown in Fig. 3.10b and Table 3.2. This convergence suggests that the mesh refinement level in scenario 2.4 is sufficient to accurately capture the thermal dynamics within the tissue. Hence, scenario 2.4 is chosen as the optimal mesh configuration for the "bioheat transfer" physics, ensuring accurate results while maintaining computational efficiency.

The selection of these optimal mesh scenarios is crucial for effective simulation. By choosing scenario 1.3 for "pressure acoustics" and scenario 2.4 for "bioheat transfer", the research achieves a balance between high fidelity in the simulation results and manageable computational demands. This approach ensures that the simulations are both accurate and efficient, providing reliable data for further analysis and application in practical scenarios.

In summary, Fig. 3.10 illustrates that the maximum intensity magnitude and maximum temperature at the focal point stabilize as the number of grids increases, indicating grid independence. Table 3.2 compares multiple scenarios to identify the optimal mesh configurations. Scenario 1.3 is selected for "pressure acoustics" and scenario 2.4 for "bioheat transfer" based on the similarity of results in subsequent scenarios and the need to reduce computational costs while maintaining accuracy. This careful selection process ensures the effectiveness and efficiency of the simulations.

Fig. 3.11a displays the optimal mesh design for the "pressure acoustics" physics, highlighting the intricate and finely detailed mesh necessary to accurately capture the behavior of acoustic waves within the simulated domain. This optimal mesh configuration, as previously determined, strikes a balance between precision and computational efficiency, ensuring that the simulations accurately reflect the pressure wave phenomena without incurring excessive computational costs.

Similarly, Fig. 3.11c showcases the optimal mesh configuration for the "bioheat transfer" physics. This mesh is designed to efficiently model the thermal conduction and heat distribution within the tissue. Although coarser than the mesh used for pressure acoustics, it is sufficiently detailed to capture the essential thermal dynamics, ensuring accurate temperature predictions while optimizing computational resources.

To provide a more comprehensible visualization of the individual mesh grids and to observe the mesh grids generated for different tissue types, the meshed model is sliced and presented in Fig. 3.11b and Fig. 3.11d for each respective physics. These sliced views offer a clear perspective on how the meshes are structured within the different regions of the tissue, illustrating the variation in mesh density and element size tailored to the specific requirements of pressure acoustics and bioheat transfer simulations.

Fig. 3.11b presents a sliced view of the optimal mesh for pressure acoustics. This detailed cross-section reveals the finer mesh elements concentrated around critical regions, such as the focal point of the ultrasound waves, where high precision is essential to capture the sharp pressure gradients. The gradual transition to coarser meshes away from the focal point is also evident, demonstrating how the mesh adapts to different regions to maintain accuracy while reducing unnecessary computational load.

Fig. 3.11d shows a sliced view of the optimal mesh for bioheat transfer. This visualization highlights how the mesh is configured to represent various tissue types within the domain. The mesh density is appropriately adjusted to ensure that thermal properties and heat transfer characteristics are accurately modeled across different tissues. Areas with high thermal gradients, such as regions near the heat source or the tumor, are meshed more finely, whereas areas with more uniform temperature distributions utilize coarser meshes.

These sliced views in Fig. 3.11b and Fig. 3.11d provide valuable insights into the spatial distribution of mesh elements and how the mesh design caters to the specific needs of each physics simulation. By examining these visualizations, one can appreciate the meticulous approach taken to ensure that each region of the tissue is accurately represented, contributing to the overall reliability and effectiveness of the simulations.

In summary, Fig. 3.11a and Fig. 3.11c display the optimal mesh designs for pressure

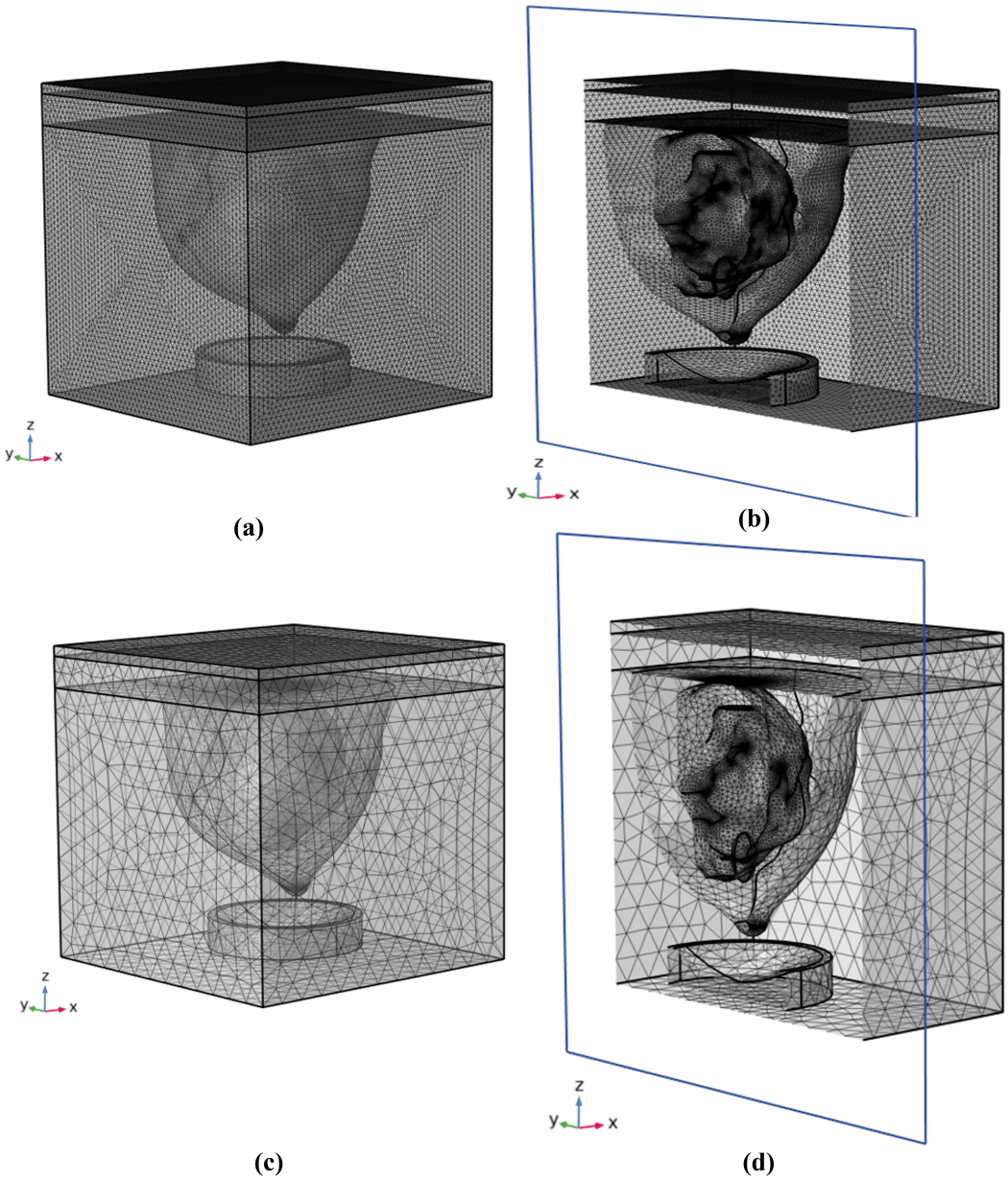


Figure 3.11: Optimum grid generation considered for each physics. "Pressure acoustics" physics: (a) whole geometry, (b) sliced magnified model. "Bioheat transfer" physics: (c) whole geometry, (d) sliced magnified model.

acoustics and bioheat transfer physics, respectively. The sliced views in Fig. 3.11b and Fig. 3.11d offer a detailed visualization of the mesh grids, illustrating the tailored mesh configurations for different tissue types and regions. These visualizations highlight the careful balance between precision and computational efficiency achieved in the mesh design, ensuring accurate and reliable simulation results.

3.7 Validation and Experiment

To ensure the accuracy and reliability of our simulation methods, we first undertake the validation of the acoustic wave generation simulation, commonly referred to as the "pressure acoustics" physics. This step is crucial for confirming that our simulation accurately models the behavior of acoustic waves under the specified conditions. Subsequently, we perform the validation of the heat transfer simulation, known as the "bioheat transfer" physics. This validation is essential to ensure that our simulation correctly represents the thermal dynamics and heat distribution within the biological tissue. Additionally, we integrate experimental procedures to further substantiate the validity of our simulation results. These two validation steps, along with the detailed experimental procedure, are thoroughly presented and discussed in the following sections. This comprehensive approach allows us to establish confidence in our simulation methods and their applicability to real-world scenarios.

3.7.1 Experimental Procedure

To verify the accuracy of the utilized simulation, HIFU was implemented on bovine liver tissue. In the *ex vivo* experiments, maintaining actual blood flow is not feasible, so the blood perfusion effect is neglected in this experimental setup. Before HIFU irradiation, the bovine liver tissue was degassed to remove dissolved gases that could lead to cavitation and boiling. This degassing process involved placing the tissue in a vacuum chamber to reduce the gas content, thus minimizing the risk of cavitation during the procedure. After degassing, the tissue samples were placed in a degassed water bath maintained at a physiological temperature of 37°C to mimic *in vivo* conditions. The HIFU transducer was carefully calibrated and positioned to deliver focused ultrasound to the target areas within the tissue samples. Temperature rise within the tissue was monitored using thermal imaging and thermocouples strategically placed within the tissue. The experimental results, including temperature rise data, were then compared with simulation predictions to validate the accuracy of the simulation model. This comprehensive approach ensures that

the simulation accurately represents the thermal and acoustic behavior of the tissue under HIFU treatment, thereby confirming the reliability of the model for practical applications.

3.7.2 Pressure Acoustics Phenomenon (Montienthong & Rattanadecho Study [114])

To validate the initial stage of our simulation, we utilize the results obtained by Montienthong and Rattanadecho [114]. Their study employed a different breast model from the ARBP model implemented in this study. Specifically, they conducted a 2D axisymmetric simulation of HIFU in a cylindrical-shaped breast, which includes a sphere-shaped tumor and a vessel passing through it [114]. The cylindrical breast model in their study is composed of three distinct tissue types: fat, glands, and muscle, each with a cylindrical configuration. This breast tissue is situated within a larger cylinder that represents the surrounding water environment. The transducer used in their simulation is bowl-shaped with a central hole and is also immersed in the water. In their research, two different ultrasound frequencies, 1 MHz and 1.5 MHz, are considered, along with two different tumor sizes, 5 mm and 10 mm. These parameters are critical for analyzing the interaction of the focused ultrasound waves with the breast tissue and tumor. By comparing our simulation results with the findings from Montienthong and Rattanadecho's study, we can effectively validate the accuracy and robustness of our simulation model, ensuring that it reliably mimics the complex interactions within the breast tissue during HIFU treatment.

To ensure consistency and comparability, we adopt the same initial and boundary conditions as described in Montienthong and Rattanadecho's study. Specifically, we simulate the scenario involving a 1 MHz ultrasound frequency and a 5 mm tumor, which allows us to directly compare our findings with theirs. In our simulation, we obtain the total acoustic pressure field and the distribution of sound intensity magnitude within the breast tissue. These parameters are crucial for understanding how the ultrasound waves propagate and interact with the tissue and the embedded tumor.

To facilitate a quantitative comparison, we focus on two key metrics: the maximum total acoustic pressure and the maximum sound intensity magnitude across the entire simulation domain. These metrics provide a clear indication of the peak values that the tissue is subjected to, which are critical for evaluating the efficacy and safety of the HIFU treatment. By comparing these values with those reported in Montienthong and Rattanadecho's study, we can assess the accuracy and reliability of our simulation model.

The results of this comparative analysis are visually represented in Fig. 3.12, which illustrates the maximum total acoustic pressure and the maximum sound intensity magni-

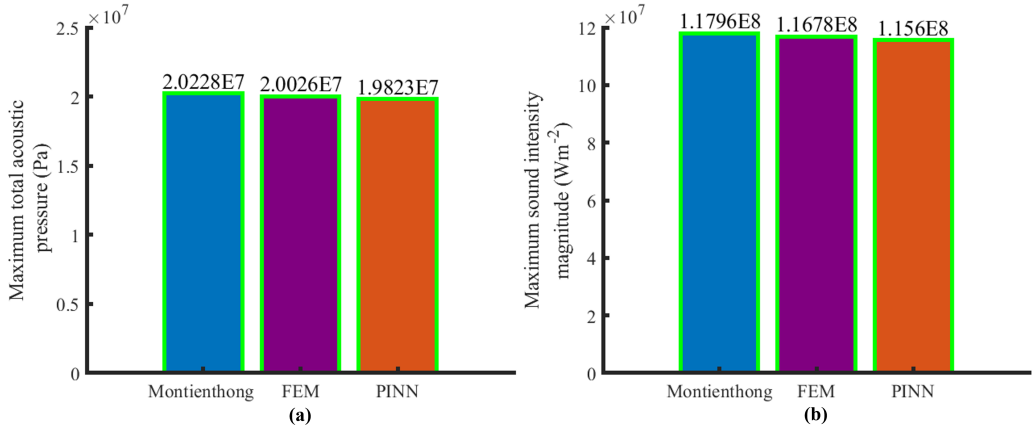


Figure 3.12: Comparison of the maximum total acoustic pressure and the maximum sound intensity magnitude obtained from our simulations (FEM and PINN) and the Montienthong & Rattanadecho's simulation.

tude for both Montienthong and Rattanadecho's simulation and our simulation. This plot not only highlights the similarities and differences between the two studies but also underscores the validity of our simulation approach. Through this rigorous validation process, we ensure that our simulation model is robust and capable of accurately replicating the physical phenomena observed in real-world HIFU treatments.

It is apparent that there exist minor discrepancies between our simulation results and those of Montienthong and Rattanadecho. These differences could be attributed to several factors, including slight variations in model parameters, numerical methods, or computational precision. However, these small deviations can be considered acceptable within a tolerable margin of error, typically encountered in complex simulation studies.

The observed discrepancies do not significantly impact the overall accuracy and reliability of our simulation model. In fact, such variations are expected due to the inherent complexities and approximations involved in simulating biological tissues and their interactions with focused ultrasound. It is important to note that the primary trends and key results, such as the distribution patterns of acoustic pressure and sound intensity magnitude, closely align with those reported by Montienthong and Rattanadecho.

Therefore, despite the minor differences, our simulation model effectively captures the essential physical phenomena and provides a robust framework for further analysis and application. These findings reinforce the validity of our approach and underscore the

potential of our model to accurately simulate focused ultrasound treatments in breast tissue, paving the way for future advancements and refinements in this field.

3.7.3 Heat Transfer Phenomenon (Montienthong & Rattanadecho Study [114])

To verify the accuracy of our bioheat transfer predictions, we compare our results with the simulations conducted by Montienthong and Rattanadecho. We ensure consistency by utilizing the same geometric configuration and operating conditions as those detailed in their study. This involves replicating their setup to maintain the integrity of the comparison, ensuring that any observed differences or similarities are due to the simulation methodologies rather than variations in the experimental conditions.

The temperature distributions predicted in the central region of the tumor (the focal point) during the progression of the ablation process are depicted in Fig. 3.13. This figure presents a side-by-side comparison of our results with those obtained by Montienthong and Rattanadecho. The graphical representation highlights the temperature changes over time, providing a clear visual correlation between the two studies.

It is evident from Fig. 3.13 that our present study aligns well with the findings of Montienthong and Rattanadecho. The temperature profiles at the focal point exhibit similar trends and magnitudes, indicating a good agreement between the two sets of results. This alignment validates our bioheat transfer model, confirming its accuracy in predicting the thermal effects of focused ultrasound ablation in biological tissues.

This comparison not only demonstrates the reliability of our simulation but also reinforces the robustness of our approach. By closely matching the established results of Montienthong and Rattanadecho, we establish confidence in our model's predictive capabilities. This successful validation paves the way for further applications of our simulation in optimizing focused ultrasound treatments and enhancing their efficacy in clinical settings.

Table 3.3 presents the outcomes of a comprehensive comparative assessment performed through relative error measurements. This analysis is centered on the evaluation of present simulations, experimental data, and the findings reported by [114]. Specifically, it examines three critical parameters: the highest overall acoustic pressure, the maximum magnitude of sound intensity across the entire area, and the maximum temperature achieved at the focal point during the ablation process. By employing relative error analysis, we are able to quantify the discrepancies between the different sets of data. A detailed comparison of the

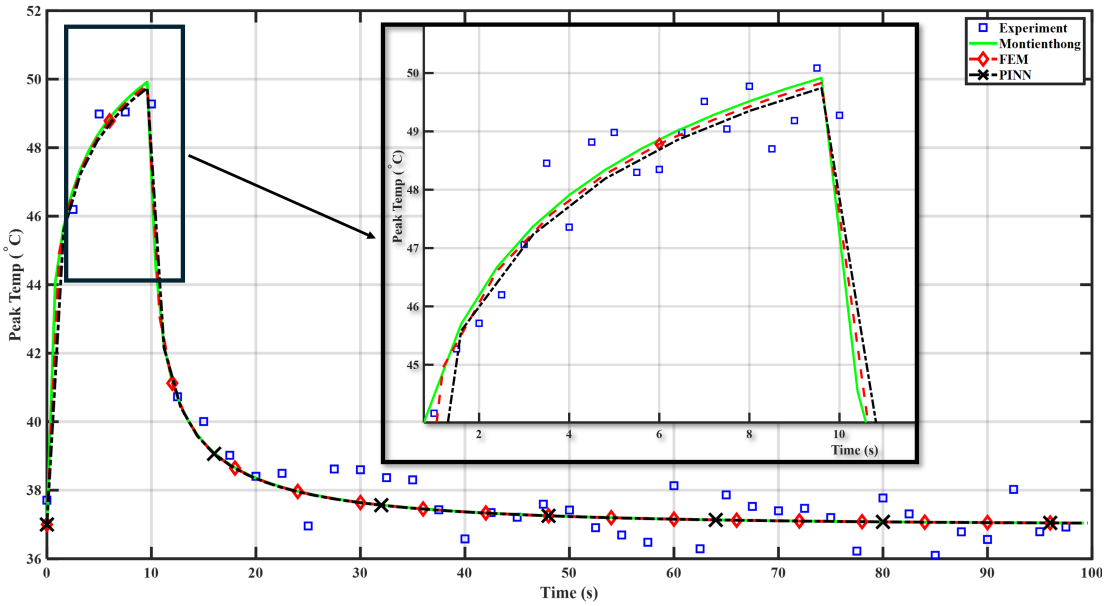


Figure 3.13: Comparison of FEM and deep learning simulations, experimental results, and Montienthong & Rattanadecho simulation plots of the temperature distribution in the focal point during the time.

results obtained from Montienthong & Rattanadecho with our own simulations reveals a satisfactory level of agreement, as evidenced by the relative error values listed in Table 3.3. This thorough assessment underscores the reliability of our simulation methods and their consistency with both experimental results and previously published data.

Table 3.3: Comparison between our simulations results, experiment, and Montienthong & Rattanadecho's simulation results [114].

Parameters	FEM (% error)	PINN (% error)	Experiment (%error)	Montienthong & Rattanadecho's result
Maximum total acoustic pressure (Pa)	2.0026E7 (-2 %)	1.9823E7 (-2 %)	-	2.0228E7
Maximum sound intensity magnitude (Wm^{-2})	1.1678E8 (-1 %)	1.156E8 (-2 %)	-	1.1796E8
Maximum Temperature (°C)	49.95 (0.1 %)	50 (0.2 %)	50.04 (0.28 %)	49.9

Chapter 4

Deep Learning Method for HIFU Pathway Scanning

4.1 Problem Description

The tumor overlaying skin is readily in touch with degassed water during HIFU therapy, which is administered under spinal or general anesthesia with the patient resting in a prone or supine posture. The use of degassed water ensures optimal acoustic coupling between the HIFU transducer and the patient's body, enhancing the efficiency of the ultrasound waves in reaching the tumor. During the procedure, advanced imaging techniques, such as US and MR imaging, are employed to precisely identify and select the tumor mass within the target region. These imaging modalities provide high-resolution, real-time images that allow for accurate delineation of the tumor boundaries [88].

The tumor lesion is made up of multiple two-dimensional (2-D) cross-slices, and the shapes and sizes of the slices are seldom the same. Each cross-section of the tumor can vary significantly in its geometry, presenting a challenge for treatment planning. To address this, the tumor volume is often segmented into numerous cross-slices with interval distances ranging from 5 to 10 mm, depending on the chosen therapy approach and the specific characteristics of the tumor [170]. This segmentation allows for a more targeted and systematic treatment of the tumor.

Once the cross-slices are defined, the target locations within each slice are determined based on the acquired images. These target locations are then subjected to focused ultrasound beams, which are precisely directed to ablate the tumor tissue. The process of

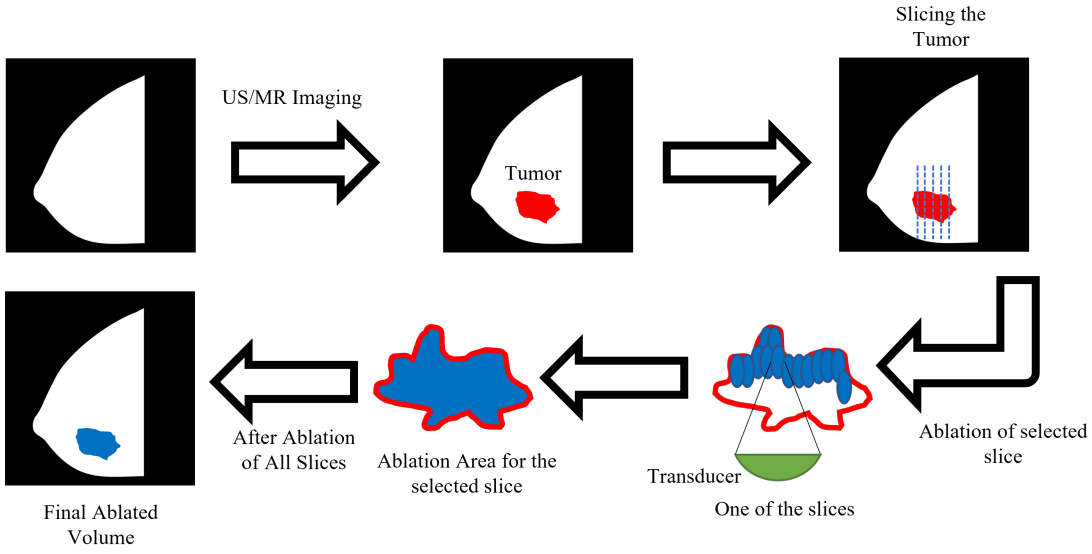


Figure 4.1: Schematics of the problem description.

focusing the ultrasound beams on specific points within the tumor slices ensures that the entire tumor volume is covered effectively. A therapeutic plan is meticulously developed to ensure that the treatment is comprehensive, efficient, and minimally invasive to the surrounding healthy tissue. This plan takes into account the need to cover the whole tumor volume completely, execute the procedure rapidly, and minimize any potential damage to normal tissues.

Fig. 4.1 illustrates the schematic of the HIFU surgery processes, providing a visual representation of the key steps involved in the procedure. This figure highlights the integration of imaging, planning, and focused ultrasound delivery, demonstrating the coordinated efforts required to achieve successful tumor ablation. The schematic serves as a valuable reference for understanding the intricate process of HIFU therapy and the precision needed to effectively treat tumor lesions.

The goals of this study were to propose a novel ML-based approach to significantly reduce the treatment time and ensure that the build-up of normal tissue overheating is considered, particularly when successive focal points are very close to each other. Overheating of normal tissue can lead to unwanted side effects and complications, making it critical to manage and mitigate during HIFU therapy. To achieve these goals, the FEM was employed to simulate a variety of treatment scenarios, allowing for detailed analysis

and comparison of the resultant lesion shapes and sizes under different conditions.

In this study, the focus is on breast tumors, which are often located near vital organs such as the heart, lungs, rib cage, and major blood vessels. This proximity to critical structures presents additional challenges for treatment, as it requires precise targeting and careful management to avoid damaging healthy tissues. However, the methods and findings of this study are not limited to breast tumors alone and can be extended to other types of tumors as well.

Breast tumors were selected as a model to test the AI-based HIFU optimization approach for several reasons. Firstly, breast cancer is of significant clinical importance, with high prevalence and substantial impact on patient health and outcomes. Secondly, the anatomical considerations of the breast, with its complex structure and proximity to vital organs, make it a challenging and relevant area for developing advanced treatment techniques. Thirdly, there is a strong need for non-invasive treatment options in breast cancer therapy to improve patient comfort and reduce recovery times. Additionally, the complexity of treatment planning for breast tumors, due to their variable size, shape, and location, provides an excellent test case for the capabilities of AI-driven optimization.

Furthermore, advancements in breast cancer research have provided a robust foundation of knowledge and data, which can be leveraged to develop and validate new treatment approaches. The feasibility of experimental validation in breast cancer models, both *in vitro* and *in vivo*, also supports the choice of breast tumors for this study. By focusing on breast tumors, the study aims to demonstrate the effectiveness of the proposed ML-based HIFU optimization approach and pave the way for its application to other types of tumors in future research.

4.2 Image Processing Procedure

In the preoperative treatment process, detection of the exact tumor geometry is required to set the most beneficial therapeutic plan and avoid any invasion of normal tissue. To obtain precise information on the breast and tumor geometries, 2D MRI images of breast cancer from four patients were used in this study (Fig. 4.2). Initially, comprehensive 3D MRI scans of the breast were obtained for each patient. These scans provided a detailed volumetric representation of the breast tissue, including the tumor regions. Using advanced image processing algorithms, the tumor was segmented from the 3D MRI data. This involved identifying the boundaries of the tumor within the 3D volume, which was achieved through semantic segmentation techniques employing a convolutional neural network (CNN) [39].

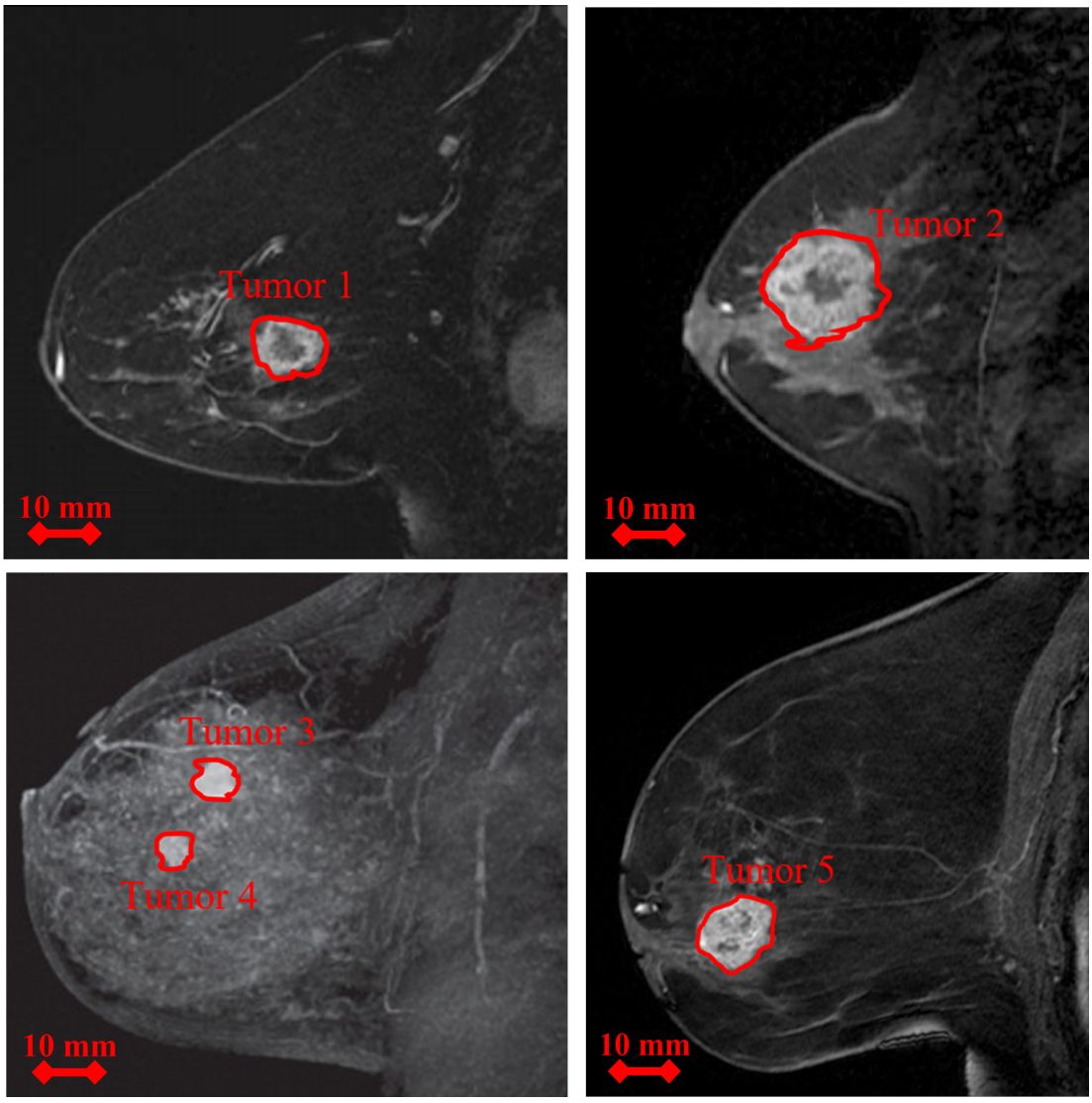


Figure 4.2: Segmented breast MRI of four patients.

After segmentation, the 3D tumor volume was systematically sliced into multiple 2D images. The slicing was done at regular intervals, every 5 mm, based on the resolution and the specific anatomy of the tumor. These intervals were chosen to ensure that the 2D slices accurately represented the spatial characteristics of the tumor without significant loss of information. The rationale for extracting 2D images from the 3D volume lies in the computational efficiency and ease of analysis. Working with 2D slices allows for the application of various image processing techniques and machine learning models that are well-established for 2D data. Additionally, 2D images facilitate the visualization and manual verification of tumor boundaries, which is crucial for accurate treatment planning.

According to the Helsinki Agreement, the whole study was thoroughly explained to the patients. MRIs with and without contrast were performed on the Iran Breast Cancer Society patients in Tehran, Iran. The contrast-enhanced MRIs helped in better delineation of the tumor boundaries and provided additional information about the vascular structure of the tumor, which is essential for accurate segmentation and treatment planning.

As mentioned earlier, the aim was to propose an optimal therapeutic plan based on the unique geometry features of each patient's tumor. The detailed 3D reconstruction and subsequent 2D slicing allowed for a comprehensive analysis of the tumor's spatial characteristics. This detailed information was used to tailor the HIFU treatment plan for each patient, ensuring that the entire tumor volume was targeted while minimizing the exposure of surrounding healthy tissues. By utilizing advanced imaging and segmentation techniques, this study aimed to enhance the precision and efficacy of HIFU therapy for breast cancer, ultimately improving patient outcomes.

The CNN used for segmentation was trained on a comprehensive dataset of annotated MRI images, which included high-contrast and non-high-contrast regions of breast cancer. The training dataset was sourced from multiple medical institutions and included images with varied contrast levels, anatomical variations, and different types of breast cancer to ensure robustness and generalizability. This diversity in the dataset was crucial for the model to learn and adapt to a wide range of imaging scenarios and tumor presentations.

The performance of the CNN was rigorously validated using a separate validation set, which also included diverse MRI images to simulate real-world clinical conditions. Several metrics were employed to evaluate the CNN's performance, including accuracy, sensitivity, specificity, and the Dice coefficient. Accuracy measured the overall correctness of the segmentation, sensitivity assessed the model's ability to correctly identify tumor regions, specificity evaluated its capacity to avoid false positives, and the Dice coefficient quantified the overlap between the predicted and actual tumor regions. The model achieved high scores across these metrics, indicating its reliability and effectiveness in accurately

segmenting breast tumors.

To ensure the medical appropriateness of the enclosed areas, the segmented regions produced by the CNN were meticulously reviewed by experienced radiologists. This review process involved a detailed comparison of the CNN-generated segmentations against the original MRI images. Radiologists checked for consistency in identifying tumor boundaries, including challenging non-high-contrast regions where the differentiation between tumor and normal tissue is less pronounced. This expert validation was essential to confirm that the segmentation results were not only accurate but also clinically relevant and suitable for guiding HIFU treatment planning.

Additionally, the review by radiologists provided an extra layer of quality assurance, helping to identify and correct any potential segmentation errors made by the CNN. This collaborative approach between AI and medical experts ensured that the final segmentation outputs were robust and reliable, ultimately enhancing the precision of the preoperative planning and the safety of the HIFU therapy. By combining advanced machine learning techniques with expert medical oversight, this study aimed to push the boundaries of current breast cancer treatment, leveraging technology to improve patient outcomes.

4.3 Deep Learning Computation

4.3.1 Model-Based Neural Network

Training a deep learning system to recognize a nonlinear map from high-dimensional data pairs of inputs and outputs is a challenging task. Researchers have found that experimentally established rules can be leveraged to regulate the time-dependent dynamics of a predefined system [156, 97, 58]. These rules serve as an underlying data framework, which can be utilized as a regularization factor. This regularization helps limit the space of potential solutions to a field domain that is permissible in the desired calculations, thereby ensuring that the model's predictions remain physically plausible. By incorporating such structured data into the learning algorithm, the performance of the model can be significantly enhanced. This enhancement occurs because the structured data boosts the functional content of the data, enabling the learning algorithm to find the optimal solution with minimal training data. Furthermore, it aids in the model's ability to generalize effectively to new, unseen data [102, 6]. This approach not only improves the efficiency of the training process but also enhances the robustness and accuracy of the deep learning system in complex, real-world applications.

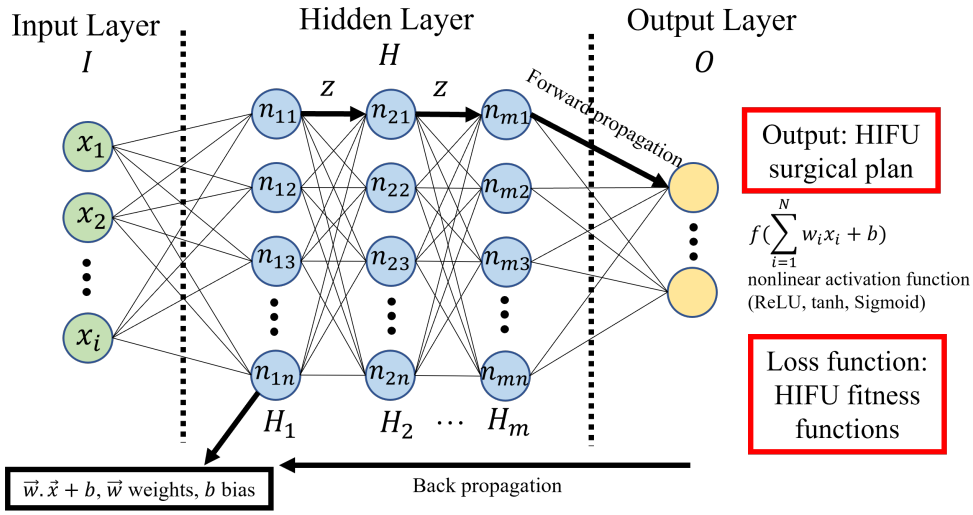


Figure 4.3: Diagram of NN architecture for finding optimal HIFU pathway. The input layer of the NN includes tumor's spatial inputs. The output layer computes the solution of the given model and embeds it into the loss function. By minimizing the loss function, NN can generate the surgical plan with respect to the previous conditions.

Given the recent development in model-based deep learning techniques, the architecture of a neural network can be illustrated with an input/output layer, hidden layers comprising neurons, and the associated weights and biases, as depicted in Fig. 4.3. This neural network design has demonstrated the capability to manage complex simulation models and accurately predict solutions by incorporating both nonlinear and linear PDEs directly into the solution process. Moreover, by treating the constraints of surgical HIFU procedures as a loss function, the model ensures that the predictions are aligned with the specific requirements of HIFU treatments. The inclusion of these PDEs allows the neural network to learn and adapt to the intricacies of the problem domain, making it possible to predict the optimal presurgical HIFU plan effectively. This approach not only enhances the precision of the model's predictions but also streamlines the process of developing tailored treatment plans, ensuring that the proposed solutions adhere to the stringent constraints and criteria essential for successful HIFU surgeries. The combination of advanced deep learning techniques and domain-specific knowledge embedded in the model exemplifies a significant step forward in medical treatment planning and optimization.

4.3.2 Deep Learning-Based Presurgical Plan

To properly cover a vast target zone with HIFU, many sonications are required. During treatment, the HIFU transducer follows a predetermined path through the tissue, delivering focused ultrasound energy to specific points. The treatment is transient, taking place at discrete points within the tissue where the HIFU focus is directed. The total number of sonications, denoted as N, typically falls within the tens. Each sonication's length determines the amount of energy delivered during a single sonication, denoted as t_h, and the duration of the subsequent cooling interval, denoted as t_c.

The cooling interval refers to the time period during which the HIFU device is paused to allow the treated tissue to cool down. This interval is crucial to prevent overheating and potential damage to the surrounding healthy tissue. Each sonication can therefore be described as a 4-tuple S_i, consisting of two spatial coordinates of the beam focus, as well as the sonication and cooling intervals t_h and t_c:

$$I = (S_1, S_2, ..., S_N), where\ S_i = (z_i, r_i, t_{h,i}, t_{c,i}). \tag{4.1}$$

As a result, the patient management problem involves determining the optimal locations and sonication periods for a specific number of ablations to effectively destroy the target volume while minimizing damage to the surrounding healthy tissue. This involves calculating the precise spatial coordinates where the ultrasound energy should be focused and timing the sonication and cooling intervals to maximize treatment efficacy and safety. By carefully planning these parameters, the HIFU treatment can be optimized to achieve the desired therapeutic outcomes, ensuring that the targeted tissue is adequately treated while sparing the adjacent healthy structures.

The NN thermal damage model generates a comprehensive spatial map of cumulative equivalent minutes at 43 degrees Celsius (CEM_{43}) that encompasses the entire treatment region I. This map is essential for visualizing the extent of thermal damage caused by the HIFU therapy. To delineate areas of damaged tissue, the CEM_{43} map is subjected to a thresholding process at a value of 240, creating a binary mask that clearly identifies regions of thermal damage. In the evaluation of HIFU therapy's effectiveness, it is crucial to ensure that all tissue within the designated target zone is completely ablated, thereby achieving the intended therapeutic outcome. Simultaneously, it is equally important to safeguard the surrounding tissues outside the tumor, often referred to as the prohibited region, ensuring they remain unaffected by the therapy. This precise control and distinction between the treated and untreated areas are vital for both the efficacy and safety of the HIFU treatment.

The fitness functions for presurgical treatment planning problems can be formulated as follows:

$$f_1 = \int_0^Z \int_0^R (\overline{C} * D) dr dz. \tag{4.2}$$

$$f_2 = \int_0^Z \int_0^R (C * \overline{D}) dr dz. \tag{4.3}$$

$$C = \begin{cases} 0 & \text{for } CEM_{43} \leq 240 \\ 1 & \text{for } CEM_{43} > 240 \end{cases}, \; C \in \mathbb{R}^+, \; \overline{C} \in \mathbb{R}^+. \tag{4.4}$$

In these equations, f_1 and f_2 represent the fitness functions designed to optimize the treatment planning process. The variable C is a function that determines whether a specific region has been sufficiently heated during the HIFU treatment. Specifically, C equals 0 if the cumulative equivalent minutes at 43 degrees Celsius (CEM_{43}) is less than or equal to 240, indicating insufficient thermal damage, and equals 1 if CEM_{43} exceeds 240, indicating adequate thermal damage. Here, C and its complement $\overline{C}$ are real, non-negative functions ($\mathbb{R}^+$).

The binary mask D represents the treated area, identifying the regions where the therapy has been applied, while the complementary mask $\overline{D}$ represents the non-treated zones. These masks are crucial for distinguishing between treated and untreated areas within the spatial domain defined by Z (depth) and R (radius).

Because C is expressed as a spatial function, it allows the user to specify the urgency or priority with which different locations within the treatment area should be addressed or protected. This capability is essential for optimizing the treatment plan, as it enables the incorporation of two critical aspects into the fitness functions:

By finely tuning the shapes of the target (treated) and prohibited (non-treated) areas, the treatment plan can be optimized to maximize therapeutic efficacy while minimizing collateral damage. By introducing a gradient, the fitness function can effectively guide the optimization process, directing it away from prohibited areas and towards desired treatment regions. This gradient ensures a smooth and efficient prediction and optimization process.

The ultimate goal of these fitness functions is to maximize the efficacy of the treatment by removing as much fitness capability as feasible from undesired areas, thereby enhancing the overall quality and safety of the presurgical treatment plan.

To achieve an optimal presurgical plan, it is crucial to accurately define the target area for the algorithm. The boundary points on each 2D slice of the tumor are represented by

two coordinates, (z, r), which capture the geometric characteristics of that specific region. These coordinates, along with the total number of sonications required, are fed into the NN as input data.

During the training process, the NN computes the optimal thermal dose parameters, which include the precise location, heating duration, and cooling times for the treatment. The algorithm then moves to the next area and repeats this process. After determining the treatment parameters for each region, the first fitness function (f_1) is evaluated. If any treated area lies outside the tumor, this function will yield a positive value, indicating an error. Consequently, the location of the proposed treatment area is adjusted to ensure that f_1 returns to zero, thereby preventing the treatment from encroaching into and damaging the prohibited area.

Once the treatment parameters are established for all designated areas, the algorithm assesses whether the entire target area has been effectively treated. This is achieved by examining the second fitness function (f_2). If any untreated regions remain, f_2 will have a positive value. Conversely, if the entire target area is uniformly treated, the value of f_2 will be zero. A positive value of f_2 indicates that the treated areas are too large to be fully covered by a single sonication. Therefore, the entire process is repeated with different sonication pathways to ensure comprehensive coverage of the target area.

This iterative loop continues until the entire target area is adequately treated. Each proposed treatment plan is then evaluated using HIFU simulation to estimate the final loss function, ensuring the plan's effectiveness and safety. This algorithmic process is visually depicted in Fig. 4.4.

The proposed deep learning method ingeniously integrates the fundamental principles of physics with NNs to tackle the intricate challenges associated with HIFU presurgical planning. By embedding numerical solutions of the governing physical laws directly into the neural network's loss function, this innovative approach allows the model to inherently learn from the physics underlying the problem.

This methodology capitalizes on the NN's exceptional ability to approximate complex functions. By incorporating the physical laws into the training process, the model ensures that the solutions it generates are not only accurate but also physically plausible. This integration significantly reduces the need for extensive datasets, which are often difficult and expensive to obtain. Consequently, the model's reliance on large amounts of empirical data is minimized, making it more efficient and practical for real-world applications.

Furthermore, by embedding the physical principles into the loss function, the model enhances its generalizability. This means that the NN can perform well even on new, unseen data, as it has learned the underlying physical behaviors rather than just memorizing

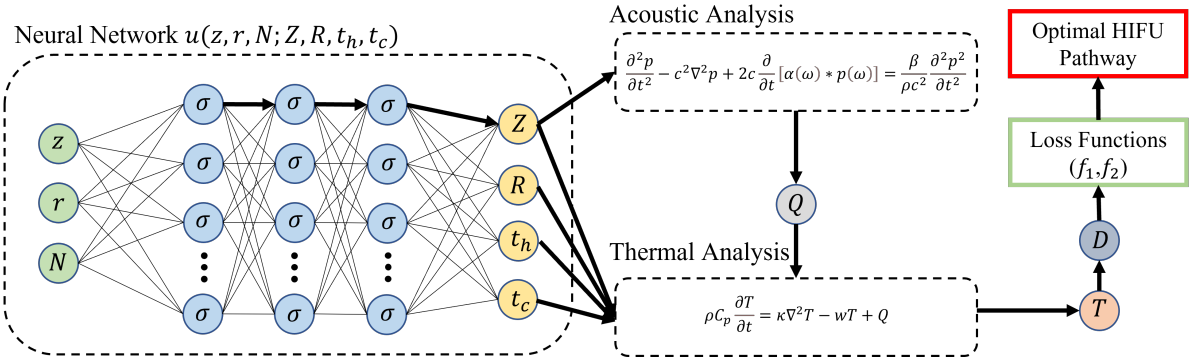


Figure 4.4: Diagram of NN architecture for solving the 2D optimal pathway scanning to predict the HIFU surgical plan. The first section is the NN with two spatial inputs z,r and the total number of sonication N, and the HIFU pathway parameters as the output value. The next two sections are acoustic and thermal analyses. The last section represents the HIFU loss function embedded with the deep learning algorithm, with the training sonication output. By minimizing the loss function, NN can generate the optimal HIFU pathway with respect to the predefined constraints.

patterns from the training dataset. This improved generalizability is crucial for medical applications like HIFU, where the ability to accurately predict and plan treatment across diverse patient scenarios is essential for effective and safe outcomes.

In summary, this approach leverages the strengths of both deep learning and physical modeling. It combines the predictive power of neural networks with the reliability and accuracy of physics-based constraints, leading to a robust, efficient, and generalizable solution for complex HIFU presurgical planning problems. This novel method represents a significant advancement in the field, offering a more reliable and practical tool for medical professionals in planning and optimizing HIFU treatments.

The NN architecture utilized in this study comprises 9 layers, each containing 20 neurons. This specific architecture was meticulously chosen to strike a balance between computational efficiency and the ability to capture complex nonlinear relationships within the data. By selecting a moderate number of layers and neurons, the model maintains an effective balance, avoiding excessive computational demands while still being able to model intricate patterns and interactions within the dataset.

For the hidden layers, the Rectified Linear Unit (ReLU) activation function was employed. ReLU is favored in deep learning due to its capability to mitigate the vanishing

gradient problem, which often plagues deeper networks. Additionally, ReLU accelerates convergence during the training process, allowing the network to learn more efficiently.

The neural network was trained using the Adam optimizer, a widely-used optimization algorithm in machine learning known for its adaptive learning rate and efficient handling of sparse gradients. The learning rate was set to 0.001, providing a balanced approach to learning speed and stability. The chosen loss function was Mean Squared Error (MSE), which is particularly suitable for regression tasks that involve continuous output variables, ensuring that the network's predictions are as close as possible to the actual values.

To ensure the model's convergence, training was conducted for 100 epochs. This duration was determined to be sufficient for the network to learn the underlying patterns without overfitting. A batch size of 32 was used during training, balancing computational efficiency with training stability, allowing for efficient gradient computation and weight updates.

The total loss for the model is computed as the sum of two fitness functions, f_1 and f_2. This combined loss approach facilitates the simultaneous optimization of both parameters, ensuring that the treatment plans are both effective and safe. The gradients of the total loss with respect to the NN parameters are calculated using backpropagation, a fundamental algorithm in neural network training. These gradients provide critical information on how much each NN parameter needs to change to reduce the total loss.

By adjusting its parameters based on these gradients, the NN can effectively minimize both f_1 and f_2. This simultaneous optimization process ensures that the treatment plans generated are not only accurate but also adhere to safety constraints, preventing damage to non-targeted tissues. Moreover, the use of a neural network enables rapid optimization and real-time adjustments in the treatment planning process, significantly enhancing the efficiency and responsiveness of presurgical planning for HIFU treatments. This capability is crucial in a clinical setting where timely and precise adjustments can significantly impact patient outcomes.

Chapter 5

HIFU Induced Lesion Segmentation

5.1 Problem Definition

Medical images play a crucial role as the primary source of information for surgical procedures, especially in the context of noninvasive treatments. These images provide detailed insights into the patient's anatomy, allowing surgeons and medical professionals to plan and execute procedures with precision. The objective is to fully automate the image processing workflow, thereby establishing a reliable and accurate foundation for both diagnosis and therapy. This automation not only enhances the speed and efficiency of medical procedures but also reduces the potential for human error, ensuring more consistent and high-quality outcomes.

In addition to medical images, other critical data, such as physiological signals, offer real-time information about the patient's current physical status. These signals, including heart rate, blood pressure, and oxygen levels, provide a comprehensive view of the patient's health, enabling the medical team to make informed decisions during treatment.

The proposed image-guided HIFU treatment is meticulously performed under the close supervision and approval of a physician. This ensures that every aspect of the procedure is carefully monitored, with the physician making critical decisions based on the real-time imaging and physiological data. The integration of advanced imaging techniques with expert medical oversight aims to improve the effectiveness of the treatment, minimize risks, and enhance patient outcomes.

Fig. 5.1 illustrates a comprehensive framework for intelligent theranostics, which integrates advanced diagnostic and therapeutic processes to enhance patient care. The frame-

work begins with smart diagnostics and planning processes that extract critical image information from US devices. These devices capture detailed images of the patient's anatomy, providing essential data that is crucial for both diagnosing conditions and planning treatments.

Once the image data is extracted, it is compiled into a global data set that encompasses all relevant medical information. This data set serves as a centralized repository of patient-specific information, including the anatomical details and any physiological parameters that have been monitored. The global data set is then utilized to establish a personalized treatment plan tailored to the specific needs of the patient. This ensures that the treatment is not only effective but also optimized for the individual's unique medical condition.

The next step in the framework involves the use of a HIFU transducer to treat the target area identified during the diagnostic phase. The HIFU transducer delivers precise therapeutic energy to the affected area, with the aim of achieving the desired therapeutic outcome without the need for invasive procedures.

Throughout the therapy, medical imaging and physiological signs are continuously monitored to track the progress and effectiveness of the treatment. This real-time monitoring is critical for ensuring that the therapy is proceeding as planned and allows for any necessary adjustments to be made promptly.

Moreover, to ensure the highest level of safety and efficacy, the entire process is supervised by a physician. The doctor plays a crucial role in validating and monitoring all the information throughout the therapy, making informed decisions based on the real-time data. This oversight is essential for mitigating risks and ensuring that the treatment is both safe and successful, ultimately leading to better patient outcomes.

Accurate preoperative image segmentation is essential to begin with the precise contouring of the intra-operative lesion, which forms the basis of a successful surgical procedure. This process requires attention to both structural and sequence scales, each of which plays a crucial role in ensuring the effectiveness of the treatment. The structural scale involves capturing detailed information from the image itself, which includes the shapes and boundaries of the tissues, while the sequence scale ensures that the spatial location of these structures is accurately correlated across different stages of the procedure.

Intra-operative initialization relies heavily on the fusion of structural information with accurate spatial location correlation. This means that the detailed structural data obtained from the preoperative imaging must be seamlessly integrated with the location-specific information to guide the intra-operative phase. By transferring this fused information from the preoperative stage to the intra-operative stage, surgeons are equipped with a comprehensive understanding of the lesion, which is critical for precise treatment.

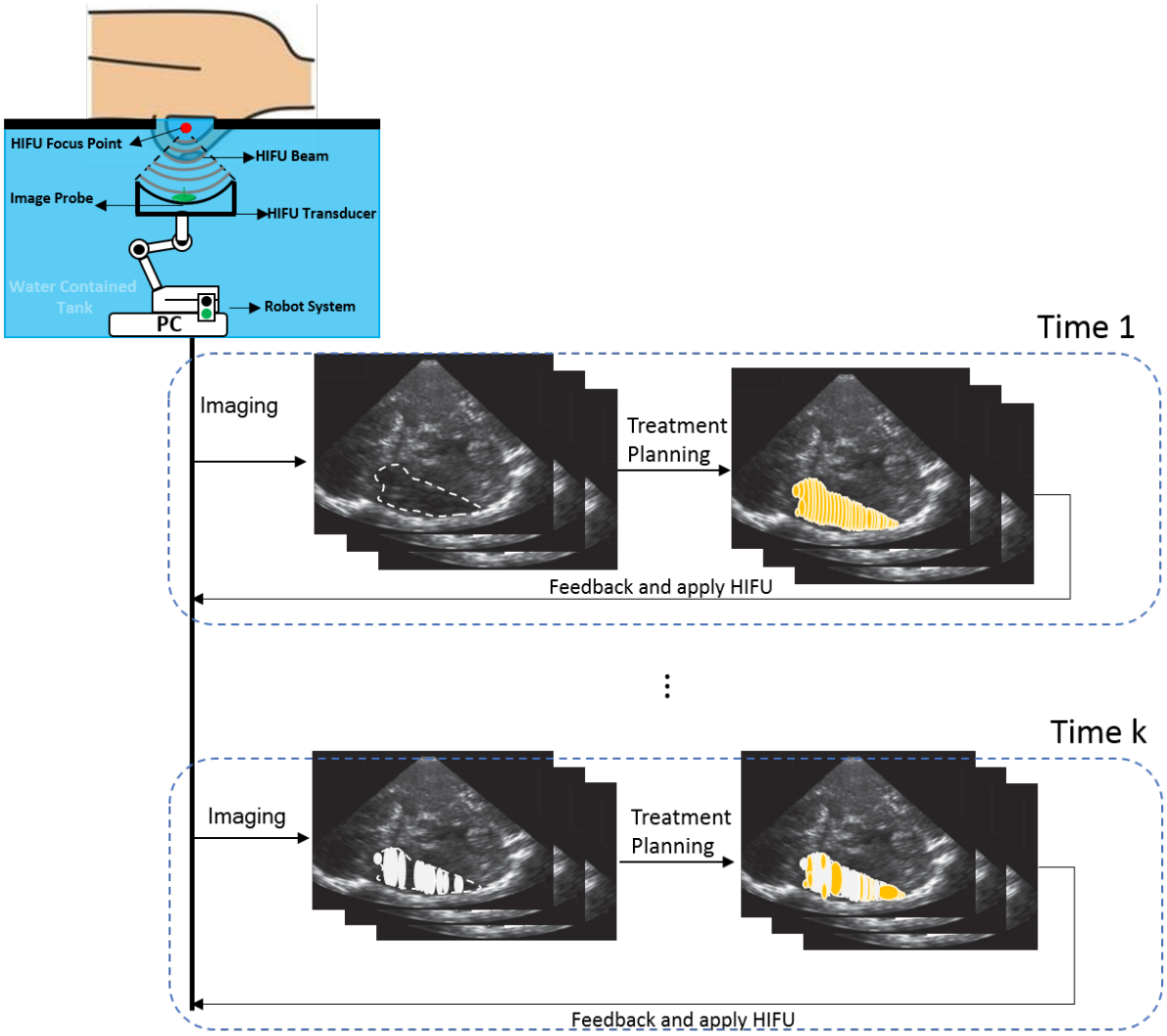


Figure 5.1: The proposed intelligent HIFU therapeutical framework is applied in the image-based HIFU diagnostic and treatment processing. The framework includes diagnosis and treatment parts. In the diagnosis part, morphology and spatial information in preoperative and intra-operative medical images can be accurately obtained and provided to the treatment strategy.

During the intra-operative stage, the fundamental therapeutic approach is based on the abnormality information derived from advanced image processing techniques. This information is pivotal in identifying the exact region that needs to be targeted during the procedure. With the physician's oversight and approval, the automatically determined target region is then subjected to treatment, ensuring that the therapy is applied precisely where it is needed.

However, the procedure also requires careful accident prevention and management strategies. For instance, if the patient experiences discomfort and moves unexpectedly, this can lead to unintended changes in the focus of the treatment, necessitating an immediate pause in the procedure. To mitigate such risks, large-movement alerts are issued, enabling the medical team to respond promptly to any changes that could compromise the treatment's accuracy.

The proposed intelligent HIFU treatment mode represents a significant advancement by combining automated image data processing with results that are verified by a physician. In this sophisticated approach, intra-operative lesion tracking becomes a critical component of the HIFU surgery. Real-time ultrasound scanning is enhanced by employing an advanced morphological active contour method, which continuously adjusts the contour of the lesion, ensuring that the treatment remains accurately targeted.

Furthermore, the development of a pixel-wise segmentation model is crucial, as it allows for the creation of a highly precise pixel-level tracking model. This model provides physicians with incredibly accurate information during the HIFU surgery, which is essential for delivering effective treatment. Moreover, having such precise lesion information enables real-time feedback that can be used to update and optimize the treatment plan for subsequent sonications, thereby improving the overall outcome of the procedure.

5.2 B-Mode Imaging Simulation

5.2.1 Governing Equations

The complex behavior of acoustic wave propagation through a medium with spatially varying acoustic properties and classical thermoviscous absorption can be rigorously modeled using a system of coupled partial differential equations. This mathematical framework accounts for the nonlinear interactions between the waves and the medium, capturing the intricacies of wave distortion, attenuation, and energy distribution as they traverse through

different regions with varying acoustic impedances. Moreover, the incorporation of thermoviscous effects within these equations enables a more accurate representation of energy losses due to both thermal conduction and viscous dissipation, making the model highly effective in simulating real-world scenarios where such factors are significant. These coupled partial differential equations thus provide a comprehensive tool for understanding and predicting the behavior of acoustic waves in complex media [164].

$$\frac{\partial u}{\partial t} = -\frac{1}{\rho_0}\nabla p + F. \tag{5.1}$$

$$\frac{\partial \rho}{\partial t} = -(2\rho + \rho_0)\nabla . u - u.\nabla \rho_0 + M. \tag{5.2}$$

$$p = c_0^2(\rho + d.\nabla \rho_0 + \frac{B}{2A}\frac{\rho^2}{\rho_0} + 2\alpha_0 c_0 \frac{\partial \rho}{\partial t}). \tag{5.3}$$

The acoustic field within a medium is comprehensively represented by several key variables, including pressure (p), particle velocity (u), particle displacement (d), and acoustic density (ρ). These variables are all functions of both position (x) and time (t), reflecting the dynamic nature of acoustic wave propagation. The medium through which the sound waves travel is characterized by important physical parameters such as mass density (ρ_0), sound speed (c_0), non-linearity parameter (B/A), and absorption coefficient (α_0). Notably, these parameters are not constant but can vary spatially, allowing for a more accurate modeling of heterogeneous media where properties change from one region to another.

The relationship between pressure and density within this framework includes a loss term that accounts for acoustic absorption, a critical factor in accurately simulating wave propagation in real-world environments. This absorption is modeled by the term $\alpha \approx \alpha_0 \omega^2$, where α_0 is the absorption coefficient pre-factor, with units of Np $(\text{rad/s})^{-2}\text{m}^{-1}$, indicating its dependence on both frequency and the material properties of the medium. The absorption term ensures that the model captures the attenuation of the wave as it propagates, which is essential for understanding energy loss due to mechanisms like thermal conduction and viscous effects.

Additionally, the equations governing the acoustic field incorporate two linear source terms: F and M. The term F represents the input of body forces per unit mass, measured in units of N kg^{-1} (or equivalently m s^{-2}), which could correspond to external forces acting on the medium. The term M, on the other hand, represents the time rate of mass input

per unit volume, with units of kg m^{-3} s^{-1}, which could account for sources such as fluid injection or other mass transfer processes within the medium.

These variables and parameters, when combined, contribute to a system of equations that can be transformed into a specific form of the Westervelt equation. The Westervelt equation is a fundamental nonlinear partial differential equation that describes the propagation of finite amplitude sound waves in a thermoviscous medium, capturing the complex interactions between wave propagation, absorption, and nonlinearity [76][109].

$$\nabla^2 p - \frac{1}{c_0^2}\frac{\partial^p}{\partial t^2} - \frac{1}{\rho_0}\nabla\rho_0\nabla p + \frac{\beta}{\rho_0 c_0^4}\frac{\partial^2 p^2}{\partial t^2} + \frac{2\alpha_0}{c_0}\frac{\partial^3 p}{\partial t^3} = \rho_0\nabla.F - \frac{\partial M}{\partial t}. \tag{5.4}$$

In this context, the parameter β is defined as $\beta = 1 + \frac{B}{2A}$, where B and A are the coefficients related to the nonlinearity of the medium. This parameter β is a crucial dimensionless quantity that quantifies the degree of nonlinearity in the acoustic wave propagation. The term B/A itself is known as the nonlinearity parameter of the medium, and it describes the relationship between the amplitude of the wave and the resulting distortion due to nonlinear effects. By adding 1 to half of this nonlinearity parameter, β effectively adjusts the overall impact of nonlinearity on the wave, making it an important factor in the equations governing nonlinear acoustic phenomena. This adjustment allows the model to more accurately reflect the behavior of waves in media where nonlinearity plays a significant role in the propagation dynamics.

5.2.2 k-space Method

In the field of acoustics, solving PDEs is essential for modeling wave propagation, and several numerical methods are commonly employed for this purpose. The three primary methods are the FDM, the FEM, and the boundary-element method. Each of these techniques has its strengths and is widely used across various applications in acoustic modeling.

The FDM involves discretizing the spatial and temporal domains into a grid and approximating the derivatives in the PDEs using finite differences. This method is relatively simple to implement and is effective for solving a wide range of problems, especially in structured grids. The FEM, on the other hand, is based on discretizing the domain into elements and using piecewise polynomial functions to approximate the solution. This approach is particularly advantageous for complex geometries and inhomogeneous materials, where the flexibility in mesh design allows for more accurate modeling. The boundary-element method is distinct in that it reduces the problem dimensionality by focusing on

the boundaries of the domain, making it highly efficient for problems involving infinite or semi-infinite domains, such as radiation and scattering problems.

However, these traditional methods often face significant challenges when applied to high-frequency or broadband wave problems in the time domain. Specifically, to accurately capture the wave behavior, these methods require a large number of grid points per wavelength and very small time steps. This requirement is necessary to minimize numerical dispersion—an artifact that can distort the wave as it propagates through the grid. The consequence of these stringent requirements is that simulations can become highly inefficient and time-consuming, especially for large-scale or high-resolution problems.

To address these inefficiencies, alternative numerical techniques have been developed. One such method is the pseudo-spectral (PS) method, which is an extension of the finite-difference method. The PS method improves accuracy by using global basis functions, such as trigonometric or polynomial functions, to represent the solution over the entire domain. This approach can significantly reduce the number of grid points needed per wavelength, thereby mitigating the issue of numerical dispersion and enhancing computational efficiency.

Additionally, the k-space approach offers a powerful solution to the challenges posed by time-stepping in high-frequency simulations. The k-space method modifies the standard finite-difference time-domain method by incorporating wavenumber-dependent corrections, allowing for larger time steps without sacrificing accuracy. This approach effectively addresses the issue of time-domain inefficiency, making it a valuable tool for simulating broadband acoustic waves.

Together, the pseudo-spectral method and the k-space approach provide robust alternatives to traditional numerical methods, enabling more efficient and accurate simulations of high-frequency and broadband acoustic waves. These advanced techniques are particularly useful in applications where precision and computational efficiency are critical, such as in the design of acoustic devices, medical imaging, and environmental acoustics.

Linear interpolation is a straightforward technique used in basic FD schemes to estimate the gradient of a field between grid points or mesh nodes. This method involves drawing a straight line between two adjacent points and using this line to approximate the gradient, making it a relatively simple and computationally inexpensive approach. However, the accuracy of linear interpolation is limited by its assumption that the field varies linearly between points, which may not be the case in more complex or rapidly changing fields.

To achieve a more accurate estimation of the gradient, higher-order interpolation methods can be employed. Instead of relying on a simple linear fit, these methods use higher-order polynomials to approximate the field. By fitting a polynomial to more nodes sur-

rounding the point of interest, the method can better capture the curvature and more accurately represent the underlying field's variation. The degree of the polynomial increases with the number of nodes used, and as a result, the accuracy of the gradient estimation improves. This approach allows for more precise calculations of derivatives, which are essential in many applications where subtle variations in the field can significantly impact the outcome of the simulation.

The PS method takes this concept a step further by employing a global rather than local approach to gradient estimation. Instead of fitting a polynomial to a small number of nodes, the PS method fits a Fourier series to all the data points in the domain. A Fourier series represents the field as a sum of sinusoidal functions, each with a specific frequency, amplitude, and phase. Because the Fourier series can capture both high and low-frequency components of the field, it provides a highly accurate global approximation.

This global approach offers two major advantages. First, the use of the fast Fourier transform (FFT) allows for the efficient computation of the Fourier coefficients. The FFT is an algorithm that can quickly calculate the amplitudes of the sinusoidal components, making the PS method computationally feasible even for large datasets. Second, the sinusoidal basis functions used in the Fourier series require significantly fewer nodes per wavelength to achieve the same accuracy as other methods. While traditional methods might require six to ten nodes per wavelength to reduce numerical dispersion, the PS method, with its sinusoidal basis, needs only two nodes per wavelength. This reduction in the number of nodes directly translates into lower computational costs and memory usage, making the PS method particularly advantageous for high-resolution simulations.

Overall, by fitting a Fourier series to the entire domain and leveraging the computational efficiency of the FFT, the pseudo-spectral method provides a powerful and accurate tool for gradient estimation and field approximation. This makes it particularly useful in applications where precision and computational efficiency are critical, such as in fluid dynamics, electromagnetics, and acoustic wave propagation [147, 162].

5.2.3 Numerical Simulation

The k-Wave simulation toolbox is a versatile and powerful set of functions designed to simulate the time evolution of an acoustic wave field within various media, whether homogeneous or heterogeneous, and across multiple dimensions, including 1D, 2D, and 3D, using the k-space method [163]. This method is particularly advantageous in modeling the complex behavior of acoustic waves as it allows for accurate simulations over large time steps without introducing significant numerical dispersion, which is often a challenge in

conventional methods. The k-Wave toolbox is not only adept at simulating wave propagation but also extends its capabilities to time reversal image reconstruction, a technique commonly used in photoacoustic imaging and other applications.

In time reversal image reconstruction, the toolbox's functions are utilized to estimate the initial photoacoustic pressure distribution from data gathered over a measurement surface, which can be either linear in 2D or planar in 3D. This process involves the backward propagation of the recorded acoustic signals to reconstruct the image of the original pressure source, enabling high-resolution imaging of structures within a medium. This is particularly useful in medical imaging, where precise reconstruction of internal features is essential for accurate diagnostics.

The toolbox also includes comprehensive geometry creation functions that allow users to define both Cartesian- and grid-based geometries with ease. These functions can generate a variety of shapes, such as circles, arcs, disks, spheres, shells, and balls, which are often needed to model the boundaries or internal structures within the simulation domain. For Cartesian-based geometries, the functions return the exact geometric coordinates of the shape, enabling precise placement and manipulation within the simulation environment. On the other hand, grid-based geometries are represented by a binary matrix, where 1s indicate the presence of the shape and 0s represent the absence, providing a straightforward way to incorporate complex structures into the simulation grid.

In addition to these core functions, the k-Wave toolbox is equipped with a range of utility functions that streamline various tasks essential for setting up and running simulations. These utility functions include tools for grid creation, which help define the spatial domain of the simulation; matrix smoothing, which can be used to reduce numerical artifacts and improve the stability of the simulation; and matrix interpolation, which allows for the adjustment of data resolution. Furthermore, the toolbox provides functions for file loading, enabling easy access to external data sources or previous simulation results, and other general-purpose tasks that enhance the user experience and make the setup process more efficient.

Overall, the k-Wave simulation toolbox offers a comprehensive suite of functions that cater to a wide range of acoustic simulation needs, from wave field evolution and image reconstruction to geometry creation and utility operations. Its flexibility and efficiency make it a valuable tool for researchers and engineers working in fields such as acoustics, medical imaging, and non-destructive testing.

The Matlab-based B-mode simulation model is a sophisticated tool designed to simulate ultrasound imaging by leveraging the k-Wave toolbox, a powerful resource for acoustic wave modeling. This model is particularly valuable as it allows for the customization of tissue

parameters based on the specific anatomical characteristics of a patient, making it highly adaptable and relevant for personalized medical applications. By adjusting the tissue parameters within the model, users can create more accurate simulations that reflect the unique properties of an individual's tissues, leading to better diagnostic insights.

The underlying computational framework of this model employs a k-space pseudo-spectral scheme, which is a key component in its ability to accurately simulate wave propagation. In this scheme, spatial gradients are calculated using the Fourier collocation spectral method, a technique that enables high precision by representing the spatial domain as a series of sinusoidal functions. This method is particularly effective for capturing the details of wave interactions within the tissue, ensuring that even small-scale features are accurately modeled.

Temporal gradients, on the other hand, are calculated using a k-space corrected finite difference scheme. This innovative approach combines the accuracy of spectral methods with the stability and simplicity of finite difference methods. The k-space correction allows the scheme to maintain accuracy across a wide range of frequencies, and it is exact and stable when applied to homogeneous media. For heterogeneous media, which are more complex and varied in their acoustic properties, this scheme offers a significant advantage by allowing for larger time steps without compromising accuracy. This is a crucial feature, as it enables faster simulations while still providing results that are as precise as those generated by conventional pseudo-spectral time-domain methods.

The simulation domain in this model is discretized into a grid, where each grid point represents a specific location within the tissue. The resolution of this grid—both spatial and temporal—is a critical factor in the accuracy of the simulation. To ensure that the model produces reliable results, the spatial and temporal resolution are determined through convergence testing. This process involves running simulations at various resolutions to identify the point at which further increases in resolution no longer significantly improve the accuracy of the results. By optimizing the resolution through convergence testing, the model balances the need for precision with computational efficiency, making it a practical tool for clinical and research applications.

Overall, the Matlab-based B-mode simulation model, with its integration of the k-Wave toolbox and advanced computational techniques, provides a robust and flexible platform for ultrasound imaging simulation. Its ability to customize tissue parameters, coupled with the precision of its k-space pseudo-spectral scheme, makes it an invaluable resource for simulating patient-specific ultrasound images with high accuracy and efficiency.

5.3 AI-Assisted Lesion Segmentation

This section introduces a novel approach to pixel-wise semantic image segmentation specifically tailored for the task of lesion segmentation within HIFU therapeutic framework. The proposed model leverages advanced B-mode imaging techniques to achieve highly precise and sensitive segmentation of lesions, ensuring that the process is not only accurate but also capable of operating in real-time. This innovation is particularly significant in the context of HIFU therapy, where the ability to precisely identify and target lesions is crucial for effective treatment outcomes. The model's design addresses the challenges of real-time processing while maintaining a high level of accuracy, making it a robust solution for clinical applications.

Fig. 5.2 presents the primary architecture and workflow of an advanced AI algorithm rooted in a transformers-based model [143]. This framework is composed of two essential components that work in tandem to achieve precise region-of-interest segmentation. The first component focuses on the pre-processing of B-mode ultrasound images, which is a critical step in preparing the data for subsequent analysis. Specifically, for each sonication, two B-mode images are obtained and then subjected to a series of processing steps. These steps include cropping the images based on prior knowledge of the sonication's coordinates to focus on the relevant area, resizing the cropped images to a standardized size of 224x224 pixels to ensure consistency, and calculating the before-after differences between the images to generate a three-channel input. This composite image, which encapsulates essential spatial and temporal information, is then fed into the Swin-Unet model [125] for precise segmentation of the region of interest. The Swin-Unet model, a sophisticated variant of the U-Net architecture enhanced with transformer-based modules, is specifically designed to handle the complex segmentation tasks required in this context. Further details on the architecture and functioning of the Swin-Unet model, including its advantages in handling medical imaging data, are provided in the following section, where the underlying mechanisms and performance metrics are discussed in greater depth.

5.3.1 Swin-Unet

Swin-Unet is an advanced variant of the well-known U-Net architecture [143], designed specifically to integrate the powerful capabilities of Swin-Transformers within the traditional encoder-decoder framework, enhanced by the use of skip connections [125]. This fusion of technologies allows Swin-Unet to effectively capture and process hierarchical features from medical images, which is critical for tasks like segmentation that require high levels of precision and context-awareness.

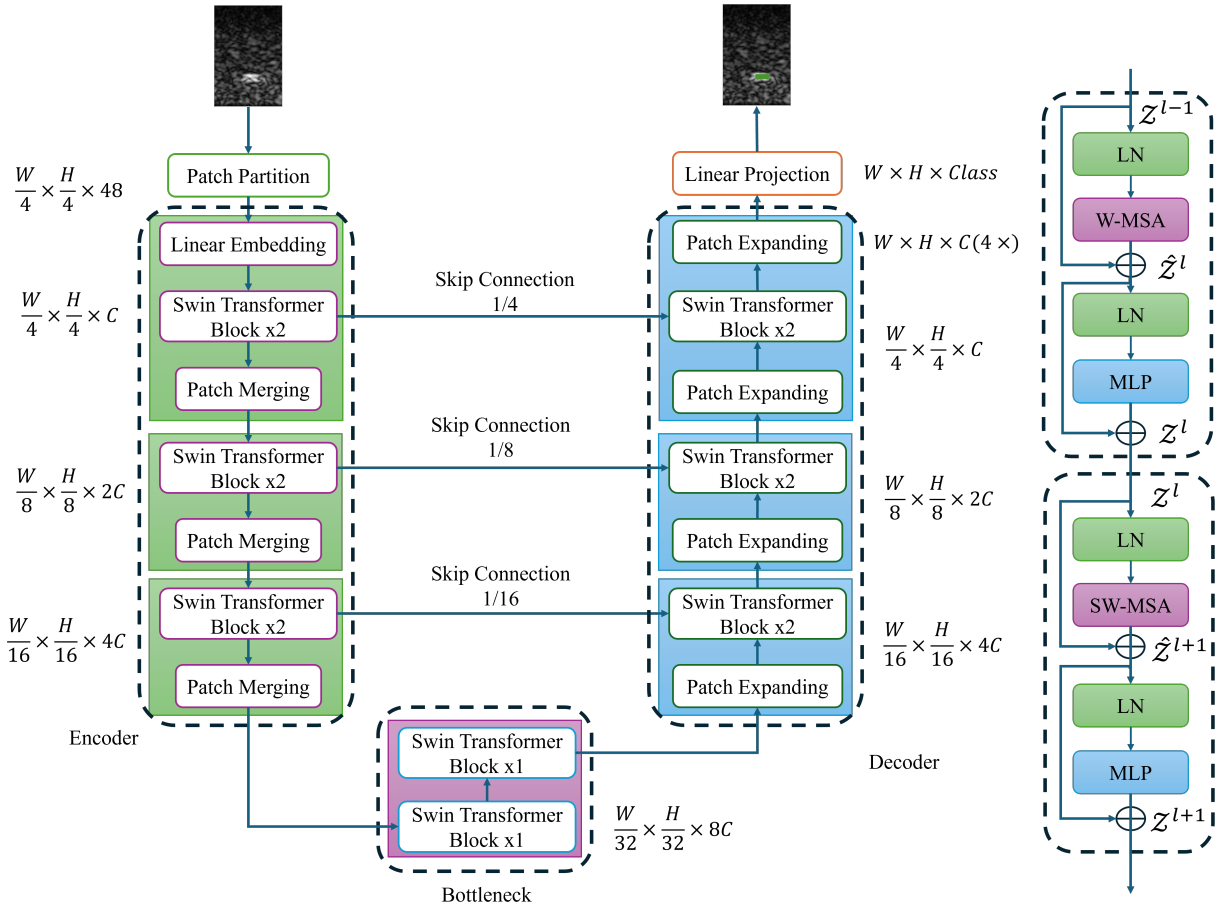


Figure 5.2: The integration of machine learning with ultrasound imaging involves pre-processing of B-mode images taken before and after HIFU treatment by clipping them to a predetermined surgical region. The images are then resized to 224×224 gray-scale resolutions and concatenated with their pixel-wise difference to form a three-channel image that is fed to the Swin-Unet model, which outputs the segmented region of the HIFU ablation.

At the heart of this architecture lies the Swin-Transformer block, which is a sophisticated hierarchical structure that applies a series of operations to the feature map in a multi-scale, recursive manner. This multi-scale processing enables the model to capture details at varying levels of granularity, which is essential for accurately segmenting complex structures such as lesions in medical images. As depicted in Fig. 5.2, the Swin-Transformer block employed in this model comprises five key operations: the windowed multi-head self-attention module (W-MSA), the shifted window multi-head self-attention mechanism (SW-MSA), a pair of feed-forward layers (MLP) activated by the GELU function [62], and Layer Normalization (LN) [11]. Each of these components plays a crucial role in enhancing the model's ability to focus on relevant features and maintain stability during training.

The W-MSA module allows the model to perform self-attention within fixed windows of the image, focusing on local regions, while the SW-MSA extends this capability by shifting the windows, enabling the model to achieve a global understanding of the image without the computational burden of full self-attention. This strategic combination ensures that Swin-Unet can effectively balance local detail and global context, which is particularly advantageous in medical imaging where both fine details and broader patterns are critical.

The feed-forward layers (MLP), which consist of linear transformations followed by RELU activation, further refine the output of the attention mechanisms by applying non-linear transformations, adding depth and complexity to the model's decision-making process. These layers are followed by Layer Normalization, which helps stabilize the training process by normalizing the inputs to each layer, thereby improving convergence rates and overall performance.

Moreover, the encoder-decoder structure of Swin-Unet is built upon a series of down-sampling and up-sampling operations that modify the spatial resolution of the feature maps, enabling the model to capture and integrate features at different scales. Down-sampling reduces the spatial dimensions by a factor of two, allowing the model to focus on broader patterns, while up-sampling restores the original resolution, enabling precise localization. These operations are crucial for ensuring that the model can segment lesions at multiple levels of detail, from coarse to fine, which is vital for accurate diagnosis and treatment planning.

For instance, with an input image size of 2242243 and a patch size of 44, the encoder initially processes non-overlapping patches of size $W/4H/43$, corresponding to 565648 for the given input resolution. The first stage of the encoder involves a linear embedding module that projects these input patches into a higher-dimensional space, defined by dimension C, which is then processed by the subsequent Swin blocks. The processing within each

Swin block follows the formulation:

$$z^{(l)} = z^{(l-1)} + \text{MHSelfAttn}(z^{(l-1)} + \text{FFN}(z^{(l-1)})) \tag{5.5}$$

where $z^{(l-1)}$ represents the input to the l-th block, and MHSelfAttn and FFN denote the shifted window multi-head self-attention mechanism and the feed-forward network, respectively. This formulation highlights the recursive nature of the architecture, where each block refines the feature representation before passing it to the next stage.

Finally, Swin-Unet employs the same self-attention mechanism as the original Swin-Transformers [95], where the attention function is computed as:

$$Attention(Q, K, V) = SoftMax(\frac{QK^T}{\sqrt{d}} + B)V \tag{5.6}$$

In this equation, Q, K, and V are the query, key, and value matrices, respectively, and B represents the bias matrix, which is constructed according to the specifications detailed in ref. [21]. This attention mechanism is central to the model's ability to selectively focus on different parts of the image, ensuring that the most relevant features are emphasized during the segmentation process. By combining these sophisticated components, Swin-Unet offers a powerful tool for medical image segmentation, capable of delivering high levels of accuracy and sensitivity required for clinical applications.

The Swin blocks within the encoder stage of Swin-Unet are followed by a critical component known as the patch merging block. This block plays a vital role in reducing the spatial resolution of the feature maps by merging each set of 22 neighboring patches through concatenation of their features. As a result, the feature resolution is effectively reduced by a factor of two after each patch merging block, thereby enabling the model to focus on more abstract, higher-level features as it progresses deeper into the network. This reduction in resolution is essential for capturing global context, which is crucial for accurate segmentation in complex medical imaging tasks.

To seamlessly connect the encoder and decoder stages, Swin-Unet adopts a strategy similar to that of the vanilla U-Net architecture by introducing a bottleneck layer. This bottleneck is constructed by incorporating two consecutive Swin blocks that maintain both the feature dimensionality and resolution unchanged. The purpose of the bottleneck is to act as a bridge that allows the model to capture deep, abstract features at the lowest resolution before the decoder begins the process of reconstructing the image to its original resolution. By maintaining the same dimensionality and resolution, the model preserves the integrity of the learned features while transitioning from the encoder to the decoder.

In the decoder stage of Swin-Unet, the architecture mirrors the symmetrical structure of the encoder, ensuring a consistent flow of information as the model reconstructs the high-resolution output. Similar to the encoder, Swin blocks are employed in the decoder to extract deep abstract features. However, instead of the patch merging layers used in the encoder, the decoder introduces patch expanding blocks. These blocks are designed to reverse the down-sampling process by increasing the resolution of the feature maps through an up-sampling operation. Specifically, the patch expanding layer reconfigures the feature maps from adjacent dimensions into a higher resolution output, effectively doubling the spatial resolution while reducing the feature dimensionality by half. This operation is crucial for reconstructing the fine details of the original image.

To illustrate, consider the first patch expanding layer, where the input features are initially subjected to a linear layer transformation that doubles the feature dimension. This transformation is followed by a rearrange operation that increases the spatial resolution of the input features to twice their original size while simultaneously reducing the feature dimension to one-fourth of the original input dimension. This meticulous reconfiguration ensures that the model can effectively recover the high-resolution details necessary for precise segmentation.

A key feature of Swin-Unet is its use of skip connections, which are established between corresponding Swin blocks in the encoder and decoder stages. These skip connections are instrumental in preserving the spatial information and enabling the fusion of information from both shallow and deep features. By directly connecting the encoder's shallow layers to the corresponding decoder layers, the model ensures that high-resolution details captured in the early stages are retained throughout the network. This approach prevents the loss of critical information that could occur due to the down-sampling process and the merging of blocks, thereby enhancing the overall accuracy and robustness of the segmentation results.

In summary, the architecture of Swin-Unet is carefully designed to balance the extraction of deep, abstract features with the preservation of fine details, making it an effective tool for medical image segmentation tasks. The combination of Swin blocks, patch merging, and patch expanding layers, along with the strategic use of skip connections, allows Swin-Unet to achieve high levels of precision and sensitivity, which are essential for clinical applications.

5.3.2 Training Procedure

During the training phase of the Swin-Unet neural network, the model's parameters are fine-tuned using a carefully curated set of masks that have been meticulously labeled by

human experts. These masks serve as ground truth references, guiding the network in learning how to accurately segment lesions or other regions of interest in medical images. The training process begins with a series of essential preprocessing steps applied to the input images. These steps include cropping the images to focus on relevant areas, resizing them to a standardized resolution to ensure consistency across the dataset, and normalizing the pixel values to stabilize the training process. Additionally, data augmentation techniques such as horizontal and vertical flipping, along with affine transformations, are employed. These augmentations are crucial for enhancing the model's robustness by exposing it to a wider variety of scenarios, thereby reducing the risk of overfitting and ensuring that the model can generalize well to unseen data.

To optimize the Swin-Unet model's weight parameters, a sophisticated loss function is employed. This function is a linear combination of Binary Cross Entropy (BCE) and Soft Dice Loss, two powerful metrics that together ensure the model achieves high segmentation accuracy and per-pixel precision. The Binary Cross Entropy component measures the discrepancy between the predicted probability and the actual label on a per-pixel basis, making it particularly effective for handling imbalanced datasets where some classes may dominate. On the other hand, the Soft Dice Loss is designed to optimize the overlap between the predicted segmentation and the ground truth, making it sensitive to small segmentation errors that could be critical in medical imaging. By combining these two loss functions, the training process not only improves segmentation accuracy but also enhances the model's ability to generalize across different data distributions, which is vital for clinical applications. Furthermore, this combined loss function provides robustness against adversarial attacks, ensuring that the model maintains its performance even when confronted with challenging or corrupted inputs.

In addition to the loss function, several other hyperparameters and training settings are carefully configured to optimize the model's performance. A learning rate of 2e-4 is selected to control the speed at which the model's parameters are updated during training, striking a balance between convergence speed and stability. The batch size is set to 8, allowing the model to process multiple images simultaneously, which enhances computational efficiency and ensures that the gradients are averaged over a sufficient number of samples. To further refine the learning process, a ReduceLROnPlateau scheduler is employed. This scheduler dynamically adjusts the learning rate by reducing it when the model's performance plateaus, thereby preventing the model from getting stuck in local minima and ensuring continued progress towards optimal performance.

The training process is set to run for a maximum of 200 epochs, providing ample opportunity for the model to learn the intricate patterns present in the data while also allowing for early stopping if convergence is achieved before reaching the maximum number

of epochs. The AdamW optimizer is chosen for its ability to handle sparse gradients on noisy data, making it well-suited for the complexities of medical image segmentation. This optimizer is a variant of the traditional Adam optimizer, with an added mechanism for weight decay, which helps prevent overfitting by penalizing large weights.

The entire training process is implemented using the PyTorch library, a powerful and flexible deep learning framework that facilitates efficient model development and experimentation. The model is trained on a single NVIDIA RTX 3080Ti GPU, which provides the computational power necessary to handle the large datasets and complex operations involved in Swin-Unet training. The GPU's 16GB memory ensures that even high-resolution images can be processed without running into memory constraints, allowing for smooth and efficient training.

In summary, the training phase of Swin-Unet involves a comprehensive and meticulously designed process that combines advanced preprocessing, data augmentation, loss functions, and optimization techniques. These elements work together to create a model that is not only highly accurate and precise in its segmentation tasks but also robust and generalizable across different data distributions, making it an invaluable tool in the field of medical imaging.

Chapter 6

Results and Discussions

6.1 PINN Simulation

In this section, we present a comprehensive analysis of the outcomes derived from various simulated physical processes, which are organized into distinct subsections for clarity and depth of understanding. We begin by showcasing the field of total acoustic pressure, which provides insight into how sound waves propagate and interact within the modeled domain. This is followed by a detailed examination of the distribution of sound intensity magnitude, highlighting the regions within the domain that experience varying levels of acoustic energy concentration. These visualizations are crucial for understanding the acoustic environment and its potential effects on the tissue.

Subsequently, we delve into the thermal response of the breast model, specifically focusing on the distribution of temperature resulting from the absorption of acoustic energy. This analysis allows us to observe how the absorbed energy translates into heat within the tissue, providing a basis for understanding the thermal dynamics at play. The temperature distribution maps offer critical insights into the areas that are likely to experience significant heating, which is a key factor in the therapeutic effectiveness of the procedure.

Finally, we assess the biological impact of the increased temperature by presenting the extent of necrotized tissue. This section includes a detailed evaluation of the amount of both tumor and healthy breast tissue that undergoes necrosis due to the thermal effects. By quantifying the tissue damage, we can evaluate the precision and efficacy of the treatment in targeting the tumor while minimizing collateral damage to surrounding healthy tissue. This comprehensive analysis provides a holistic view of the simulated physical processes, offering valuable insights into the potential clinical outcomes of the procedure.

6.1.1 Acoustic Field Generation

As previously mentioned, an attempt is made to generate a concentrated ultrasonic wave at the tumor site using a bowl-shaped acoustic transducer operating at a frequency of 1.1 MHz. Fig. 6.1 displays the contours of total acoustic pressure and sound intensity magnitude, respectively. These contours depict the three cut planes (1 to 3) which include the x-y, z-y, and x-z surfaces passing through the center of the tumor.

To provide a clearer depiction of the acoustic physics simulation outcomes, Fig. 6.2 and 6.3 illustrate the distribution of acoustic pressure and intensity magnitude along various x, y, and z directions, with the z-direction specifically aligned with the propagation of the acoustic wave. This directional analysis allows for a detailed understanding of how the acoustic waves interact with the tissue, particularly in the critical z-direction, which is aligned with the focused energy delivery.

As shown in Fig. 6.2, the pressure amplitude is notably higher at the tumor site. This increase is a direct consequence of the focused acoustic waves, which are designed to concentrate energy within the tumor. The result is a significant enhancement in sound intensity and, consequently, higher energy deposition within the tumor region. This concentration of energy is crucial for effective treatment, as it ensures that the maximum therapeutic effect is localized to the target area, minimizing exposure to surrounding healthy tissues.

Fig. 6.3 further emphasizes this phenomenon by highlighting a prominent peak in sound intensity within the tumor. This peak indicates that the acoustic waves are effectively focused, leading to rapid heat generation as the intense acoustic power dissipates within the tissue. The high sound intensity directly correlates with increased thermal effects, which are essential for inducing the desired necrotic effect on the tumor.

Following the simulation of pressure acoustics, it is imperative to simulate the bioheat transfer physics to accurately quantify the heat generated and the resulting temperature rise in the tumor region. This step is crucial for understanding the thermal dynamics that result from the acoustic energy deposition. The outcomes of this bioheat transfer simulation, which provide insights into the thermal effects on the tumor and surrounding tissue, are presented in the next subsection. These results will further elucidate the effectiveness of the acoustic treatment in achieving the desired thermal outcomes for tumor ablation.

6.1.2 Temperature Distribution

The focused ultrasonic wave generates heat in the targeted area, leading to a temperature increase, as depicted in Fig. 6.4 (a to f) after 1 second across various cut planes. This

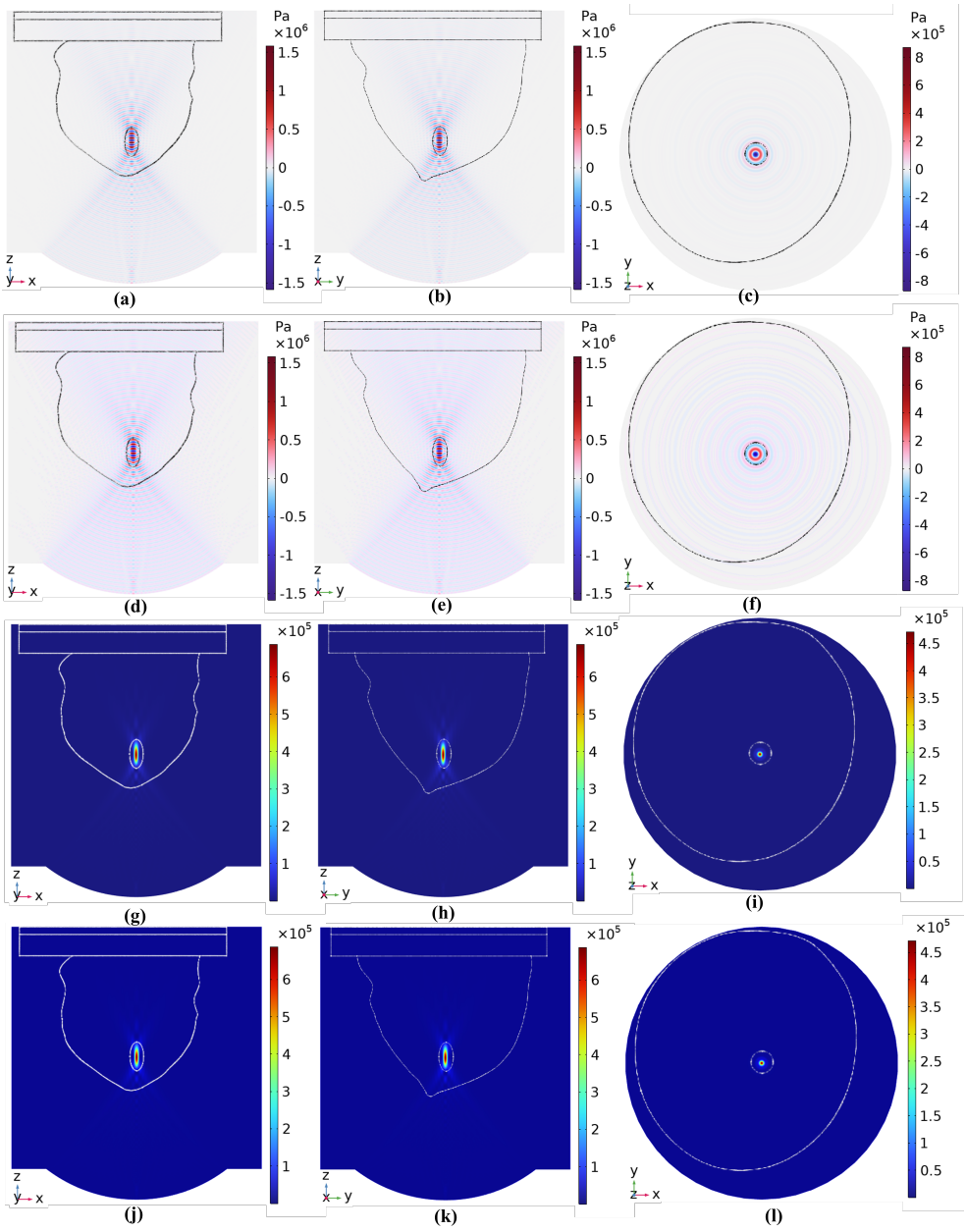


Figure 6.1: Total acoustic pressure field, (a) FEM cut plane 1, (b) FEM cut plane 2, (c) FEM cut plane 3, (d) PINN cut plane 1, (e) PINN cut plane 2, (f) PINN cut plane 3. Sound intensity magnitude (Wm^{-2}), (g) FEM cut plane 1, (h) FEM cut plane 2, (i) FEM cut plane 3, (j) PINN cut plane 1, (k) PINN cut plane 2, (l) PINN cut plane 3.

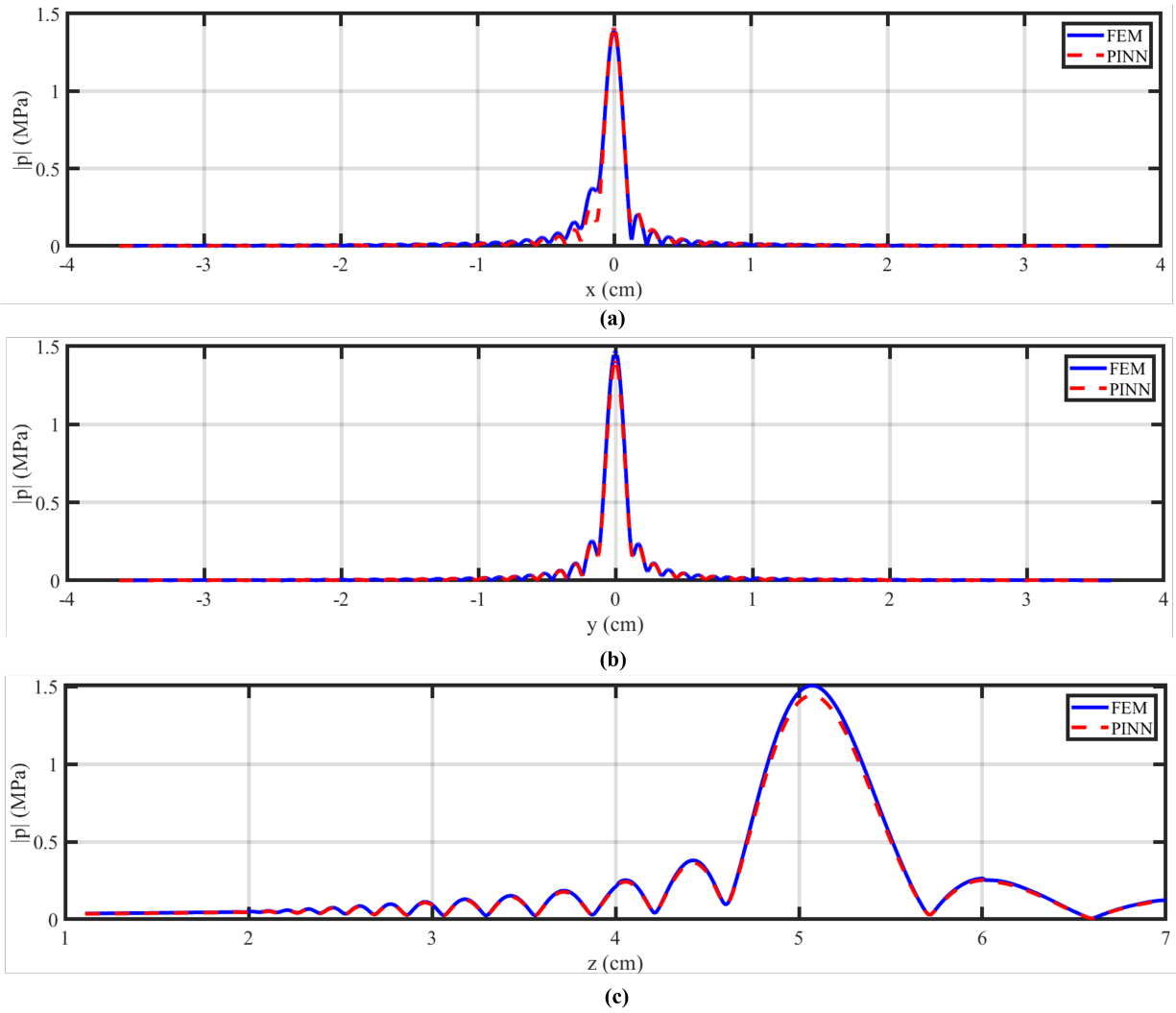


Figure 6.2: Absolute pressure distribution along lines passing through the tumor's center in different directions, (a) x-direction, (b) y-direction, (c) z-direction.

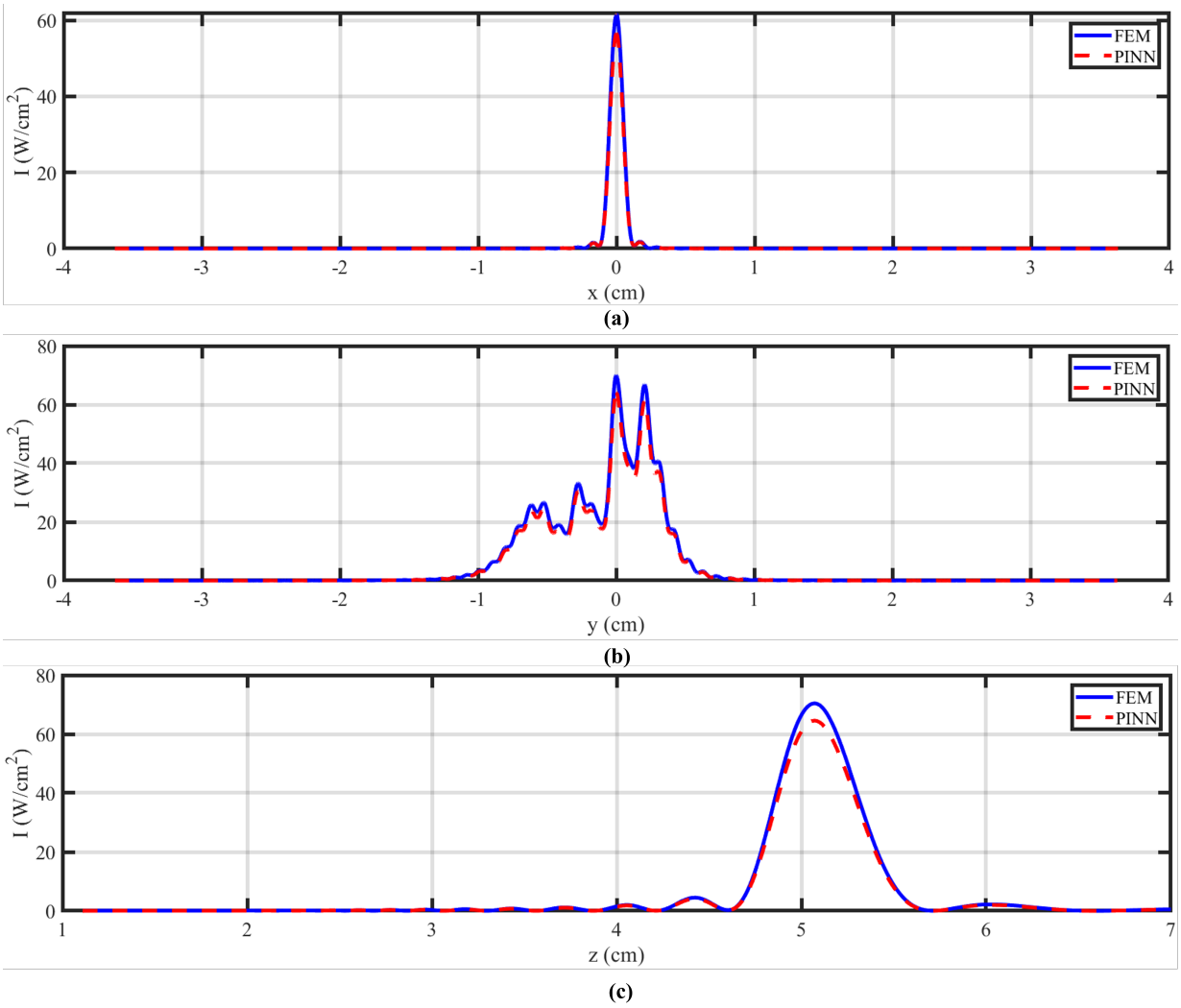


Figure 6.3: Sound intensity magnitude distribution along lines passing through the tumor's center in different directions, (a) x-direction, (b) y-direction, (c) z-direction.

heat generation is a direct result of the concentrated acoustic energy being absorbed by the tissue, which in turn elevates the local temperature. To provide a clearer understanding of the temperature distribution within the tumor, Fig. 6.5 presents detailed temperature plots along lines that pass through the tumor's center in different directions. These plots allow for a precise visualization of how the temperature varies within the tumor, offering insights into the spatial temperature gradients that develop during the exposure.

By comparing the temperature distribution shown in Fig. 6.4 (a to f) with the sound intensity patterns in Fig. 6.1 (g to l), a clear correlation emerges. Specifically, areas with higher sound intensity exhibit a more pronounced temperature increase, confirming the effectiveness of the focused ultrasonic waves in concentrating energy within the desired regions. In the tumor area, this results in a temperature rise to approximately 38.5 °C after just 1 second of exposure. However, it is important to note that this temperature is still below the threshold required for rapid tissue destruction.

For effective thermal ablation, which leads to tissue coagulation or necrosis, the temperature needs to be elevated to between 46 and 56 °C and maintained for a sufficient duration [49]. To achieve this, the ablation time was extended to 10 seconds, and a 10 nm transducer displacement was applied to enhance energy delivery. The Arrhenius kinetic equation (Eq. 3.6) was then used to calculate the extent of tissue necrosis during this extended period. This equation provides a quantitative measure of the thermal damage, allowing for a precise estimation of the necrotized area.

The outcomes of this extended simulation, including the visualization of the necrotized tissue, are presented in the subsequent subsection. These results will offer a comprehensive view of the thermal effects induced by the focused ultrasonic waves, illustrating the potential for achieving effective tumor ablation under the simulated conditions. This analysis is crucial for understanding the parameters required to optimize the procedure for clinical applications.

6.1.3 Distribution of Necrotized Tissue Fraction

Fig. 6.4 (g to l) illustrates the distribution of necrotic tissue after 10 seconds of focused ultrasound exposure, depicting the contour of the necrotic tissue fraction across different cut planes of the breast model. These images reveal that nearly the entire tumor has been effectively eradicated, with some surrounding normal tissue also showing signs of necrosis. The areas exhibiting the maximum necrotic tissue fraction indicate regions of complete tissue necrosis, confirming the efficacy of the focused ultrasonic waves in targeting and ablating the tumor.

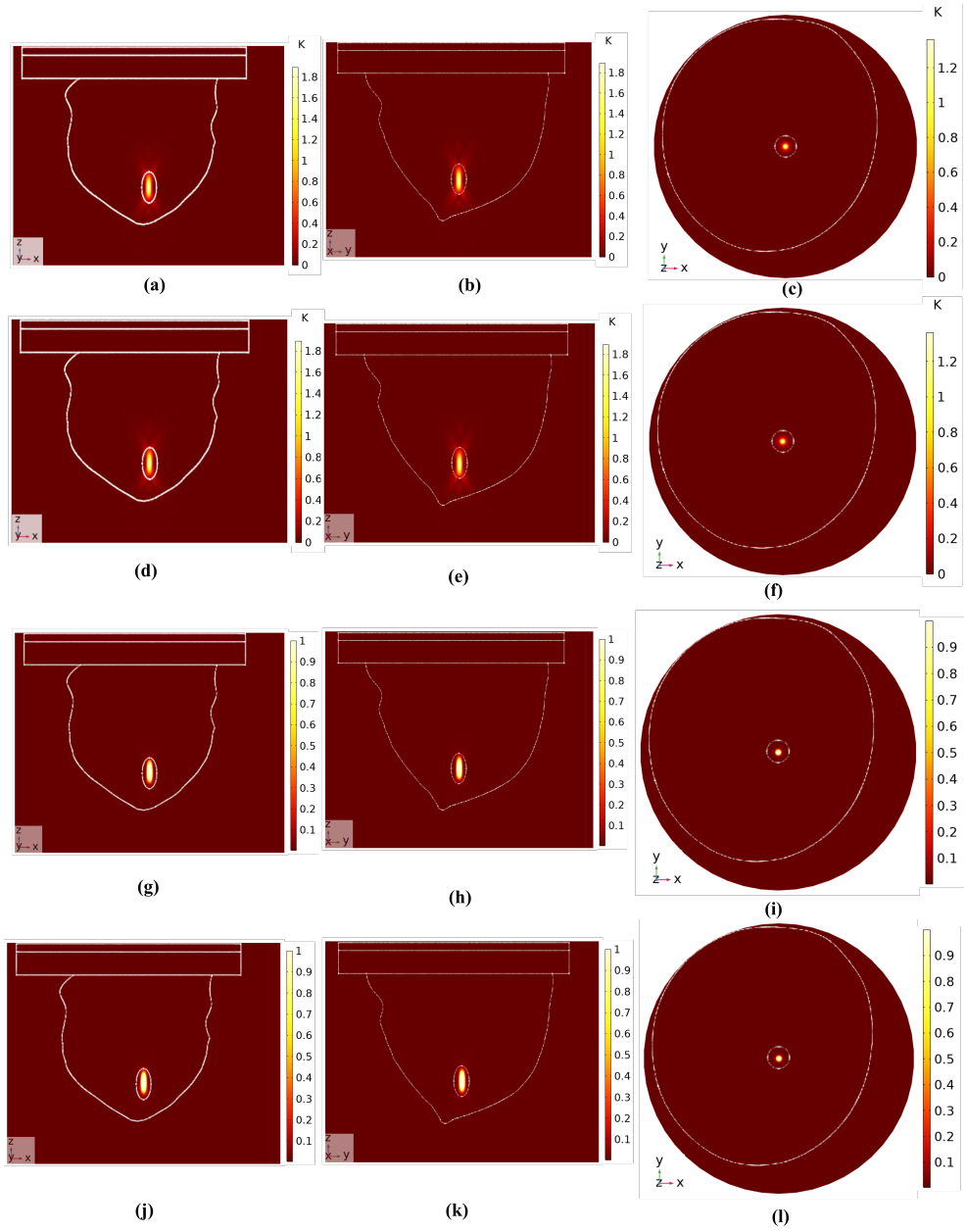


Figure 6.4: Distribution of temperature after 1 second, (a) FEM cut plane 1, (b) FEM cut plane 2, (c) FEM cut plane 3, (d) PINN cut plane 1, (e) PINN cut plane 2, (f) PINN cut plane 3. Distribution of necrotic tissue fraction after 10 s of the ablation process, (g) FEM cut plane 1, (h) FEM cut plane 2, (i) FEM cut plane 3, (j) PINN cut plane 1, (k) PINN cut plane 2, (l) PINN cut plane 3.

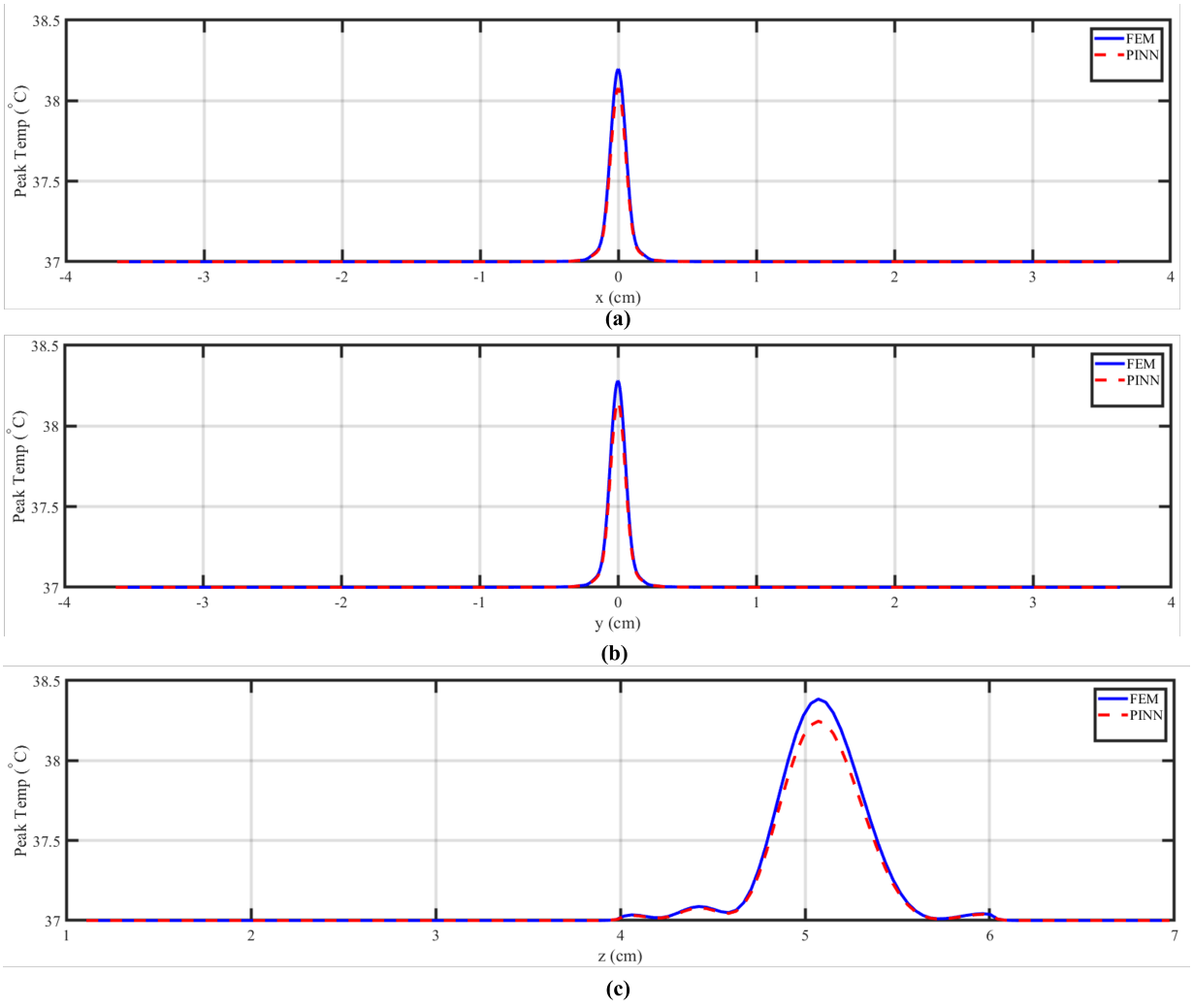


Figure 6.5: Temperature distribution after 1 s along lines passing through the tumpr's center in different directions, (a) x-direction, (b) y-direction, (c) z-direction.

By comparing Fig. 6.4 (g to l) with the temperature distribution shown in Fig. 6.4 (a to f), a clear relationship can be observed between the extent of necrosis and the corresponding temperature increase. Regions that experienced higher temperatures during the initial exposure period are more likely to undergo significant tissue ablation after the 10-second exposure. This correlation underscores the importance of achieving and maintaining adequate thermal thresholds within the targeted area to ensure effective tumor destruction while minimizing damage to surrounding healthy tissue.

To provide further insight into the spatial distribution of tissue necrosis, Fig. 6.6 presents plots showing the necrotic tissue fraction along lines passing through the tumor's center in various x, y, and z directions after 10 seconds of the ablation process. These plots offer a detailed view of how the necrosis extends in different directions within the tissue, reflecting the focused nature of the ultrasonic waves and their ability to selectively ablate the tumor. This detailed analysis is crucial for understanding the effectiveness of the treatment and optimizing the parameters to achieve the desired therapeutic outcomes with minimal side effects.

As shown in Fig. 6.6, the proportion of necrotized tissue at the tumor's center reaches its maximum value of one, indicating complete ablation in that region. However, this proportion decreases as one moves away from the center, revealing that not all areas of the tumor undergo complete necrosis. This gradient suggests that certain peripheral regions of the tumor may remain partially untreated under the current simulation parameters, highlighting the need for further optimization to achieve full tumor ablation.

To enhance the efficacy of the treatment and ensure complete ablation of the tumor, clinicians can consider adjusting several key parameters. One approach is to briefly alter the position of the acoustic pulse generator, which would shift the focal point of the ultrasonic waves and allow for the targeted treatment of different tumor areas. Another method involves increasing the input pulse pressure, which would raise the ablation temperature and potentially lead to more extensive tissue necrosis. Additionally, extending the duration of the acoustic pulse would increase the exposure time, giving the ultrasonic waves more time to elevate the temperature and induce necrosis throughout the tumor.

For tumors that are not fully treated in a single session, multiple FUS ablation sessions could be employed. By targeting untreated or partially treated areas in subsequent sessions, clinicians can progressively ablate the entire tumor while minimizing the risk of damaging surrounding healthy tissue.

To provide a more comprehensive understanding of the ablation process, Fig. 6.7 presents plots of both the temperature and the necrotic tissue fraction at the tumor's center throughout the 100-second ablation process. These plots offer valuable insights into

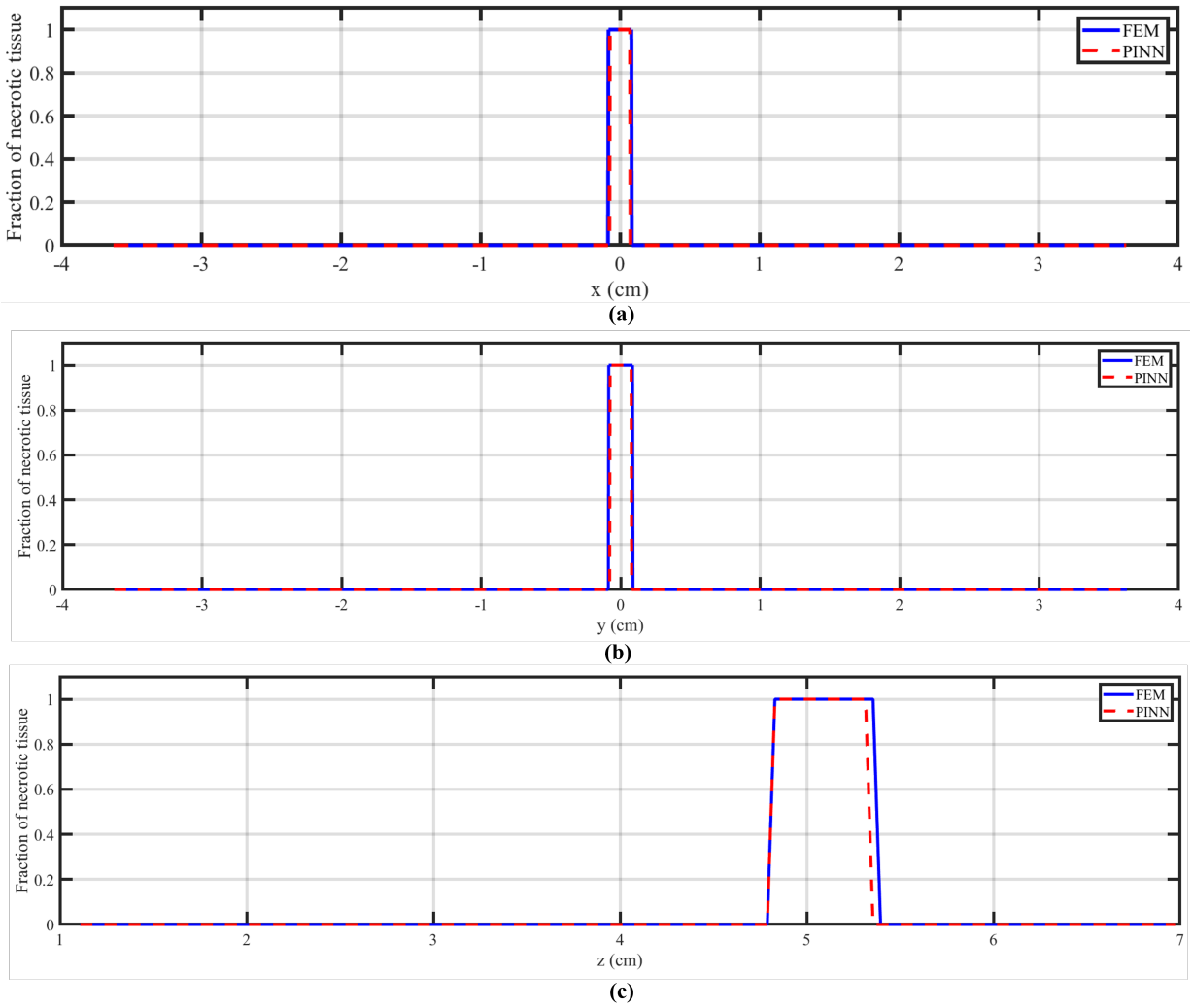


Figure 6.6: Fraction of necrotic tissue after 10 s ablation process along lines passing through tumor's center in different directions, (a) x-direction, (b) y-direction, (c) z-direction.

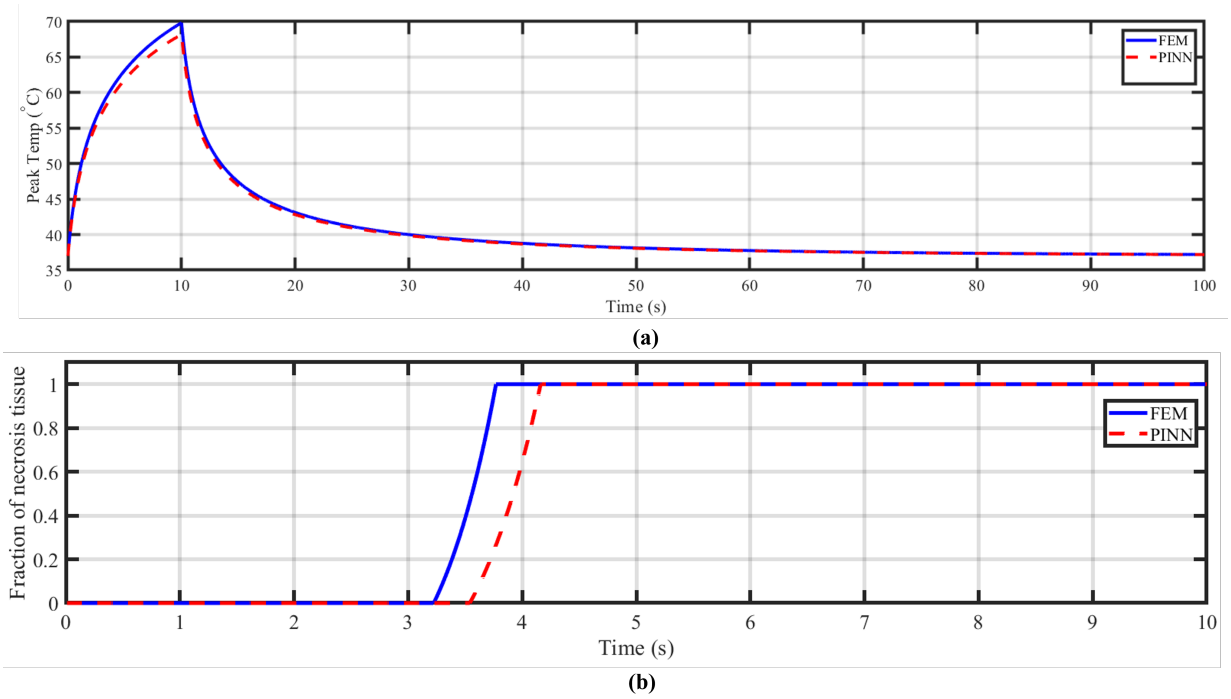


Figure 6.7: Temperature and fraction of necrotic tissue at the tumor's center during ablation time: (a) Temperature change, (b) fraction of necrotic tissue.

the dynamics of temperature rise and tissue necrosis over time, allowing for a detailed evaluation of how different treatment parameters impact the overall effectiveness of the ablation. This information is critical for optimizing the procedure to achieve complete tumor ablation while maintaining the safety and precision required for clinical applications.

As observed in Fig. 6.7a, during the initial 10 seconds of the FUS treatment, the temperature at the center of the tumor undergoes a rapid increase, rising sharply from the baseline of 37 °C to approximately 70 °C. This rapid temperature elevation is a direct result of the intense acoustic energy focused on the tumor, leading to significant heat generation within the targeted area. The high temperature is crucial for inducing thermal ablation, effectively destroying the tumor cells at the center.

Following the cessation of the FUS source, the temperature at the tumor's center begins to gradually decrease, returning to the baseline of 37 °C. This cooling phase is primarily due to the natural heat transfer processes within the body, including conduction and convection, as well as the cooling effect provided by blood perfusion. Blood flow in the

surrounding tissue helps dissipate the accumulated heat, restoring the thermal equilibrium in the treated area.

Conversely, as depicted in Fig. 6.7b, the fraction of necrotic tissue at the tumor's center steadily increases throughout the treatment. Notably, this fraction reaches approximately 1 after just 4 seconds, indicating that nearly 100% of the tumor tissue at the center has been ablated. This suggests that the focused ultrasound treatment is highly effective in achieving complete necrosis at the tumor's core within a relatively short period, making it a powerful tool for precise tumor ablation. The continued rise in necrotic tissue fraction, even as the temperature begins to decrease, highlights the irreversible damage inflicted by the initial thermal spike, ensuring that the tumor cells are effectively destroyed despite the subsequent cooling.

6.1.4 Realistic Clinical Approach

The previously described approach of focusing FUS solely at the tumor's center for 10 seconds, followed by 90 seconds of thermal diffusion, has limitations in achieving complete ablation, particularly for larger tumors. This method, while useful for demonstrating the FUS process and showcasing the capabilities of our deep learning platform, does not align with current clinical practices where more efficient strategies are employed. In real-world clinical settings, the goal is to ensure comprehensive ablation of the entire tumor volume, which requires a more sophisticated approach.

To address this, we now adopt a more realistic clinical methodology that reflects the practices used in modern FUS treatments. In clinical systems, a more effective technique involves rapidly generating multiple lesions across the tumor volume by dynamically adjusting the transducer focus. This approach not only enhances the coverage of the tumor but also mitigates uncertainties related to thermal diffusion and the heat sink effect caused by blood perfusion, which can reduce the efficacy of the treatment if not properly managed.

In this study, we applied a FUS therapy protocol designed to create three faster lesions: one at the tumor's center and two additional lesions 3 mm away on the right and left sides along the x-axis. The transducer was strategically moved, and its focal point was adjusted to target each location. FUS waves were generated for 6 seconds at each focal point, with 5-second intervals allocated for repositioning the transducer. This sequential treatment strategy ensures that different parts of the tumor are exposed to the therapeutic ultrasound, increasing the likelihood of complete tumor ablation.

After treating the tumor from these three focal points, the simulation continued without any further acoustic energy input until reaching a total time of 100 seconds. This extended

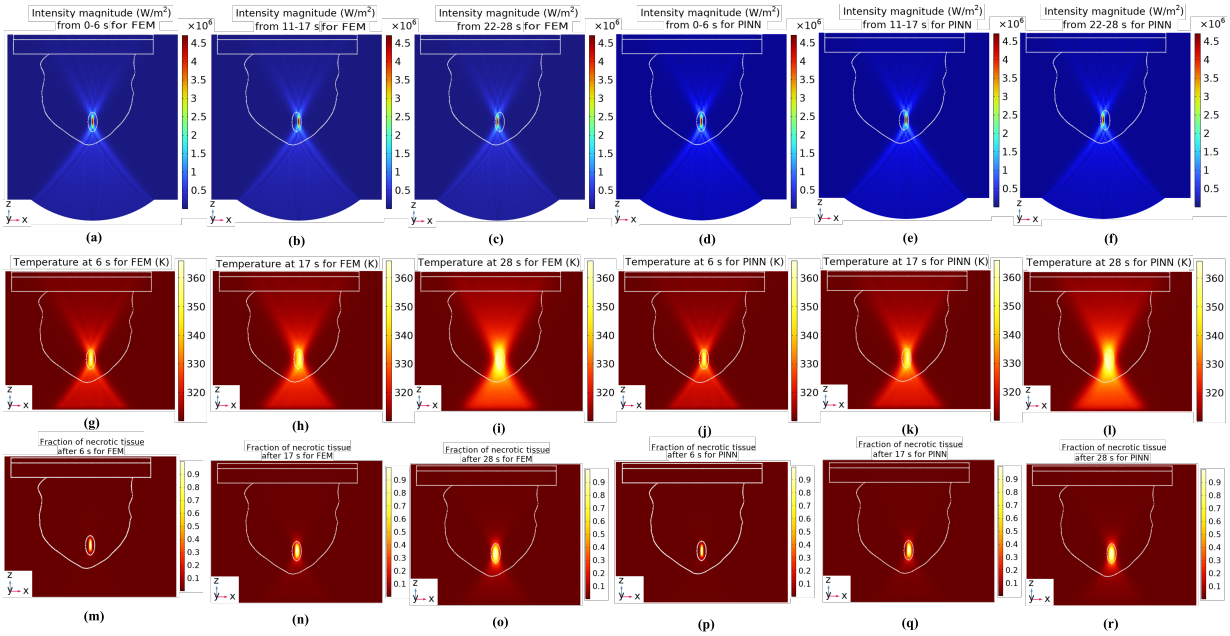


Figure 6.8: (a-f) sound intensity magnitude in the cut plane 1 during each of the three lesion processes for FEM and PINN, (g-l) temperature distribution in the cut plane at the end of each lesson process for FEM and PINN, (m-r) fraction of necrotic tissue distribution in the cut plane 1 at the end of each lesion process for FEM and PINN.

period allowed us to observe the effects of thermal diffusion and the cooling influence of blood perfusion, providing a comprehensive understanding of the FUS ablation outcomes. The results from this approach demonstrate how our platform can predict and optimize FUS treatment outcomes in actual clinical settings, offering a valuable tool for enhancing the precision and efficacy of tumor ablation therapies.

The diagram in Fig. 6.8 (a to c) illustrates the distribution of sound intensity magnitude within the cut plane 1 for the FEM during the three distinct lesion processes, occurring between 0-6, 11-17, and 22-28 seconds. Correspondingly, Fig. 6.8 (d to f) shows the same distribution for the PINN model, with the x-z surface passing through the tumor's midpoint for each lesion. These images provide a comparative view of how sound intensity is concentrated within the tumor across the different focal points during each stage of the treatment.

Additionally, Fig. 6.8 (g to r) presents the resulting distribution of temperature and

the fraction of necrotic tissue at the conclusion of each lesion process within cut plane 1, again for both FEM and PINN models. These visualizations are shown at 6, 17, and 28 seconds for the first, second, and third lesions, respectively. The comparison highlights how each method models the thermal and necrotic outcomes of the treatment, providing insights into their effectiveness and accuracy.

The three distinct focal points in these processes generate a significant sound intensity magnitude of approximately 4.5E+6 Wm^{-2}, which is a critical factor in inducing the desired thermal effects within the tumor tissue. The intense focus of acoustic energy leads to temperature increases of approximately 63, 65, and 64 °C at different points within the tumor during the respective lesion processes. These elevated temperatures are sufficient to cause significant tissue necrosis, contributing to a more uniform ablation of the tumor tissue.

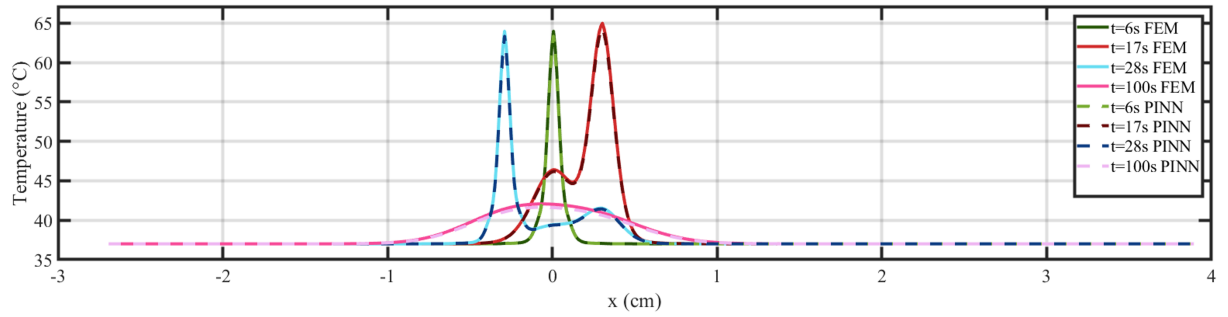
By achieving these consistent temperature increases at multiple focal points, this approach ensures a more comprehensive and uniform necrosis across the entire tumor, thereby enhancing the effectiveness of the FUS treatment. The results depicted in Fig. 6.8 demonstrate how both FEM and PINN can be utilized to predict and analyze the outcomes of such treatments, with each model offering valuable insights into the distribution of sound intensity, temperature, and tissue necrosis during the ablation process.

The figure demonstrates that after 28 seconds of FUS therapy, the fraction of necrotic tissue reaches 1 in nearly all regions of the tumor, indicating complete ablation. To gain a deeper understanding of these results and to assess the effectiveness of this clinically realistic approach, we have plotted the temperature and necrotic tissue fraction along a line passing through the tumor's center in the x direction (Fig. 6.9) at various time points during the ablation process, including the conclusion of each lesion process and the entire therapy.

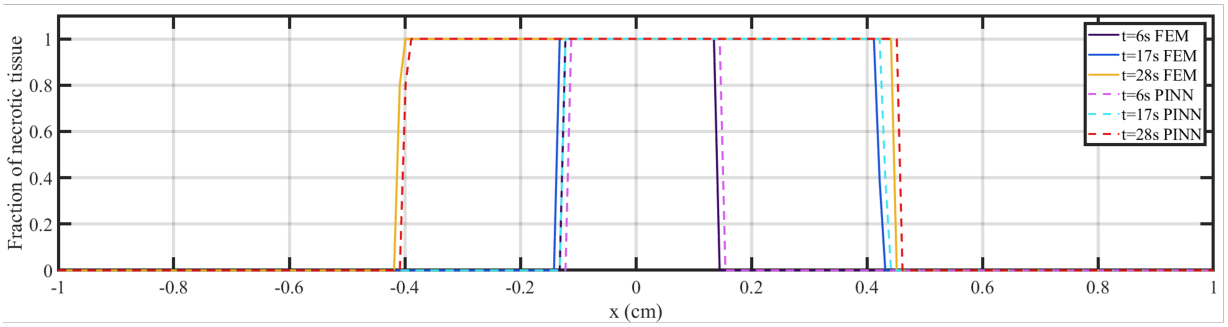
Fig. 6.9a illustrates the temperature increase at different points within the tumor—specifically at the center, right, and left sides. This plot reveals a more evenly distributed high-temperature pattern throughout the tumor, resulting from the sequential targeting of multiple focal points. The distribution of heat across the tumor is more uniform compared to earlier methods, where temperature gradients were more pronounced.

When comparing the necrotic tissue fraction in Fig. 6.9b with the earlier results shown in Fig. 6.6a, it becomes evident that this improved approach achieves a fraction of necrotic tissue reaching 1 across almost the entire tumor, including the edges. This is in stark contrast to the previous method, where the necrotic tissue fraction did not reach 1 at the tumor's periphery, leaving some areas incompletely ablated.

The success of this new approach highlights its effectiveness in uniformly and completely



(a)



(b)

Figure 6.9: Temperature and the fraction of necrotic tissue after 6 s, 17 s, 28 s, and 100 s along the line passing through the tumor's center in the x direction.

eradicating tumor tissues. By strategically adjusting the focal points and optimizing the treatment duration at each point, this method ensures a more comprehensive ablation, reducing the likelihood of residual tumor cells that could lead to recurrence. These results demonstrate the potential of this approach to significantly enhance the outcomes of FUS therapy in clinical settings, offering a more reliable and thorough treatment option for patients.

Increasing the number of lesion points across different parts of the tumor leads to more favorable outcomes without the need for extended lesion durations, which is consistent with current clinical practices. This approach allows for more comprehensive and efficient tumor ablation by targeting multiple areas within the tumor, ensuring that the entire volume is treated effectively.

The deep learning platform we have developed is capable of simulating a wide range of FUS ablation processes, accommodating variations in the number of lesions, their durations, locations, and the acoustic settings applied. This flexibility makes the platform an invaluable tool for predicting diverse FUS therapy outcomes and selecting the most efficient and effective procedure tailored to the specific size and location of the tumor. By enabling clinicians to simulate and compare different treatment strategies, the platform helps in optimizing FUS therapy, enhancing its precision and success rates.

Moreover, the use of 3D simulations within this platform provides significantly more accurate and realistic outcomes compared to traditional 2D simulations. The inclusion of three spatial dimensions allows for a more detailed representation of the tumor and surrounding tissues, capturing the complexities of sound wave propagation and thermal effects in a more lifelike manner. This leads to higher sound attenuation and a more pronounced temperature increase within the tissue, which are critical factors in achieving effective tumor ablation. As a result, 3D simulations offer a deeper understanding of the treatment dynamics and are crucial for planning and executing successful FUS therapies in clinical practice.

The augmented temperature increase observed in our simulation, especially when compared to the results of Montienthong & Rattanadecho's study [114], underscores the significant advantages of utilizing 3D simulations in FUS therapy. While our study demonstrates a temperature rise to approximately 64-65 °C (as shown in Fig. 6.9a), their research achieved a lower temperature increase, reaching only 50-51 °C despite employing the same acoustic frequency and similar focal lengths (refer to Figs. 14 and 15 in their paper). This discrepancy highlights the superior accuracy of 3D simulations, which are capable of capturing the complex and realistic geometry of the breast model, including asymmetric details that profoundly influence acoustic wave propagation and heat transfer.

The use of 3D simulations allows for a more precise representation of these complexities, leading to more accurate and clinically relevant results than what can be achieved with 2D axisymmetric models. The inclusion of asymmetric anatomical features in the simulation contributes to a more accurate prediction of temperature distribution and tissue necrosis, which are crucial for optimizing FUS therapy outcomes.

Furthermore, the PINN model's ability to generalize across different tumor types and breast anatomies is pivotal for its clinical applicability. While our study effectively demonstrates the model's capabilities for a specific anatomy and tumor type, extending its application to a broader range of scenarios requires careful consideration. To generalize effectively, it is necessary to define new anatomical geometries and FUS specifications that accurately reflect the diversity of patient anatomies and tumor characteristics encountered in clinical practice.

The training dataset used in our study was based on specific configurations of an anatomical phantom, designed to capture particular scenarios involving acoustic pressure, sound intensity, and temperature distributions. However, this dataset does not encompass the full spectrum of breast anatomies and tumor types, which means the model may not perform optimally for cases that differ significantly from those represented in the training data. As a result, applying the model to diverse clinical scenarios will require precise input configurations tailored to the specific anatomy and tumor characteristics of each patient.

To achieve accurate FUS treatment predictions across a wide range of clinical cases, future work should focus on expanding the training dataset to include a broader variety of anatomical geometries and tumor types. This will enhance the model's ability to generalize and improve its performance in predicting FUS outcomes for patients with different breast anatomies and tumor characteristics. By refining the model and its training data, we can move closer to realizing the full potential of FUS therapy in personalized cancer treatment.

When scaling the PINN approach to more complex anatomical structures, several challenges emerge, primarily related to increased model complexity and heightened computational demands. However, the inherent modularity of PINNs makes them particularly well-suited for managing such complexity, enabling the model to be adapted to handle detailed and intricate anatomical features.

One effective strategy for managing this complexity is hierarchical modeling. In this approach, the anatomical structure is divided into smaller, more manageable subdomains. Each subdomain can be independently modeled using the PINN framework, allowing for focused and efficient computation within each region. This modular approach not only simplifies the modeling process but also facilitates parallel computation, thereby reducing the overall computational load.

Once the individual subdomains are modeled, the results can be integrated to create a comprehensive model of the entire anatomical structure. This integration process involves ensuring continuity and consistency across the boundaries of the subdomains, which is critical for maintaining the accuracy and reliability of the overall model. Hierarchical modeling is particularly advantageous in complex anatomical regions, where different areas may require varying levels of detail and computational focus.

To further enhance the efficiency and accuracy of the PINN approach, adaptive mesh refinement (AMR) techniques can be employed. AMR allows for the dynamic allocation of computational resources, concentrating them on regions with high complexity or significant changes, such as tumor boundaries or areas with steep temperature gradients. By refining the mesh in these critical regions, the model can capture finer details and more accurately simulate physical processes like acoustic wave propagation and heat transfer.

The use of AMR ensures that computational resources are utilized where they are most needed, enabling more detailed modeling in critical areas without overwhelming the overall computational capacity. This approach is particularly useful in FUS therapy, where precise modeling of temperature distribution and tissue necrosis is essential for optimizing treatment outcomes.

In summary, while scaling the PINN approach to more complex anatomical structures presents challenges, the modular and adaptable nature of PINNs, combined with hierarchical modeling and adaptive mesh refinement techniques, provides a robust framework for managing this complexity. These strategies allow for the detailed and accurate simulation of complex anatomical features, making PINNs a powerful tool for advanced medical modeling and simulation in clinical settings.

6.1.5 Validation and Computational Efficiency

To assess the accuracy and reliability of the PINN model, the predicted temperature distributions were compared with results obtained from the FEM. The comparison was quantitatively evaluated using several validation metrics, including Mean Squared Error (MSE), Root Mean Squared Error (RMSE), Mean Absolute Error (MAE), and correlation coefficients.

The summarized results are presented in Tables 6.1, which showcase the validation metrics for the PINN model against the FEM results. The data reveals that the PINN model's predictions are in close agreement with the FEM results. The low values of MSE, RMSE, and MAE demonstrate the high accuracy of the PINN model in predicting temperature distributions within the simulated environment. These metrics indicate that the

Table 6.1: Validation Metrics for Comparison with FEM Results.

Metric	Value for FEM
MSE	0.0025
RMSE	0.05
MAE	0.03
Correlation Coefficient	0.98

Table 6.2: Computational Time and Resource Usage Comparison.

Method	Computational Time (hours)	Memory Usage (GB)
PINN Model	5	8
FEM Simulation	115	16

errors between the predicted values and the FEM reference values are minimal, reflecting the model's precision.

Furthermore, the high correlation coefficients suggest a strong linear relationship between the predicted temperatures from the PINN model and the reference temperatures from the FEM simulations. This strong correlation further confirms the reliability of the PINN model, indicating that it can effectively replicate the results of more traditional and well-established FEM simulations.

Overall, the validation metrics presented in Tables 6.1 provide robust evidence of the PINN model's accuracy and reliability in predicting temperature distributions. This close match with FEM results not only validates the PINN approach but also highlights its potential as a powerful tool for simulating complex physical processes in medical applications, such as FUS therapy.

One of the key advantages of the PINN model is its remarkable computational efficiency compared to conventional FEM techniques. A detailed comparison of computational time and resource usage between the PINN model and FEM simulations, as presented in Table 6.2, highlights this significant benefit.

The results show that the PINN model drastically reduces both computational time and memory usage. Specifically, the PINN model completed the simulations in just 5 hours, while the FEM simulations required approximately 115 hours to achieve similar results. This reduction in computational time by the PINN model represents a substantial improvement in efficiency, allowing for quicker turnaround times in simulations.

In addition to time savings, the PINN model also demonstrates more efficient use of computational resources. The model used only 8 GB of memory, compared to the 16 GB

required for FEM simulations. This halving of memory usage further emphasizes the resource efficiency of the PINN model, making it not only faster but also less demanding on hardware.

These substantial differences in computational time and memory usage underscore the efficiency of the PINN model, particularly in the context of clinical applications where timely results are crucial. In scenarios such as FUS ablation, where treatment planning and real-time decision-making are vital, the ability to quickly and accurately simulate outcomes can significantly enhance the effectiveness of the therapy.

By leveraging its computational efficiency, the PINN model enables rapid and precise simulations of FUS ablation processes, making it an invaluable tool for treatment planning and optimization. The ability to conduct fast and resource-efficient simulations allows clinicians to explore various treatment scenarios, optimize parameters, and make informed decisions more quickly, ultimately improving patient outcomes and the overall efficiency of clinical workflows.

6.1.6 Uncertainty Quantification

Uncertainty quantification (UQ) is critical for validating and ensuring the robustness of predictive models, particularly in clinical applications where accurate and reliable predictions are essential. In this study, we addressed uncertainties in both model parameters and input data to enhance the reliability of the PINN predictions.

Key parameters such as tissue properties— including thermal conductivity, specific heat capacity, and blood perfusion rates—along with variations in input data like FUS wave intensity and focal point, can have a significant impact on model predictions. To account for these uncertainties, we employed Monte Carlo simulations, running multiple simulations with parameters sampled from their respective probability distributions. This approach allowed us to capture the variability in the predicted outcomes and to provide statistical measures such as mean, variance, and confidence intervals for key predicted quantities like temperature distribution and necrotic tissue fraction.

The Monte Carlo simulations enabled us to assess the range of possible outcomes under different scenarios, offering a more comprehensive understanding of the potential variability in clinical results. These statistical measures are invaluable for clinicians as they provide a quantifiable assessment of the reliability and robustness of the predictions made by the PINN model.

In addition to Monte Carlo simulations, sensitivity analysis was performed to identify the parameters that most significantly affect the model outputs. This analysis, summarized

Table 6.3: Sensitivity Analysis Results.

Parameter	Range	% Change in Maximum Temperature	% Change in Necrotic Tissue Fraction
Thermal Conductivity	0.4 - 0.6 W/m·K	±5%	±3%
Specific Heat Capacity	3500 - 4000 J/kg·K	±4%	±2%
Blood Perfusion Rate	0.001 - 0.005 s^{-1}	±7%	±5%
Initial Tumor Temperature	36.5°C - 37.5°C	±2%	±1%
FUS Power	30 - 50 W	±10%	±8%

Table 6.4: Uncertainty Quantification Results.

Quantity	Mean	Standard Deviation	95% Confidence Interval
Maximum Temperature (°C)	70.0	2.5	[65.2, 74.8]
Necrotic Tissue Fraction (%)	90.0	5.0	[80.2, 99.8]

in Table 6.3, involved varying one parameter at a time while holding all others constant to determine its individual impact on predicted temperature distribution and necrotic tissue fraction. The sensitivity analysis revealed which parameters have the greatest influence on the outcomes, guiding future efforts to refine and improve model accuracy by focusing on these critical factors.

Furthermore, Bayesian methods were utilized to update the probability distributions of the model parameters based on prior knowledge and observed data. By incorporating prior uncertainties and refining these distributions with new data, the Bayesian approach enhances the model's predictive accuracy. This method allows for the systematic integration of prior information and real-time observations, leading to more informed and reliable predictions.

Overall, the combination of uncertainty quantification techniques—Monte Carlo simulations, sensitivity analysis, and Bayesian updating—provides a robust framework for validating the PINN model in clinical applications. These methods ensure that the model can reliably predict outcomes under varying conditions, making it a powerful tool for clinical decision-making and treatment planning in focused ultrasound therapies.

The UQ results are presented in Table 6.4, which includes the mean and standard deviation of key predicted quantities, along with their corresponding 95% confidence intervals. These results provide a detailed statistical assessment of the model's predictions, reflecting how uncertainties in model parameters and input data influence the outputs.

The mean values indicate the expected outcomes, while the standard deviations show the extent of variability around these means due to the uncertainties considered in the analysis. The 95% confidence intervals offer a range within which the true values are likely to fall, giving a sense of the precision and reliability of the model's predictions.

Notably, the narrow confidence intervals reported in Table 6.4 suggest that the PINN model predictions are relatively insensitive to the variations in the parameters. This insensitivity implies that, even when accounting for uncertainties in tissue properties, blood perfusion rates, FUS wave intensity, and focus, the model consistently produces accurate and reliable predictions. This robustness is crucial for clinical applications, where consistent and dependable results are necessary for effective treatment planning and patient care.

The narrow confidence intervals and low variability further enhance confidence in the PINN model's clinical applicability, indicating that it can reliably predict outcomes under a range of conditions and parameter variations. This makes the PINN model a valuable tool for clinicians, providing a strong foundation for making informed decisions in the context of focused ultrasound therapy.

6.2 Pathway Scanning

The experiments conducted in this study are designed to achieve three primary objectives. First, they aim to confirm the hypothesis that AI can effectively create appropriate HIFU treatment plans. This involves evaluating the AI's ability to generate precise and reliable treatment protocols that meet clinical standards. Second, the experiments seek to develop suitable fitness functions for the algorithm, which are critical for optimizing the AI's performance. These fitness functions serve as the criteria by which the AI evaluates and refines its treatment plans, ensuring that the generated plans are not only effective but also efficient and tailored to individual patient needs. Third, the study assesses the AI's computational complexity, examining how resource-intensive the process is in terms of time and computational power. Understanding the computational demands is crucial for determining the feasibility of implementing such AI-driven methods in real-time clinical settings.

The study was conducted in real-world settings, providing a practical evaluation of the proposed method. This included the use of material properties, transducer parameters, and simulation parameters that were generated using actual patient data, a real-world HIFU transducer, and advanced numerical analysis techniques. By leveraging real-world data and equipment, the study ensures that the findings are directly applicable to clinical practice, enhancing the potential for AI-driven HIFU treatment planning to be adopted in medical settings.

6.2.1 Computational Results

This section evaluates the AI's capability to devise an effective treatment plan tailored for a specific patient. The primary focus is on the AI's ability to generate a treatment plan that is both effective and precise. The optimal solution, as defined in this study, ensures that the entire targeted region is treated while sparing normal tissue from any adverse effects. This is achieved when the fitness value of the solution equals zero, indicating that the treatment plan has met all criteria for effectiveness and safety.

The proposed algorithm's performance is illustrated in Fig. 6.10, which shows the treatment plan for each epoch of the AI-based algorithm during the simulation. The boundary of the target area, derived from MR image processing, is highlighted with a red line. The treated area, where the CEM value exceeds 240, is shown in blue, while the affected area, with CEM values between 80 and 240, is depicted in yellow. As the treatment progresses, the plan expands to ensure that the entire tumor is covered completely. The algorithm ultimately suggests 13 consecutive sonications, resulting in a more uniform thermal field than methods that apply the same HIFU energy across all treatment locations [187].

As anticipated, the algorithm iteratively adjusts the treatment plan to achieve uniform coverage of the tumor. The shapes of the lesions change dynamically to satisfy the two critical fitness functions: (1) avoiding damage to areas outside the tumor, and (2) ensuring complete tumor coverage with minimal treatment time. As the treatment sites become closer, the influence of heat from surrounding lesions on the current target causes rapid changes in lesion size during the final stages. This leads to lesion coalescence, ensuring that the final solution is seamless, with no gaps in coverage.

Moreover, the iterative approach employed by the algorithm minimizes the risk of excessive lesion coalescence while promoting uniform lesion generation with the fewest sonication sessions. This method also offers the advantage of low computational overhead, making it feasible for use in pre-treatment planning. Consequently, the optimal presurgical strategy proposed by this approach will undergo further testing *in vitro*, providing a robust foundation for its potential application in clinical settings.

The first finding of this study indicates that the quality of the AI-generated treatment plan improves as the number of sonications increases. Specifically, as the AI is able to utilize a greater number of sonications, the precision of coverage control is enhanced, allowing for more accurate targeting of the tumor. This increased precision is achieved by employing shorter or smaller sonication sessions, which contribute to a more refined treatment plan.

However, this improvement in treatment quality comes with a trade-off. As the number of sonications increases, the overall length of the therapy also extends. This prolonged

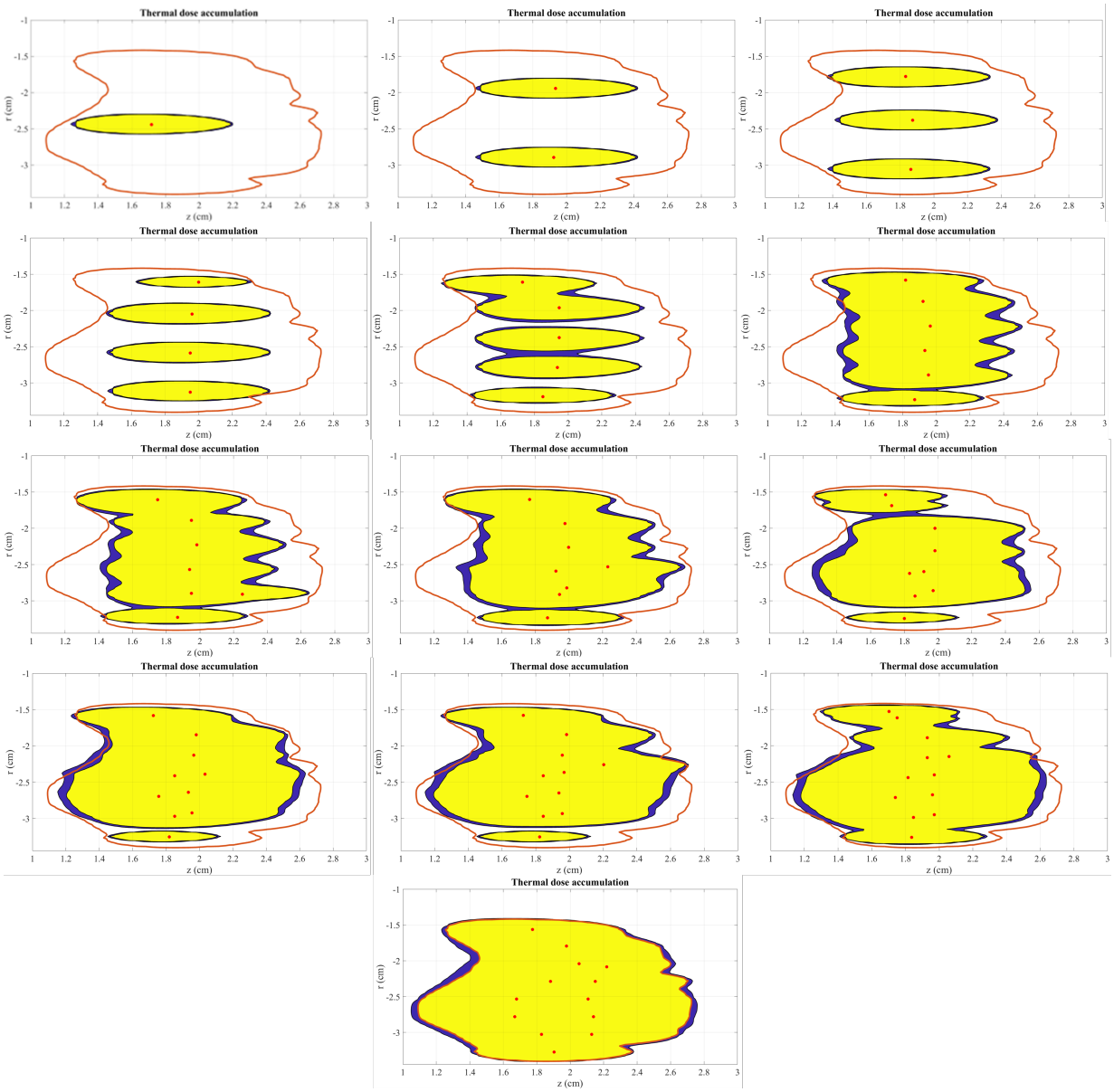


Figure 6.10: The process that AI finds the best presurgical plan for a desired tumor.

duration can present challenges for both the patient and the computational process. For the patient, a longer treatment time may result in discomfort or difficulty in maintaining the necessary position throughout the procedure. For the AI, an extended treatment plan requires more iterations of the ANN, which increases the computational complexity and time required to evaluate and optimize the plan. Therefore, while a higher number of sonications can lead to better treatment outcomes, it also necessitates careful consideration of the balance between treatment quality and the practical limitations of therapy duration and computational demands.

In the majority of its runs, the AI successfully develops appropriate treatment plans, provided that the minimum number of sonications is not overly restrictive. As the number of sonications (N) increases, the algorithm evaluates the trade-off between the quality of the treatment plan and the number of sonications required. This iterative process continues until the algorithm ensures that the entire tumor is adequately covered. By progressively increasing the number of sonications, the AI optimizes the treatment plan to achieve complete tumor coverage while balancing the investment in terms of sonication sessions. This approach allows the AI to refine the treatment plan, improving its effectiveness without unnecessarily prolonging the therapy.

The heat source was configured using the nominal parameters of the H101 Sonic transducer and a single-element transducer. With a radius of curvature of 51.74 mm and an aperture diameter of 64 mm, combined with a frequency of 1 MHz, the resulting concentrated beam has an elliptical size of approximately 10 $\times$ 1.4 mm. The spatial peak of the heat deposition rate, or spatial peak intensity, was set at 1000 W/cm^2, a value that is closely aligned with those used in clinical treatments. This setup ensures that the heat source is appropriately focused and powerful enough to achieve the desired therapeutic effects while adhering to clinically relevant parameters (Eq. 3.5).

According to numerical convergence tests, the parameters of the numerical thermal model were set as follows:

- Discretized simulation domain size 810×668 grid points, periodic boundary condition.
- Spatial resolution 0.05 mm.
- Temporal resolution 0.01 s.
- The total length of the simulation $\sum_{i=0}^{N}(t_{h,i} + t_{c,i})$.
- Allowed positions of the ultrasound focus center limited to the bounding box at grid positions.

- Maximum sonication and cooling periods $t_h = [1, 3s]$, $t_c = [0, 2s]$.
- Number of sonications considered $N \in \{1, 2, \ldots, \infty\}$.

The chosen sonication and cooling periods for the HIFU treatment were determined based on a combination of experimental setups, simulation results, and clinical considerations. These parameters were carefully selected to ensure effective and safe treatment while minimizing the total treatment time. In HIFU treatments, managing the temperature of both the targeted tissue and surrounding healthy tissues is crucial, with cooling playing an essential role in this process.

In the simulation, a uniform cooling condition was assumed across the entire tissue area, which simplifies the modeling process by providing consistent and controlled cooling. This uniform approach ensures that heat is dissipated evenly, preventing the formation of hot spots. However, in actual clinical practice, cooling is typically applied specifically to the propagation path of the HIFU beam using methods such as water bags, cooling pads, or other localized cooling devices. To more accurately reflect clinical conditions, boundary conditions in the simulations can be set to maintain a constant temperature at the edges of the tissue, simulating the effect of a water bath or other cooling medium.

While the initial settings for the heating (t_h) and cooling (t_c) periods are within specified ranges, the NN-based optimization process introduces flexibility. Depending on the shape and size of the planned treatment area, as well as the physician's recommendations, the heating and cooling time ranges can be adjusted to higher upper bounds. This flexibility allows for the optimization of overall treatment efficacy and duration, ensuring that the treatment is both effective and efficient.

In this section, the four treatment plans are visualized (Figs. 6.11, 6.12, 6.13, and 6.14). Each plot in these figures represents a single sonication layer in the sequential treatment plan. The yellow spots on the lesion maps indicate areas where the CEM_{43} have exceeded 240 minutes, signifying effective treatment. The blue areas represent regions that have not yet been adequately treated, where the temperature rise is minimal ($80 < CEM_{43} < 240$).

The first figure for each tumor displays the target area where the algorithm attempts to find an optimal treatment plan. The second figure in each sequence shows the actual treatment area following the first layer of sonication, including the cooling period. This image illustrates that some energy from the earlier layers has not yet dissipated, allowing the subsequent sonication layers to build upon this residual energy, effectively elevating the treated region.

The final figure for each patient demonstrates that the entire target area is eventually covered. Throughout this process, the algorithm continuously monitors the potential for

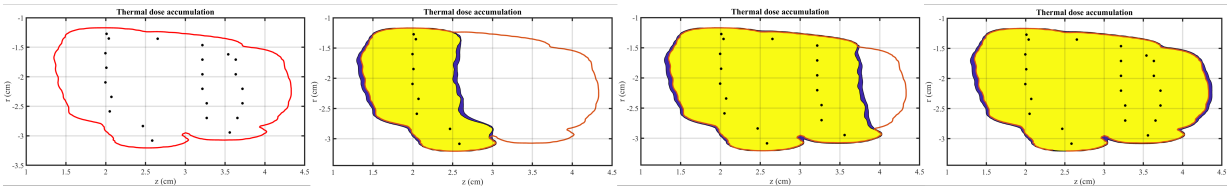


Figure 6.11: Presurgical plan for patient 1.

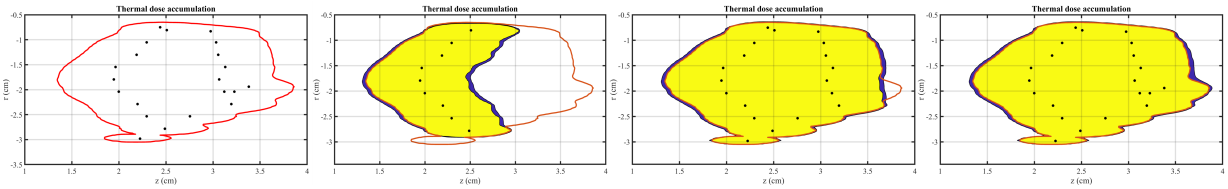


Figure 6.12: Presurgical plan for patient 2.

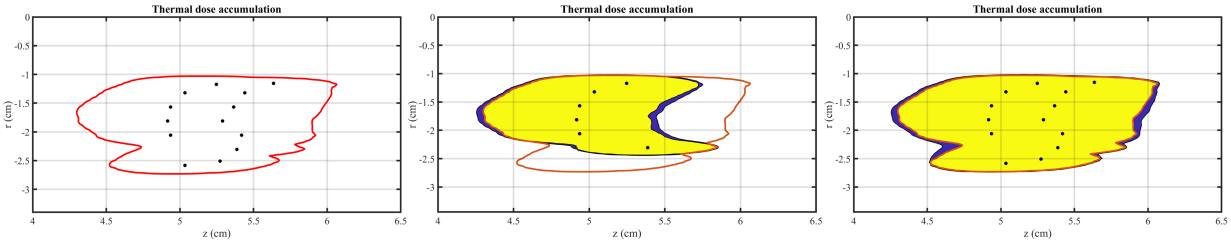


Figure 6.13: Presurgical plan for patient 3.

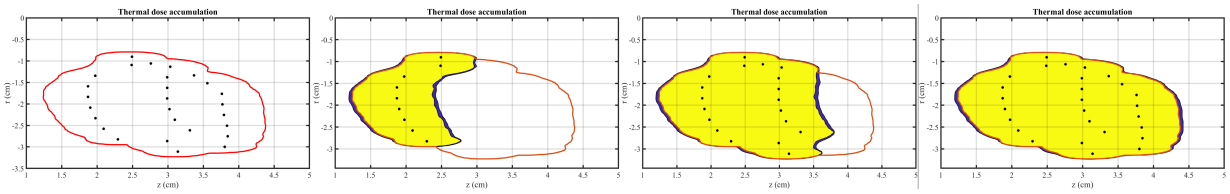


Figure 6.14: Presurgical plan for patient 4.

overheating normal tissue. If the cumulative temperature in any prohibited area begins to rise too quickly, the solution procedure is adjusted to implement a less harmful approach. This ensures that the treatment remains safe and effective.

Over the course of the treatment, the non-treated areas, which indicate regions where treatment failed due to insufficient energy deposition, gradually decrease. By the end of the treatment, no mistreated areas, which denote regions where prohibited zones were harmed, remain. This indicates that the treatment was successful in targeting the tumor while minimizing damage to surrounding healthy tissue.

The fitness value evaluates the quality of the treatment plan by incorporating a combination of two key metrics (see Eqs. 4.2 and 4.3), which are essential for determining the overall effectiveness and precision of the procedure. Table 6.5 provides a detailed breakdown of the treatment parameters used at each sonication session across all four patients involved in the study. For each patient, the first two columns specify the coordinates that define the focal point's location, which in turn determines the exact placement of the transducer to ensure optimal targeting of the area of interest. The remaining two columns provide recommendations for both the heating and cooling durations, which are crucial for managing the thermal effects during and after each sonication. This table can be a valuable resource for HIFU therapists, as it can be used not only to inform their clinical decisions but also to assist in evaluating and refining their presurgical treatment plans to enhance patient outcomes.

The number of sonications and the total treatment time can vary significantly between patients due to several contributing factors, including tumor size, shape, and location. In this study, as shown in Table 6.5, Patient 3 required fewer sonications compared to Patient 4, who needed a higher number of sonications. This discrepancy can be attributed to the differences in tumor characteristics. Patient 3 had a smaller, more regularly shaped tumor, which allowed for fewer sonications to achieve complete ablation. Tumors with regular shapes, such as spheres or ellipsoids, are more geometrically simple and symmetrical, enabling efficient coverage with fewer sonications, as each sonication can target a larger portion of the tumor volume.

In contrast, Patient 4 had an irregularly shaped tumor, which presented more complexity due to its asymmetrical and intricate geometry, including protrusions and indentations. Such irregularities require additional sonications to ensure thorough and uniform coverage of the entire tumor. The increased number of sonications is necessary to address the additional complexity and to ensure that all regions of the tumor are effectively treated.

To highlight the efficiency and accuracy of our proposed method, a comparative analysis was performed between our previous method, which relied solely on an optimization

Table 6.5: Treatment parameters calculated by the proposed algorithm for each patient.

Number of sonication	Patient 1				Patient 2				Patient 3				Patient 4			
	z (cm)	r (cm)	$t_h(s)$	t_c (s)	z (cm)	r (cm)	$t_h(s)$	t_c (s)	z (cm)	r (cm)	$t_h(s)$	t_c (s)	z (cm)	r (cm)	$t_h(s)$	t_c (s)
1	2.99	1.88	2.9	0.2	1.87	1.84	2.2	1	3.1	2.37	2.7	0.8	2.3	2.83	2.6	0.4
2	2.99	1.63	2.9	1.2	1.87	1.59	2.4	0.2	3.02	2.12	2.9	1.5	2.09	2.58	2.6	1.1
3	2.99	1.38	3	1.1	3.14	3.11	2	1.9	2.99	1.88	2.9	0.2	1.98	2.33	2.3	0.7
4	3.03	1.13	2.3	1.4	2.99	2.86	2.8	1.7	3.79	2.26	2.3	0.9	1.9	2.09	2.2	1
5	2.76	1.06	0.2	0.9	3.31	2.62	2.2	0.3	3.77	2.01	2.7	0.4	1.87	1.84	2.4	0.2
6	3.8	3	2.1	1.1	3.1	2.37	1.3	1.5	3.76	1.77	2.8	1.1	1.87	1.59	2	1.9
7	3.85	2.75	2.2	1.2	3.02	2.12	2.3	0	3.56	1.52	2.1	1.1	1.97	1.34	2.8	1.7
8	3.84	2.51	3	1	2.99	1.88	2.9	0.2	3.37	1.34	0.6	1.5	2.49	1.1	2.2	0.3
9	3.79	2.26	2.3	0.9	2.3	2.83	2.1	0.5	2.49	1.1	2.2	0.3	2.49	0.9	1.3	1.5
10	1.97	1.34	2.8	1.7	2.09	2.58	2.7	0.8	2.49	0.9	1.3	1.5	3.14	3.11	2.3	0
11	2.49	1.1	2.2	0.3	1.98	2.33	2.9	1.5	3.14	3.11	2.3	0	2.99	2.86	2.9	0.2
12	2.49	0.9	1.3	1.5	1.9	2.09	2.3	1.4	2.99	2.86	2.9	0.2	3.31	2.62	2.1	0.5
13	3.14	3.11	2.3	0	1.87	1.84	0.2	0.9	3.31	2.62	2.1	0.5	3.1	2.37	2.7	0.8
14	2.99	2.86	2.9	0.2	1.87	1.59	2.1	1.1					3.02	2.12	2.9	1.5
15	3.31	2.62	2.1	0.5	1.97	1.34	2.2	1.2					2.99	1.88	2.9	0.2
16	3.1	2.37	2.7	0.8	2.49	1.1	3	1					2.99	1.63	2.9	1.2
17	3.79	2.26	2.3	0.9	2.49	0.9	2.3	0.9					2.99	1.38	3	1.1
18	3.77	2.01	2.7	0.4	3.79	2.26	2.3	0.9					3.03	1.13	2.3	1.4
19	3.76	1.77	2.8	1.1	3.77	2.01	2.7	0.4					2.76	1.06	0.2	0.9
20	3.56	1.52	2.1	1.1	3.76	1.77	2.8	1.1					3.8	3	2.1	1.1
21	3.37	1.34	0.6	1.5	3.56	1.52	2.1	1.1					3.85	2.75	2.2	1.2
22	3.79	2.26	2.3	0.9									3.84	2.51	3	1
23	3.1	2.37	2.7	0.8									3.79	2.26	2.3	0.9
24													3.77	2.01	2.7	0.4
25													3.76	1.77	2.8	1.1
26													3.56	1.52	2.1	1.1
27													3.37	1.34	0.6	1.5

algorithm, and our current AI-based approach. The results, presented in Table 6.6, demonstrate the superiority of the AI-based optimization, with a reduction of 10% in MAE and a significant 30% decrease in total treatment time. MAE, a commonly used measure of prediction accuracy, quantifies the average absolute difference between predicted and actual values, providing insight into the model's precision. Additionally, the Dice Score, or Dice Similarity Coefficient, was used to assess the overlap between predicted and actual tumor segmentation, reflecting the accuracy of the segmentation tasks. The Dice Score is calculated as twice the size of the intersection between the two sets divided by the sum of their sizes, making it a valuable metric for evaluating the performance of segmentation models in ensuring accurate targeting during treatment.

Table 6.6 presents the MAE and total treatment time for the planned treatment area and thermal dose range, comparing the predicted treatment parameters and coverage achieved by the previous optimization method with those of the AI-based approach. This comparison highlights the improvements brought by the AI-based method, demonstrating more accurate parameter predictions and more efficient tumor coverage. The AI-based approach shows significant advancements over the traditional optimization technique in terms of reducing both MAE and total treatment time.

Table 6.6: Quantitative comparison between our previous work [87] and the current AI approach.

	Previous Work		Current Work	
Patient No.	MAE (mm^2)	Total Time (s)	MAE (mm^2)	Total Time (s)
1	0.3309	95.03	0.2978	73.1
2	0.4781	92.60	0.4302	71.2
3	0.5754	51.74	0.4978	39.8
4	0.2411	113.49	0.2170	87.3

In contrast, Table 6.7 focuses on calculating the MAE and Dice Score for the actual coagulation area and thermal dose range. The actual coagulation area was derived from thermal imaging and histological analysis of the treated tissue, providing a precise assessment of the regions where effective tissue coagulation occurred. By using these methods, the study accurately identified the regions affected by the treatment, allowing for an evaluation of the treatment's success.

Table 6.7: Quantitative comparison between experiments and simulations.

Trial No.	MAE (mm^2)	Dice Score (%)
1	0.3981	99.94
2	0.2757	99.96
3	0.2874	99.95
4	0.3469	99.94
5	0.3324	99.95
6	0.3137	99.95
7	0.2372	99.96
8	0.2723	99.96
9	0.3563	99.95
Average	0.3133	99.95

The reduction in both MAE and total treatment time in this study compared to the previous one can be attributed to the AI-based approach's superior ability to optimize treatment parameters. Unlike traditional methods, which may rely on more straightforward algorithms, the AI model has the capacity to recognize and analyze complex patterns and relationships within the treatment data. This allows for more precise predictions of optimal treatment settings, such as sonication location, duration, and thermal dosing.

As a result, the AI-based method delivers better coverage of the tumor with fewer

sonications and shorter overall treatment times, which enhances treatment efficiency. This improvement not only leads to more effective ablation but also reduces the risk of over-exposure to surrounding healthy tissues. Ultimately, the AI-based approach allows for a more tailored and refined treatment plan, contributing to improved patient outcomes and the overall success of the procedure.

6.2.2 Experimental Validation

Validation of Numerical Simulation

Subsequently, the effectiveness of the numerical HIFU treatment was evaluated through nine distinct trials conducted on bovine liver tissue. After HIFU irradiation, the tissue samples were fixed and sectioned to obtain thin slices for detailed analysis. These slices were aligned to match the planes used in the simulation for direct comparison between predicted and actual outcomes. The results from these nine experiments are depicted in Fig. 6.15. In the first and third columns, the lesion patterns predicted by the numerical simulations are displayed, while the second and fourth columns illustrate the actual treated areas post-HIFU exposure. Each of these trials involved three sonications, with a one-second cooling interval between them.

The spacing between sonications varied between 0 and 5 mm in both the radial (r) and axial (z) directions, while the heating durations were consistently set at 3 seconds. In this figure, the labels such as "$r = 0$, $z = 0$," etc., located in the top left of each graph, indicate the specific coordinates in the radial (r) and axial (z) directions at which the data is presented. The vertical axis (r in cm) represents the radial distance from the HIFU focal point, while the horizontal axis (z in cm) corresponds to the axial distance along the HIFU beam. For instance, a graph labeled "$r = 0$" shows data along the central axis ($r = 0$) of the HIFU beam, where temperature or thermal dose varies along the z-axis. Conversely, a label such as "$r = 3$ mm" indicates data at a radial distance of 3 mm from the central axis, with corresponding variations along the z-axis.

Furthermore, a quantitative assessment of the proposed surgical plan is provided in Table 6.7, where both MAE and Dice Scores are reported for each of the nine individual trials. Although some minor regions failed to receive the full intended thermal dosage of 240 CEM_{43}, a comparison between the planned and actual treated areas demonstrates a notably high level of concordance. The discrepancies observed between the predicted and actual results may be attributed to several factors, including variations in thermal diffusion within the tissue, slight differences in acoustic properties between the *ex vivo*

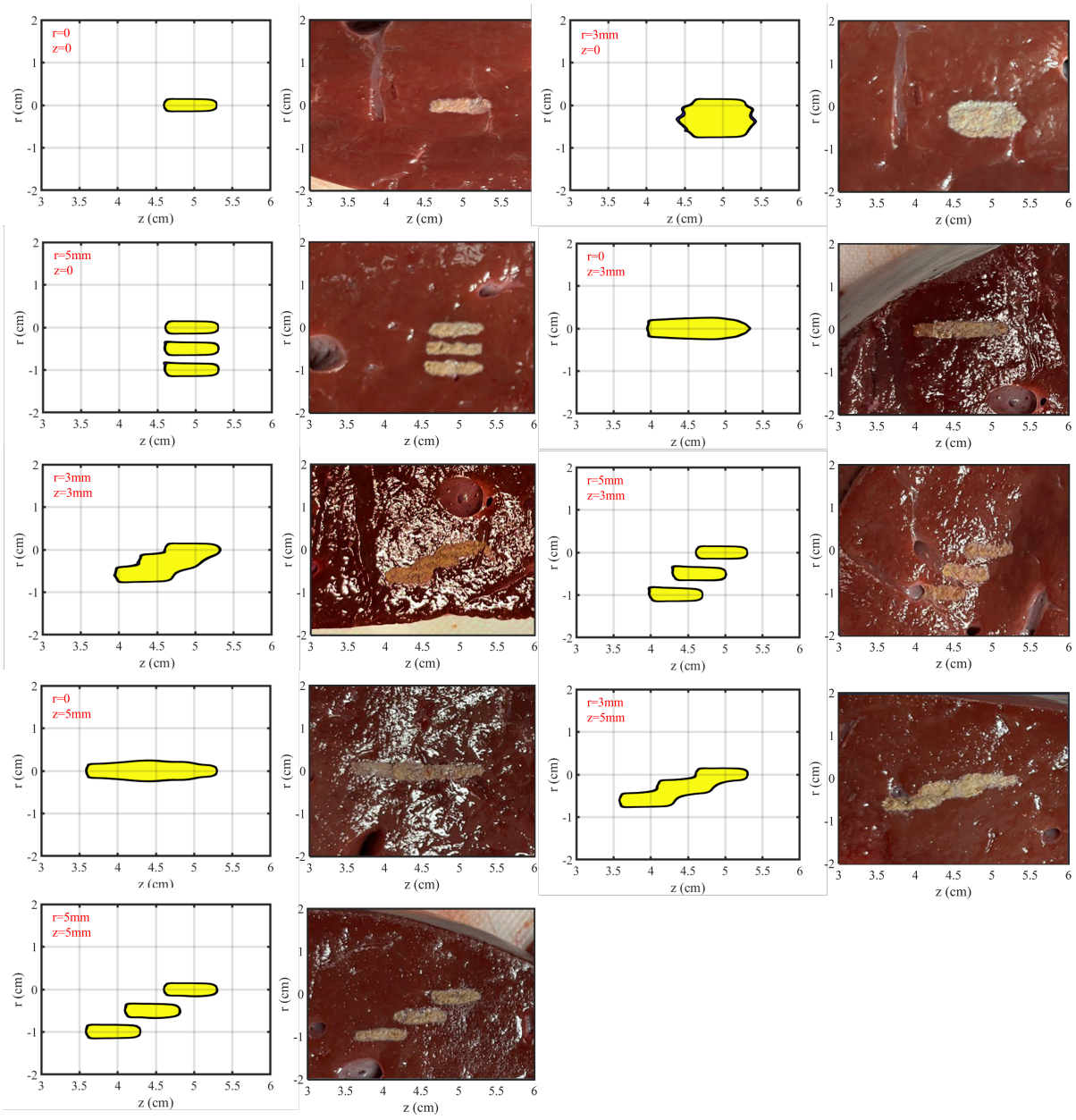


Figure 6.15: Comparison of the numerical simulation with experimental treatment plan composed of 3 sonications.

tissue and the assumptions used in simulations, and potential errors introduced during imaging. Despite these minor deviations, the overall agreement between the numerical predictions and experimental outcomes indicates the effectiveness of the AI-based planning approach, providing valuable insights for future clinical applications of HIFU therapy.

During the experiments, the temperature increase within the tissue was continuously monitored through a combination of thermal imaging and thermocouples. The thermocouples were carefully inserted into the bovine liver tissue at specific depths and locations to directly measure temperature within the target area, including at the precise location of the HIFU focus. To ensure accurate and repeatable placement, the thermocouples were positioned using a stereotactic frame, which provided high precision in locating them within the tissue. One thermocouple was positioned directly at the HIFU focal point to measure the temperature at the center of the treatment zone, while additional thermocouples were placed in surrounding regions to monitor the temperature gradients and ensure safe and uniform heating.

The temperature distributions predicted by the numerical model at the central region of the tumor, specifically at the HIFU focal point, during the ablation process are shown in Fig. 6.16. These predictions cover the full course of the treatment, including 10 seconds of heating followed by a 90-second cooling period. The figure also presents the corresponding experimental results, allowing for a direct comparison between the predicted and observed temperature profiles. The strong alignment between the numerical predictions and the experimental findings demonstrates that our model accurately captures the thermal dynamics within the tissue, including the temperature rise and subsequent cooling phases. This good agreement between the simulation and experimental data highlights the reliability and effectiveness of the model in predicting temperature distributions during HIFU treatment, further supporting its potential application in clinical settings.

Validation of the Proposed AI Method

To verify the accuracy of the proposed AI-based method, five preset HIFU treatment plans were developed and tested on bovine liver tissue, while also being implemented using a conventional clinical procedure as outlined in [170]. The treatment planning region, indicated by green lines in Fig. 6.17, was carefully outlined to precisely correspond with the targeted tumor area in the bovine liver samples. In addition to determining the location of each sonication point (z, r), optimal heating (t_h) and cooling (t_c) times were established through iterative testing and refined by comparing them to simulation predictions.

The experimental results revealed that the AI-optimized parameters led to a signifi-

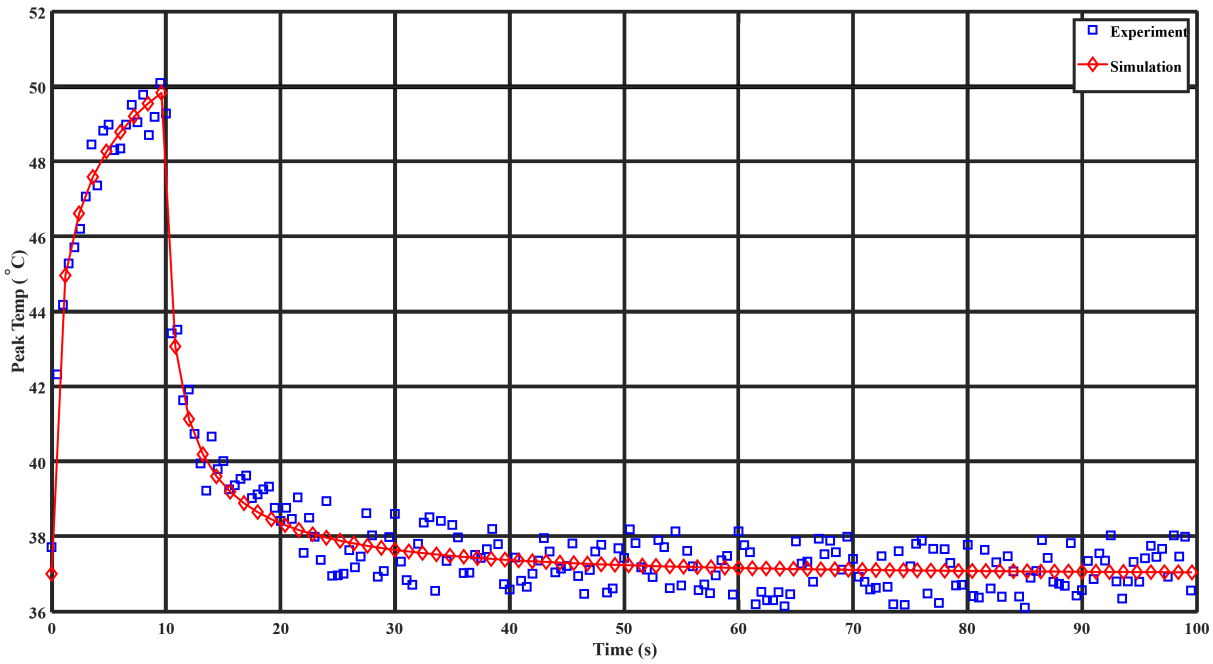


Figure 6.16: Comparison of simulation and experimental results for the temperature distribution in the focal point during HIFU sonications including 10 s heating and 90 s cooling.

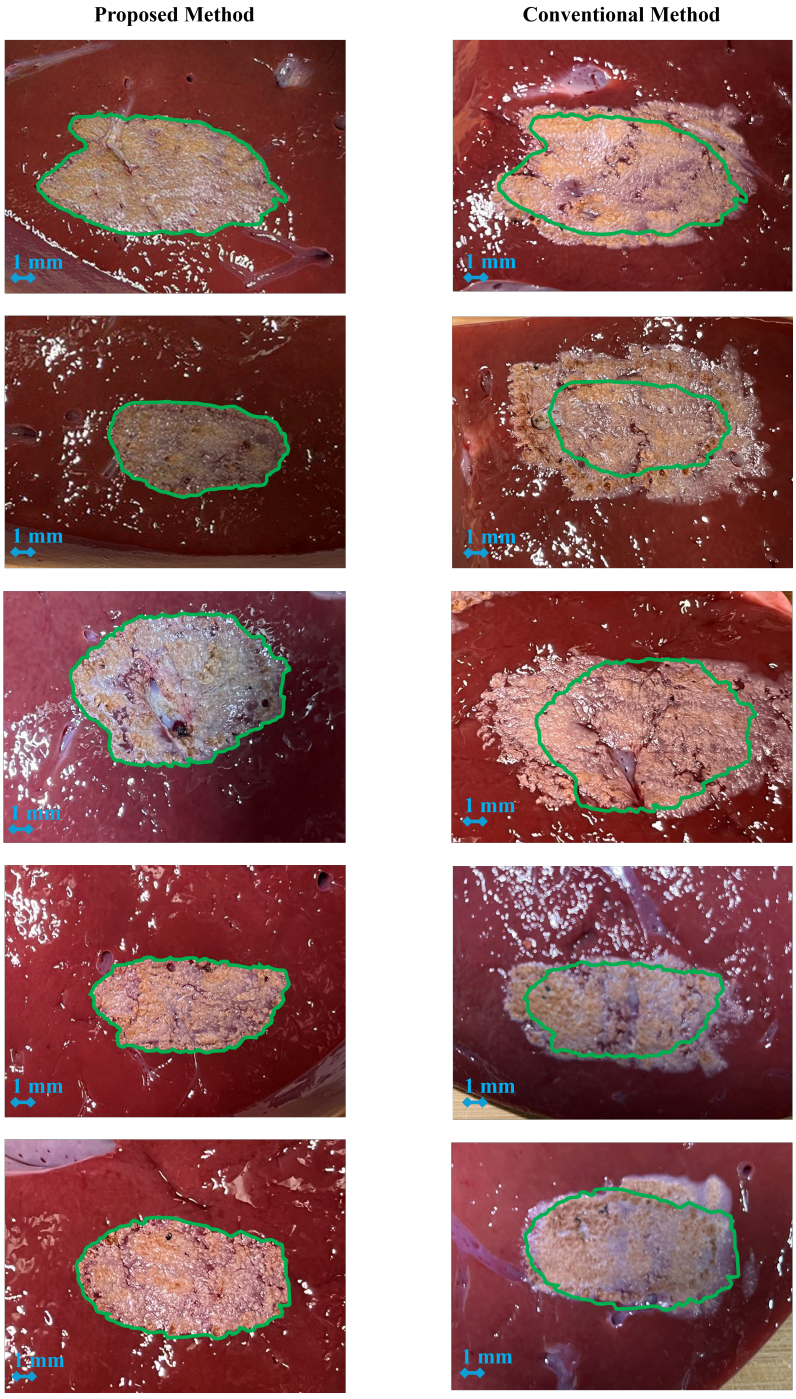


Figure 6.17: Comparison of the AI proposed method with conventional treatment plan.

cantly higher effectiveness of the treatment compared to the conventional method. The acoustic and thermal simulation results, combined with the deep learning approach, were validated by comparing the predicted treatment outcomes with the actual experimental results. This comparison confirmed the reliability of the AI-based method in conducting *ex vivo* HIFU treatments.

Table 6.8 provides a detailed comparison of the Mean Absolute Error (MAE) and Dice Score for the actual coagulation area and thermal dose range, assessing both the AI-optimized approach and the conventional clinical procedure. The results clearly demonstrate that the AI method outperformed the traditional approach, offering more accurate predictions of the coagulation area and better overall coverage of the tumor with a higher Dice Score. This validation further underscores the potential of the AI method in enhancing the precision and efficacy of HIFU treatment plans in clinical practice.

Table 6.8: Quantitative comparison between the proposed AI method and the conventional approach.

	Proposed Method		Conventional Method	
Trial No.	MAE (mm^2)	Dice Score (%)	MAE (mm^2)	Dice Score (%)
1	0.3693	96.55	7.5154	75.04
2	0.1529	99.47	11.2328	68.89
3	0.1039	99.92	9.3274	69.35
4	0.4481	96.10	5.6069	77.88
5	0.1982	98.92	6.2231	76.54

6.3 HIFU-Induced Lesion Segmentation

6.3.1 B-Mode Imaging Simulation

In this section, the qualitative outcomes achieved by the B-mode imaging simulation framework proposed in this study for the task of HIFU lesion segmentation are presented and analyzed in detail. The framework is designed to simulate the thermal effects of HIFU on tissue, and its application in lesion segmentation provides critical insights into the treatment's precision. Fig. 6.18 visually depicts the thermal dose accumulation region induced by HIFU simulation, which is displayed alongside the corresponding B-mode imaging simulation results. This visualization captures the progressive evolution of thermal effects on

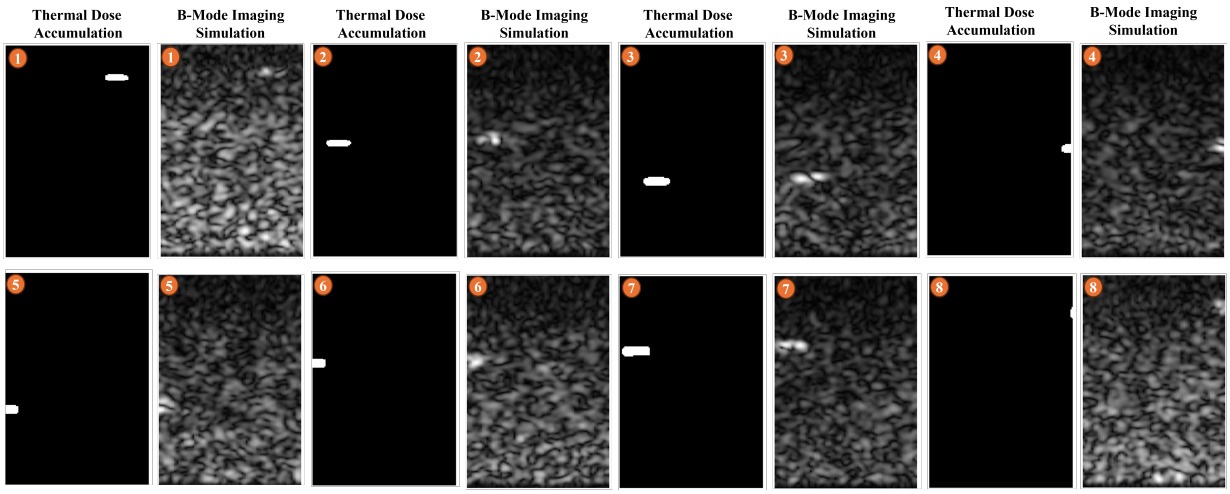


Figure 6.18: A series of frames from a simulation study, showcasing the progression and visualization of thermal dose accumulation induced by HIFU and the corresponding B-mode ultrasound images. Each frame sequentially reveals the development of the thermal region and its detection via B-mode imaging, demonstrating the dynamic response of tissue to HIFU therapy over time.

tissue as a result of HIFU exposure, allowing for a step-by-step examination of how thermal energy is absorbed and propagated within the targeted area.

The sequence of images presented in Fig. 6.18 highlights the different stages of tissue response to HIFU. Initially, the frames show minimal interaction between the ultrasound waves and the tissue, characterized by little to no visible change in the tissue's appearance. As the exposure continues, the images reveal more pronounced thermal effects, demonstrating the gradual increase in energy absorption and thermal propagation. These changes are clearly reflected in the B-mode simulation, which captures the dynamic interaction between the ultrasound waves and the tissue over time. As the thermal effects intensify, the tissue's appearance in the B-mode images evolves, offering a clear visual representation of the lesion formation process. This progression provides valuable qualitative data for understanding the relationship between HIFU-induced thermal effects and the resulting tissue changes, ultimately aiding in the accurate segmentation of lesions.

The comparative analysis of the simulated thermal dose regions and the resultant B-mode images offers valuable insights into the correlation between ultrasound energy deposition and the observable changes in tissue structure. By juxtaposing the two, the evolving

thermal dose regions serve as a clear indicator of the amount of energy absorbed by the tissue, which is progressively visualized in the B-mode images. As the simulation progresses, the expansion of the thermal dose regions suggests an increasing concentration of absorbed ultrasound energy, a trend that corresponds directly with the increasingly highlighted areas in the B-mode images. These highlighted regions mark the areas where significant tissue changes are occurring, offering a real-time visual representation of the thermal effects induced by HIFU exposure.

This relationship between energy deposition and tissue alteration underscores the crucial role of B-mode imaging in monitoring and evaluating tissue responses to HIFU. The B-mode images not only reflect the immediate effects of energy absorption but also provide a non-invasive tool to observe and track the dynamic changes in tissue structure throughout the thermal therapy process. By capturing these changes with precision, B-mode imaging enhances the ability to assess the efficacy of HIFU treatments, ensuring that the thermal effects are accurately targeted and that the lesion formation process is closely monitored. This integration of simulated thermal dose data with B-mode imaging results ultimately strengthens the framework's potential as a reliable method for observing the progression and outcomes of thermal therapies.

The simulated images underscore the remarkable precision of HIFU in targeting specific tissue areas while sparing the surrounding regions from unintended thermal effects. This level of precision is essential for therapeutic applications, particularly in tumor ablation, where minimizing collateral damage to healthy tissue is of paramount importance. In clinical contexts, the ability to focus energy exclusively on the targeted lesion enhances the safety and efficacy of treatments, making HIFU a highly valuable tool for non-invasive therapies.

The clear delineation of treated areas, as evidenced in both the thermal dose simulation and the B-mode images, confirms the accuracy and reliability of the simulation model. This alignment between simulated thermal regions and their corresponding visualization in the B-mode images validates the framework's capacity to accurately predict tissue responses under HIFU exposure. The consistency between these two forms of data reinforces the relevance of this simulation model for real-world clinical applications, providing a robust tool for visualizing and assessing the outcomes of HIFU treatments.

Furthermore, this precise targeting capability offers deeper insights into the biological effects of HIFU on tissues, allowing researchers and clinicians to better understand the nuances of energy deposition and tissue interaction. This understanding paves the way for potential adjustments and optimizations in HIFU treatments, enabling practitioners to fine-tune the parameters to achieve even more effective and controlled therapeutic out-

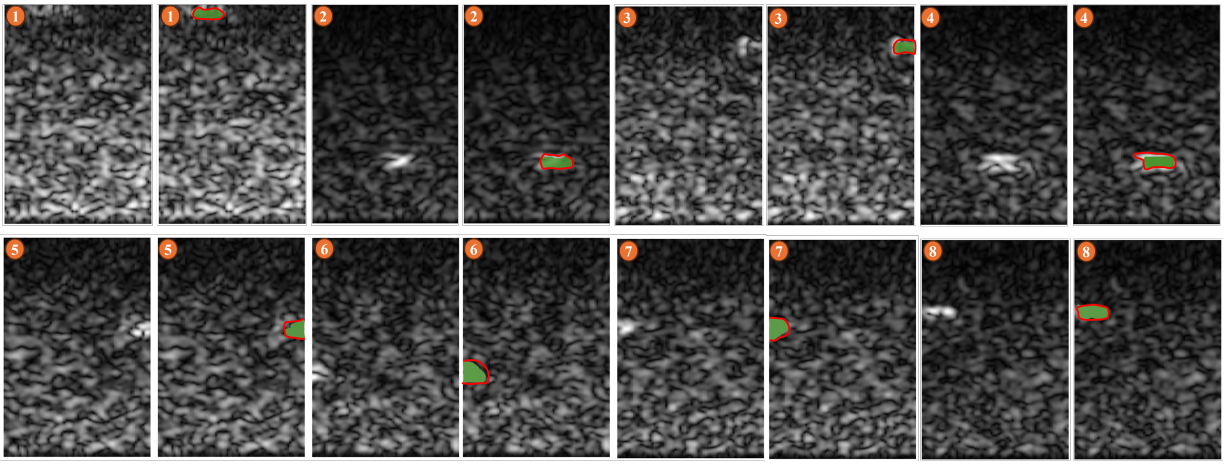


Figure 6.19: A detailed evaluation of the proposed framework's performance shows that the red areas represent the actual lesion, while the green regions indicate the segmented areas. Any discrepancies between the red and green regions in each sub-image are considered errors in HIFU segmentation.

comes, particularly in complex cases such as tumor ablation. Ultimately, the integration of simulation and imaging strengthens the case for HIFU as a safe, precise, and adaptable modality in therapeutic applications.

6.3.2 Image Segmentation

Several visual instances of the segmentation results are illustrated in Fig. 6.19. Each figure contains B-mode images captured before and after sonication, accompanied by the predicted ablated regions highlighted in green. The ground truth boundary of the ablated region is marked with red closed curves. Based on these visualizations, it becomes apparent that the model excels in capturing both global and long-range semantic information interactions, contributing to its superior segmentation outcomes. The ability to accurately represent complex interactions across the entire image allows the model to generate precise predictions of ablated areas in most cases.

However, when the model encounters boundary regions, some limitations emerge, as it may exhibit both over-segmentation and under-segmentation. This issue can be attributed to the fact that regions near boundaries often receive less sonication power compared to other areas, leading to a lower degree of ablation and increased uncertainty in the model's

predictions. Consequently, this uncertainty can result in less accurate segmentation at these boundaries. To address this challenge, a postprocessing step can be employed, which excludes boundary regions from being classified as ablated, based on the specific treatment strategies used. This step can help refine the overall segmentation accuracy by mitigating the influence of boundary-related uncertainties.

An in-depth performance analysis of the proposed framework is presented in Fig. 6.20, where areas of under-segmentation are highlighted by orange pixels, indicating regions where the model failed to accurately predict the ablation. On the other hand, accurately segmented regions are represented by yellow pixels, while areas that were over-segmented are indicated by green pixels. This detailed analysis provides further insights into the strengths and limitations of the model in different regions of the images.

Furthermore, a quantitative evaluation of the proposed segmentation framework is provided in Table 6.9, where metrics such as Mean Absolute Errors (MAE) and Dice Scores are reported for five distinct sonications. Despite the limited amount of training data available, the model achieves noteworthy performance. Specifically, the proposed framework attains an average MAE of 0.039 and an average Dice Score of 94.34%, demonstrating its ability to accurately segment ablated regions. Additionally, the model's average segmentation time during test-time is 21±4 milliseconds, making it a highly desirable solution for real-time applications, where rapid and reliable segmentation is crucial for effective treatment. This combination of high accuracy and fast processing time highlights the potential of the segmentation framework for real-world clinical scenarios.

Table 6.9: The results present the performance evaluation of the proposed segmentation framework. Each row summarizes an experiment, detailing the mean absolute errors and dice scores to assess the framework's performance.

Sonication	**Mean Absolute Error**	**Dice Score**
1	0.053	92.96%
2	0.045	91.85%
3	0.026	96.00%
4	0.027	96.32%
5	0.042	94.57%
Average	0.039	94.34%

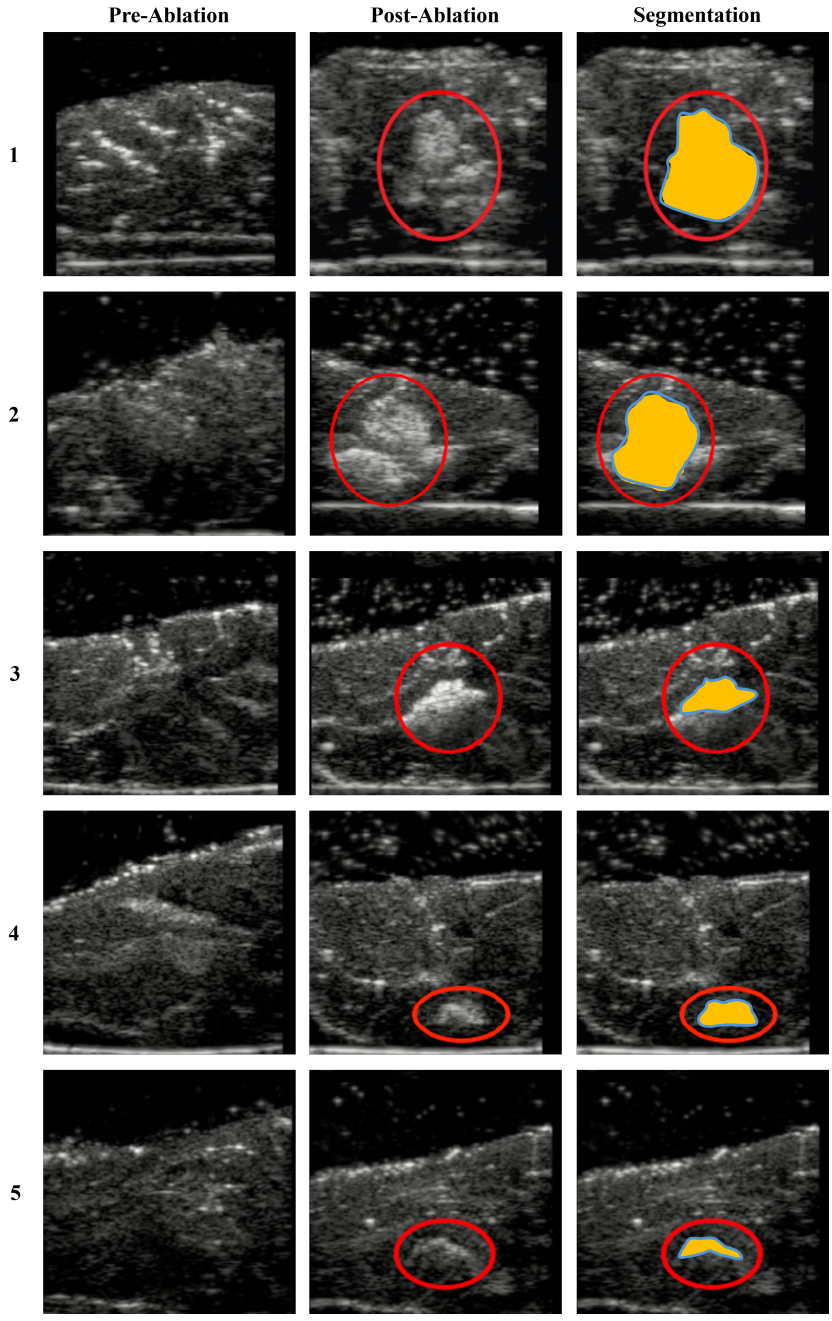


Figure 6.20: A detailed evaluation of the proposed framework's performance for *ex vivo* experiment shows that the blue areas represent the actual lesion, while the yellow regions indicate the segmented areas. Any discrepancies between the blue and yellow regions in each sub-image are considered errors in HIFU segmentation.

Chapter 7

Conclusion and Future Work

7.1 PINN-Based HIFU

This study introduces a comprehensive and innovative deep learning framework based on PINN for the precise 3D simulation of FUS ablation in breast tissue. The framework is designed to accurately replicate essential physical parameters involved in the ablation process, including acoustic pressure, sound intensity, temperature distribution, and the extent of necrotic tissue generated during treatment. Our model was meticulously validated through comparisons with existing numerical data and FEM simulations, showing strong alignment and demonstrating its reliability in reproducing realistic FUS ablation effects within an anatomically accurate breast phantom.

The simulation results reveal that using a bowl-shaped acoustic transducer can effectively concentrate ultrasound waves on the tumor site, creating a focal point that raises the local temperature sufficiently to induce extensive tumor cell necrosis. This focused heating effect confirms the potential of FUS as a non-invasive therapeutic approach for breast cancer treatment, where precision in targeting and controlling ablation zones is crucial. Our findings not only underscore the capability of PINN-based models in medical simulation but also highlight the potential for applying deep learning to improve the accuracy and efficiency of personalized, non-invasive cancer therapies.

In our study, we explored a clinically relevant approach that addresses multiple tumor lesions simultaneously, aiming to achieve a more uniform temperature distribution across the treatment area and enhance the effectiveness of tumor ablation. This approach demonstrates the significant advantages of 3D simulations over traditional 2D models, as

3D models can more accurately capture the complex dynamics involved in FUS ablation processes, including the interaction between multiple lesions and surrounding tissues.

Our deep learning model, built on this 3D framework, offers promising capabilities for personalized treatment planning, potentially transforming clinical outcomes by providing precise, patient-specific predictions of temperature elevation and ablation zones. This level of precision is critical for optimizing FUS treatments, ensuring targeted ablation with minimal impact on surrounding healthy tissue.

However, the model's effectiveness hinges on several factors, including the quality and diversity of the training data used to develop it. For the model to be truly effective and generalizable to a wide range of patient cases, it requires rigorous testing, extensive validation, and adaptation to diverse anatomical variations and tumor characteristics. Additionally, before implementation in clinical settings, the model must undergo thorough clinical trials to confirm its safety, reliability, and efficacy across different patient populations. This careful and systematic approach to validation will be essential for translating our deep learning framework from research to real-world applications in FUS-based cancer treatment.

Future research efforts should prioritize expanding the dataset to include a broader range of patient anatomies, tumor characteristics, and treatment scenarios, enhancing the model's robustness and generalizability. Improving model interpretability is also crucial, as it would allow clinicians to better understand the decision-making processes within the model, fostering greater confidence in its predictions and promoting its acceptance in clinical environments. Additionally, seamlessly integrating this model into existing clinical workflows is essential, as it would enable real-time, data-driven treatment planning and decision support during FUS procedures.

To ensure the model's long-term utility in clinical settings, a framework for continuous monitoring and adaptation should be developed. This would involve routinely updating the model based on new patient data and outcomes, enabling it to evolve alongside advancements in medical knowledge and technology. Such an adaptive approach would not only maintain the model's relevance over time but also enhance its effectiveness and reliability in providing personalized, precise FUS ablation treatments in diverse clinical scenarios.

7.2 Presurgical Planning

HIFU offers a promising, minimally invasive approach for cancer treatment by using focused ultrasound waves to thermally ablate tumor tissue without the need for surgical incisions. However, one of the major challenges in HIFU therapy lies in the precise targeting of the

ultrasound beam. Accurate beam focusing is essential to selectively destroy tumor cells while preserving surrounding healthy tissue, a requirement that demands thorough and meticulous preoperative planning.

Traditionally, treatment planning for HIFU has relied on manual or semi-automated methods, where clinicians adjust parameters and positions to optimize targeting. While effective, these methods are both time-intensive and computationally demanding, often involving complex simulations and iterative adjustments. This not only prolongs the preparation time for each patient but also places a considerable burden on computational resources.

In response to these limitations, there is a growing interest in the development of fully automated treatment planning techniques. Automated planning has the potential to significantly streamline the process, making it faster, more efficient, and potentially more accurate by reducing human error. Advanced algorithms and machine learning models could analyze patient-specific data, including tumor size, shape, and location, to generate optimal treatment plans with minimal intervention from clinicians. By simplifying and accelerating the planning phase, fully automated approaches could facilitate wider adoption of HIFU, improve patient outcomes, and support a more personalized approach to cancer treatment.

This study presents a novel optimization technique based on deep learning for enhancing the precision and effectiveness of HIFU in tumor ablation. By incorporating deep learning into the HIFU treatment planning process, the approach achieved impressive outcomes, with inaccurately treated or untreated areas constituting only 0.06 percent of the total treatment area. This minimal level of error highlights the potential of deep learning to create treatment plans that are nearly optimal, effectively balancing tumor coverage and preservation of surrounding healthy tissue.

One of the primary benefits of this deep learning-based method is its simplicity and efficiency. Unlike traditional planning approaches that may require complex, multi-step processes, this technique requires only a patient's anatomical map along with data specifying the target region and areas to avoid. The neural network then automates the rest of the planning process, optimizing treatment parameters and beam positioning to maximize therapeutic impact while minimizing harm to healthy tissue. This streamlined, automated approach not only reduces planning time but also minimizes the reliance on extensive clinician intervention, making it a powerful tool for enhancing the accessibility and accuracy of HIFU tumor ablation treatments.

This study showcases the promise of an AI-based algorithm in optimizing HIFU treatment parameters for the safe and effective ablation of breast tumors. Utilizing ML techniques, the proposed method dynamically adjusts sonication points and key parameters

in real-time, resulting in significantly reduced treatment time and enhanced precision in targeting tumor tissue. This adaptive approach helps to streamline the treatment process, allowing for more accurate energy delivery that conforms closely to the intended ablation zone while minimizing the risk of damage to surrounding healthy tissue.

Experimental validation conducted on bovine liver tissue demonstrated a strong correlation between the planned ablation regions and the actual treated areas, emphasizing the accuracy and robustness of this approach. The high level of agreement between the intended and achieved outcomes highlights the potential of this AI-driven technique to improve the reliability and efficacy of HIFU treatments. By automating the adjustment of sonication parameters based on real-time feedback, this method could pave the way for more precise, efficient, and personalized cancer treatments, making HIFU a more accessible and effective option in clinical oncology.

7.3 Lesion Segmentation

This project introduces an innovative real-time ablation segmentation framework designed for use during HIFU surgeries. The framework processes B-mode ultrasound images captured before and after HIFU sonications, utilizing them to accurately segment the ablated lesions in near real-time. By creating a three-channel tensor that combines pre- and post-sonication images with their matrix difference, the framework provides input to a Swin-Unet network, which performs precise segmentation of the ablated areas.

To overcome the challenge of limited training data, the framework leverages both simulated and real B-mode images specific to HIFU therapy, expanding the dataset and improving model performance. Experimental validation conducted on chicken breast tissue demonstrated high segmentation accuracy, underscoring the framework's potential effectiveness. Notably, this approach is, to the best of our knowledge, the first to address the problem of real-time lesion segmentation during HIFU procedures. This pioneering framework could significantly enhance the precision and safety of HIFU treatments by providing clinicians with reliable, real-time visualization of ablated regions, aiding in monitoring and adjusting the procedure as needed.

7.4 Limitations and Future Work

While our study provides a comprehensive simulation of FUS ablation using a PINN model, it is essential to recognize certain limitations that may impact the overall accuracy and

applicability of the findings. One significant limitation lies in the use of the traditional Pennes Bioheat Equation to model thermal effects, as this approach assumes homogeneous or isotropic blood perfusion throughout the tissue. Such assumptions may not accurately represent the true biological conditions, given that breast tissue, especially within and around tumors, often exhibits heterogeneity and anisotropy in blood perfusion. These factors can lead to variations in heat transfer dynamics, affecting the accuracy of simulated ablation effects. Recent studies have proposed modifications to the Pennes equation to better account for spatial variability in blood perfusion rates [149, 148]. This is particularly relevant in areas of tumor hypoxia, where reduced blood flow can alter the deposition of thermal energy, lowering the tissue's responsiveness to ablation treatments.

Additionally, the current model assumes linear acoustic propagation for FUS waves, which simplifies the acoustic behavior within the tissue but may not fully capture the complexities inherent to real-world conditions. In practice, FUS waves can exhibit nonlinear propagation characteristics, especially in high-intensity focused ultrasound treatments. These nonlinear effects can cause significant deviations in pressure distribution and influence the temperature rise at the focal point of the ultrasound beam. Such discrepancies between the simulated linear model and the actual nonlinear acoustic behavior may result in deviations between predicted and actual acoustic pressure values in high-intensity regions. These differences highlight the need for further research to refine our model to incorporate nonlinear effects, which could enhance its predictive power and improve the precision of simulated ablation outcomes.

Furthermore, it is crucial to account for the continuous regenerative capacity of living tissues due to oxygen supply from arterial blood, which serves to counterbalance thermal degradation under quasi-static thermal conditions. In biological tissues, heating can result in either reversible (repairable) thermal damage, where cells recover function after exposure, or irreversible (lethal) thermal cell death, which permanently impairs or destroys cellular structures. At the critical interface between tumor and surrounding healthy tissue, the regeneration of healthy cells plays an essential role in triggering immune responses that actively work to suppress, prevent, and limit thermal damage within tolerable bounds, such that the thermal damage coefficient remains within $\Omega \leq 1$. This immune-triggered, partial self-regeneration at the tumor periphery, driven by an ongoing supply of oxygen and nutrients, acts as a protective mechanism to preserve surrounding tissue integrity. Consequently, this regenerative effect should be factored into models of thermal damage kinetics, as it introduces a dynamic layer of tissue response that can influence the predicted extent and effectiveness of thermal ablation, especially near the tumor boundary.

The current bio-heat model does not fully capture the influence of large blood vessels and thermal relaxation in biological tissues, both of which play crucial roles in heat transfer.

Large blood vessels act as heat sinks, rapidly dissipating thermal energy and altering the spatial distribution of heat, particularly around vascularized regions. This effect can significantly impact temperature gradients, reducing the precision of simulated thermal fields. Thermal relaxation, on the other hand, addresses the time delay in heat conduction through tissues, reflecting the non-instantaneous response of biological matter to thermal changes. Ignoring these factors introduces potential inaccuracies, as they can lead to overestimations or underestimations of thermal effects in both tumor and surrounding tissues.

To improve the accuracy and clinical relevance of our simulations, future work should aim to incorporate a modified bioheat equation into the PINN framework, accounting for heterogeneous blood perfusion, the cooling influence of large blood vessels, and thermal relaxation effects. By refining the model with these elements, we can achieve a more realistic representation of thermal energy distribution across tissues. This enhanced framework would allow for a more nuanced analysis of thermal ablation's impact on tumors and surrounding healthy tissues, offering valuable insights to optimize FUS treatment protocols.

While the current model shows strong generalization within the scope of the training data, future work will aim to extend its applicability across a wider spectrum of breast anatomies and tumor types. This enhancement will involve expanding the dataset by incorporating additional 3D models from datasets like UWCEM and patient-specific, MRI-derived models that represent variations in breast density, tumor size, and location. By including a diverse range of anatomical scenarios, the model can better address the variability encountered in clinical settings.

To further improve adaptability, transfer learning techniques will be applied, enabling the model to efficiently adapt to new clinical cases without requiring extensive retraining. Additionally, data augmentation strategies will be employed, simulating variations in tissue properties and tumor characteristics to enrich the dataset and capture a broader range of physiological differences. Finally, rigorous testing on a variety of clinical cases will be conducted to validate the model's generalization capabilities, ensuring robustness and reliability in real-world applications. These efforts will collectively enhance the model's clinical relevance and utility in supporting tailored treatment planning for diverse patient profiles.

Our PINN-based solution efficiently operates within a mesh-free domain, presenting a simplified framework that provides initial insights into the FUS ablation process. However, we acknowledge that this model currently falls short of capturing the full complexity of real-world FUS therapy scenarios. Future work will emphasize expanding the model to account for a more comprehensive set of tissue properties, including variations in tissue

density, acoustic impedance, and perfusion rates, as well as patient-specific anatomical features. Integrating these elements will enable the model to better reflect individual physiological conditions, such as blood flow dynamics and localized temperature changes, thereby enhancing its relevance in clinical applications.

Furthermore, by incorporating advanced modeling techniques and adaptive learning approaches, we aim to significantly improve the predictive power of our deep learning platform for FUS ablation therapies. Expanding the model's scope to include other types of cancer will not only broaden its applicability but also support more personalized treatment protocols, ultimately helping to advance the field of non-invasive cancer therapies. Through these enhancements, our PINN framework will become a more robust and clinically viable tool for predicting and optimizing FUS outcomes across diverse clinical scenarios.

References

[1] Uwcem-phantom repository. https://uwcem.ece.wisc.edu/phantomRepository.html. Accessed: 2023-06-06.

[2] Ravi Aggarwal, Viknesh Sounderajah, Guy Martin, Daniel SW Ting, Alan Karthikesalingam, Dominic King, Hutan Ashrafian, and Ara Darzi. Diagnostic accuracy of deep learning in medical imaging: A systematic review and meta-analysis. *NPJ digital medicine*, 4(1):1–23, 2021.

[3] Mohamed K Almekkaway, Islam A Shehata, and Emad S Ebbini. Anatomical-based model for simulation of hifu-induced lesions in atherosclerotic plaques. *International Journal of Hyperthermia*, 31(4):433–442, 2015.

[4] Mohamed K Almekkaway, Islam A Shehata, Alyona Haritonova, John Ballard, Andrew Casper, and Emad Ebbini. Image-based numerical modeling of hifu-induced lesions. In *AIP Conference Proceedings*, volume 1816, page 020001. AIP Publishing LLC, 2017.

[5] Mohamed Almekkawy, Jie Chen, Michael D Ellis, Dieter Haemmerich, David R Holmes, Cristian A Linte, Dorin Panescu, John Pearce, Punit Prakash, and Vesna Zderic. Therapeutic systems and technologies: State-of-the-art applications, opportunities, and challenges. *IEEE reviews in biomedical engineering*, 13:325–339, 2019.

[6] Mohamed Almekkawy and Emad S Ebbini. The optimization of transcostal phased array refocusing using the semidefinite relaxation method. *IEEE transactions on ultrasonics, ferroelectrics, and frequency control*, 67(2):318–328, 2019.

[7] Mohamed Almekkawy, Daniel McMahon, Hanan Alqarni, and Jiayu He. Optimization of transcostal phased-array refocusing using sparse semidefinite relaxation method. In *2017 39th Annual International Conference of the IEEE Engineering in Medicine and Biology Society (EMBC)*, pages 1449–1452. IEEE, 2017.

[8] Mohamed Khaled Ibrahim Almekkawy. Optimization of focused ultrasound and image based modeling in image guided interventions. 2014.

[9] Nuseiba M Altarawneh, Suhuai Luo, Brian Regan, Changming Sun, and Fucang Jia. Global threshold and region-based active contour model for accurate image segmentation. *Signal & Image Processing*, 5(3):1, 2014.

[10] Gunnar Aus. Current status of hifu and cryotherapy in prostate cancer–a review. *European urology*, 50(5):927–934, 2006.

[11] Jimmy Lei Ba, Jamie Ryan Kiros, and Geoffrey E Hinton. Layer normalization. *arXiv preprint arXiv:1607.06450*, 2016.

[12] Vismaya S Bachu, Jayanidhi Kedda, Ian Suk, Jordan J Green, and Betty Tyler. High-intensity focused ultrasound: a review of mechanisms and clinical applications. *Annals of biomedical engineering*, 49(9):1975–1991, 2021.

[13] Christian Beck, Weinan E, and Arnulf Jentzen. Machine learning approximation algorithms for high-dimensional fully nonlinear partial differential equations and second-order backward stochastic differential equations. *Journal of Nonlinear Science*, 29:1563–1619, 2019.

[14] Arka Bhowmik, Ramjee Repaka, Subhash C. Mishra, and Kunal Mitra. Thermal Assessment of Ablation Limit of Subsurface Tumor During Focused Ultrasound and Laser Heating. *Journal of Thermal Science and Engineering Applications*, 8(1), 11 2015.

[15] Ch Boutelier, L Bougues, and J Timbal. Experimental study of convective heat transfer coefficient for the human body in water. *Journal of Applied Physiology*, 42(1):93–100, 1977.

[16] H Frederick Bowman, Ernest G Cravalho, and Monty Woods. Theory, measurement, and application of thermal properties of biomaterials. *Annual review of biophysics and bioengineering*, 4(1):43–80, 1975.

[17] Chris Brace. Thermal tumor ablation in clinical use. *IEEE pulse*, 2(5):28–38, 2011.

[18] Freddie Bray, Jian-Song Ren, Eric Masuyer, and Jacques Ferlay. Global estimates of cancer prevalence for 27 sites in the adult population in 2008. *International journal of cancer*, 132(5):1133–1145, 2013.

[19] Mathieu Burtnyk, Rajiv Chopra, and Michael J Bronskill. Quantitative analysis of 3-d conformal mri-guided transurethral ultrasound therapy of the prostate: Theoretical simulations. *International Journal of Hyperthermia*, 25(2):116–131, 2009.

[20] Andrea Cafarelli, Marco Mura, Alessandro Diodato, Andrea Schiappacasse, Matteo Santoro, Gastone Ciuti, and Arianna Menciassi. A computer-assisted robotic platform for focused ultrasound surgery: Assessment of high intensity focused ultrasound delivery. In *2015 37th Annual International Conference of the IEEE Engineering in Medicine and Biology Society (EMBC)*, pages 1311–1314. IEEE, 2015.

[21] Hu Cao, Yueyue Wang, Joy Chen, Dongsheng Jiang, Xiaopeng Zhang, Qi Tian, and Manning Wang. Swin-unet: Unet-like pure transformer for medical image segmentation. In *Computer Vision–ECCV 2022 Workshops: Tel Aviv, Israel, October 23–27, 2022, Proceedings, Part III*, pages 205–218. Springer, 2023.

[22] Matthew Charlton, Sophie A Stanley, Zoë Whitman, Victoria Wenn, Timothy J Coats, Mark Sims, and Jonathan P Thompson. The effect of constitutive pigmentation on the measured emissivity of human skin. *Plos one*, 15(11):e0241843, 2020.

[23] F Chavrier, JY Chapelon, A Gelet, and D Cathignol. Modeling of high-intensity focused ultrasound-induced lesions in the presence of cavitation bubbles. *The Journal of the Acoustical Society of America*, 108(1):432–440, 2000.

[24] Heng-Da Cheng, Juan Shan, Wen Ju, Yanhui Guo, and Ling Zhang. Automated breast cancer detection and classification using ultrasound images: A survey. *Pattern recognition*, 43(1):299–317, 2010.

[25] Rajiv Chopra, Mathieu Burtnyk, W Apoutou N'djin, and Michael Bronskill. Mri-controlled transurethral ultrasound therapy for localised prostate cancer. *International Journal of Hyperthermia*, 26(8):804–821, 2010.

[26] Joshua Coon, Allison Payne, and Robert Roemer. Hifu treatment time reduction in superficial tumours through focal zone path selection. *International journal of hyperthermia*, 27(5):465–481, 2011.

[27] Marta Cudova, Bradley E Treeby, and Jiri Jaros. Design of hifu treatment plans using an evolutionary strategy. In *Proceedings of the Genetic and Evolutionary Computation Conference Companion*, pages 1568–1575, 2018.

[28] Martin O Culjat, David Goldenberg, Priyamvada Tewari, and Rahul S Singh. A review of tissue substitutes for ultrasound imaging. *Ultrasound in medicine & biology*, 36(6):861–873, 2010.

[29] L Curiel, F Chavrier, B Gignoux, S Pichardo, S Chesnais, and JY Chapelon. Experimental evaluation of lesion prediction modelling in the presence of cavitation bubbles: intended for high-intensity focused ultrasound prostate treatment. *Medical and Biological Engineering and Computing*, 42(1):44–54, 2004.

[30] Douglas R Daum and Kullervo Hynynen. A 256-element ultrasonic phased array system for the treatment of large volumes of deep seated tissue. *IEEE transactions on ultrasonics, ferroelectrics, and frequency control*, 46(5):1254–1268, 1999.

[31] Douglas R Daum, Nadine B Smith, Randy King, and Kullervo Hynynen. In vivo demonstration of noninvasive thermal surgery of the liver and kidney using an ultrasonic phased array. *Ultrasound in medicine & biology*, 25(7):1087–1098, 1999.

[32] Roel Deckers, LG Merckel, B Denis De Senneville, Gerald Schubert, Max Köhler, FM Knuttel, WP Th M Mali, Chrit TW Moonen, MAAJ Van Den Bosch, and LW Bartels. Performance analysis of a dedicated breast mr-hifu system for tumor ablation in breast cancer patients. *Physics in Medicine & Biology*, 60(14):5527, 2015.

[33] Mehdi Dehghan and Mania Sabouri. A spectral element method for solving the pennes bioheat transfer equation by using triangular and quadrilateral elements. *Applied Mathematical Modelling*, 36(12):6031–6049, 2012.

[34] Manuel A Diaz, Maxim A Solovchuk, and Tony WH Sheu. A conservative numerical scheme for modeling nonlinear acoustic propagation in thermoviscous homogeneous media. *Journal of Computational Physics*, 363:200–230, 2018.

[35] Theodore J Dubinsky, Carlos Cuevas, Manjiri K Dighe, Orpheus Kolokythas, and Joo Ha Hwang. High-intensity focused ultrasound: current potential and oncologic applications. *AMERICAN JOURNAL OF ROENTGENOLOGY-NEW SERIES-*, 190(1):191, 2008.

[36] Emad S Ebbini and Charles A Cain. A spherical-section ultrasound phased array applicator for deep localized hyperthermia. *IEEE Transactions on Biomedical Engineering*, 38(7):634–643, 1991.

[37] Mehran Ebrahimi, Peter Siegler, Amen Modhafar, Claire MB Holloway, Donald B Plewes, and Anne L Martel. Using surface markers for mri guided breast conserving surgery: a feasibility survey. *Physics in Medicine & Biology*, 59(7):1589, 2014.

[38] Engineers Edge. Convective heat transfer coefficients table chart. *Engineers Edge. Available online: https://www. engineersedge. com/heat_transfer/convective_heat_transfer_coefficients__13378. htm (accessed on 2 February 2022)*, 2000.

[39] Mohamed Elawady, Ibrahim Sadek, Abd El Rahman Shabayek, Gerard Pons, and Sergi Ganau. Automatic nonlinear filtering and segmentation for breast ultrasound images. In *International Conference on Image Analysis and Recognition*, pages 206–213. Springer, 2016.

[40] IA Shehata Elhelf, H Albahar, U Shah, A Oto, E Cressman, and M Almekkawy. High intensity focused ultrasound: the fundamentals, clinical applications and research trends. *Diagnostic and interventional imaging*, 99(6):349–359, 2018.

[41] Julia K Enholm, Max O Kohler, Bruno Quesson, Charles Mougenot, Chrit TW Moonen, and Shunmugavelu D Sokka. Improved volumetric mr-hifu ablation by robust binary feedback control. *IEEE Transactions on Biomedical Engineering*, 57(1):103–113, 2009.

[42] Jeremy Epah, Katalin Pálfi, Franziska Luise Dienst, Pedro Felipe Malacarne, Rolf Bremer, Michael Salamon, Sandeep Kumar, Hanjoong Jo, Christoph Schürmann, and Ralf Peter Brandes. 3d imaging and quantitative analysis of vascular networks: a comparison of ultramicroscopy and micro-computed tomography. *Theranostics*, 8(8):2117, 2018.

[43] Xiaobing Fan and Kullervo Hynynen. Ultrasound surgery using multiple sonications—treatment time considerations. *Ultrasound in medicine & biology*, 22(4):471–482, 1996.

[44] Fiona M Fennessy and Clare M Tempany. Mri-guided focused ultrasound surgery of uterine leiomyomas1. *Academic radiology*, 12(9):1158–1166, 2005.

[45] Loreto B Feril, Rodney L Fernan, and Katsuro Tachibana. High-intensity focused ultrasound in the treatment of breast cancer. *Current Medicinal Chemistry*, 28(25):5179–5188, 2021.

[46] Jacques Ferlay, Isabelle Soerjomataram, Rajesh Dikshit, Sultan Eser, Colin Mathers, Marise Rebelo, Donald Maxwell Parkin, David Forman, and Freddie Bray. Cancer incidence and mortality worldwide: sources, methods and major patterns in globocan 2012. *International journal of cancer*, 136(5):E359–E386, 2015.

[47] EA Filonenko, G ter Haar, I Rivens, and VA Khokhlova. Prediction of ablation volume for different hifu exposure regimes. In *Proceedings of the 3rd International Symposium on Therapeutic Ultrasound*, pages 22–25. Lyon, 2003.

[48] Marinos Giannakou, Theocharis Drakos, Antria Filippou CUT, and Christakis Damianou CUT. Evaluation of navigation algorithms for reducing the near-field heating and the treatment time. 2021.

[49] LS Goldstein, MW Dewhirst, M Repacholi, and L Kheifets. Summary, conclusions and recommendations: adverse temperature levels in the human body. *International Journal of Hyperthermia*, 19(3):373–384, 2003.

[50] Stephen A Goss, Leon A Frizzell, Jeffrey T Kouzmanoff, Joseph M Barich, and Jeffrey M Yang. Sparse random ultrasound phased array for focal surgery. *IEEE transactions on ultrasonics, ferroelectrics, and frequency control*, 43(6):1111–1121, 1996.

[51] Yanhui Guo, Abdulkadir Şengür, and Jia-Wei Tian. A novel breast ultrasound image segmentation algorithm based on neutrosophic similarity score and level set. *Computer methods and programs in biomedicine*, 123:43–53, 2016.

[52] Pragya Gupta and Atul Srivastava. Numerical analysis of thermal response of tissues subjected to high intensity focused ultrasound. *International Journal of Hyperthermia*, 35(1):419–434, 2018.

[53] Pragya Gupta and Atul Srivastava. Non-fourier transient thermal analysis of biological tissue phantoms subjected to high intensity focused ultrasound. *International Journal of Heat and Mass Transfer*, 136:1052–1063, 2019.

[54] Miklos Gyongy and Constantin-C Coussios. Passive spatial mapping of inertial cavitation during hifu exposure. *IEEE Transactions on Biomedical Engineering*, 57(1):48–56, 2009.

[55] Gail ter Haar. Acoustic surgery. *Physics today*, 54(12):29–34, 2001.

[56] Ghada Hamed, Mohammed Abd El-Rahman Marey, Safaa El-Sayed Amin, and Mohamed Fahmy Tolba. Deep learning in breast cancer detection and classification. In *Proceedings of the International Conference on Artificial Intelligence and Computer Vision (AICV2020)*, pages 322–333. Springer, 2020.

[57] Mark F Hamilton, David T Blackstock, et al. *Nonlinear acoustics*, volume 237. Academic press San Diego, 1998.

[58] Jiequn Han, Arnulf Jentzen, and Weinan E. Solving high-dimensional partial differential equations using deep learning. *Proceedings of the National Academy of Sciences*, 115(34):8505–8510, 2018.

[59] PA Hasgall, F Di Gennaro, C Baumgartner, E Neufeld, B Lloyd, MC Gosselin, D Payne, A Klingenböck, and N Kuster. It'is database for thermal and electromagnetic parameters of biological tissues, version 4.0. *IT'IS*, 2018.

[60] Kaiming He, Xiangyu Zhang, Shaoqing Ren, and Jian Sun. Deep residual learning for image recognition. In *Proceedings of the IEEE conference on computer vision and pattern recognition*, pages 770–778, 2016.

[61] SX He. The noninvasive treatment of 251 cases of advanced pancreatic cancer with focused ultrasound surgery. In *Proceedings from the 2nd International Symposium on Therapeutic Ultrasound, 2002*, 2002.

[62] Dan Hendrycks and Kevin Gimpel. Gaussian error linear units (gelus). *arXiv preprint arXiv:1606.08415*, 2016.

[63] Gina K Hesley, Joel P Felmlee, John B Gebhart, Kelly T Dunagan, Krzysztof R Gorny, Jessica B Kesler, Kathleen R Brandt, Janel N Glantz, and Bobbie S Gostout. Noninvasive treatment of uterine fibroids: early mayo clinic experience with magnetic resonance imaging-guided focused ultrasound. In *Mayo Clinic Proceedings*, volume 81, pages 936–942. Elsevier, 2006.

[64] Jonathan Hindley, Wladyslaw M Gedroyc, Lesley Regan, Elizabeth Stewart, Clare Tempany, Kullervo Hynnen, Nathan Macdanold, Yael Inbar, Yacov Itzchak, Jaron Rabinovici, et al. Mri guidance of focused ultrasound therapy of uterine fibroids: early results. *American Journal of Roentgenology*, 183(6):1713–1719, 2004.

[65] Torsten Hopp, Nicole V Ruiter, and Neb Duric. Breast tissue characterization by sound speed: correlation with mammograms using a 2d/3d image registration. In *2012 IEEE International Ultrasonics Symposium*, pages 1–4. IEEE, 2012.

[66] Jinlan Huang, R Glynn Holt, Robin O Cleveland, and Ronald A Roy. Experimental validation of a tractable numerical model for focused ultrasound heating in flow-through tissue phantoms. *The Journal of the Acoustical Society of America*, 116(4):2451–2458, 2004.

[67] Qinghua Huang, Yaozhong Luo, and Qiangzhi Zhang. Breast ultrasound image segmentation: a survey. *International journal of computer assisted radiology and surgery*, 12(3):493–507, 2017.

[68] Stefan Hunsche, Dieter Sauner, Faycal El Majdoub, Clemens Neudorfer, Jörg Poggenborg, Axel Goßmann, and Mohammad Maarouf. Intensity-based 2d 3d registration for lead localization in robot guided deep brain stimulation. *Physics in Medicine & Biology*, 62(6):2417, 2017.

[69] K Hynynen, R Roemer, D Anhalt, C Johnson, ZX Xu, W Swindell, and T Cetas. A scanned, focused, multiple transducer ultrasonic system for localized hyperthermia treatments. *International Journal of Hyperthermia*, 26(1):1–11, 2010.

[70] Kullervo Hynynen, Oliver Pomeroy, Darrell N Smith, Peter E Huber, Nathan J McDannold, Joachim Kettenbach, Janet Baum, Samuel Singer, and Ferenc A Jolesz. Mr imaging-guided focused ultrasound surgery of fibroadenomas in the breast: a feasibility study. *Radiology*, 219(1):176–185, 2001.

[71] RO Illing, JE Kennedy, F Wu, GR Ter Haar, AS Protheroe, PJ Friend, FV Gleeson, DW Cranston, RR Phillips, and MR Middleton. The safety and feasibility of extracorporeal high-intensity focused ultrasound (hifu) for the treatment of liver and kidney tumours in a western population. *British journal of cancer*, 93(8):890–895, 2005.

[72] Tetsuya Ishikawa, Takashi Okai, Kazuaki Sasaki, Shin-ichiro Umemura, Rei Fujiwara, Miki Kushima, Mitsuyoshi Ichihara, and Kiyotake Ichizuka. Functional and histological changes in rat femoral arteries by hifu exposure. *Ultrasound in medicine & biology*, 29(10):1471–1477, 2003.

[73] Zahra Izadifar, Zohreh Izadifar, Dean Chapman, and Paul Babyn. An introduction to high intensity focused ultrasound: systematic review on principles, devices, and clinical applications. *Journal of clinical medicine*, 9(2):460, 2020.

[74] Pankaj K Jain, Neeraj Sharma, Argiris A Giannopoulos, Luca Saba, Andrew Nicolaides, and Jasjit S Suri. Hybrid deep learning segmentation models for atheroscle-

rotic plaque in internal carotid artery b-mode ultrasound. *Computers in Biology and Medicine*, 136:104721, 2021.

[75] Hyun Joo Jang, Jae-Young Lee, Don-Haeng Lee, Won-Hong Kim, and Joo Ha Hwang. Current and future clinical applications of high-intensity focused ultrasound (hifu) for pancreatic cancer. *Gut and liver*, 4(Suppl 1):S57, 2010.

[76] Jiri Jaros, Alistair P Rendell, and Bradley E Treeby. Full-wave nonlinear ultrasound simulation on distributed clusters with applications in high-intensity focused ultrasound. *The International Journal of High Performance Computing Applications*, 30(2):137–155, 2016.

[77] Katarzyna Kaczmarek, Tomasz Hornowski, Martina Kubovcikova, Milan Timko, Marceli Koralewski, and Arkadiusz Jozefczak. Heating induced by therapeutic ultrasound in the presence of magnetic nanoparticles. *ACS applied materials & interfaces*, 10(14):11554–11564, 2018.

[78] James E Kennedy. High-intensity focused ultrasound in the treatment of solid tumours. *Nature reviews cancer*, 5(4):321–327, 2005.

[79] Tatiana D Khokhlova, Michael S Canney, Donghoon Lee, Kenneth I Marro, Lawrence A Crum, Vera A Khokhlova, and Michael R Bailey. Magnetic resonance imaging of boiling induced by high intensity focused ultrasound. *The Journal of the Acoustical Society of America*, 125(4):2420–2431, 2009.

[80] Tatiana D Khokhlova, Yak-Nam Wang, Julianna C Simon, Bryan W Cunitz, Frank Starr, Marla Paun, Lawrence A Crum, Michael R Bailey, and Vera A Khokhlova. Ultrasound-guided tissue fractionation by high intensity focused ultrasound in an in vivo porcine liver model. *Proceedings of the National Academy of Sciences*, 111(22):8161–8166, 2014.

[81] JS Kim. Architectural acoustics. *Sejin Co*, 2014.

[82] H Christoph Klingler, Martin Susani, Ralf Seip, Julian Mauermann, Naren Sanghvi, and Michael J Marberger. A novel approach to energy ablative therapy of small renal tumours: laparoscopic high-intensity focused ultrasound. *European urology*, 53(4):810–818, 2008.

[83] Jieun Koh and Min Jung Kim. Introduction of a new staging system of breast cancer for radiologists: an emphasis on the prognostic stage. *Korean journal of radiology*, 20(1):69–82, 2019.

[84] Max O Köhler, Charles Mougenot, Bruno Quesson, Julia Enholm, Brigitte Le Bail, Christophe Laurent, Chrit TW Moonen, and Gösta J Ehnholm. Volumetric hifu ablation under 3d guidance of rapid mri thermometry. *Medical physics*, 36(8):3521–3535, 2009.

[85] Sapna Singh Kshatri and Deepak Singh. Convolutional neural network in medical image analysis: a review. *Archives of Computational Methods in Engineering*, 30(4):2793–2810, 2023.

[86] Keith J Laidler. The development of the arrhenius equation. *Journal of chemical Education*, 61(6):494, 1984.

[87] Salman Lari, Sang Wook Han, Jong Uk Kim, and Hyock Ju Kwon. Design of hifu treatment plans using thermodynamic equilibrium algorithm. *Algorithms*, 15(11):399, 2022.

[88] Salman Lari, Mohammad Kohandel, and Hyock Ju Kwon. Model based deep learning method for focused ultrasound pathway scanning. *Scientific Reports*, 14(1):20042, 2024.

[89] Salman Lari, Hossein Rajabzadeh, Mohammad Kohandel, and Hyock Ju Kwon. A holistic physics-informed neural network solution for precise destruction of breast tumors using focused ultrasound on a realistic breast model. *Mathematical Biosciences and Engineering*, 21(10):7337–7372, 2024.

[90] Yann LeCun, Yoshua Bengio, and Geoffrey Hinton. Deep learning. *nature*, 521(7553):436–444, 2015.

[91] Hongen Liao, Masafumi Noguchi, Takashi Maruyama, Yoshihiro Muragaki, Etsuko Kobayashi, Hiroshi Iseki, and Ichiro Sakuma. An integrated diagnosis and therapeutic system using intra-operative 5-aminolevulinic-acid-induced fluorescence guided robotic laser ablation for precision neurosurgery. *Medical image analysis*, 16(3):754–766, 2012.

[92] Fang Liu, Zhenlin Hu, Lei Qiu, Chun Hui, Chao Li, Pei Zhong, and Junping Zhang. Boosting high-intensity focused ultrasound-induced anti-tumor immunity using a sparse-scan strategy that can more effectively promote dendritic cell maturation. *Journal of translational medicine*, 8(1):1–12, 2010.

[93] Hao-Li Liu, Win-Li Lin, and Yung-Yaw Chen. A fast and conformal heating scheme for producing large thermal lesions using a 2d ultrasound phased array. *International journal of hyperthermia*, 23(1):69–82, 2007.

[94] Xu Liu, Zhimin Huo, and Jiwu Zhang. Automated segmentation of breast lesions in ultrasound images. In *2005 IEEE Engineering in Medicine and Biology 27th Annual Conference*, pages 7433–7435. IEEE, 2006.

[95] Ze Liu, Yutong Lin, Yue Cao, Han Hu, Yixuan Wei, Zheng Zhang, Stephen Lin, and Baining Guo. Swin transformer: Hierarchical vision transformer using shifted windows. In *Proceedings of the IEEE/CVF international conference on computer vision*, pages 10012–10022, 2021.

[96] Frederic L Lizzi, Robert Muratore, Cheri X Deng, Jeffrey A Ketterling, S Kaisar Alam, Samuel Mikaelian, and Andrew Kalisz. Radiation-force technique to monitor lesions during ultrasonic therapy. *Ultrasound in medicine & biology*, 29(11):1593–1605, 2003.

[97] Lu Lu, Xuhui Meng, Zhiping Mao, and George Em Karniadakis. Deepxde: A deep learning library for solving differential equations. *SIAM review*, 63(1):208–228, 2021.

[98] Hui Luo, Guofeng Shen, and Yazhu Chen. Treatment planning of scanning time and path for phased high-intensity focused ultrasound surgery. In *2009 2nd International Conference on Biomedical Engineering and Informatics*, pages 1–4. IEEE, 2009.

[99] Matti Malinen, Tomi Huttunen, Jari P Kaipio, and Kullervo Hynynen. Scanning path optimization for ultrasound surgery. *Physics in Medicine & Biology*, 50(15):3473, 2005.

[100] Rachel L Manthe, Susan P Foy, Nishanth Krishnamurthy, Blanka Sharma, and Vinod Labhasetwar. Tumor ablation and nanotechnology. *Molecular pharmaceutics*, 7(6):1880–1898, 2010.

[101] M Marinova, M Rauch, HH Schild, and HM Strunk. Novel non-invasive treatment with high-intensity focused ultrasound (hifu). *Ultraschall in der Medizin-European Journal of Ultrasound*, 37(01):46–55, 2016.

[102] Michael S Maslakowski, Sheikh J Ilham, Timothy Hall, Thyagarajan Subramanian, Mehdi Kiani, and Mohamed Almekkawy. The characterization and assembly of an efficient, cost effective focused ultrasound transducer. In *2020 IEEE 14th Dallas Circuits and Systems Conference (DCAS)*, pages 1–6. IEEE, 2020.

[103] Starting Matlab. Matlab. *The MathWorks, Natick, MA*, 2012.

[104] Nathan McDannold, Clare M Tempany, Fiona M Fennessy, Minna J So, Frank J Rybicki, Elizabeth A Stewart, Ferenc A Jolesz, and Kullervo Hynynen. Uterine leiomyomas: Mr imaging–based thermometry and thermal dosimetry during focused ultrasound thermal ablation. *Radiology*, 240(1):263, 2006.

[105] Nathan J McDannold, Ferenc A Jolesz, and Kullervo H Hynynen. Determination of the optimal delay between sonications during focused ultrasound surgery in rabbits by using mr imaging to monitor thermal buildup in vivo. *Radiology*, 211(2):419–426, 1999.

[106] Robert J McGough, ML Kessler, ES Ebbini, and CA Cain. Treatment planning for hyperthermia with ultrasound phased arrays. *IEEE transactions on ultrasonics, ferroelectrics, and frequency control*, 43(6):1074–1084, 1996.

[107] D McMahon and M Almekkawy. Optimization of transcostal phased-array refocusing using iterative sparse semidefinite relaxation method. In *2017 IEEE Signal Processing in Medicine and Biology Symposium (SPMB)*, pages 1–3. IEEE, 2017.

[108] Daniel McMahon and Mohamed Almekkawy. Elements selection for transcostal hifu refocusing method: Simulation study. *IEEE transactions on ultrasonics, ferroelectrics, and frequency control*, 67(7):1366–1376, 2020.

[109] Ja S Mendousse. Nonlinear dissipative distortion of progressive sound waves at moderate amplitudes. *The Journal of the Acoustical Society of America*, 25(1):51–54, 1953.

[110] Arkadiusz Miaskowski and Bartosz Sawicki. Magnetic fluid hyperthermia modeling based on phantom measurements and realistic breast model. *IEEE transactions on biomedical engineering*, 60(7):1806–1813, 2013.

[111] D Miklavčič, G Serša, E Brecelj, Julie Gehl, D Soden, Giuseppe Bianchi, Pietro Ruggieri, Carlo Riccardo Rossi, Luigi G Campana, and Tomaz Jarm. Electrochemotherapy: technological advancements for efficient electroporation-based treatment of internal tumors. *Medical & biological engineering & computing*, 50(12):1213–1225, 2012.

[112] Sampa Misra, Seungwan Jeon, Ravi Managuli, Seiyon Lee, Gyuwon Kim, Chiho Yoon, Seungchul Lee, Richard G Barr, and Chulhong Kim. Bi-modal transfer learning for classifying breast cancers via combined b-mode and ultrasound strain imaging.

IEEE Transactions on Ultrasonics, Ferroelectrics, and Frequency Control, 69(1):222–232, 2021.

[113] M Mohammadpour and B Firoozabadi. High intensity focused ultrasound (hifu) ablation of porous liver: Numerical analysis of heat transfer and hemodynamics. *Applied Thermal Engineering*, 170:115014, 2020.

[114] Prempreeya Montienthong and Phadungsak Rattanadecho. Focused ultrasound ablation for the treatment of patients with localized deformed breast cancer: Computer simulation. *Journal of Heat Transfer*, 141(10), 2019.

[115] Woo Kyung Moon, Chung-Ming Lo, Rong-Tai Chen, Yi-Wei Shen, Jung Min Chang, Chiun-Sheng Huang, Jeon-Hor Chen, Wei-Wen Hsu, and Ruey-Feng Chang. Tumor detection in automated breast ultrasound images using quantitative tissue clustering. *Medical physics*, 41(4):042901, 2014.

[116] Colman Moore and Jesse V Jokerst. Strategies for image-guided therapy, surgery, and drug delivery using photoacoustic imaging. *Theranostics*, 9(6):1550, 2019.

[117] Charles Mougenot, Bruno Quesson, Baudouin Denis de Senneville, Philippe Lourenco de Oliveira, Sara Sprinkhuizen, Jean Palussière, Nicolas Grenier, and Chrit TW Moonen. Three-dimensional spatial and temporal temperature control with mr thermometry-guided focused ultrasound (mrghifu). *Magnetic Resonance in Medicine: An Official Journal of the International Society for Magnetic Resonance in Medicine*, 61(3):603–614, 2009.

[118] Charles Mougenot, Rares Salomir, Jean Palussiere, Nicolas Grenier, and Chrit TW Moonen. Automatic spatial and temporal temperature control for mr-guided focused ultrasound using fast 3d mr thermometry and multispiral trajectory of the focal point. *Magnetic Resonance in Medicine: An Official Journal of the International Society for Magnetic Resonance in Medicine*, 52(5):1005–1015, 2004.

[119] Alessandro Napoli, Michele Anzidei, Federica Ciolina, Eugenio Marotta, Beatrice Cavallo Marincola, Giulia Brachetti, Luisa Di Mare, Gaia Cartocci, Fabrizio Boni, Vincenzo Noce, et al. Mr-guided high-intensity focused ultrasound: current status of an emerging technology. *Cardiovascular and interventional radiology*, 36(5):1190–1203, 2013.

[120] Bo Ni, Zhiyuan Liu, Xiantao Cai, Michele Nappi, and Shaohua Wan. Segmentation of ultrasound image sequences by combing a novel deep siamese network with a deformable contour model. *Neural Computing and Applications*, pages 1–15, 2022.

[121] Yicheng Ni, Stefaan Mulier, Y Miao, Luc Michel, and Gilberte Marchal. A review of the general aspects of radiofrequency ablation. *Abdominal imaging*, 30(4):381–400, 2005.

[122] Zhenyuan Ning, Shengzhou Zhong, Qianjin Feng, Wufan Chen, and Yu Zhang. Smu-net: Saliency-guided morphology-aware u-net for breast lesion segmentation in ultrasound image. *IEEE transactions on medical imaging*, 2021.

[123] J Alison Noble and Djamal Boukerroui. Ultrasound image segmentation: a survey. *IEEE Transactions on medical imaging*, 25(8):987–1010, 2006.

[124] Jáuber C Oliveira and Fermín S Viloche Bazán. Poisson approach for evaluating numerical methods for the two-dimensional wave equation constrained to absorbing boundary conditions. *Applied mathematics and computation*, 209(2):273–284, 2009.

[125] A Emin Orhan and Xaq Pitkow. Skip connections eliminate singularities. *arXiv preprint arXiv:1701.09175*, 2017.

[126] Neil R Owen, Michael R Bailey, James Hossack, and Lawrence A Crum. A method to synchronize high-intensity, focused ultrasound with an arbitrary ultrasound imager. *IEEE transactions on ultrasonics, ferroelectrics, and frequency control*, 53(3):645–650, 2006.

[127] Allison Payne, Urvi Vyas, Adam Blankespoor, Douglas Christensen, and Robert Roemer. Minimisation of hifu pulse heating and interpulse cooling times. *International journal of hyperthermia*, 26(2):198–208, 2010.

[128] Mirjam CL Peek and Feng Wu. High-intensity focused ultrasound in the treatment of breast tumours. *Ecancermedicalscience*, 12, 2018.

[129] Harry H Pennes. Analysis of tissue and arterial blood temperatures in the resting human forearm. *Journal of applied physiology*, 1(2):93–122, 1948.

[130] Allan Pinkus. Approximation theory of the mlp model in neural networks. *Acta numerica*, 8:143–195, 1999.

[131] Kui Qian, Chenghai Li, Zhengyang Ni, Juan Tu, Xiasheng Guo, and Dong Zhang. Uniform tissue lesion formation induced by high-intensity focused ultrasound along a spiral pathway. *Ultrasonics*, 77:38–46, 2017.

[132] Long Quan, Dong Zhang, Yan Yang, Yu Liu, and Qianqing Qin. Segmentation of tumor ultrasound image via region-based ncut method. *Wuhan University Journal of Natural Sciences*, 18(4):313–318, 2013.

[133] AmericanCollegeof Radiology. Illustrated breast imaging reporting and data system (bi-rads) ed. *ACo Radiology*, 2003.

[134] Reza Rahpeima and Chao-An Lin. Numerical study of magnetic hyperthermia ablation of breast tumor on an anatomically realistic breast phantom. *Plos one*, 17(9):e0274801, 2022.

[135] Reza Rahpeima, M Soltani, and Farshad Moradi Kashkooli. Numerical study of microwave induced thermoacoustic imaging for initial detection of cancer of breast on anatomically realistic breast phantom. *Computer Methods and Programs in Biomedicine*, 196:105606, 2020.

[136] Maziar Raissi and George Em Karniadakis. Hidden physics models: Machine learning of nonlinear partial differential equations. *Journal of Computational Physics*, 357:125–141, 2018.

[137] Maziar Raissi, Paris Perdikaris, and George E Karniadakis. Physics-informed neural networks: A deep learning framework for solving forward and inverse problems involving nonlinear partial differential equations. *Journal of Computational physics*, 378:686–707, 2019.

[138] John C Rewcastle. High intensity focused ultrasound for prostate cancer: a review of the scientific foundation, technology and clinical outcomes. *Technology in cancer research & treatment*, 5(6):619–625, 2006.

[139] Mohsen Rezaeian, Amir Sedaghatkish, and M Soltani. Numerical modeling of high-intensity focused ultrasound-mediated intraperitoneal delivery of thermosensitive liposomal doxorubicin for cancer chemotherapy. *Drug delivery*, 26(1):898–917, 2019.

[140] Siegel RL. Cancer statistics, 2020., 2020.

[141] Paulo S Rodrigues and Gilson A Giraldi. Improving the non-extensive medical image segmentation based on tsallis entropy. *Pattern Analysis and Applications*, 14(4):369–379, 2011.

[142] R Roemer and AH Payne. Minimization of hifu dose delivery time. *International Society of Therapeutic Ultrasound*, 2007.

[143] Olaf Ronneberger, Philipp Fischer, and Thomas Brox. U-net: Convolutional networks for biomedical image segmentation. In *Medical Image Computing and Computer-Assisted Intervention–MICCAI 2015: 18th International Conference, Munich, Germany, October 5-9, 2015, Proceedings, Part III 18*, pages 234–241. Springer, 2015.

[144] Luis G Rosa, Jonathan S Zia, Omer T Inan, and Gregory S Sawicki. Machine learning to extract muscle fascicle length changes from dynamic ultrasound images in real-time. *PloS one*, 16(5):e0246611, 2021.

[145] JP Michiel Sedelaar, René G Aarnink, Geert JLH van Leenders, Harrie P Beerlage, Frans MJ Debruyne, Hessel Wijkstra, and Jean JMCH de la Rosette. The application of three–dimensional contrast–enhanced ultrasound to measure volume of affected tissue after hifu treatment for localized prostate cancer. *European urology*, 37(5):559–568, 2000.

[146] Wensheng Shen, Jun Zhang, and Fuqian Yang. Modeling and numerical simulation of bioheat transfer and biomechanics in soft tissue. *Mathematical and Computer Modelling*, 41(11-12):1251–1265, 2005.

[147] Yae-Lin Sheu and Pai-Chi Li. Simulations of photoacoustic wave propagation using a finite-difference time-domain method with berenger's perfectly matched layers. *The Journal of the Acoustical Society of America*, 124(6):3471–3480, 2008.

[148] Manpreet Singh. Incorporating vascular-stasis based blood perfusion to evaluate the thermal signatures of cell-death using modified arrhenius equation with regeneration of living tissues during nanoparticle-assisted thermal therapy. *International Communications in Heat and Mass Transfer*, 135:106046, 2022.

[149] Manpreet Singh. Modified pennes bioheat equation with heterogeneous blood perfusion: A newer perspective. *International Journal of Heat and Mass Transfer*, 218:124698, 2024.

[150] Justin Sirignano and Konstantinos Spiliopoulos. Dgm: A deep learning algorithm for solving partial differential equations. *Journal of computational physics*, 375:1339–1364, 2018.

[151] M Soltani, Reza Rahpeima, and Farshad Moradi Kashkooli. Breast cancer diagnosis with a microwave thermoacoustic imaging technique—a numerical approach. *Medical & biological engineering & computing*, 57:1497–1513, 2019.

[152] Joshua E Soneson. A user-friendly software package for hifu simulation. In *AIP Conference Proceedings*, volume 1113, pages 165–169. American Institute of Physics, 2009.

[153] Visa Suomi, Jiri Jaros, Bradley Treeby, and Robin O Cleveland. Full modeling of high-intensity focused ultrasound and thermal heating in the kidney using realistic patient models. *IEEE Transactions on Biomedical Engineering*, 65(5):969–979, 2017.

[154] I Suramo, M Päivänsalo, and V Myllylä. Cranio-caudal movements of the liver, pancreas and kidneys in respiration. *Acta radiologica. Diagnosis*, 25(2):129–131, 1984.

[155] Dassault Systemes. Solidworks 2019. *Dessault Systemes: Vélizy-Villacoublay, France*, 2011.

[156] Alexandre M Tartakovsky, Carlos Ortiz Marrero, Paris Perdikaris, Guzel D Tartakovsky, and David Barajas-Solano. Learning parameters and constitutive relationships with physics informed deep neural networks. *arXiv preprint arXiv:1808.03398*, 2018.

[157] ¿ Gail ter Haar and Constantin Coussios. High intensity focused ultrasound: physical principles and devices. *International journal of hyperthermia*, 23(2):89–104, 2007.

[158] Gail Ter Haar. Ultrasound mediated drug delivery: A 21st century phoenix?, 2012.

[159] Gail Ter Haar. Hifu tissue ablation: concept and devices. *Therapeutic Ultrasound*, pages 3–20, 2016.

[160] Stefan Thüroff and Christian Chaussy. High-intensity focused ultrasound for prostate cancer. *Li-Ming Su, Young Stephen C, editors. Early Dignosis and Treatment of Cancer: Prostate Cancer*, pages 177–92, 2010.

[161] Ying Tong, Yangyang Liu, Manxue Zhao, Lin Meng, and Jiachao Zhang. Improved u-net malf model for lesion segmentation in breast ultrasound images. *Biomedical Signal Processing and Control*, 68:102721, 2021.

[162] BE Treeby and Jie Pan. A practical examination of the errors arising in the direct collocation boundary element method for acoustic scattering. *Engineering analysis with boundary elements*, 33(11):1302–1315, 2009.

[163] Bradley E Treeby and Benjamin T Cox. k-wave: Matlab toolbox for the simulation and reconstruction of photoacoustic wave fields. *Journal of biomedical optics*, 15(2):021314–021314, 2010.

[164] Bradley E Treeby, Jiri Jaros, Alistair P Rendell, and BT Cox. Modeling nonlinear ultrasound propagation in heterogeneous media with power law absorption using k-space pseudospectral method. *The Journal of the Acoustical Society of America*, 131(6):4324–4336, 2012.

[165] Masayuki Tsuneki. Deep learning models in medical image analysis. *Journal of Oral Biosciences*, 64(3):312–320, 2022.

[166] Juan J Valencia and PN Quested. Thermophysical properties. *Modeling for casting and solidification processing*, 189, 2001.

[167] Jonathan W Valvano, JR Cochran, and Kenneth R Diller. Thermal conductivity and diffusivity of biomaterials measured with self-heated thermistors. *International Journal of Thermophysics*, 6:301–311, 1985.

[168] Heng Wang, Jianan Wu, Zihan Zhuo, and Jintian Tang. A three-dimensional model and numerical simulation regarding thermoseed mediated magnetic induction therapy conformal hyperthermia. *Technology and Health Care*, 24(s2):S827–S839, 2016.

[169] NA Watkin, GR Ter Haar, and I Rivens. The intensity dependence of the site of maximal energy deposition in focused ultrasound surgery. *Ultrasound in medicine & biology*, 22(4):483–491, 1996.

[170] Feng Wu, Wen-Zhi Chen, Jin Bai, Jian-Zhong Zou, Zhi-Long Wang, Hui Zhu, and Zhi-Biao Wang. Pathological changes in human malignant carcinoma treated with high-intensity focused ultrasound. *Ultrasound in medicine & biology*, 27(8):1099–1106, 2001.

[171] Feng Wu, Wen-Zhi Chen, Jin Bai, Jian-Zhong Zou, Zhi-Long Wang, Hui Zhu, and Zhi-Biao Wang. Tumor vessel destruction resulting from high-intensity focused ultrasound in patients with solid malignancies. *Ultrasound in medicine & biology*, 28(4):535–542, 2002.

[172] Feng Wu, Zhi-Biao Wang, Wen-Zhi Chen, JIN Bai, HUI Zhu, and Tian-Yu Qiao. Preliminary experience using high intensity focused ultrasound for the treatment of patients with advanced stage renal malignancy. *The Journal of urology*, 170(6):2237–2240, 2003.

[173] Feng Wu, Zhi-Biao Wang, Wen-Zhi Chen, Jian-Zhong Zou, Jin Bai, Hui Zhu, Ke-Quan Li, Fang-Lin Xie, Cheng-Bing Jin, Hai-Bing Su, et al. Extracorporeal focused ultrasound surgery for treatment of human solid carcinomas: early chinese clinical experience. *Ultrasound in medicine & biology*, 30(2):245–260, 2004.

[174] Min Xian, Yingtao Zhang, Heng-Da Cheng, Fei Xu, Boyu Zhang, and Jianrui Ding. Automatic breast ultrasound image segmentation: A survey. *Pattern Recognition*, 79:340–355, 2018.

[175] Cheng Xue, Lei Zhu, Huazhu Fu, Xiaowei Hu, Xiaomeng Li, Hai Zhang, and Pheng-Ann Heng. Global guidance network for breast lesion segmentation in ultrasound images. *Medical image analysis*, 70:101989, 2021.

[176] Hui Yao, Pornchai Phukpattaranont, and Emad S Ebbini. Nonlinear imaging methods for characterization of hifu-induced lesions. In *Thermal Treatment of Tissue: Energy Delivery and Assessment II*, volume 4954, pages 183–191. SPIE, 2003.

[177] Kyungho Yoon, Wonhye Lee, Phillip Croce, Amanda Cammalleri, and Seung-Schik Yoo. Multi-resolution simulation of focused ultrasound propagation through ovine skull from a single-element transducer. *Physics in Medicine & Biology*, 63(10):105001, 2018.

[178] E Zastrow. Database of 3d grid-based numerical breast phantoms for use in computational electromagnetics simulations e. zastrow, sk davis, m. lazebnik, f. kelcz, bd van veen, and sc hagness department of electrical and computer engineering university of wisconsin-madison.

[179] Dong Zhang, Menglong Xu, Long Quan, Yan Yang, Qianqing Qin, and Wenbin Zhu. Segmentation of tumor ultrasound image in hifu therapy based on texture and boundary encoding. *Physics in Medicine & Biology*, 60(5):1807, 2015.

[180] Ju Zhang, Chen Wang, and Yun Cheng. Comparison of despeckle filters for breast ultrasound images. *Circuits, Systems, and Signal Processing*, 34(1):185–208, 2015.

[181] Hui Zhong, Ming-Xi Wan, Yi-Feng Jiang, and Su-Pin Wang. Monitoring imaging of lesions induced by high intensity focused ultrasound based on differential ultrasonic attenuation and integrated backscatter estimation. *Ultrasound in medicine & biology*, 33(1):82–94, 2007.

[182] Ran Zhou, M Reza Azarpazhooh, J David Spence, Samineh Hashemi, Wei Ma, Xinyao Cheng, Haitao Gan, Mingyue Ding, and Aaron Fenster. Deep learning-based carotid plaque segmentation from b-mode ultrasound images. *Ultrasound in Medicine & Biology*, 47(9):2723–2733, 2021.

[183] S Kevin Zhou, Hayit Greenspan, Christos Davatzikos, James S Duncan, Bram Van Ginneken, Anant Madabhushi, Jerry L Prince, Daniel Rueckert, and Ronald M Summers. A review of deep learning in medical imaging: Imaging traits, technology trends, case studies with progress highlights, and future promises. *Proceedings of the IEEE*, 2021.

[184] Yu-Feng Zhou. High intensity focused ultrasound in clinical tumor ablation. *World journal of clinical oncology*, 2(1):8, 2011.

[185] Yufeng Zhou. Generation of uniform lesions in high intensity focused ultrasound ablation. *Ultrasonics*, 53(2):495–505, 2013.

[186] Yufeng Zhou, Steven G Kargl, and Joo Ha Hwang. Producing uniform lesion pattern in hifu ablation. In *AIP Conference Proceedings*, volume 1113, pages 91–95. American Institute of Physics, 2009.

[187] Yufeng Zhou, Steven G Kargl, and Joo Ha Hwang. The effect of the scanning pathway in high-intensity focused ultrasound therapy on lesion production. *Ultrasound in medicine & biology*, 37(9):1457–1468, 2011.

[188] Zhuhuang Zhou, Weiwei Wu, Shuicai Wu, Po-Hsiang Tsui, Chung-Chih Lin, Ling Zhang, and Tianfu Wang. Semi-automatic breast ultrasound image segmentation based on mean shift and graph cuts. *Ultrasonic imaging*, 36(4):256–276, 2014.

[189] Zhemin Zhuang, Nan Li, Alex Noel Joseph Raj, Vijayalakshmi GV Mahesh, and Shunmin Qiu. An rdau-net model for lesion segmentation in breast ultrasound images. *PloS one*, 14(8):e0221535, 2019.